MONTMORILLONITE AND MODIFIED MONTMORILLONITE SUPPORTED ZnO CATALYSTS

by

Ayşe Hazal PEKCAN

B.S., Chemistry, İstanbul University, 2012

Submitted to the Institute for Graduate Studies in
Science and Engineering in partial fulfillment of
the requirements for the degree of
Master of Science

Graduate Program in Chemistry
Boğaziçi University
2015

MONTMORILLONITE AND MODIFIED MONTMORILLONITE SUPPORTED ZnO CATALYSTS

APPROVED BY:

Assoc. Prof. Ayşe Neren Ökte (Thesis Supervisor)	…..……..…….....
Assoc. Prof. Sinan Şen	…….
Prof. Duygu Avcı Semiz	……..……

DATE OF APPROVAL: 25.05.2015

ACKNOWLEDGEMENTS

I would like to thank my supervisor Assoc. Prof. A. Neren Ökte for her patience, guidance and encouragement in every stage of this project. Her wisdom is widened my horizon. I am really grateful to have the chance to work with her, it was a precious experience.

I also express my thanks to Assoc. Prof. Sinan Şen and Prof. Duygu Avcı Semiz for being my committee members, reviewing my work and making guiding comments.

Additionally, I would like to thank Assoc. Prof Sinan Şen from Yalova University, Polymer Engineering Department. He kindly provided the modified clay materials which are used in this project. Moreover, I want to thank Emre Tekay, who prepared the modified clay, from Yalova University, Polymer Engineering Department.

I would like to extend my thanks to Elif Doğan, Havvanur Selçuk and all the faculty members in the Boğaziçi University Chemistry Department for their altruism and kindness during my master education. I wish to thank Bilge Gedik Uluocak for SEM analysis and Erkan Karabekmez for XRD analysis.

Another person that I really want to thank for her help and encouragement for this project is Duygu Tuncel. Her light show me the way when I lose my hope. At the end we are more than friends and our sistership will last forever. Also I want to thank my colleagues Taner Özden, Aktan Polat, Tankut Türel, Ari Hakgör, Oya Arıca, Seval Bayrak Özen, Güliz Kıvançlı, Ayşenur Özdemir, Gizem Kırevliyası, Birses Debir and Sesil Agopcan for moral support and their friendship.

My deepest thanks belong to Cafer Çetin. I know him just for few months but he already filled my world and I cannot imagine a life without him. Even when he is far away, he tried his best to cheer me up. I am really appreciated for his love and support.

In addition to these, it is a good opportunity to express my thanks to my father (Merih Pekcan), my mother (Gülşen Pekcan) and my brother (Hasan Ali Pekcan) who dedicate their life to me without hesitating. I felt your unconditional love in every stage of my life. I am the luckiest person as being your daughter.

This study supported by Boğaziçi University Research Foundation (Project No. 14B05P11/8820)

ABSTRACT

MONTMORILLONITE AND MODIFIED MONTMORILLONITE SUPPORTED ZnO CATALYSTS

The purpose of this study is to prepare ZnO supported montmorillonite based catalysts by using co-precipitation technique. The photocatalytic activities of the as-prepared catalysts are studied for degradation/decolorization of methyl orange (MO) under UV irradiation. The morphological aspects of the catalysts are examined by X-ray diffractometer (XRD), scanning electron microscopy (SEM) with energy dispersive X-ray (EDX) and elemental mapping analysis, surface area analyzer (BET) and UV-Vis diffuse reflectance spectrometry (UV-Vis DRS). XRD results supply information about the ZnO crystalline sizes of the catalysts. SEM (EDX) analysis shows the differences in the surface morphologies of the bare clays and supported catalysts. For all supported catalysts, the characteristic ZnO band edge is detected within UV region and also increments in the surface areas and pore volumes are noticed by the BET measurements. Freundlich adsorption model explains the dark adsorption behavior of the supported catalysts. ZnO loading amounts, affect the photoactivities. Degradation/decolorization processes follow pseudo first order kinetics. Langmuir-Hinshelwood model is found to be applicable for the supported catalysts. The re-use abilities of the catalysts are controlled. A decomposition mechanism of the MO is postulated.

ÖZET

MONTMORİLLONİT VE MODİFİYE EDİLMİŞ MONTMORİLLONİT İLE DESTEKLENMİŞ ZnO KATALİSTLERİ

Bu çalışmanın amacı montmorillonit temelli materyallerle desteklenmiş ZnO katalistlerinin çöktürme yöntemiyle hazırlanmasıdır. Hazırlanan katalistlerin UV ışıkla aktiviteleri metil oranj (MO) degradasyon/dekolarizasyonu ile takip edilmiştir. Katalistlerin biçimsel özellikleri X-ışını kırınım ölçer (XRD), enerji dağılımlı X-ışınları analizi ve elementel dağılım haritası beraberindeki taramalı elektron mikroskobu (SEM-EDX) yüzey alanı analizi (BET) ve dağınık yansıtmalı UV-Vis spektrometresi (UV-Vis DRS) ile analiz edilmiştir. XRD analizi ZnO katalistlerinin kristal boyutuyla ilgili bilgi vermektedir. SEM (EDX) analizleri kil materyalleri ve desteklenmiş katalistler arasındaki yapısal farklılıkları göstermektedir. Bütün desteklenmiş killerde ZnO nanokristallerine ait olan band-edge UV bölgesinde saptanmış ve ayrıca BET ölçümlerinde katalistlerin yüzey alanları ve gözenek hacimlerinin artış gösterdiği gözlemlenmiştir. Freundlich adsorpsiyon modeli desteklenmiş katalistlerin karanlıkta adsorplama sürecini açıklamaktadır. ZnO yükleme miktarının fotoaktiviteyi etkilediği bulunmuştur. Desteklenmiş katalistleri degradasyon/dekolorizasyon süreçleri görünür birinci mertebe kinetiğine uymaktadır. Langmuir-Hinshelwood modeli desteklenmiş katalistler için uygulanabilir bulunmuştur. Desteklenmiş katalistlerin tekrar kullanılabilirlikleri kontrol edilmiştir. MO parçalanma sürecini açıklayan bir mekanizma belirlenmiştir.

TABLE OF CONTENTS

ACKNOWLEDGEMENTS iii
ABSTRACT v
ÖZET vi
TABLE OF CONTENTS viii
LIST OF FIGURES xi
LIST OF TABLES xxxii
LIST OF SYMBOLS xxxiv
LIST OF ACRONYMS / ABBREVIATIONS xxxv
1. INTRODUCTION 1
2. THEORY 3
2.1. Heterogeneous Photocatalysis 3
2.2. Zinc Oxide 6
2.3. Factors Effecting Surface and Morphological Aspects in Photocatalysis 7
2.4. Kinetic Studies 11
2.4.1. Dark Adsorption Kinetics 11
2.4.2. Adsoption Isotherms 12
2.4.3. Experiments Followed Under UV Irradiation 13
2.5. Preparation of ZnO Nanoparticles: Co-precipitation Method 14
2.6. Support 15
2.6.1. Montmorillonite 15
2.6.2. Organically Modified Montmorillonite Clays 17
2.7. Literature Survey 18
3. EXPERIMENTAL 24
3.1. Materials 24

3.1.1. Methyl Orange 24
3.2. Preparation and Characterization of ZnO Catalysts 25
3.3. Preparation of NC1, NC2 and MMT2 Supports 27
3.3.1. NC1 27
3.3.2. NC2 28
3.3.3. MMT2 29
3.4. Preparation of Supported Catalysts 30
3.4. Analysis 31
3.4.1. Characterization Techniques 31
3.4.2. Photocatalytic Experiments 31
3.5. Postulated Mechanism of MO Decomposition 33
4. RESULTS AND DISCUSSION 36
4.1. Characterization Results of the ZnO-MMT Catalysts 36
4.1.1. XRD Analysis 36
4.1.2. SEM-EDX Analysis 38
4.1.3. Nitrogen Adsorption-Desorption Isotherms 40
4.1.4. UV-Vis DRS Analysis 43
4.2. Photoactivities of ZnO-MMT Catalysts 45
4.2.1. Control Experiments 45
4.2.2. Dark Adsorption Experiments 46
4.2.2.1. Adsorption Kinetics. 46
4.2.2.2. Adsorption Isotherms. 47
4.2.3. Photocatalytic Experiments 56
4.2.3.1. Effect of ZnO Loading. 56
4.2.3.2. Effect of Initial MO Concentration. 58
4.3. Characterization Results of the ZnO-NC1 Catalysts 62
4.3.1. XRD Analysis 62

4.3.2. SEM-EDX Analysis 64
4.3.3. Nitrogen Adsorption-Desorption Isotherms 67
4.3.4. UV-Vis DRS Analysis 69
4.4. Photoactivities of ZnO-NC1 Catalysts 72
4.4.1. Control Experiments 72
4.4.2. Dark Adsorption Experiments 73
4.4.2.1. Adsortion Kinetics. 73
4.4.2.2. Adsorption Isotherms. 74
4.4.3. Photocatalytic Experiments 83
4.4.3.1. Effect of ZnO Loading 83
4.4.3.2. Effect of Initial MO Concentration. 85
4.5. Characterization Results of the ZnO-NC2 Catalysts 90
4.5.1. XRD Analysis 90
4.5.2. SEM-EDX Analysis 92
4.5.3. Nitrogen Adsorption-Desorption Isotherms 94
4.5.4. UV-Vis DRS Analysis 97
4.6. Photoactivities of ZnO-NC2 Catalysts 99
4.6.1. Control Experiments 99
4.6.2. Dark Adsorption Experiments 101
4.6.2.1. Adsorption Kinetics. 101
4.6.2.2. Adsorption Isotherms. 101
4.6.3. Photocatalytic Experiments 100
4.6.3.1. Effect of ZnO Loading 110
4.6.3.2. Effect of Initial MO Concentration. 112
4.7. Characterization Results of the ZnO-MMT2 Catalysts 117
4.7.1. XRD Analysis 117
4.7.2. SEM-EDX Analysis 120

4.7.3. Nitrogen Adsorption-Desorption Isotherms 122
4.7.4. UV-Vis DRS Analysis..... 124
4.8. Photoactivities of ZnO-MMT2 Catalysts..... 127
4.8.1. Control Experiments..... 127
4.8.2. Dark Adsorption Experiments 128
4.8.2.1. Adsortion Kinetics..... 128
4.8.2.2. Adsorption Isotherms. 129
4.8.3. Photocatalytic Experiments 138
4.8.3.1. Effect of ZnO Loading..... 138
4.8.3.2. Effect of Initial MO Concentration. 140
4.9. Reuse Properties of Supported Catalysts 145
4.10. General Remarks..... 150
5. CONCLUSION..... 152
REFERENCES..... 153

LIST OF FIGURES

Figure 2.1. Photocatalytic degradation mechanism. 5

Figure 2.2. Band positions and band gap energies of the several semiconductors. 6

Figure 2.3. Crystal structure of wurtzite. 7

Figure 2.4. Relation between band gap energy and semiconductor material. 9

Figure 2.5. Structure of montmorillonite. 17

Figure 3.1. Chemical structure of methyl orange. 25

Figure 3.2. UV-vis spectra of MO. 25

Figure 3.3. XRD pattern of 0.25M ZnO. 26

Figure 3.4. SEM image of 0.25M ZnO. Inset: EDX analysis. 26

Figure 3.5. Molecular structure of methyldihydroxyethyl hydrogenated tallow ammonium. 27

Figure 3.6. Modification mechanism of Na-MMT with 25-30 wt % methyl dihydroxyethyl hydrogenated tallow ammonium. 27

Figure 3.7. Molecular structure of octadecylamine. 28

Figure 3.8. Molecular structure of aminopropyltriethoxysilane. 28

Figure 3.9. Modification mechanism of Na-MMT with 15-35 wt % octadecylamine and 0.5-5 wt % aminopropyltriethoxysilane. 29

Figure 3.10. Molecular structure of CTAB. 29

Figure 3.11. Modification mechanism of Na-MMT with cetyltrimethyl ammonium bromide. 30

Figure 3.12. Irradiation box used in photocatalytic degradation experiments. 32

Figure 3.13. Emission spectrum of a fluorescent lamp used in UV-irradiation box. 33

Figure 3.14. Calibration plots of MO at 278 nm (degradation) and 464 nm (decolorization). 33

Figure 3.15. Proposed decomposition mechanism of MO. 35

Figure 4.1. XRD patterns of MMT and supported catalysts (300˚C). (Z: ZnO). 37

Figure 4.2. XRD patterns of MMT and supported catalysts (500˚C). (Z: ZnO). 38

Figure 4.3. SEM image of MMT. 39

Figure 4.4. SEM image of 0.25M ZnO-MMT and mapping images of 0.25M ZnO - MMT, Zn, Al, Mg, O and Si. 40

Figure 4.5. Nitrogen adsorption - desorption isotherms of MMT, 0.25M ZnO and supported catalysts prepared at 300˚C. 41

Figure 4.6. Pore size distribution plots of MMT and supported catalysts prepared at 300˚C. 41

Figure 4.7. Nitrogen adsorption-desorption isotherms of MMT, 0.25M ZnO and supported catalysts prepared at 500˚C. 42

Figure 4.8. Pore size distribution plots of MMT and supported catalysts prepared at 500˚C. 42

Figure 4.9. UV - Vis DRS spectra of MMT and supported catalysts prepared at 300˚C. Inset: UV-Vis DRS spectra of 0.25M ZnO (500˚C). 43

Figure 4.10. UV-vis DRS spectra of supported catalysts prepared at 500˚C. 44

Figure 4.11. Band gap adsorption edges of supported catalysts. Inset: Band gap adsorption edges of 0.25M ZnO (500˚C). 44

Figure 4.12. Band gap adsorption edges of supported catalysts. 45

Figure 4.13. Control experiments in the dark. Conditions: pH: 6.5 (Natural), $[MO]_0$ = 3.27 mg/L, T = 298 K, Flow rate = 2000 rpm. 46

Figure 4.14. Control experiments under UV irradiation. Inset: Photolysis of MO. Conditions: pH: 6.5 (Natural), $[MO]_0$= 3.27 mg/L, T= 298K, Flow rate= 2000 rpm. 46

Figure 4.15. Pseudo first order kinetics for degradation of MO in the presence of 0.5M ZnO-MMT (300˚C). Conditions: pH= 6.5 (Natural), $[MO]_0$= 16.32 mg/L, T= 298 K, Flow rate= 2000 rpm. 48

Figure 4.16. Pseudo first order kinetics for decolorization of MO in the presence of 0.5M ZnO-MMT (300˚C). Conditions: pH= 6.5 (Natural), $[MO]_0$ = 16.32 mg/L, Calcination= 300˚C, T= 298 K; Flow rate= 2000 rpm. 48

Figure 4.17. Pseudo first order kinetics for degradation of MO in the presence of 0.5M ZnO-MMT (500˚C). Conditions: pH= 6.5 (Natural), $[MO]_0$= 16.32 mg/L, T= 298 K, Flow rate= 2000 rpm. 49

Figure 4.18. Pseudo first order kinetics for decolorization of MO in the presence of 0.5M ZnO-MMT (500˚C). Conditions: pH= 6.5 (Natural), $[MO]_0$= 16.32 mg/L, T= 298 K, Flow rate= 2000 rpm. 49

Figure 4.19. Pseudo second order kinetics for degradation of MO in the presence of 0.5M ZnO-MMT (300˚C). Conditions: pH=6.5 (Natural), $[MO]_0$= 16.32 mg/L, T= 298 K, Flow rate= 2000 rpm. 50

Figure 4.20. Pseudo second order kinetics for decolorization of MO in the presence of 0.5M ZnO-MMT (300˚C). Conditions: pH= 6.5 (Natural), $[MO]_0$= 16.32 mg/L, T= 298 K, Flow rate= 2000 rpm. 50

Figure 4.21. Pseudo second order kinetics for degradation of MO in the presence of 0.5M ZnO-MMT (500˚C). Conditions: pH= 6.5 (Natural), $[MO]_0$= 16.32 mg/L, T= 298 K, Flow rate= 2000 rpm. 51

Figure 4.22. Pseudo second order kinetics for decolorization of MO in the presence of 0.5M ZnO-MMT (500˚C). Conditions: pH= 6.5 (Natural), $[MO]_0$ = 16.32 mg/L, T= 298 K, Flow rate= 2000 rpm. 51

Figure 4.23. Freundlich adsorption isotherm for degradation of MO in the presence of 0.5M ZnO-MMT (300˚C). Conditions: pH= 6.5 (Natural), T= 298K, Flow rate= 2000 rpm. 52

Figure 4.24. Freundlich adsorption isotherm for decolorization of MO in the presence of 0.5M ZnO-MMT (300˚C). Conditions: pH= 6.5 (Natural), T = 298K, Flow rate = 2000 rpm. 52

Figure 4.25. Freundlich adsorption isotherm for degradation of MO in the presence of 0.5M ZnO - MMT (500˚C). Conditions: pH = 6.5 (Natural), T = 298K, Flow rate= 2000 rpm. 53

Figure 4.26. Freundlich adsorption isotherm for decolorization of MO in the presence of 0.5M ZnO-MMT (500˚C). Conditions: pH = 6.5 (Natural), T= 298K, Flow rate= 2000 rpm. 53

Figure 4.27. Langmuir adsorption isotherm for decolorization of MO in the presence of 0.5M ZnO-MMT (300˚C). Inset: C_e/q_e vs. C_e plot. Conditions: pH = 6.5 (Natural), T = 298K, Flow rate= 2000 rpm. 54

Figure 4.28. Langmuir adsorption isotherm for decolorization of MO in the presence of 0.5M ZnO-MMT (300˚C). Inset: C_e/q_e vs. C_e plot. Conditions: pH = 6.5 (Natural), T = 298K, Flow rate= 2000 rpm. 54

Figure 4.29. Langmuir adsorption isotherm for degradation of MO in the presence of 0.5M ZnO-MMT (500˚C). Inset: C_e/q_e vs. C_e plot. Conditions: pH = 6.5 (Natural), T = 298K, Flow rate = 2000 rpm. 55

Figure 4.30. Langmuir adsorption isotherm for decolorization of MO in the presence of 0.5M ZnO-MMT (500˚C). Inset: C_e/q_e vs. C_e plot. Conditions: pH = 6.5 (Natural), T = 298K, Flow rate = 2000 rpm. 55

Figure 4.31. MO degradation in the presence of supported catalysts prepared at 300˚C. Conditions: pH = 6.5 (Natural), $[MO]_0$= 3.27 mg/L, T = 298 K, Flow rate= 2000 rpm. 56

Figure 4.32. MO decolorization in the presence of supported catalysts prepared at 300˚C. Conditions: pH= 6.5 (Natural), $[MO]_0$= 3.27 mg/L, T= 298 K, Flow rate= 2000 rpm. 57

Figure 4.33. MO degradation in the presence of supported catalysts prepared at 500˚C. Conditions: pH= 6.5 (Natural), $[MO]_0$= 3.27 mg/L, T= 298 K, Flow rate= 2000 rpm. 57

Figure 4.34. MO degradation in the presence of supported catalysts prepared at 500˚C. Conditions: pH= 6.5 (Natural), $[MO]_0$= 3.27 mg/L, T= 298 K, Flow rate= 2000 rpm. 58

Figure 4.35. MO degradation at initial MO concentrations in the presence of 0.5M ZnO-MMT (300˚C) and 0.5M ZnO-MMT (500˚C). Conditions: pH = 6.5 (Natural), T= 298 K, Flow rate= 2000 rpm. 59

Figure 4.36. MO degradation at initial MO concentrations in the presence of 0.5M ZnO-MMT (300˚C) and 0.5M ZnO-MMT (500˚C). Conditions: pH = 6.5 (Natural), T= 298 K, Flow rate= 2000 rpm. 59

Figure 4.37. Pseudo-first order kinetics for degradation of MO in the presence of 0.5M ZnO-MMT (300˚C). Inset: Langmuir-Hinshelwood analysis. Conditions: pH = 6.5 (Natural), T = 298 K, Flow rate = 2000 rpm. 60

Figure 4.38. Pseudo-first order kinetics for decolorization of MO in the presence of 0.5M ZnO-MMT (300˚C). Inset: Langmuir-Hinshelwood analysis. Conditions: pH = 6.5 (Natural), T = 298 K, Flow rate = 2000 rpm. 60

Figure 4.39. Pseudo-first order kinetics for degradation of MO in the presence of 0.5M ZnO-MMT (500˚C). Inset: Langmuir-Hinshelwood analysis. Conditions: pH = 6.5 (Natural), T = 298 K, Flow rate = 2000 rpm. 61

Figure 4.40. Pseudo-first order kinetics for decolorization of MO in the presence of 0.5M ZnO-MMT (500˚C). Inset: Langmuir-Hinshelwood analysis. Conditions: pH = 6.5 (Natural), T = 298 K, Flow rate = 2000 rpm. 61

Figure 4.41. XRD patterns of NC1 (A) and supported catalysts (300 ^{o}C) (B-D). (Z: ZnO)..... 64

Figure 4.42. XRD patterns of NC1 (A) and supported catalysts (500^{o}C) (B-D). (Z: ZnO)..... 64

Figure 4.43. SEM image of NC1. 66

Figure 4.44. SEM image of 0.25M ZnO-NC1 (500 ^{o}C) and mapping images of 0.25M ZnO-NC1, Zn, Al, Mg, O and Si. 66

Figure 4.45. Nitrogen adsorption-desorption isotherms of NC1 and supported catalysts prepared at 300˚C. 67

Figure 4.46. Pore size distribution plots of NC1 and supported catalysts prepared at 300˚C. 68

Figure 4.47. Nitrogen adsorption-desorption isotherms of NC1 and supported catalysts prepared at 500˚C. 68

Figure 4.48. Pore size distribution plots of NC1 and supported catalysts prepared at 300˚C. 69

Figure 4.49. UV-Vis DRS spectra of NC1 and supported catalysts prepared at 300˚C. Inset: UV - Vis DRS spectra of 0.25M ZnO (500˚C). 70

Figure 4.50. UV-Vis DRS spectra of supported catalysts prepared at 500˚C. 70

Figure 4.51. Band gap adsorption edges of supported catalysts. Inset: Band gap adsorption edges of 0.25M ZnO (500˚ C). 71

Figure 4.52. Band gap adsorption edges of supported catalysts. 71

Figure 4.53. Control experiments in the dark. Conditions: pH: 6.5 (Natural), $[MO]_0$ = 3.27 mg/L, T = 298 K, Flow rate = 2000 rpm. 72

Figure 4.54. Control experiments under UV irradiation. Inset: Photolysis of MO. Conditions: pH: 6.5 (Natural), $[MO]_0$= 3.27 mg/L, T= 298K, Flow rate= 2000 rpm. 73

Figure 4.55. Pseudo first order kinetics for degradation of MO in the presence of 0.5M ZnO-NC1 (300˚C). Conditions: pH= 6.5 (Natural), $[MO]_0$= 8.17 mg/L, T= 298 K, Flow rate= 2000 rpm. 75

Figure 4.56. Pseudo first order kinetics for decolorization of MO in the presence of 0.5M ZnO-NC1 (300˚C). Conditions: pH= 6.5 (Natural), $[MO]_0$= 8.17 mg/L, T= 298 K, Flow rate= 2000 rpm. 75

Figure 4.57. Pseudo first order kinetics for degradation of MO in the presence of 0.5M ZnO-NC1 (500˚C). Conditions: pH = 6.5 (Natural), $[MO]_0$ = 8.17 mg/L, T = 298 K, Flow rate = 2000 rpm. 76

Figure 4.58. Pseudo first order kinetics for decolorization of MO in the presence of 0.5M ZnO-NC1 (500˚C). Conditions: pH= 6.5 (Natural), $[MO]_0$= 8.17 mg/L, T = 298 K, Flow rate = 2000 rpm. 76

Figure 4.59. Pseudo second order kinetics for degradation of MO in the presence of 0.5M ZnO-NC1 (300˚C). Conditions: pH= 6.5 (Natural), $[MO]_0$ = 8.17 mg/L, T = 298 K, Flow rate = 2000 rpm. 77

Figure 4.60. Pseudo second order kinetics for decolorization of MO in the presence of 0.5M ZnO-NC1 (300˚C). Conditions: pH= 6.5 (Natural), $[MO]_0$ = 8.17 mg/L, T = 298 K, Flow rate = 2000 rpm. 77

Figure 4.61. Pseudo second order kinetics for degradation of MO in the presence of 0.5M ZnO-NC1 (500˚C). Conditions: pH= 6.5 (Natural), $[MO]_0$= 8.17 mg/L, T = 298 K, Flow rate = 2000 rpm. 78

Figure 4.62. Pseudo second order kinetics for decolorization of MO in the presence of 0.5M ZnO - NC1 (500˚C). Conditions: pH= 6.5 (Natural), $[MO]_0$ = 8.17 mg/L, T = 298 K, Flow rate = 2000 rpm. 78

Figure 4.63. Freundlich adsorption isotherm for degradation of MO in the presence of 0.5M ZnO-NC1 (300˚C). Conditions: pH= 6.5 (Natural), T = 298K, Flow rate = 2000 rpm. 79

Figure 4.64. Freundlich adsorption isotherm for decolorization of MO in the presence of 0.5M ZnO-NC1 (300˚C). Conditions: pH= 6.5 (Natural), T = 298K, Flow rate = 2000 rpm. 79

Figure 4.65. Freundlich adsorption isotherm for degradation of MO in the presence of 0.5M ZnO-NC1 (500˚C). Conditions: pH= 6.5 (Natural), T = 298K, Flow rate = 2000 rpm. 80

Figure 4.66. Freundlich adsorption isotherm for decolorization of MO in the presence of 0.5M ZnO-NC1 (500˚C). Conditions: pH= 6.5 (Natural), T = 298K, Flow rate = 2000 rpm. 80

Figure 4.67. Langmuir adsorption isotherm for degradation of MO in the presence of 0.5M ZnO-NC1 (300˚C). Inset: C_e/q_e vs. C_e plot. Conditions: pH= 6.5 (Natural), T= 298K, Flow rate= 2000 rpm. 81

Figure 4.68. Langmuir adsorption isotherm for decolorization of MO in the presence of 0.5M ZnO-NC1 (300˚C). Inset: C_e/q_e vs. C_e plot. Conditions: pH= 6.5 (Natural), T= 298K, Flow rate= 2000 rpm. 81

Figure 4.69. Langmuir adsorption isotherm for degradation of MO in the presence of 0.5M ZnO-NC1 (500˚C). Inset: C_e/q_e vs. C_e plot. Conditions: pH= 6.5 (Natural), T= 298K, Flow rate= 2000 rpm. 82

Figure 4.70. Langmuir adsorption isotherm for decolorization of MO in the presence of 0.5M ZnO-NC1 (500˚C). Inset: C_e/q_e vs. C_e plot. Conditions: pH= 6.5 (Natural), T= 298K, Flow rate= 2000 rpm. 82

Figure 4.71. MO degradation in the presence of supported catalysts prepared at 300˚C. Conditions: pH = 6.5 (Natural), $[MO]_0$ = 3.27 mg/L, T= 298 K, Flow rate = 2000 rpm. 83

Figure 4.72. MO decolorization in the presence of supported catalysts prepared at 300˚C. Conditions: pH= 6.5 (Natural), $[MO]_0$ = 3.27 mg/L, T = 298 K, Flow rate = 2000 rpm. 84

Figure 4.73. MO degradation in the presence of supported catalysts prepared at 500˚C. Conditions: pH= 6.5 (Natural), $[MO]_0$= 3.27 mg/L, T= 298 K, Flow rate= 2000 rpm. 84

Figure 4.74. MO degradation in the presence of supported catalysts prepared at 500˚C. Conditions: pH = 6.5 (Natural), $[MO]_0$= 3.27 mg/L, T = 298 K, Flow rate = 2000 rpm. 85

Figure 4.75. MO degradation at initial MO concentrations in the presence of 0.5M ZnO-NC1 (300˚C) and 0.5M ZnO-NC1 (500˚C).Conditions: pH=6.5 (Natural), T= 298 K, Flow rate= 2000 rpm. 86

Figure 4.76. MO decolorization at initial MO concentrations in the presence of 0.5M ZnO-NC1 (300˚C) and 0.5M ZnO-NC1 (500˚C).Conditions: pH= 6.5 (Natural), T= 298 K, Flow rate= 2000 rpm. 86

Figure 4.77. Pseudo-first order kinetics for degradation of MO in the presence of 0.5M ZnO-NC1 (300˚C). Inset: Langmuir-Hinshelwood analysis. Conditions: pH= 6.5 (Natural), T= 298 K, Flow rate= 2000 rpm. 87

Figure 4.78. Pseudo-first order kinetics for decolorization of MO in the presence of 0.5M ZnO-NC1 (300˚C). Inset: Langmuir-Hinshelwood analysis. Conditions: pH=6.5 (Natural), T= 298 K, Flow rate= 2000 rpm. 87

Figure 4.79. Pseudo-first order kinetics for degradation of MO in the presence of 0.5M ZnO-NC1 (500˚C). Inset: Langmuir-Hinshelwood analysis. Conditions: pH= 6.5 (Natural), T= 298 K, Flow rate= 2000 rpm. 88

Figure 4.80. Pseudo - first order kinetics for decolorization of MO in the presence of 0.5M ZnO - NC1 (500˚C). Inset: Langmuir-Hinshelwood analysis. Conditions: pH = 6.5 (Natural), T = 298 K, Flow rate = 2000 rpm. 88

Figure 4.81. XRD patterns of NC2 (A) and supported catalysts (300˚C) (B-D). (Z: ZnO)..... 91

Figure 4.82. XRD patterns of NC2 (A) and supported catalysts (500˚C) (B-D). (Z: ZnO)..... 92

Figure 4.83. SEM image of NC2. 93

Figure 4.84. SEM image of 0.25M ZnO-NC2 (500˚C) and mapping images of 0.25M ZnO-NC2 (500˚C), Zn, Al, Mg, O and Si. 94

Figure 4.85. Nitrogen adsorption-desorption isotherms of NC2 and supported catalysts prepared at 300˚C. 95

Figure 4.86. Pore size distribution plots of NC2 and supported catalysts prepared at 300˚C. 95

Figure 4.87. Nitrogen adsorption-desorption isotherms of NC2 and supported catalysts prepared at 500˚ C. 96

Figure 4.88. Pore size distribution plots of NC2 and supported catalysts prepared at 500˚C. 96

Figure 4.89. UV UV-Vis DRS spectra of NC2 and supported catalysts prepared at 300˚C. Inset: UV-Vis DRS spectra of 0.25M ZnO (500˚C). 97

Figure 4.90. UV-Vis DRS spectra of supported catalysts prepared at 500˚C. 98

Figure 4.91. Band gap adsorption edges of supported catalysts. Inset: Band gap adsorption edges of 0.25M ZnO (500 ˚C). 98

Figure 4.92. Band gap adsorption edges of supported catalysts. 99

Figure 4.93. Control experiments in the dark. Conditions: pH: 6.5 (Natural), $[MO]_0$ = 3.27 mg/L, T = 298 K, Flow rate = 2000 rpm. 100

Figure 4.94. Control experiments under UV irradiation. Inset: Photolysis of MO. Conditions: pH: 6.5 (Natural), $[MO]_0$= 3.27 mg/L, T= 298K, Flow rate= 2000 rpm. 100

Figure 4.95. Pseudo first order kinetics for degradation of MO in the presence of 0.5M ZnO-NC2 (300˚C). Conditions: pH= 6.5 (Natural), $[MO]_0$= 8.17 mg/L, T= 298 K, Flow rate= 2000 rpm. 102

Figure 4.96. Pseudo first order kinetics for decolorization of MO in the presence of 0.5M ZnO-NC2 (300˚C). Conditions: pH= 6.5 (Natural), $[MO]_0$= 8.17 mg/L, T= 298 K, Flow rate= 2000 rpm. 103

Figure 4.97. Pseudo first order kinetics for degradation of MO in the presence of 0.5M ZnO-NC2 (500˚C). Conditions: pH= 6.5 (Natural), $[MO]_0$= 8.17 mg/L, T= 298 K, Flow rate= 2000 rpm. 103

Figure 4.98. Pseudo first order kinetics for decolorization of MO in the presence of 0.5M ZnO-NC2 (500˚C). Conditions: pH= 6.5 (Natural), $[MO]_0$= 8.17 mg/L, T= 298 K, Flow rate= 2000 rpm. 104

Figure 4.99. Pseudo second order kinetics for degradation of MO in the presence of 0.5M ZnO-NC2 (300˚C). Conditions: pH= 6.5 (Natural), $[MO]_0$= 8.17 mg/L, T= 298 K, Flow rate= 2000 rpm. 104

Figure 4.100. Pseudo second order kinetics for decolorization of MO in the presence of 0.5M ZnO-NC2 (300˚C). Conditions: pH= 6.5 (Natural), $[MO]_0$= 8.17 mg/L, T= 298 K, Flow rate= 2000 rpm. 105

Figure 4.101. Pseudo second order kinetics for degradation of MO in the presence of 0.5M ZnO-NC2 (500˚C). Conditions: pH= 6.5 (Natural), $[MO]_0$= 8.17 mg/L, T= 298 K, Flow rate= 2000 rpm. 105

Figure 4.102. Pseudo second order kinetics for decolorization of MO in the presence of 0.5M ZnO-NC2 (500˚C). Conditions: pH= 6.5 (Natural), $[MO]_0$= 8.17 mg/L, T= 298 K, Flow rate= 2000 rpm. 106

Figure 4.103. Freundlich adsorption isotherm for degradation of MO in the presence of 0.5M ZnO-NC2 (300˚C). Conditions: pH= 6.5 (Natural), T= 298K, Flow rate= 2000 rpm. 106

Figure 4.104. Freundlich adsorption isotherm for decolorization of MO in the presence of 0.5M ZnO-NC2 (300˚C). Conditions: pH= 6.5 (Natural), T= 298K, Flow rate= 2000 rpm. 107

Figure 4.105. Freundlich adsorption isotherm for degradation of MO in the presence of 0.5M ZnO-NC2 (500˚C). Conditions: pH= 6.5 (Natural), T= 298K, Flow rate= 2000 rpm. 107

Figure 4.106. Freundlich adsorption isotherm for decolorization of MO in the presence of 0.5M ZnO-NC2 (500˚C). Conditions: pH= 6.5 (Natural), T= 298K, Flow rate= 2000 rpm. 108

Figure 4.107. Langmuir adsorption isotherm for degradation of MO in the presence of 0.5M ZnO-NC2 (300˚C). Inset: C_e/q_e vs. C_e plot. Conditions: pH= 6.5 (Natural), T= 298K, Flow rate= 2000 rpm. 108

Figure 4.108. Langmuir adsorption isotherm for decolorization of MO in the presence of 0.5M ZnO-NC2 (500˚C). Inset: C_e/q_e vs. C_e plot. Conditions: pH= 6.5 (Natural), T= 298K, Flow rate= 2000 rpm. 109

Figure 4.109. Langmuir adsorption isotherm for degradation of MO in the presence of 0.5M ZnO-NC2 (500˚C). Inset: C_e/q_e vs. C_e plot. Conditions: pH= 6.5 (Natural), T= 298K, Flow rate= 2000 rpm. 109

Figure 4.110. Langmuir adsorption isotherm for decolorization of MO in the presence of 0.5M ZnO-NC2 (500˚C). Inset: C_e/q_e vs. C_e plot. Conditions: pH= 6.5 (Natural), T= 298K, Flow rate= 2000 rpm. 110

Figure 4.111. MO degradation in the presence of supported catalysts prepared at 300˚C. Conditions: pH= 6.5 (Natural), $[MO]_0$= 3.27 mg/L, T= 298 K, Flow rate= 2000 rpm. 111

Figure 4.112. MO decolorization in the presence of supported catalysts prepared at 300˚C. Conditions: pH= 6.5 (Natural), $[MO]_0$= 3.27 mg/L, T= 298 K, Flow rate= 2000 rpm. 111

Figure 4.113. MO degradation in the presence of supported catalysts prepared at 500˚C. Conditions: pH= 6.5 (Natural), [MO]0= 3.27 mg/L, T= 298 K, Flow rate= 2000 rpm. 112

Figure 4.114. MO degradation in the presence of supported catalysts prepared at 500˚C. Conditions: pH= 6.5 (Natural), $[MO]_0$= 3.27 mg/L, T= 298 K, Flow rate= 2000 rpm. 112

Figure 4.115. MO degradation at initial MO concentrations in the presence of 0.5M ZnO-NC2 (300˚C) and 0.5M ZnO-NC2 (500˚C).Conditions: pH=6.5 (Natural), T= 298 K, Flow rate= 2000 rpm. 113

Figure 4.116. MO decolorization at initial MO concentrations in the presence of 0.5M ZnO-NC2 (300˚C) and 0.5M ZnO-NC2 (500˚C).Conditions: pH= 6.5 (Natural), T= 298 K, Flow rate= 2000 rpm. 114

Figure 4.117. Pseudo-first order kinetics for degradation of MO in the presence of 0.5M ZnO-NC2 (300˚C). Inset: Langmuir-Hinshelwood analysis. Conditions: pH= 6.5 (Natural), T= 298 K, Flow rate= 2000 rpm. 114

Figure 4.118. Pseudo-first order kinetics for decolorization of MO in the presence of 0.5M ZnO-NC2 (300˚C). Inset: Langmuir-Hinshelwood analysis. Conditions: pH=6.5 (Natural), T= 298 K, Flow rate= 2000 rpm. 115

Figure 4.119. Pseudo-first order kinetics for degradation of MO in the presence of 0.5M ZnO-NC2 (500˚C). Inset: Langmuir-Hinshelwood analysis. Conditions: pH= 6.5 (Natural), T= 298 K, Flow rate= 2000 rpm. 115

Figure 4.120. Pseudo-first order kinetics for decolorization of MO in the presence of 0.5M ZnO-NC2 (500˚C). Inset: Langmuir-Hinshelwood analysis. Conditions: pH= 6.5 (Natural), T= 298 K, Flow rate= 2000 rpm. 116

Figure 4.121. XRD patterns of MMT2 (A) and supported catalysts (300˚C) (B-D). (Z: ZnO). 119

Figure 4.122. XRD patterns of MMT2 (A) and supported catalysts (500˚C) (B-D). (Z: ZnO). 119

Figure 4.123. SEM image of MMT2. 121

Figure 4.124. SEM image of 0.25M ZnO-MMT2 (500˚C) and mapping images of 0.25M ZnO-MMT2 (500˚C), Zn, Al, Mg, O and Si. 121

Figure 4.125. Nitrogen adsorption-desorption isotherms of MMT2 and supported catalysts prepared at 300˚C. 122

Figure 4.126. Pore size distribution plots of MMT2 and supported catalysts prepared at 300˚C. 123

Figure 4.127. Nitrogen adsorption-desorption isotherms of MMT2 and supported catalysts prepared at 500˚C. 123

Figure 4.128. Pore size distribution plots of MMT2 and supported catalysts prepared at 500˚C. 124

Figure 4.129. UV-Vis DRS spectra of MMT2 and supported catalysts prepared at 300˚C. Inset: UV-Vis DRS spectra of 0.25M ZnO (500˚C). 125

Figure 4.130. UV-vis DRS spectra of supported catalysts prepared at 500˚C. 125

Figure 4.131. Band gap adsorption edges of supported catalysts. Inset: Band gap adsorption edges of 0.25M ZnO (500˚C). 126

Figure 4.132. Band gap adsorption edges of supported catalysts. 126

Figure 4.133. Control experiments in the dark. Conditions: pH: 6.5 (Natural), $[MO]_0$ = 3.27 mg/L, T = 298 K, Flow rate = 2000 rpm. 127

Figure 4.134. Control experiments under UV irradiation. Inset: Photolysis of MO. Conditions: pH: 6.5 (Natural), $[MO]_0$= 3.27 mg/L, T= 298K, Flow rate= 2000 rpm. 128

Figure 4.135. Pseudo first order kinetics for degradation of MO in the presence of 0.5M ZnO-MMT2 (300˚C). Conditions: pH= 6.5 (Natural), $[MO]_0$= 8.17 mg/L, T= 298 K, Flow rate= 2000 rpm. 130

Figure 4.136. Pseudo first order kinetics for decolorization of MO in the presence of 0.5M ZnO-MMT2 (300˚C). Conditions: pH= 6.5 (Natural), $[MO]_0$= 8.17 mg/L, T= 298 K, Flow rate= 2000 rpm. 130

Figure 4.137. Pseudo first order kinetics for degradation of MO in the presence of 0.5M ZnO-MMT2 (500˚C). Conditions: pH= 6.5 (Natural), $[MO]_0$= 8.17 mg/L, T= 298 K, Flow rate= 2000 rpm. 131

Figure 4.138. Pseudo first order kinetics for decolorization of MO in the presence of 0.5M ZnO-MMT2 (500˚C). Conditions: pH= 6.5 (Natural), $[MO]_0$= 8.17 mg/L, T= 298 K, Flow rate= 2000 rpm. 131

Figure 4.139. Pseudo second order kinetics for degradation of MO in the presence of 0.5M ZnO-MMT2 (300˚C). Conditions: pH=6.5 (Natural), $[MO]_0$= 8.17 mg/L, T= 298 K, Flow rate= 2000 rpm. 132

Figure 4.140. Pseudo second order kinetics for decolorization of MO in the presence of 0.5M ZnO-MMT2 (300˚C). Conditions: pH= 6.5 (Natural), $[MO]_0$= 8.17 mg/L, T= 298 K, Flow rate= 2000 rpm. 132

Figure 4.141. Pseudo second order kinetics for degradation of MO in the presence of 0.5M ZnO-MMT2 (500˚C). Conditions: pH= 6.5 (Natural), $[MO]_0$= 8.17 mg/L, T= 298 K, Flow rate= 2000 rpm. 133

Figure 4.142. Pseudo second order kinetics for decolorization of MO in the presence of 0.5M ZnO-MMT2 (500˚C). Conditions: pH= 6.5 (Natural), $[MO]_0$= 8.17 mg/L, T= 298 K, Flow rate= 2000 rpm. 133

Figure 4.143. Freundlich adsorption isotherm for degradation of MO in the presence of 0.5M ZnO-MMT2 (300˚C). Conditions: pH= 6.5 (Natural), T= 298K, Flow rate= 2000 rpm. 134

Figure 4.144. Freundlich adsorption isotherm for decolorization of MO in the presence of 0.5M ZnO-MMT2 (300˚C). Conditions: pH= 6.5 (Natural), T= 298K, Flow rate= 2000 rpm. 134

Figure 4.145. Freundlich adsorption isotherm for degradation of MO in the presence of 0.5M ZnO-MMT2 (500˚C). Conditions: pH= 6.5 (Natural), T= 298K, Flow rate= 2000 rpm. 135

Figure 4.146. Freundlich adsorption isotherm for decolorization of MO in the presence of 0.5M ZnO-MMT2 (500˚C). Conditions: pH= 6.5 (Natural), T= 298K, Flow rate= 2000 rpm. 135

Figure 4.147. Langmuir adsorption isotherm for decolorization of MO in the presence of 0.5M ZnO-MMT2 (300˚C). Inset: C_e/qe vs. C_e plot. Conditions: pH= 6.5 (Natural), T= 298K, Flow rate= 2000 rpm. 136

Figure 4.148. Langmuir adsorption isotherm for decolorization of MO in the presence of 0.5M ZnO-MMT2 (300˚C). Inset: C_e/q_e vs. C_e plot. Conditions: pH= 6.5 (Natural), T= 298K, Flow rate= 2000 rpm. 136

Figure 4.149. Langmuir adsorption isotherm for degradation of MO in the presence of 0.5M ZnO-MMT2 (500˚C). Inset: C_e/q_e vs. C_e plot. Conditions: pH= 6.5 (Natural), T= 298K, Flow rate= 2000 rpm. 137

Figure 4.150. Langmuir adsorption isotherm for decolorization of MO in the presence of 0.5M ZnO-MMT2 (500˚C). Inset: C_e/q_e vs. C_e plot. Conditions: pH= 6.5 (Natural), T= 298K, Flow rate= 2000 rpm. 137

Figure 4.151. MO degradation in the presence of supported catalysts prepared at 300˚C. Conditions: pH= 6.5 (Natural), $[MO]_0$= 3.27 mg/L, T= 298 K, Flow rate= 2000 rpm. 138

Figure 4.152. MO decolorization in the presence of supported catalysts prepared at 300˚C. Conditions: pH= 6.5 (Natural), $[MO]_0$= 3.27 mg/L, T= 298 K, Flow rate= 2000 rpm. 139

Figure 4.153. MO degradation in the presence of supported catalysts prepared at 500˚C. Conditions: pH= 6.5 (Natural), $[MO]_0$= 3.27 mg/L, T= 298 K, Flow rate= 2000 rpm. 139

Figure 4.154. MO degradation in the presence of supported catalysts prepared at 500˚C. Conditions: pH= 6.5 (Natural), $[MO]_0$= 3.27 mg/L, T= 298 K, Flow rate= 2000 rpm. 140

Figure 4.155. MO degradation at initial MO concentrations in the presence of 0.5M ZnO-MMT2 (300˚C) and 0.5M ZnO-MMT2 (500˚C). Conditions: pH=6.5 (Natural), T= 298 K, Flow rate= 2000 rpm. 141

Figure 4.156. MO decolorization at initial MO concentrations in the presence of 0.5M ZnO-MMT2 (300˚C) and 0.5M ZnO-MMT2 (500˚C). Conditions: pH= 6.5 (Natural), T= 298 K, Flow rate= 2000 rpm. 142

Figure 4.157. Pseudo-first order kinetics for degradation of MO in the presence of 0.5M ZnO-MMT2 (300˚C). Inset: Langmuir-Hinshelwood analysis. Conditions: pH= 6.5 (Natural), T= 298 K, Flow rate= 2000 rpm. 142

Figure 4.158. Pseudo-first order kinetics for decolorization of MO in the presence of 0.5M ZnO-MMT2 (300˚C). Inset: Langmuir-Hinshelwood analysis. Conditions: pH=6.5 (Natural), T= 298 K, Flow rate= 2000 rpm. 143

Figure 4.159. Pseudo-first order kinetics for degradation of MO in the presence of 0.5M ZnO-MMT2 (500˚C). Inset: Langmuir-Hinshelwood analysis. Conditions: pH= 6.5 (Natural), T= 298 K, Flow rate= 2000 rpm. 143

Figure 4.160. Pseudo-first order kinetics for decolorization of MO in the presence of 0.5M ZnO-MMT2 (500˚C). Inset: Langmuir-Hinshelwood analysis. Conditions: pH= 6.5 (Natural), T= 298 K, Flow rate= 2000 rpm. 144

Figure 4.161. Results of recycling studies in the presence of 0.5M ZnO-MMT (300˚C). Conditions: pH: 6.5 (Natural), $[MO]_0$= 3.27 mg/L, T=298 K, Flow rate= 2000 rpm. 146

Figure 4.162. Results of recycling studies in the presence of 0.5M ZnO-MMT (500˚C). Conditions: pH: 6.5 (Natural), $[MO]_0$= 3.27 mg/L, T=298 K, Flow rate= 2000 rpm. 146

Figure 4.163. Results of recycling studies in the presence of 0.5M ZnO-NC1 (300˚C). Conditions: pH: 6.5 (Natural), $[MO]_0$= 3.27 mg/L, T=298 K, Flow rate= 2000 rpm. 147

Figure 4.164. Results of recycling studies in the presence of 0.5M ZnO-NC1 (500˚C). Conditions: pH: 6.5 (Natural), $[MO]_0$= 3.27 mg/L, T=298 K, Flow rate= 2000 rpm. 147

Figure 4.165. Results of recycling studies in the presence of 0.5M ZnO-NC2 (300˚C). Conditions: pH: 6.5 (Natural), $[MO]_0$= 3.27 mg/L, T=298 K, Flow rate= 2000 rpm. 148

Figure 4.166. Results of recycling studies in the presence of 0.5M ZnO-NC2 (500˚C). Conditions: pH: 6.5 (Natural), $[MO]_0$= 3.27 mg/L, T=298 K, Flow rate= 2000 rpm. 148

Figure 4.167. Results of recycling studies in the presence of 0.5M ZnO-MMT2 (300˚C). Conditions: pH: 6.5 (Natural), $[MO]_0$= 3.27 mg/L, T=298 K, Flow rate= 2000 rpm. 149

Figure 4.168. Results of recycling studies in the presence of 0.5M ZnO-MMT2 (500˚C). Conditions: pH: 6.5 (Natural), $[MO]_0$= 3.27 mg/L, T=298 K, Flow rate= 2000 rpm. 149

Figure 4.169. Comparison between photocatalytic activities of supported catalysts. Conditions: pH= 6.5 (Natural), $[MO]_0$= 3.27 mg/L, I= $4.7x10^{15}$ photons/s, T= 298 K, Flow rate= 2000 rpm. 151

LIST OF TABLES

Table 4.1. Crystalline sizes (D), surface areas (BET), pore volumes (V_{pore}) and pore radius (r_{pore}) of 0.25M ZnO (500^{o}C), MMT (500^{o}C) and supported catalysts. 37

Table 4.2. Elemental compositions of MMT, 0.25M ZnO (500˚C) and 0.25M ZnO-MMT (500˚C). 39

Table 4.3. Rate constants (k) and linear regression values for the degradation and decolorization processes of MO in the presence of 0.5M ZnO-MMT (300˚C). 62

Table 4.4. Rate constants (k) and linear regression values (R) for the degradation and decolorization processes of MO in the presence of 0.5M ZnO-MMT (500˚C). 62

Table 4.5. Crystalline sizes (D), surface areas (BET), pore volumes (V_{pore}) and pore radius (r_{pore}) of 0.25M ZnO, NC1 (500 ^{o}C) and supported catalysts. . .63

Table 4.6. Elemental composition of NC1 and 0.25M ZnO-NC1 (500˚C). 65

Table 4.7. Rate constants (k) and linear regression values (R) for the degradation and decolorization processes of MO in the presence of 0.5M ZnO-NC1 (300˚C). 89

Table 4.8. Rate constants (k) and linear regression values (R) for the degradation and decolorization processes of MO in the presence of 0.5M ZnO-NC1 (500˚C). 89

Table 4.9. Crystalline sizes (D), surface areas (BET), pore volumes (V_{pore}) and pore radius (r_{pore}).of 0.25M ZnO and supported catalysts. 91

Table 4.10. Elemental composition of NC2 and 0.25M ZnO-NC2 (500˚C). 93

Table 4.11. Rate constants (k) and linear regression values (R) for the degradation and decolorization processes of the different initial concentrations of MO in the presence of 0.5M ZnO-NC2 (300˚C). 116

Table 4.12. Rate constants (k) and linear regression values (R) for the degradation and decolorization processes of the different initial concentrations of MO in the presence of 0.5M ZnO-NC2 (500˚C). 117

Table 4.13. Crystalline sizes (D), surface areas (BET), pore volumes (V_{pore}) and pore radius (r_{pore}).of 0.25M ZnO and supported catalysts. 118

Table 4.14. Elemental composition of MMT2 and 0.25M ZnO-MMT2 (500˚C). 120

Table 4.15. Rate constants (k) and linear regression values (R) for the degradation and decolorization processes of the different initial concentrations of MO in the presence of 0.5M ZnO-MMT2 (300˚C). 144

Table 4.16. Rate constants (k) and linear regression values (R) for the degradation and decolorization processes of the different initial concentrations of MO in the presence of 0.5M ZnO-MMT2 (500˚C). 145

LIST OF SYMBOLS

D	Crystal Size
e^-	Electron
E_{bg}	Band Gap Energy
h^+	Hole
k_{app}	Appearent Rate Constant
k	Reaction Constant
K	Adsorption Constant
l	Path length of the Spectrophotometer
Ω	Omega
λ	Wavelength of X-ray radiation
θ	Angle between X-ray radiation

LIST OF ACRONYMS / ABBREVIATIONS

AOP	Advanced oxidation process
BET	Surface Area
CB	Conducton Band
DRS	Diffuse Reflectance Spectroscopy
EDX	Energy Dispersive X-Ray
FA	Fly ash
FWHM	Full Width Half Maximum
MO	Methyl Orange
XRD	X–Ray Diffraction
SEM	Scanning Electron Microscopy
UV-Vis	Ultra Violet-Visible
VB	Valence Band
ZnO	Zinc oxide

1. INTRODUCTION

Heterogeneous photocatalysis is presented as a low cost effective procedure for removing stable organic compound including dye molecules. The “heterogeneous” expression refers the existence of reactant and the catalysts in different phases while the reaction occurs. Briefly, the mechanism of photocatalytic processes is initiated by the band-gap illumination and this leads to production of electron-hole pairs. After separation, electrons and holes migrate to the catalysts surface; induce redox reactions with adsorbed pollutants and eventually resulting in the degradation of the pollutants.

In the past few years, ZnO has attracted much attention as a semiconductor photocatalyst, because of its distinctive optoelectronic characteristics, low cost, catalytic and photochemical properties. Besides these advantageous characteristics, separation of ZnO particles creates an operating cost after the treatment throughout several filtration methods. To overcome this problem, studies are oriented toward the use of adsorbent as supports for ZnO particles. This technique offers three potential advantages; concentration of pollutant near ZnO particles, adsorption of intermediates formed and recyclability of the adsorbents. Additionally, the catalyst immobilization technique eliminates the problems encountered in the separation or filtration steps and also helps to prevent particle aggregation, especially at high concentrations.

Clays, among various supports, are considered to be important owing to their high surface area, high thermal stability and eco-friendly nature. Montmorillonite (MMT) a commonly used clay for this purpose, being a member of smectite group, with $(Na,Ca)_{0.33}(Al,Mg)_2(Si_4O_{10})$ formula. Its structure is a 2:1 expanding crystal lattice which consists of two tetrahedral sheets sandwiching a central octahedral sheet. Beneficial properties of MMT may be advanced via modification. Organically modified forms of MMT are either commercially available or can be synthesized in laboratory conditions.

In this study, we have attempted to incorporate ZnO nanoparticles on commercially available MMT, NanoClay1 (NC1), NanoClay2 (NC2) and laboratory synthesized MMT2 supports. The as-prepared catalysts are characterized by using X-ray diffraction (XRD),

surface area (BET) measurements, UV–Vis diffuse reflectance spectra (UV–Vis DRS), and scanning electron microscopy (SEM) with energy dispersive X-ray analysis (EDX) and elemental mapping technique.

The photocatalytic performances of the supported catalysts are controlled under UV light irradiation by using methyl orange (MO) as the model dye. The reaction kinetics of the photocatalysts is examined both in the dark and under irradiation. Pseudo-first, pseudo-second order equations, Freundlich and Langmuir adsorption isotherms are applied to express the dark adsorption kinetics of the catalysts. The effect of ZnO loading amount is examined in the degradation experiments. The photocatalytic reactions are followed via pseudo-first-order kinetics and discussed in terms of Langmuir-Hinshelwood model. The repeatability of photocatalytic activity is tested and a possible degradation mechanism for the MO molecule is proposed.

2. THEORY

2.1. Heterogeneous Photocatalysis

Photocatalysis is the acceleration of a photoreaction in the presence of a catalyst. AOPs primarily involve the generation of a very powerful and non-selective oxidizing agent, the hydroxyl radical (OH•), which is used to destroy hazardous pollutants. The principle of photocatalytic degradation is well known since UV illumination onto a photocatalyst excites to produce an electron and hole-pair with a high-energy state, which migrate to the particle surface and initiate various chemical redox reactions [1].

Heterogeneously dispersed semiconductor surfaces provide both a fixed environment to influence the chemical reactivity of a wide range of adsorbates and initiate light-induced redox reactivity. Upon photoexcitation of several semiconductors nonhomogeneously suspended in either aqueous or nonaqueous solutions or in gaseous mixtures, simultaneous oxidation and reduction reactions occur. This conversion often accomplishes either a specific, selective oxidation or a complete oxidative degradation of an organic substrate present. Molecular oxygen is often assumed to serve as the oxidizing agent although details about the mode of its involvement have not been unambiguously demonstrated except in a few gas/solid reactions. The incident light that initiates this sequence is in a wavelength region (the visible or low-energy range of the ultraviolet regions of the spectrum) absorbed by the semiconductor [2].

Semiconductors are crystalline materials whose outer shell atomic levels exhibit an energy band structure with an energy gap between the valance band (highest occupied energy band) and the conduction band (lowest unoccupied band). The band gap energy of semiconductors for electronic excitation has a range from 0 eV to 3 eV [3].

The principal agent for degradation of dyes by light in the presence of photocatalysts is the •OH radical. This radical, along with others, is expected to form by

UV light illumination of the ZnO suspension containing dye through sequences of steps, some of which are likely to be as follows:

$$D_{ads} + h\upsilon \rightarrow {}^{*}D_{ads} \quad (2.1)$$

$^{*}D_{ads}$ stands for an excited dye molecule which is adsorbed on ZnO. The excited molecule on the ZnO surface injects an electron to its conduction band.

$$^{*}D_{ads} + ZnO \rightarrow ZnO(e) + D_{ads}^{+} \quad (2.2)$$

The trapped electron, ZnO(*e*), converts O_2 adsorbed on the surface into $O_2\bullet^{-}$,

$$ZnO(e) + O_2 \rightarrow O_2\bullet^{-} + ZnO \quad (2.3)$$

The excited dye can also create an electron (e^{-})-hole (h^{+}) pair in ZnO.

$$^{*}D_{ads} + ZnO^{-} \rightarrow D_{ads} + h^{+} + e^{-} \quad (2.4)$$

This hole can react with a water molecule adsorbed on the ZnO surface to produce the •OH radical.

$$h^{+} + H_2O \rightarrow OH\bullet + H^{+} \quad (2.5)$$

Another route of generation of •OH can be through the formation $HO_2\bullet$, which leads to formation of H_2O_2.

$$O_2\bullet^{-} + H^{+} \rightarrow HO_2\bullet \quad (2.6)$$

$$2HO_2\bullet \rightarrow H_2O_2 + O_2 \quad (2.7)$$

The H_2O_2 adsorbed on ZnO can also lead to the formation of •OH.

$$H_2O + O_2\bullet^{-} \rightarrow OH\bullet + O_2 + OH^{-} \quad (2.8)$$

$$OH\bullet + dye \rightarrow OH\bullet + OH^- \quad (2.9)$$

Accordingly, the overall degradation of dye molecules in the suspension of ZnO by UV light can be summarized as follows:

$$dye + OH\bullet \rightarrow intermediates\ (decolorization\ of\ dye\ molecules) \quad (2.10)$$

$$Intermediates + OH\bullet \rightarrow mineralization\ (degradation\ of\ the\ dye) \quad (2.11)$$

Equation 3.11, involving •OH, is likely to be the most favorable. However, this does not exclude the possibility of the oxidative attack at this stage by other species, such as dissolved oxygen, $HO_2\bullet$, and radicals that are subsequently formed from intermediates. The azo linkages, -N=N-, of dye are, of course, the most active site for oxidative attack by •OH radicals [4].

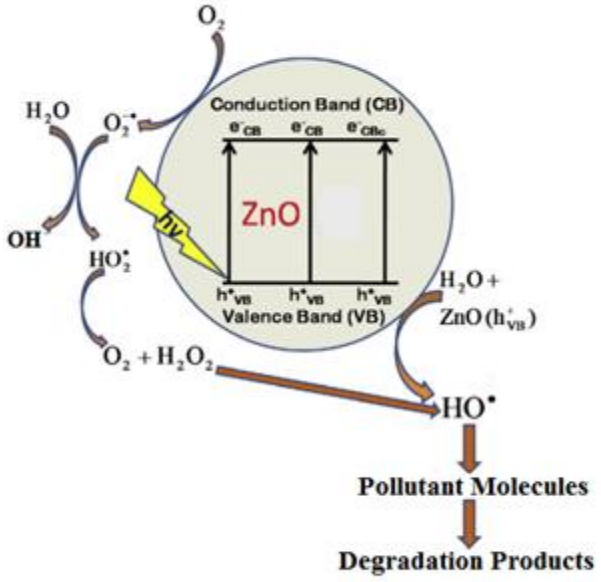


Figure 2.1. Photocatalytic degradation mechanism.

The energy level at the bottom of the conduction band reflects the reduction potential of the photo-electrons, whereas the upper most level of the valence band is a measure of the oxidizing ability of the photo-holes. The flatband potential (V_{fb}), which is fixed by the nature of the material and the proton exchange equilibria, determines the energy of the two charge carriers at the interface. Hence reductive and oxidative processes

for adsorbed couples with redox potentials more positive and more negative than the V_{fb}, of the conduction and valence band, respectively, can be driven by surface-trapped e^- and h^+ carriers [5].

For an electronically appropriate system, the conduction band minimum of the semiconductor has to be more negative than the reduction potential of H^+/H_2, while the valance band maximum needs to be more positive than the oxidation potential of O_2/H_2O [6]. Consequently, a feasible system is possible if band gap energies of the catalysts are approximately 3 eV.

Band gap of the several semiconductors and some standard potentials of redox couples are illustrated in Figure 2.2. Among the semiconductors, zinc oxide (ZnO) is one of the most widely used photocatalyst due to its valence and conduction band positions and value of the band gap energy. Additionally, a photocatalyst must be chemically and biologically inert, easy to produce, photocatalytically stable, cheap and last but not least non-toxic for human health and environment.

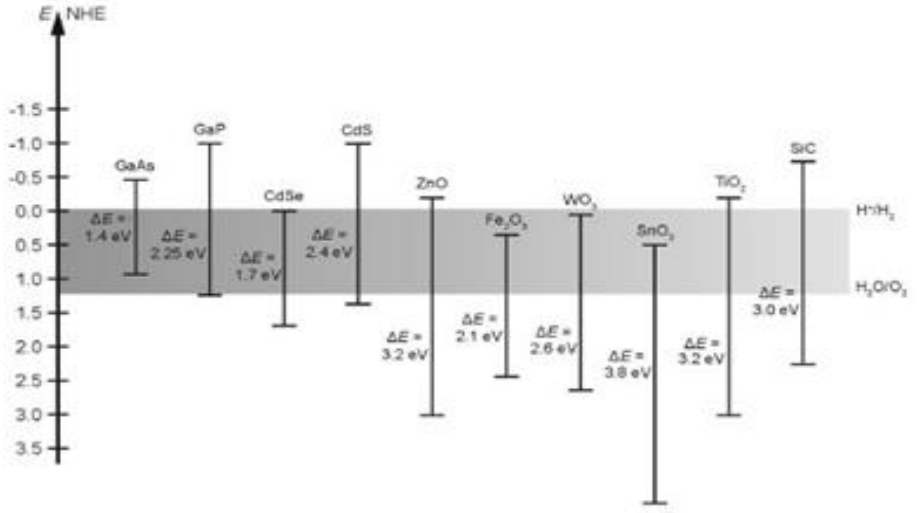


Figure 2.2. Band positions and band gap energies of the several semiconductors.

2.2. Zinc Oxide

Zinc oxide (ZnO) is an insoluble inorganic compound which is used as an additive in numerous materials and products including rubbers, plastics, ceramics, glass, cement,

lubricants, paints, ointments, adhesives, sealants, pigments, foods, batteries, ferrites, fire retardants and first aid tapes [7] [8]. It rarely occurs in nature as zincite mineral; however ZnO is mostly produced synthetically. ZnO is a polar crystal and shows a wurtzite structure with hexagonal unit cell (Figure 2.3).

ZnO is a wide-band gap semiconductor of the II-VI semiconductor group. The native doping of the semiconductor due to oxygen vacancies or zinc interstitials is n-type. This semiconductor has several favorable properties, including good transparency, high electron mobility, wide band gap (3.2 eV), and strong room-temperature luminescence. Those properties are demanding in emerging applications for transparent electrodes in liquid crystal displays, in energy-saving or heat-protecting windows, and in electronics as thin-film transistors and light-emitting diodes [9].

ZnO is an appropriate semiconductor in comparison with other nanosized metal oxides due to, its environmental stability, low cost, small particle size and great photochemical properties. Additionally, ZnO occupies a special place among wide band gap semiconductors owing to its absorption ability in the visible and UV spectral ranges [10].

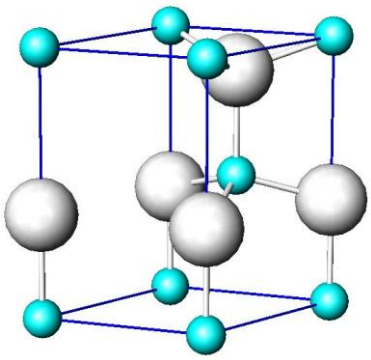


Figure 2.3. Crystal structure of wurtzite.

2.3. Factors Effecting Surface and Morphological Aspects in Photocatalysis

Results of previous investigations suggested that the porous structure and high specific surface area are beneficial to photoactivity via enhancing adsorption, which is the determining step in the heterogeneous photocatalytic reaction. Therefore, a combination of

adsorption and heterogeneous photocatalysis makes photooxidation more effective for the removal of dye compounds from wastewater [11].

BET theory is a rule for the physical adsorption of gas molecules on a solid surface and serves as the basis for an important analysis technique for the measurement of the specific surface area of a material. BET stands for Brunauer, Emmet and Teller who are the optimizers of the theory in 1938. The concept of the theory is an extension of the Langmuir theory, which is a theory for monolayer molecular adsorption, to multilayer adsorption. This theory well fits to type II and IV isotherms at the relative pressure between 0.05 and 0.35. The monolayer adsorption amount (V_m) and C (constant) parameters are calculated from the slope and intercept of BET-plot by using the least square fitting. C parameter represents the surface interaction energy, so it must take a positive value. The measurement is carried out at the liquid nitrogen temperature (77 K). The BET isotherm is not absolute for all pressure values, though in industry it is used to determine the surface areas of solids by interpreting of adsorption-desorption isotherms [12].

However, the photocatalytic activity is not necessarily dependent on catalysts surface area, but rather on the availability of active sites. Therefore, properties such as crystalline structure, pore size, density of OH groups, number and nature of trap sites (both in lattice and at the surface), and adsorption-desorption characteristics have an important role in photocatalytic efficiencies [13].

In semiconductor particles of nanometer size, a gradual transition from solid state to molecular structure occurs as the particle size decreases. In this very size regime, the physical and chemical properties of the particles strongly depend on their size. the use of quantum-sized particles as sensitizers principally implies several advantages as compared to organic dyes: the band gap and thereby the absorption range are easily adjustable by the size of the particles, the band edge type of absorption behavior is most favorable for effective light harvesting, and the surface properties of the particles can be modified in order to increase the photostability of the electrodes [14].

The average particle sizes are determined by the application of Scherrer's equation to the (101) diffraction of ZnO (Equation 2.12) [15].

$$D = \frac{A\,\lambda}{FWHM\,\cos\theta} \tag{2.12}$$

where D is the average crystal size, A is Scherrer's Constant (0.94), λ is the wavelength (0.1542 nm), FWHM is full width half maximum value of the corresponding diffraction peak in radians, θ is the diffraction peak angle.

The benefits of such a photonic band gap for semiconductors are illustrated in Figure 2.4. On the right-hand side of Figure 2.4 is a plot of the photonic dispersion, (frequency versus wave vector). On the left-hand side of Figure 2.4, sharing the same frequency axis is a plot of the electronic dispersion, showing conduction and valence bands appropriate to a semiconductor. Since atomic spacings are 1000 times shorter than optical wavelengths, the electron wave vector must be divided by 1000 to fit on the same graph with the photon wave vectors. The dots in the electron conduction and valence bands are meant to represent electrons and holes, respectively. If an electron were to recombine with a hole, they would produce a photon at the electronic-band-edge energy. As is illustrated in Figure 2.4, if a photonic band gap were to straddle the electronic band edge, then the photon produced by electron-hole recombination would have no place to go. The spontaneous radiative recombination of electrons and holes would be inhibited [16].

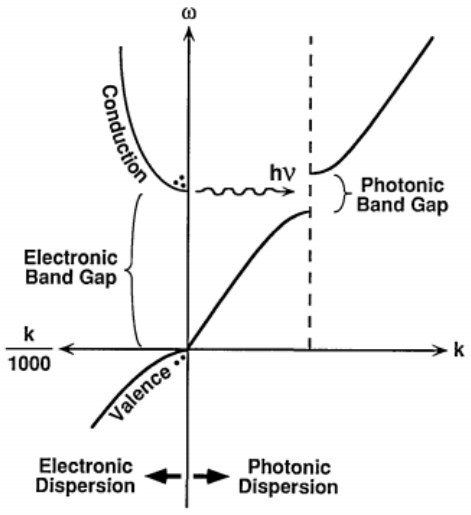


Figure 2.4. Relation between band gap energy and semiconductor material.

Band gap energies of 0.25M ZnO and supported catalysts are calculated with Kubelka-Munk equation. Originally Kubelka-Munk proposes a model to describe the behavior of light traveling inside a light-scattering specimen, which is based on the following differential equations [17]:

$$\begin{aligned} -di &= -(S+K)idx + Sjdx \\ dj &= -(S+K)jdx + Sidx \end{aligned} \tag{2.13}$$

where *i* and *j* are the intensities of light traveling inside the sample towards its un-illuminated and illuminated surfaces, respectively; dx is the differential segment along the light path; S and K are the so called K-M scattering and absorption coefficients. These last two quantities have no direct physical meaning on their own, even though they appear to represent portions of light scattered and absorbed, respectively, per unit vertical length. In the limiting case of an infinitely thick sample, thickness and sample holder have no influence on the value of reflectance (R). In this case, the Kubelka-Munk equation at any wavelength becomes:

$$\frac{K}{S} = \frac{(1-R_\infty)^2}{2R_\infty} \equiv F(R_\infty) \tag{2.14}$$

F (R_∞) is the so-called remission or Kubelka-Munk function, where,

$$R_\infty = \frac{R_{sample}}{R_{standart}} \tag{2.15}$$

In the parabolic band structure, the band gap E_g, and absorption coefficient α of a direct band gap semiconductor are related through the well known equation:

$$\alpha hv = C_1 (hv - E_g)^{\frac{1}{2}} \tag{2.16}$$

where α is the linear absorption coefficient of the material, *hv* is the photon energy and C_1 is a proportionality constant. When the material scatters in perfectly diffuse manner, the K-

M absorption coefficient K becomes equal to 2α (K=2α). In this case, considering the K-M scattering coefficient S as constant, we obtain the expression:

$$[F(R_\infty)^2 hv^2] = hv - E_g \quad (2.17)$$

Therefore, obtaining F (R∞) from Equation 2.14 and plotting the $[F(R\infty)\ hv]^2$ against *hv*, the band gap E_g of a powder sample can be extracted.

2.4. Kinetic Studies

2.4.1. Dark Adsorption Kinetics

Adsorption details of MO on supported catalysts in detail under dark conditions. The amount of MO adsorbed per gram of adsorbent (for all 0.5M ZnO loaded supports) at time t (min) (q_t) are found by the following equation [18]

$$q_t = \frac{(C_0 - C_t)V}{m} \quad (2.18)$$

where C_0 is the initial concentration of MO in solution, C_t is the concentration of MO at time t, V is the volume of the solution and m is the mass of catalyst used. C_t is replaced with C_e (concentration of MO at equilibrium), and q_e can be found as the amount of adsorbend MO molecule per gram of adsorbent at equilibrium.

The pseudo first order and the pseudo second order model are applied to all catalyst systems to better understand their adsorption kinetics. The pseudo first order equation is given by the following equation

$$\frac{dq_t}{dt} = k_1 (q_e - q_t) \quad (2.19)$$

where k_1 is the pseudo-first order rate constant. After the integration of the Equation 2.19 by using the integral limits of $q_t = 0$ at $t = 0$ and $q_t = q_t$ at $t = t$,

$$\ln(q_e - q_t) = \ln q_e - k_1 t \quad (2.20)$$

is obtained. The plot of ln (q_e-q_t) versus t gave a straight line with correlation coefficients. The rate constant (k_1) was calculated from the slope of this line.

The pseudo second order equation is displayed as follows

$$\frac{dq_e}{dt} = k_2 (qe - qt)^2 \quad (2.21)$$

After the integration of the equation by the integral limits of q_t=0 at t=0 and q_t=q_t at t=t, Equation 2.21 becomes

$$\frac{t}{q_t} = \left(\frac{1}{k_2 q_e^2}\right) + \frac{t}{q_e} \quad (2.22)$$

The linearity obtained in the plot of t/q_t versus t results in correlation coefficients for decolorization and degradation experiments.

2.4.2. Adsoption Isotherms

Freundlich isotherm is an empirical equation that can be applied to heterogeneous systems. It suggests that adsorption energy exponentially decreases on completion of the sorptional centers of an adsorbent. The linearized form of the Freundlich isotherm is given in the following equation [19, 20]

$$\ln q_e = \ln K_F + b_F \ln C_e \quad (2.23)$$

where K_F is the Freundlich constant, b_F is the adsorption intensity constant and C_e is the concentration of the MO at equilibrium.

Langmuir theory assumes that, adsorption occurs at a specific homogenous site on the adsorbent and there are no interactions among the adsorbate molecules [21]. The linearized equation of the Langmuir model is given as Equation 2.24.

$$\frac{C_e}{q_e} = \frac{C_e}{q_{max}} + \frac{1}{q_{max} K_L} \quad (2.24)$$

where q_{max} is the maximum capacity of the adsorbent and K_L is the Langmuir adsorption constant.

This two well know kinetic models are applied to all 0.5M ZnO loaded catalysts to determine adsorption kinetics.

2.4.3. Experiments Followed Under UV Irradiation

To examine catalysts kinetics under UV irradiation four different MO concentrations are prepared in the range of 3.27 mg/L to 32.27 mg/L. Pseudo first order kinetics is followed by the rate equation (Equation 2.25).

$$R = \frac{dC}{dt} = kC \quad (2.25)$$

where R is the rate of degradation reaction, C is the concentration of MO molecule at time t and k is the rate constant. The equation can be simplified by integration

$$\ln \frac{C_0}{C} = kt \quad (2.26)$$

where C_0 accepted as the equilibrium concentration of the MO after dark adsorption.

Langmuir-Hinshelwood model is also applied to analyze the photocatalytic degradation kinetics of supported catalysts. This model simplified to fit experimental results (Equation 2.27)

$$R = \frac{k_r K C_t}{1 + K C_t} = k_{app} C_t \quad (2.27)$$

where R is the rate of degradation reaction, k_{app} apparent first order rate constant, C_t is the remaining concentration of MO in solution by time, t is the time of reaction, K is adsorption coefficient of MO on the supported catalyst and k_r is the reaction constant. Hence the rate constant can be found from Equation 2.28

$$\frac{1}{R} = \frac{1+KC_t}{k_r KC_t} \tag{2.28}$$

This equation can be arranged like

$$\frac{1}{k_{app}C_t} = \frac{KC_t}{KC_t k_r} + \frac{1}{k_r C_t K} \tag{2.29}$$

Consequently, the Equation 3.18 is obtained by substitution of C_0 in place of C_t as the equilibrium concentration of MO molecule after dark adsorption.

$$\frac{1}{R} = \frac{1}{k_{app}C_0} = \frac{1}{k_r KC_0} + \frac{1}{k_r} \tag{2.30}$$

2.5. Preparation of ZnO Nanoparticles: Co-precipitation Method

Crystal size and surface properties of ZnO can be determined by the preparation method so it has significant role. Many methods have been described in the literature for the production of ZnO nanostructures such as laser ablation, hydrothermal methods, electrochemical depositions, sol–gel method, chemical vapor deposition, thermal decomposition and combustion method. Recently, ZnO nanoparticles are prepared by ultrasound, microwave-assisted combustion method, two-step mechanochemical-thermal synthesis, anodization, co-precipitation, and electrophoretic deposition [22]. Among these, application of co-precipitation method is easier technique and precursors of this method are more accessible. This method has more advantageous such as, requires minimal manipulation, simple equipment, low synthesis temperature, easier compositional and particle size control by varying the reaction conditions and initial reactants ratio. On the other hand, the process is limited to cationic solutions with similar solubility products. Hydroxides, carbonates, sulphates and oxalates are mostly used materials as precursor [23].

2.6. Support

ZnO may be one of the most favorite photocatalyst but using its bare form has some limitations. For instance, due to the small particle size, the catalysts tend to rapid agglomeration that inhibits active sides of the photocatalyst and eventually reduce the catalytic efficiency. It is also challenging to recover pure ZnO powders from water when they are used in aqueous systems [24]. The small particle size leads to high filtration costs of catalysts removal and recycling difficulties, thus hindering its industrial application. Moreover, due to the natural non-porous structure of the metal oxide catalysts, bare ZnO shows low adsorption ability for the pollutants in wastewater.

To overcome these limitations, ZnO nanoparticles may immobilized on the adsorbent materials such as, silica [25], alumina [26], activated carbon [27], zeolites [28] and clays [29].

An appropriate support material should sufficiently bond either via physically or chemically to the photocatalyst without reducing its reactivity. The basic concept is based on the physisorption of reactants on inert substrates followed by their surface diffusion to the interface between the adsorptive sites and photocatalytic sites. The first step is achieved by using supports with large surface area for adsorption and high adsorption capacity for the target substances, while the other is accomplished only if the adsorption strength is moderate enough to allow diffusion of adsorbed substrates to the loaded semiconductor [30]. A support material must be stable against degradation by strong oxidative radicals generated by the photocatalyst, non-toxic regarding to the environment and human health and cheap. Clays are ideal candidates for such materials with a layered structure offering a variety of applications such as, catalyst stabilizing medium for nanoparticles and acting as a host for guest species.

2.6.1. Montmorillonite

Clays are widely used materials in such fields; polymer nano-composites, adsorbent for heavy metal ions, catalyst, photochemical reactions, ceramics, paper filling and coating,

sensors and biosensors, due to their high specific surface area, chemical and mechanical stabilities and several surface and structure properties. Montmorillonite (MMT), a member of semctite group, is the most preferred clay for industrial usage. General formula of MMT is $(Na,Ca)_{0.33}(Al,Mg)_2(Si_4O_{10})$. MMT is an alteration product of volcanic tuff and ash, forming bentonite beds, and of pegmatite dikes and wall rock bordering hydrothermal mineral deposits. It forms under alkaline conditions of poor drainage, with Mg, Ca, Na and K in the soil [31]. Its structure is a 2:1 expanding crystal lattice which consists of two tetrahedral sheets sandwiching a central octahedral sheet (Figure 2.5) [32]. The layers are continuous among the both width and length directions. The bonds between layers are weak but also have excellent cleavage which allows water and other molecules entering to the gap between the layers and causes the expansion of the gap. The pillared clays are thermally stable up to about 400-500^oC [33].

In their inner blocks, all corners of silica tetrahedral are connected to adjacent blocks, but in outer blocks some of the corners contain Si atoms bound to hydroxyls (Si–OH). These silanol groups at the external surface of the silicate are usually accessible to organic species and act as neutral adsorption sites. Furthermore, some isomorphic substitutions occur in the tetrahedral sheet of the lattice leading to negatively charged adsorption sites which are occupied by exchangeable cations. These features make it powerful nano-absorbent for organic molecules and organic cations [34]. Its adsorption capability may be used to improve a photo-catalytic process. [35]. Previous works have showed that supported or composite materials posses more advantageous properties for practical applications than does pure photocatalysts, such as ZnO [36]. For this purpose among various porous compounds, montmorillonite is a widely used one due to its controllable pore dimensions, high specific surface area and specific catalytic properties depending on the type of silicate layers and pillaring agents [37, 38].

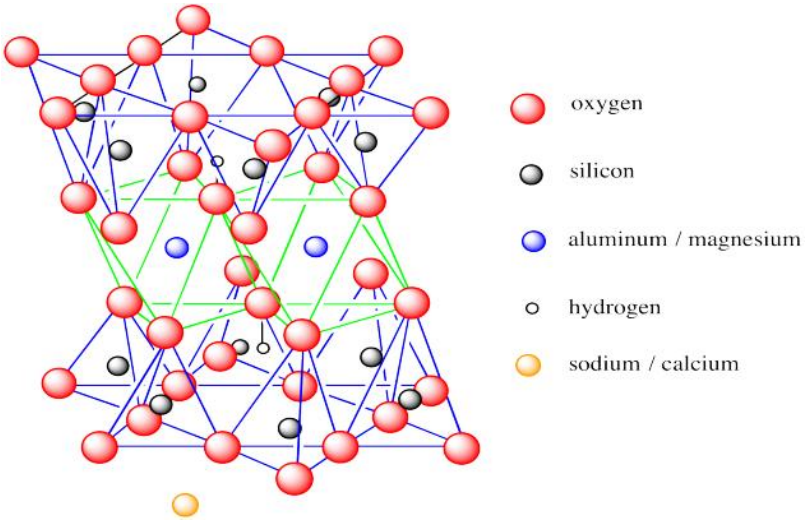


Figure 2.5. Structure of montmorillonite.

2.6.2. Organically Modified Montmorillonite Clays

The organically modified forms of MMT are called as nanoclays or organoclays. Nanoclays can be used in polymer composite materials, various kinds of resins, painting, thermal insulation material, plastic and ceramic materials to enhance functions and value. [39]. In industrial applications, nanoclays reveals high wear-resistancy, good durability, heat stability, excellent flame retard property, low viscosity, excellent dispersivity, great fluidity [40, 41].

Nanoclays contain alternating organic and inorganic layers. The organic layer is comprised of the quaternary ammonium compounds ion exchanged on the surface. This hydrophobic layer acts as an organic phase into which organic substances that are dissolved in water can partition. The partitioning efficiency should be a function of water solubility of the organic substance since the two phases available to it are water and the quaternary compound in the gallery of the clay [42]. Moreover, organic phase between the layers increases d-spacing value of the clay and converts its hydrophilic nature to organophilic, which concludes with excellent adsorption property [43].

2.7. Literature Survey

Gieseking worked on the behavior of methylene blue against modified clay minerals. He reported that methylene blue to be very effective in replacing interlayer cations of clay minerals. Montmorillonite, beidellite and nontronite types of clay minerals were treated with solutions of the hydrochlorides or hydroiodides of the various amines. The clay minerals adsorbed the organic ions, giving rise to basal spacing greater than those of the same clay minerals saturated with smaller cations such as calcium or hydrogen [44].

Jordan investigated some of the factors involved with the swelling of organoclays and the extent of the conversion of the clay from hydrophilic to hydrophobic. Organophilic bentonites were prepared by the reaction of bentonite with various aliphatic ammonium salts. The swelling of the organoclays was studied in several organic liquids and liquid mixtures. It is concluded that the degree of solvation depends on the extent of the surface coating of the clay particles by organic matter, the degree of saturation of the exchange capacity of the clay mineral by organic cations and the nature of the organic liquid [45].

Chou and McAtee studied on thermal decomposition of organo-ammonium compounds exchanged onto montmorillonite and hectorite by means of differential thermal analysis and heating-oscillating X-ray diffraction methods. It was found that the room temperature d001 remains unchanged during the initial heating period. Each sample then showed a gradual but essentially continual decrease in d-spacing value as the temperature was increased to about 200˚C. Further heating of the samples resulted in a decomposition of the hydrocarbon chain leaving a residue of carbon which then oxidizes at a temperature of about 500˚C [46].

Xie at al. offered the nanoscopic phase distribution as well as synergism between polymer and the layered silicate resulted in additional properties, such as flame retardency, enhanced barrier properties and ablation resistance, which were not observed in either component. However, the effect of chemical variation of organic modifiers on the thermal stability of the organically exchanged montmorillonite is discussed and concluded as the chain length of exchange cations has almost no influence on the decomposition temperature of organically modified layered silicates [47].

Beall examined the physical chemistry of the organo-clays sorption mechanism and the use of organo-clays has proven to be very viable for many water treatment applications. Organo-clays operate via a partitioning phenomenon and had a synergistic effect with activated carbon and other unit processes such as reverse osmosis. Organo-clay sorbents have been widely applied commercially on off shore platforms to clean acid well returns and produced water as well as a variety of process waters. Organo-clays have proven to be the technology of choice for treating oily wastewaters. [48].

In the study of Yalçın *et al*., the adsorption kinetics of cethyltrimethylammonium bromide (CTAB) onto powdered active carbon [49] was calculated and compared with the pseudo first- order, second-order kinetic models and intraparticle diffusion model. The results showed that the pseudo-second-order adsorption mechanism is predominant and the overall rate of the CTAB adsorption process appeared to be controlled by more than one step, namely both the external mass transfer and intraparticle diffusion mechanisms.

Self-assembly of organic molecules on montmorillonite is investigated by Beall and Goss. They reported that, the self-assembly of small polar molecules mediated by ion–dipole bonding to the exchangeable cation on the montmorillonite surface appears to be controlled by two factors. The first is the role of the polar head group and the second is the carbon chain length [50].

In 2005 intercalation of montmorillonite with octadecylamine under several conditions was reported by Santano at al. Octadecylamine was protonated in situ with HCl to obtain octadecylammonium cations. Water and water/ethanol mixtures were used as reaction medium, and the ratios amine/clay and HCl/amine were also varied. Co-intercalation of octadecylammonium and of the inorganic polycation $[Al_{13}O_4(OH)_{24}(H_2O)_{12}]^{7+}$ was considered. Hence, intercalated solids with basal spacings between 17 and 22 Å, also with a high fixation of organic matter is observed [51].

In the study of Capkova *et al*. [52], structural analysis of Na-montmorillonite co-intercalated with octadecylamine and stearic acid was carried out using combination of experiment: X-ray powder diffraction (XRD) and IR spectroscopy and the presence of

octadecylammonium stearate in the samples was confirmed. Intercalated samples in ambient conditions undergo gradual decomposition, accompanied by the release of octadecylammonium stearate (ODST) from the interlayer space and rearrangement of the interlayer structure. ODST intercalated at temperature 80˚C into Na-MMT exhibited a highly disordered structure with a maximum basal spacing within the range 27–39 Å.

The study of Ha *et al*. [53] explained the effects of clay concentrations on the fracture behavior of surface-modified MMT/epoxy nanocomposites. For this purpose, fracture tests were performed using samples with four different clay concentration levels. After the fracture tests, SEM was performed on the fracture surfaces to examine the fracture mechanism depending on the clay concentration level. The analysis were concluded as, MMT modification using 3-aminopropyltriethoxysilane produces good dispersion of MMT in the epoxy and increases the intercalation effect. Fracture toughness decreased up to 4 wt% of MMT and increased at 6 wt%, followed by another decrease at 10 wt%. This occurs due to the increased brittleness of nanocomposite and increased debondings between MMT and epoxy, as well as voids.

In another study of Ha *et al*., the effect of montmorillonite (MMT) clay modification (with 3-aminopropyltriethoxysilane) and concentration on the tensile behavior of MMT/epoxy nanocomposite were investigated. MMT/epoxy nanocomposite samples were fabricated by mixing the unmodified and the surface-modified MMT of 2, 6, and 10 wt%, respectively, with epoxy resin. The XRD results showed that the *d*-spacing between layers increased by more than 55% with the 3-aminopropyltriethoxysilane modification of MMT. Tensile strength and elastic modulus of surface-modified MMT/epoxy nanocomposite were larger than those of unmodified MMT/epoxy nanocomposite, and the modification effect increased with clay concentration. This occurred due to the increased exfoliation of clays along with the improved interfacial strength by the surface modification [54].

Effects of surface-modification of clay using 3-aminopropropyltriethoxysilane were examined by Ha and Rhee. The results of wear tests showed that the friction coefficient and specific wear rate of surface-modified clay/epoxy nanocomposites were lower than those of unmodified clay/epoxy nanocomposites, regardless of sliding speed. The decrease

in friction coefficient by surface modification of clays seems to occur due to the improved dispersion of clays into the epoxy matrix and improved adhesion with the epoxy [55].

In the study of Wicklein *et al.* [56] a new type of hybrid biomaterials based on the clay minerals montmorillonite and sepiolite as well as phosphatidylcholine (PC), were prepared. The obtained supported lipid membranes were further investigated by X-ray diffraction, multinuclear solid state NMR, Fourier transformed IR spectroscopy and thermal analysis. The characterization results suggested that bilayer formation both on the external sepiolite surface as well as in the intracrystalline space of the montmorillonite. From these results an adsorption model based on electrostatic interaction between the polar phospholipid headgroups and the silicate surface was postulated. PC intercalation in montmorillonite causes an interlayer swelling of about 4.2 nm, which was compatible with an intracrystalline PC arrangement in form of a lipid bilayer being protected by the rigid silicate framework.

Photocatalytic and photochemical degradation of methylene blue (MB) with ZnO/montmorillonite was investigated by Fatimah et al. Synthesis of a ZnO/MMT photocatalyst based on an Indonesian natural montmorillonite was conducted using a sol–gel intercalation method. The activity was evaluated in photocatalytic and photochemical degradation of methylene blue (MB) with and without H_2O_2. Characterization with XRD, SEM, TEM and UV-Vis diffuse reflectance showed that the ZnO particles were successfully distributed in montmorillonite support and ZnO/MMT had lower band gap energy. The increased adsorption of MB on ZnO/MMT resulted in faster photodegradation. The kinetics of the reaction obeyed the Langmuir–Hinshelwood model [57].

In 2011 Mana *et al*. presented their research [58] about the spent bleaching earth from an edible oil refinery that treated with an aqueous cetyltrimethylammonium bromide solution in order to remove the edible oil impregnating the solid material and to intercalate the ammonium cation in the interlayer space of the bentonite. The prepared organophilic bentonite was used to remove the dye acid black 10B from the aqueous solution. The maximum removal capacity obtained (100 mg g^{-1}) was better than those of some non conventional sorbents.

Nanocomposites of polybutylene adipate-co-terephthalate (PBAT) with montmorillonite (MMT) nanoparticles were prepared via melt blending. Natural MMT was modified by either octadecylamine (ODA) or dihexylamine (DHA). Neat PBAT was graftedwith maleic anhydride via melt grafting process. From the results of transmission electron microscope (TEM), the dispersion of ODA-modified MMT in the PBAT matrix was more homogeneous than that of neat MMT. The addition of organoclay could increase the cooling crystallization temperature of PBAT, as observed by differential scanning calorimetry (DSC). Furthermore, the results of thermogravimetric analyzer (TGA) showed that the addition of ODA-modified MMT can improve the thermal stability of PBAT nanocomposites. The tensile strength is little affected, while the Young's modulus was increased with the addition of nanoclays. The grafting of PBAT with MA resulted in improved interaction between polymer matrix and the silicate layer due to the formation of chemical/physical bonds, thus the dispersion of organoclays was enhanced. By grafting PBAT with MA, the enzymatic biodegradation of the nanocomposite was increased, while the photodegradation of PBAT is little affected. In addition, the transmission of water vapor was reduced by the addition of organically modified MMT [59].

Zinc oxide was prepared in the interlayer space of cetyltrimethylammonium-smectites by the reaction between the aqueous solutions of zinc chloride and sodium hydroxide in the presence of cetyltrimethylammonium-smectites. The formation of zinc oxide nanoparticles in the interlayer space of cetyltrimethylammonium-smectites was indicated by the transmission electron micrograph, diffuse reflectance absorption and the photoluminescence spectra. The photoluminescence of zinc oxide was affected by the interactions with cetyltrimethylammonium cation and silicate layer, intensities of zinc oxide in cetyltrimethylammonium-saponite were higher than those in cetyltrimethylammonium-montmorillonite because of the quenching impurity in montmorillonite. Thus, the luminescence characteristics (both intensity and the energy) were controlled by the host–guest interactions with selection of host and modification. The zinc oxide nanoparticles were formed on the inner and/or outer surfaces of cetyltrimethylammonium-smectites. The intensity of the blue emission is higher when the loading amount of zinc oxide decreased, while the green emission increased with increasing the zinc oxide loading [60].

In the study of Patil *et al*. [61], montmorillonite clay was incorporated with ZnO to get ZnO-MMT nanocomposite. The nanocomposite was successfully used for removal of Rhodamine 6G by photocatalytic degradation and adsorption. The experimental results showed that ZnO-montmorillonite was promising for removal of Rhodamine 6G from aqueous solution. The q_e (the amount of Rhodamine 6G adsorbed per gram of adsorbent at equilibrium) values for Rhodamine 6G adsorption were dependent on contact time, pH, dye concentration and adsorbent dose. The amount of dye adsorbed (mg/g) was found to be increase with increase in contact time and initial dye concentration and to decrease with increase in catalyst dose. The adsorption kinetics was found to confirm pseudo-second-order kinetics.

3. EXPERIMENTAL

3.1 Materials

Montmorillonite (MMT) and its modified forms NC1, NC2 and MMT2 are used as support materials. Montmorillonite is donated from Süd Chemie (Moosburg, Germany). NC1 (Aldrich), NC2 (Aldrich), zinc nitrate hexahydrate ($Zn(NO_3)_2.6H_2O$) (99.0%, Merck), sodium carbonate (Na_2CO_3) (Analytical Grade, Merck) and methyl orange (Merck) are used as provided by the suppliers without further purification. Deionized water, purified with an Elga-Pure Water Purificatio (UHQ II) system, is used in all experiments.

3.1.1. Methyl Orange

The discharging water after the industrial processes includes organic dyes that are the major sources of environmental contaminations due to their high toxicity to aquatic creatures and carcinogenic effects on humans. Hence, this waste water needed to be purifying from this dye stuffs and effluents. Azo dyes are an abundant class of synthetic, colored and organic compounds that are characterized by the presence of one or more azo bonds (-N=N-). Due to the complicated aromatic structures and chemical stability of azo dyes, conventional treatment methods either are ineffective in removing them from wastewater, or they can only transfer them to another phase, causing secondary pollution. [62]. Therefore, heterogeneous catalysis is a promising method for decomposition of azo dyes. Methyl orange (MO) is a widely used model compound as an azo dye. It has sulfonic groups, which are responsible for the high solubility in water and also has chromophore groups corresponding UV active region (Figure 3.1). UV-Vis Spectrophotometer (UV-2450, Shimadzu) is used to monitor the absorbance spectra of MO with an absorbance band at 278 nm (for the aromatic content of MO) and another band at 464 nm (for the color of MO solution) (Figure 3.2).

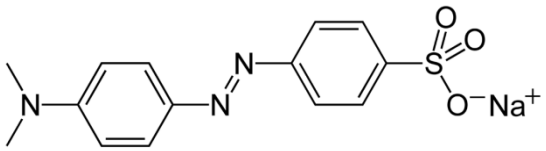


Figure 3.1. Chemical structure of methyl orange.

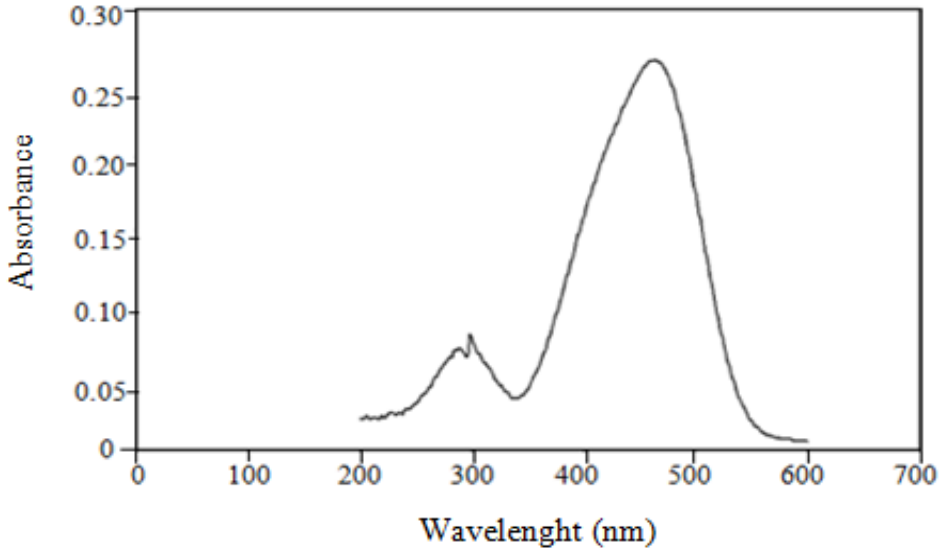


Figure 3.2. UV-Vis spectra of MO.

3.2. Preparation and Characterization of ZnO Catalysts

ZnO catalysts in the absence of the support materials are prepared by a co-precipitation method using $Zn(NO_3)_2.6H_2O$ and Na_2CO_3 precursors as described in the study of Anandan et al. [63]. The precursors with certain concentrations (0.125M, 0.25M and 0.5M) are separately dissolved in deionized water. Then, 100 mL of $Zn(NO_3)_2.6H_2O$ are slowly added into vigorously stirred 100 mL of Na_2CO_3 solution. The resulting white suspension is agitated by magnetic stirrer for 2 h at room temperature. This step is followed by several washings and centrifugations at 4000 rpm. Then, the catalysts are dried at 100ºC for 12 h. The calcination step is done in a muffle furnace using ambient air at 500ºC with a heating rate of 10ºC min^{-1} for 5 h. Finally, the catalysts are ground into fine powder, stored in dark and named as 0.125M ZnO, 0.25M ZnO and 0.5M ZnO.

XRD analysis of 0.25M ZnO shows the distinctive ZnO peak (101) at 36.4^o (2θ) (Figure 3.3). Other ZnO reflections of (100), (002), (102), (110), (103) and (200) are

detected at 31.9˚, 34.6˚, 47.7˚, 56.7˚, 63.1˚ and 66.6˚ (2θ) respectively. The ZnO nanoparticles in the image of 0.25M ZnO are reasonably uniform in size and the morphologies takes on kidney like shape with detection of only Zn (88.8 wt %) and O (11.2 wt %) peaks in the EDX analysis (Figure 3.4 and inset).

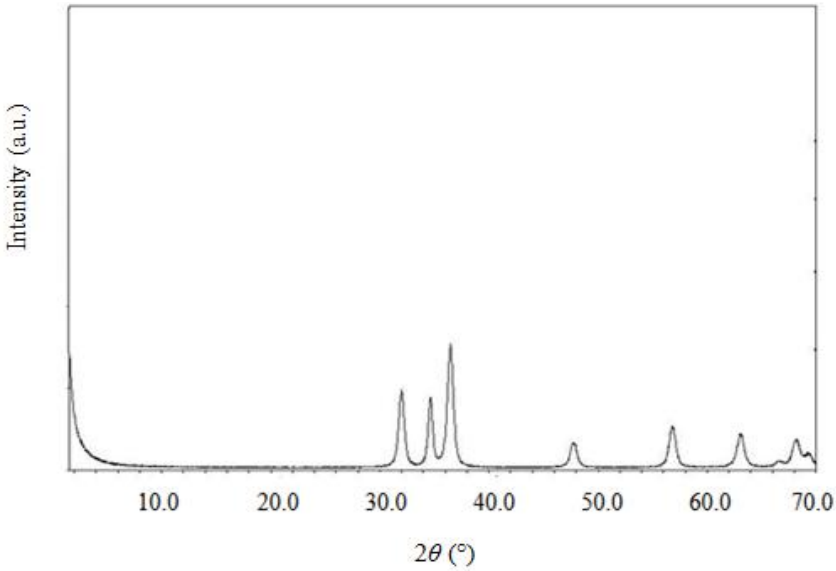


Figure 3.3. XRD pattern of 0.25M ZnO.

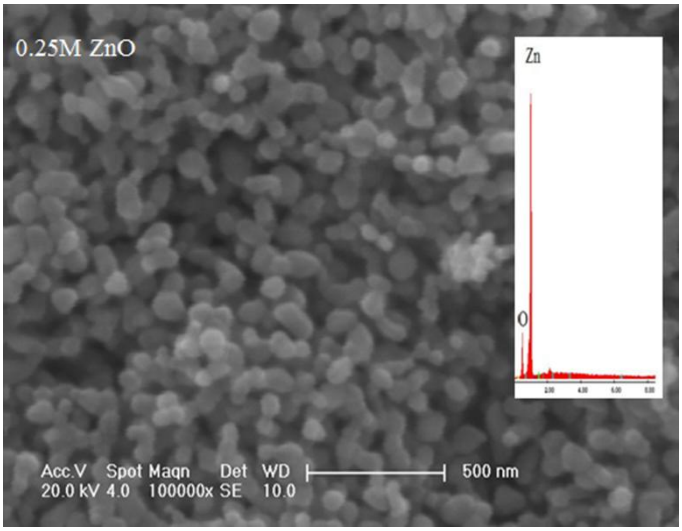


Figure 3.4. SEM image of 0.25M ZnO. Inset: EDX analysis.

3.3. Preparation of NC1, NC2 and MMT2 Supports

3.3.1. NC1

MMT modified with 25-30 wt % methyldihydroxyethyl hydrogenated tallow ammonium (NC1) is commercially available. Figure 3.5 illustrates molecular structure of methyldihydroxyethyl hydrogenated tallow ammonium. Also organic material has chloride as anion. Tallow contains ~65% C_{18}, ~30% C_{16}, ~5% C_{14}. The modification mechanism of NC1 is shown in Figure 3.6. In theory, methyldihyroxyethyl hydrogenated tallow ammonium molecule swells between silicate layers of MMT and an ion-exchange reaction occurs. Consequently, the expansion between layers is observed and an organophilic nature is achieved. This organophilic nature is stable up to 300˚C, above this temperature organic modifier decomposes and clay turns its hydrophilic nature again.

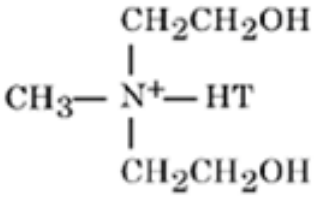


Figure 3.5. Molecular structure of methyldihydroxyethyl hydrogenated tallow ammonium.

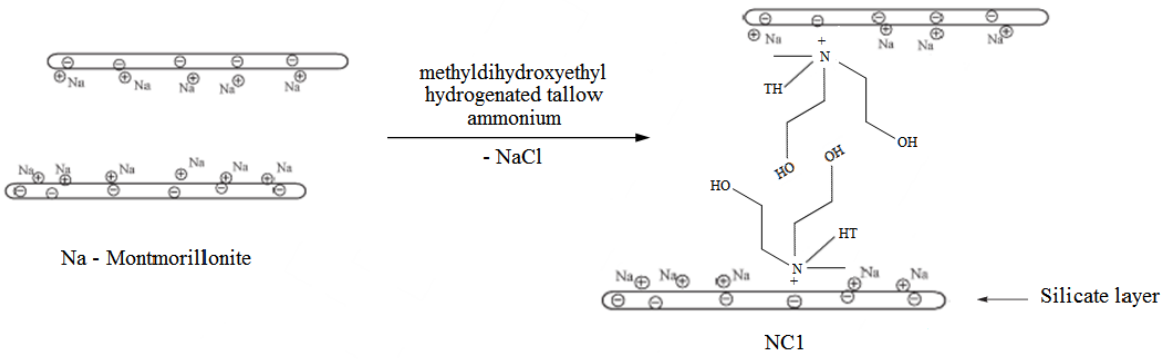


Figure 3.6. Modification mechanism of Na-MMT with 25-30 wt % methyl dihydroxyethyl hydrogenated tallow ammonium.

3.3.2. NC2

MMT modified with 15-35 wt % octadecylamine and 0.5-5 wt % aminopropyltriethoxysilane (NC2) is commercially available. Molecular structures of octadecylamine and aminopropyltriethoxysilane are shown in Figure 3.7 and Figure 3.8, respectively. The modification mechanism of NC2 is illustrated in Figure 3.9. Theoretically, octadecylamine and aminopropylethoxysilane molecules swell between silicate layers of MMT and an ion-exchange reaction occurs. This interaction leads to increment in the space between the layers. Also, this organic modification turns hydrophilic nature to organophilic which is stable through 300˚C. Consequently, clay may adsorb organic materials easily. Over 300˚C organic modification materials decompose and clay regains its hydrophilic nature again.

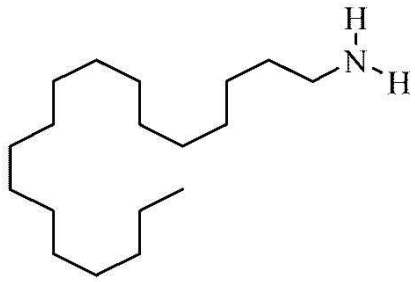


Figure 3.7. Molecular structure of octadecylamine.

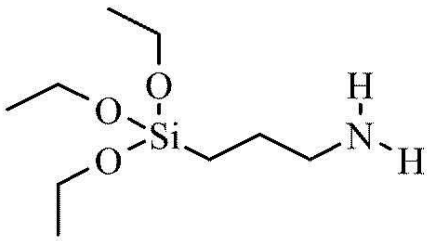


Figure 3.8. Molecular structure of aminopropyltriethoxysilane.

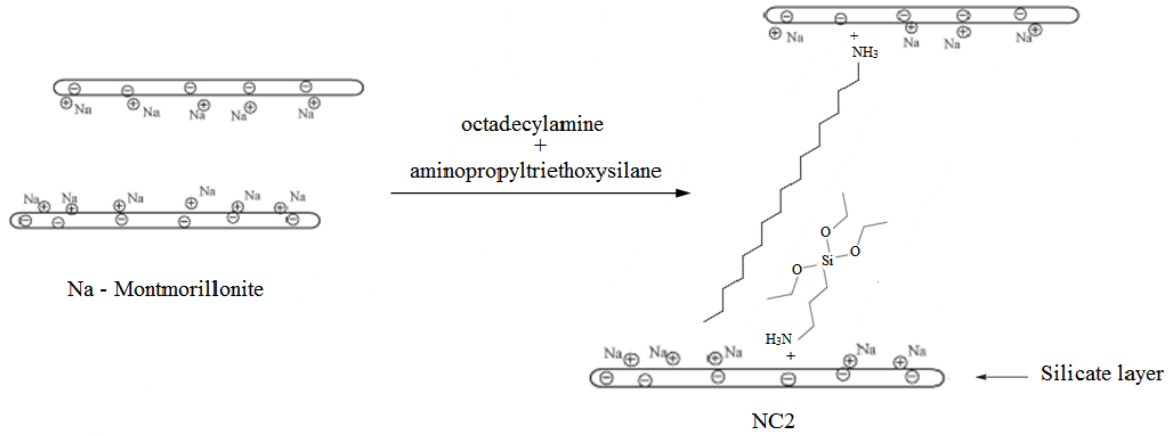


Figure 3.9. Modification mechanism of Na-MMT with 15-35 wt % octadecylamine and 0.5-5 wt % aminopropyltriethoxysilane.

3.3.3. MMT2

MMT modified with cetyl trimethyl ammonium bromide (MMT2) is prepared in laboratory conditions. 4 g of MMT is dispersed in 300 mL deionized water at 50˚C, also separately 4 g cethyl trimethyl ammonium bromide (CTAB) is solved in 200 mL. After a while CTAB solution is slowly added onto MMT solution and obtained mixture is stirred at 50˚C for 4 hours. After 4 hours the organically modified MMT is recovered from any excess ions by several washing and centrifugation applications. Final product is dried at 50˚C in a vacuum oven for 48 hours.

Molecular structure of CTAB is illustrated in Figue 3.10 and proposed modification mechanism of MMT2 is demonstrated in Figure 3.11. Organic material penetrates between layers of MMT and cation exchange happens among silicate layer and swelling agent, though an interaction occurs. This interaction leads to expansion between the layers and it makes the clay organophilic which is stable up to 300˚C. Above 300˚C organic modifier decomposes and clay turns its hydrophilic nature again.

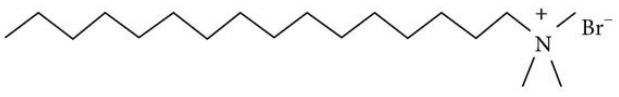


Figure 3.10. Molecular structure of CTAB.

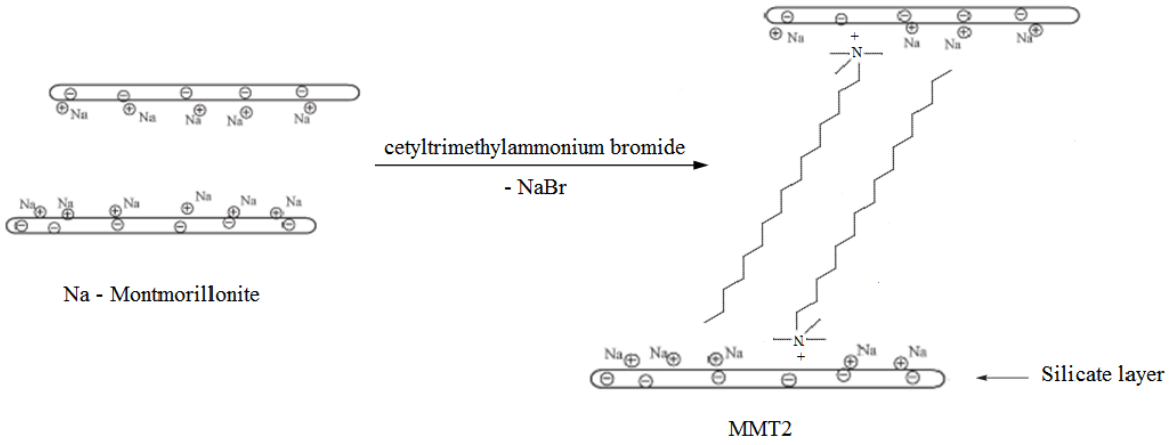


Figure 3.11. Modification mechanism of Na-MMT with cetyltrimethyl ammonium bromide.

3.4. Preparation of Supported Catalysts

Supported catalysts are prepared with the addition of 2 g support materials suspended in water (about 2 h) into the precursor's 200 mL solution. The same precursor concentrations are used as mentioned in section 3.2. After stirring the mixed suspension about 12 h at room temperature, several centrifugations (at 4000 rpm) and washings are applied. The resulting supported catalysts are dried at 100˚C for 12 h and then, calcinated in a muffle furnace using ambient air at 300^{o}C and 500˚C with a heating rate of 10˚C min for 5 h. Finally, the catalysts are ground into fine powder, stored in dark and named as; 0.125M ZnO-MMT (300˚C), 0.25M ZnO-MMT (300˚C), 0.5M ZnO-MMT (300˚C), 0.125M ZnO-NC1 (300˚C), 0.25M ZnO-NC1 (300˚C), 0.5M ZnO-NC1 (300˚C), 0.125M ZnO-NC2 (300˚C), 0.25M ZnO-NC2 (300˚C), 0.5M ZnO-NC2 (300˚C), 0.125M ZnO-MMT2 (300˚C), 0.25M ZnO- MMT2 (300˚C), 0.5M ZnO- MMT2 (300˚C), 0.125M ZnO-MMT (500˚C), 0.25M ZnO-MMT (500˚C), 0.5M ZnO-MMT (500˚C), 0.125M ZnO-NC1 (500˚C), 0.25M ZnO-NC1 (500˚C), 0.5M ZnO-NC1 (500˚C), 0.125M ZnO-NC2 (500˚C), 0.25M ZnO-NC2 (500˚C), 0.5M ZnO-NC2 (500˚C), 0.125M ZnO-MMT2 (500˚C), 0.25M ZnO- MMT2 (500˚C), 0.5M ZnO- MMT2 (500˚C).

3.4. Analysis

3.4.1. Characterization Techniques

The structural features of raw supports (MMT, NC1, NC2, and MMT2) and supported catalysts are examined with different analytical methods. The X-ray diffraction (XRD) is used to determine the crystal structure of the raw support and supported catalysts. The XRD patterns of all catalysts are recorded on a Rigaku-D/MAX-Ultima diffractometer with Cu Kα radiation (λ = 1.54 Å) operating at 40 kV and 40 mA and scanning rate of 2˚ min^{-1}. The scanning range 0˚-70˚ (2θ) is used to determine all materials.

The surface morphologies of the raw support and supported catalysts are obtained with Scanning Electron Microscopy (SEM) in combination with Energy Dispersive X-ray analysis on an ESEM-FEG/EDAX Philips XL-30 instrument operating at 20kV using powder of materials supported on carbon tape.

The BET (Brunauner-Emmet-Teller) isotherms are recorded at liquid nitrogen temperature 77 K by using Quantachrome Nova 2200e automated gas adsorption system. Multi-point BET and BJH method are used to establish the specific surface area and the pore sizes, respectively.

The UV-Vis diffuse reflectance spectra (UV-Vis DRS) of the supports and all supported catalysts is obtained using a UV-Vis spectrophotometer (UV-2450, Shimadzu), which is equipped with an integrating sphere reflectance accessory. The baseline correction is done with respect to $BaSO_4$. The spectra are recorded in the range of 200-600 nm for all prepared materials.

3.4.2. Photocatalytic Experiments

Photocatalytic degradation experiments of all catalysts are investigated in a laboratory constructed irradiation box. Eight black light fluorescent lamps (8x15 W) which supplies light of wavelength 320-440 nm are fitted out on the two sides of the box (Figure 3.12). A fan is placed back side of the box to eliminate any heat effects of the lamps. The

incident photon flux for all lamps is measured as $7.8x10^{-9}$ einstein/s using potassium ferrioxalate actinometer in the previous works [64]. A pyrex erlenmeyer flask, which has an air inlet on its bottom and an outlet on its top, is used as reaction media. A pump is used for air circulation and connection between erlenmeyer and air pump is supplied with Tygon tubing. During the experiment catalyst is mixed in the MO or MB solutions with a magnetic stirrer.

Before the illumination, catalysts and MO solution mixed in the dark 30 minutes to reach equilibrium condition under continuous circulation. All experiments are carried out at room temperature and at natural pH of all catalysts. While experiment is going on, degradation intermediates are not concerned. Aliquots (approximately 5 mL) are taken from the outlet of erlenmeyer flax at certain time intervals and analyzed after filtering Millipore filters (0.22 μm). The absorbance spectra of MO are followed by UV-Vis Spectrophotometer (Shimadzu 2450). The absorbance at 278 nm represents the aromatic content of MO and the decrease of the band at this wavelength indicates the degradation of MO's aromatic moiety. The absorbance at 464 nm is in consequence of the color of MO solution and decolorization of MO is followed by reduction of this band.



Figure.3.12. Irradiation box used in photocatalytic degradation experiments.

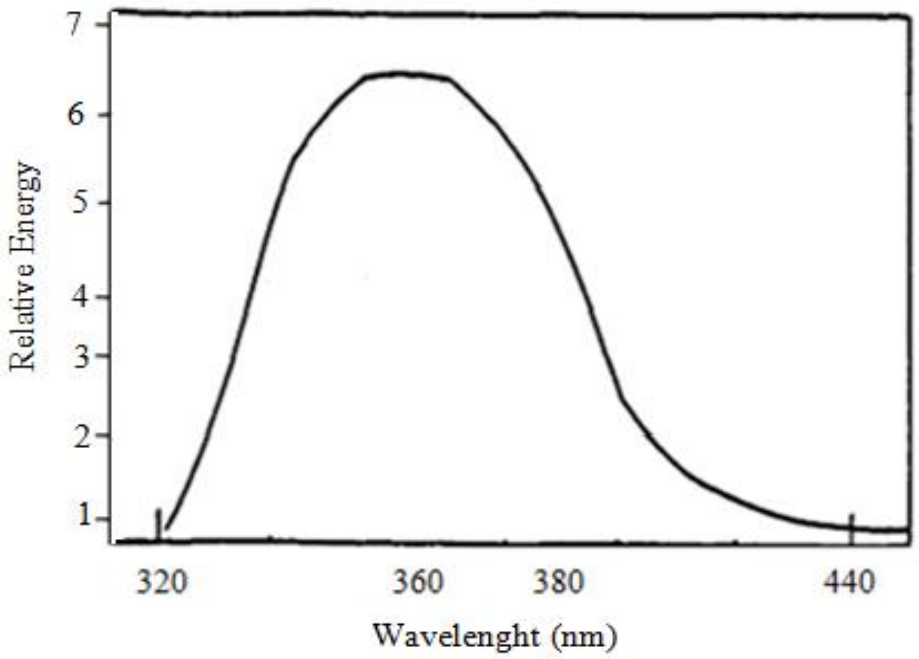


Figure 3.13. Emission spectrum of a fluorescent lamp used in the UV-irradiation box.

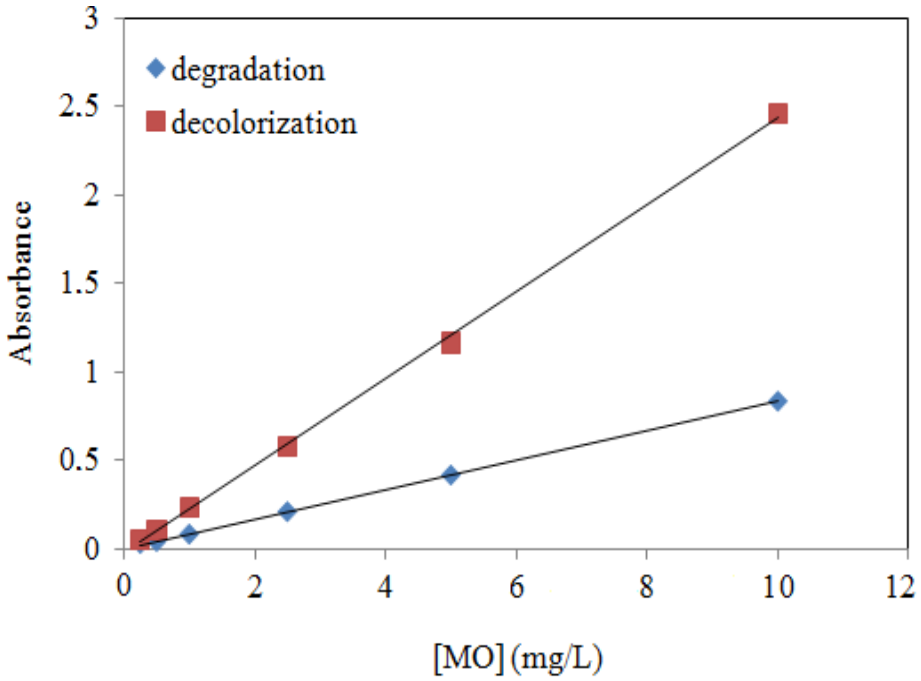


Figure 3.14. Calibration plots of MO at 278 nm (degradation) and 464 nm (decolorization).

3.5. Postulated Mechanism of MO Decomposition

Figure 3.15 demonstrates a possible decomposition mechanism for MO molecule. The photocatalytic degradation mechanism starts with the illumination of ZnO

nanoparticles and production of electron–hole pairs and photogenerated holes react with H_2O molecules and produce •OH radicals. In the line of the previous studies, though intermediates forming in the photocatalytic decolorization process of MO are not identified, the following routes of MO; substitution of methyl groups with hydrogen atoms in the aminic group results in the formation of product 1 and ipso-substitution by a hydroxyl radical can take place at the carbon position which carries the sulphonic moiety (products 2 and 3).

The decay profile of the products includes the subsequent attacks of hydroxyl radicals, known as highly reactive electrophilic oxidants. The main reaction pathway (60% of •OH radicals) is the addition of the hydroxyl radical to the double bond of the azo group, resulting in the rapid disappearance of color; however, addition to the aromatic ring also occurs (40% of •OH radicals). Further hydroxyl radical attacks and the increment in hydroxyl radical concentration in the solution increase the yield of OH-adduct in the degradation progress of each product. The opening of the dye aromatic rings due to consecutive oxidation reactions leads to low-molecular weight compounds as previously reported. In the course of degradation, inorganic anions (SO_4^{2-}, NH_4^+) can progressively form. Although bleaching reaction is very fast, complete mineralization of the dye to yield small molecules, such as CO_2 and H_2O takes much longer [65].

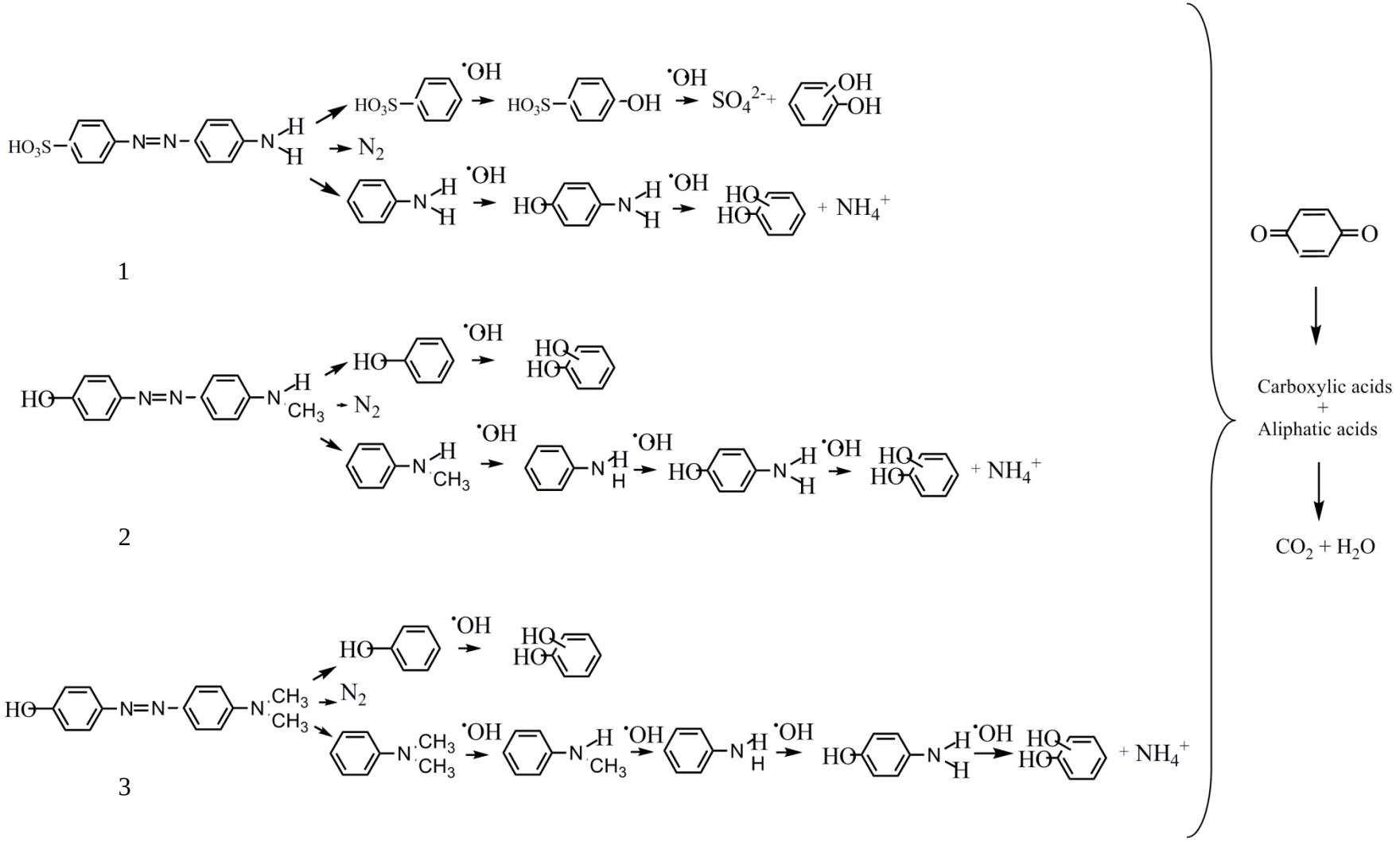


Figure 3.15. Proposed decomposition mechanism of MO.

4. RESULTS AND DISCUSSION

4.1. Characterization Results of the ZnO-MMT Catalysts

4.1.1. XRD Analysis

Figure 4.1 and Figure 4.2 show the XRD spectras of bare MMT, 0.125M ZnO-MMT (300˚C), 0.25M ZnO-MMT (300˚C), 0.5M ZnO-MMT (300˚C), 0.125M ZnO-MMT (500˚C), 0.25M ZnO-MMT (500˚C) and 0.5M ZnO-MMT (500˚C) catalysts. The characteristic (001) reflection of MMT is observed at 7.04˚ (2θ) with a d-spacing value of 12.8 Å. Also, small reflection peaks are observed at 19.9˚, 21.8˚, 26.6˚ and 61.6˚ (2θ), corresponding to crystoballite and quartz phases. [66]. In the XRD patterns of supported catalysts, characteristic MMT peak is not detected which indicating destruction of neat oriented layers. However, there is still space among the layers as also noticed in the study of Morgan et. al. [67]. ZnO diffraction peaks of (100), (002), (101), (102), (110), (103) and (200) are observed at 31.9˚, 34.6˚, 36.4˚, 47.7˚, 56.7˚, 63.1˚ and 66.6˚ (2θ), respectively (Figure 4.1 and Figure 4.2). Among these, the most intense (101) reflection at 36.4˚ (2θ) is considered as the characteristic ZnO peak. Meanwhile, the supported catalysts show broader and lower intense diffractions, ZnO diffraction peaks get sharper when the loading amount increases.

The crystalline size of ZnO nanoparticles (D_{ZnO}) based on the broadening of the most intense (101) diffraction is calculated by employing Scherrer's equation (Table 4.1). For the catalysts calcinated 300˚C, crystalline sizes of ZnO nanoparticles are quite similar and less than that bare ZnO. The sizes are also found to be similar in the case of 0.125M ZnO-MMT (500˚C) and 0.25M ZnO-MMT (500˚C) catalysts. However, a slight increase (16.41 nm) is noticed in the presence of 0.5M ZnO-MMT (500˚C). The disorder created on the surface of the clay increases with the loading concentration of ZnO and hence, the possibility for the formation of aggregates becomes inevitable.

Table 4.1. Crystalline sizes (D), surface areas (BET), pore volumes (V_{pore}) and pore radius (r_{pore}) of 0.25M ZnO (500°C), MMT (500°C) and supported catalysts.

Catalyst	**2θ (˚)**	**D (nm)**	**BET (m^2/g)**	**V_{pore} (cm^3/g)**	**r_{pore} (Å)**
0.25M ZnO (500˚C)	36.4	15.20	7.6	0.013	17.8
MMT	7.04	-	28.0	0.027	14.9
0.125M ZnO-MMT (300˚C)	36.4	14.58	38.5	0.070	16.4
0.25M ZnO-MMT (300˚C)	36.4	13.35	42.9	0.078	15.7
0.5M ZnO-MMT (300˚C)	36.4	14.04	40.9	0.072	20.1
0.125M ZnO-MMT (500˚C)	36.4	14.27	32.8	0.055	17.7
0.25M ZnO-MMT (500˚C)	36.4	14.06	34.9	0.062	20.6
0.5M ZnO-MMT (500˚C)	36.4	16.41	26.0	0.042	14.9

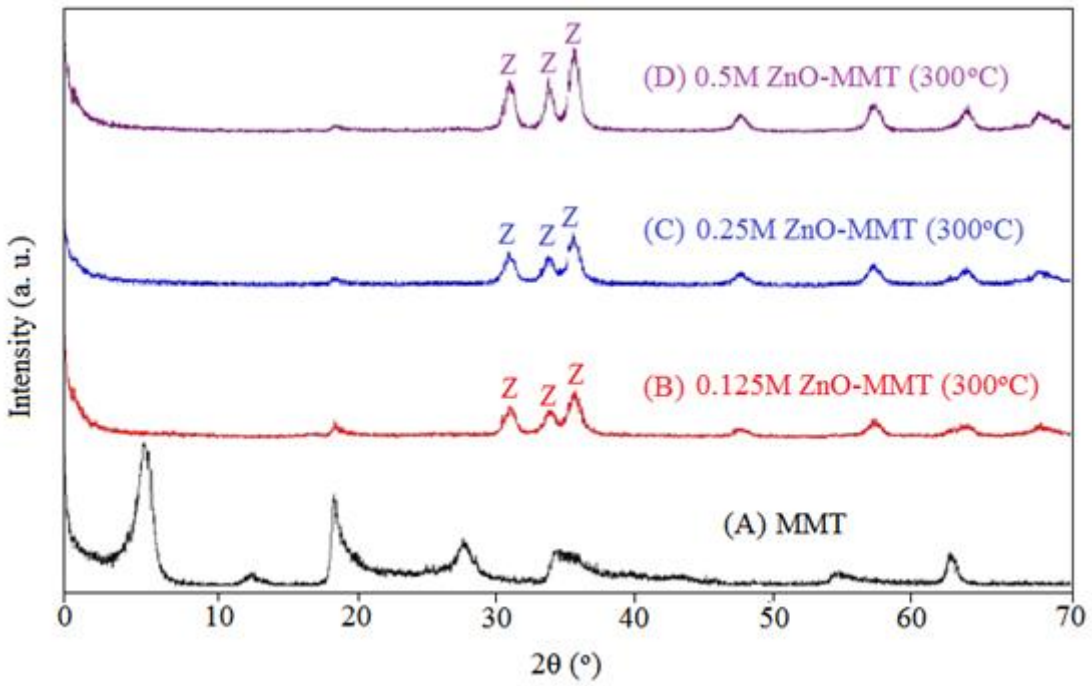


Figure 4.1. XRD patterns of MMT (A) and supported catalysts (300˚C) (B-D). (Z: ZnO).

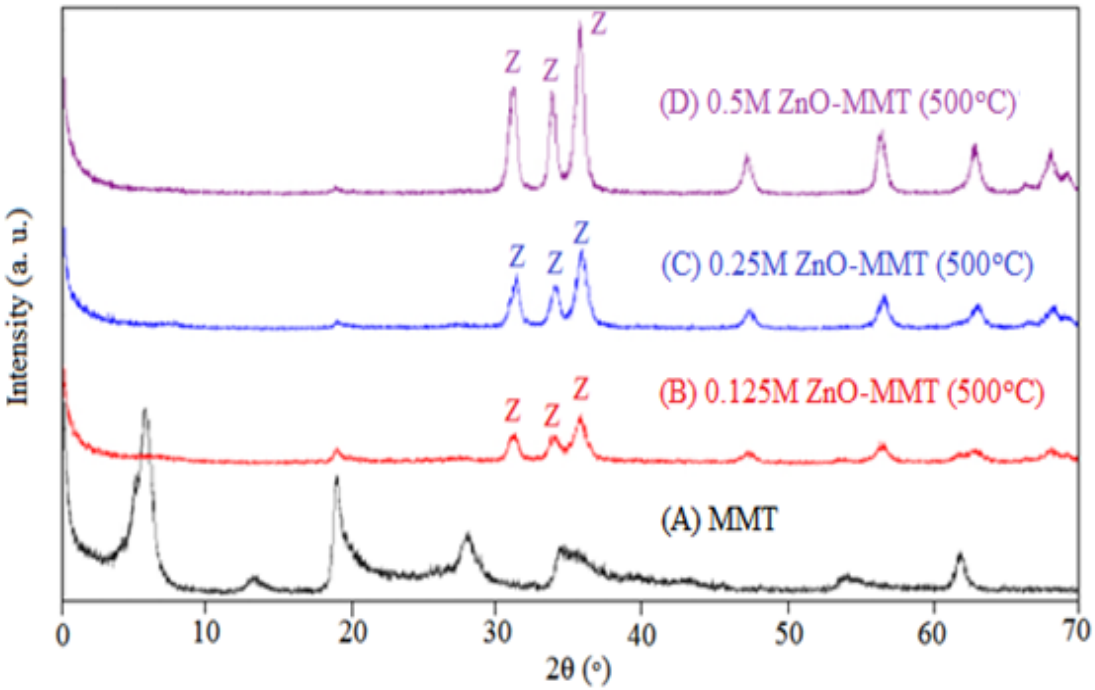


Figure 4.2. XRD patterns of MMT (A) and supported catalysts (500˚C) (B-D). (Z: ZnO).

4.1.2. SEM-EDX Analysis

Surface morphologies of the bare MMT and 0.25M ZnO-MMT (500˚C) are investigated by SEM (EDX) analysis. Bare MMT has a curly flake like structure (Figure 4.3). Based on the EDX analysis, major Si and Al components and minor Fe, Mg and Na constitutes of MMT are detected (Table 4.2). For 0.25M ZnO-MMT (500˚C), Zn and O elemental compositions are noticeable.

SEM micrograph and mapping images of 0.25M ZnO-MMT (500˚C) are displayed in the Figure 4.4. Although the structure of MMT is retained following the ZnO treatment, homogenously distributed ZnO nanoparticles over the surface of the support are detected. This is also evidenced in the EDX data (Table 4.2). Besides, MMT has no Zn, 0.25M ZnO-MMT (500˚C) shows 53.07% Zn component. The reduction in the silica and alumina percentages may also correspond to the location of ZnO nanoparticles in the silica matrix of the clay.

Table 4.2. Elemental compositions of MMT, 0.25M ZnO (500˚C) and 0.25M ZnO-MMT (500˚C).

	MMT	**0.25M ZnO (500˚C)**	**0.25M ZnO-MMT (500˚C)**
Components	**Wt %**	**Wt %**	**Wt %**
Zn	-	88.79	53.07
Si	30.27	-	18.83
O	27.73	11.21	18.31
Al	22.38	-	6.91
Fe	3.08	-	-
Mg	5.76	-	2.88
Na	1.79	-	-

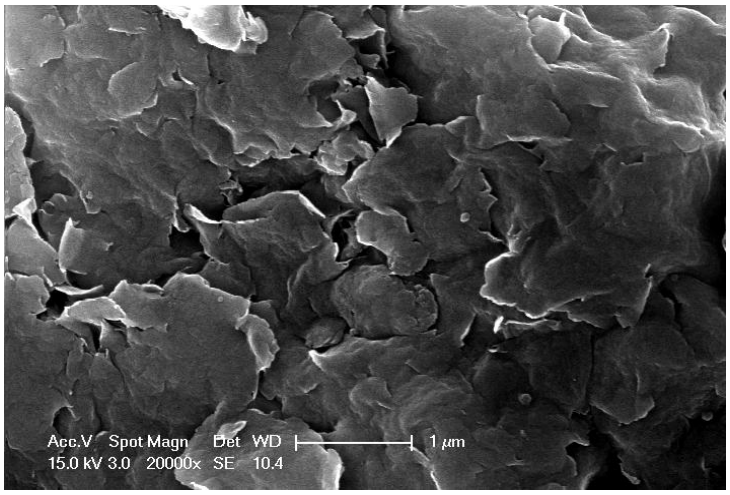


Figure 4.3. SEM image of MMT.

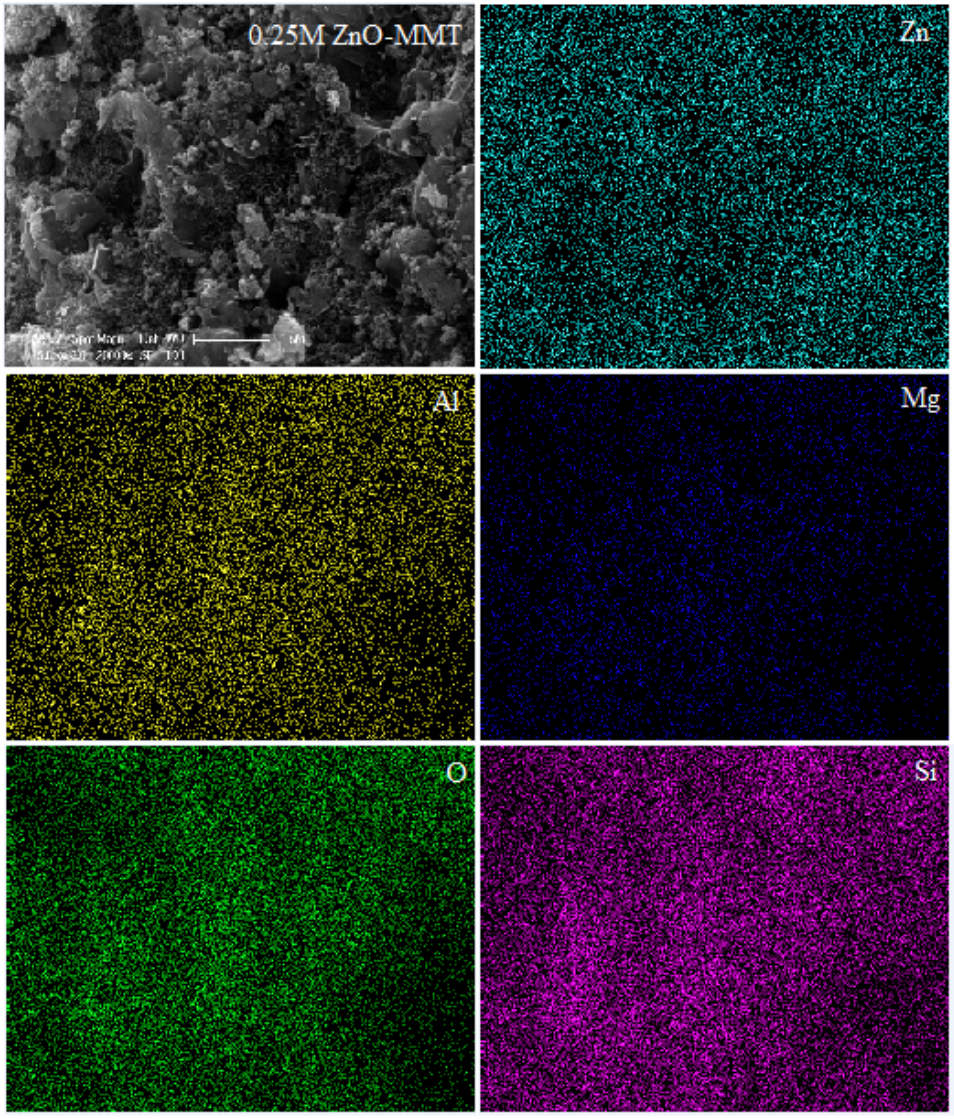


Figure 4.4. SEM image of 0.25M ZnO-MMT and mapping images of 0.25M ZnO-MMT, Zn, Al, Mg, O and Si.

4.1.3. Nitrogen Adsorption-Desorption Isotherms

Nitrogen adsorption-desorption isotherms and pore size distribution plots of the MMT and supported catalysts are illustrated in the Figure 4.5, Figure 4.6, Figure 4.7 and Figure 4.8. ZnO shows Type II isotherms which is specific for non-porous materials (Figure 4.7). However, MMT and supported catalysts exhibits Type IV isotherms, owing to their mesoporous structure. The increment in the loading concentration of ZnO narrows the hysteresis loops. The pore size distribution curves display that the pores of the supported catalysts exist in the typical mesoporous region of 20-40 Å (Figure 4.6 and Figure 4.8). In

comparison to raw MMT, supported catalysts have higher surface areas and pore volumes (Table 4.1). Pore sizes and surface areas of the catalysts prepared at 300˚C do not change distinctively. The decrements in the surface and porosity of 0.5M ZnO-MMT (500˚C) in comparison to 0.125M ZnO-MMT (500˚C) and 0.25M ZnO-MMT (500˚C) are not significant, thus an adverse effect in the activity of this catalyst is not expected.

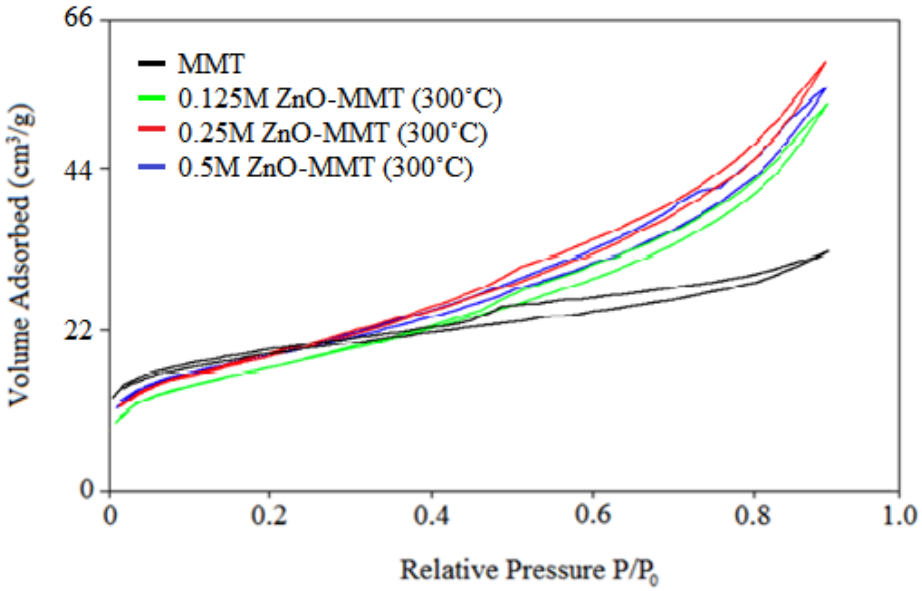


Figure 4.5. Nitrogen adsorption-desorption isotherms of MMT, 0.25M ZnO and supported catalysts prepared at 300˚C.

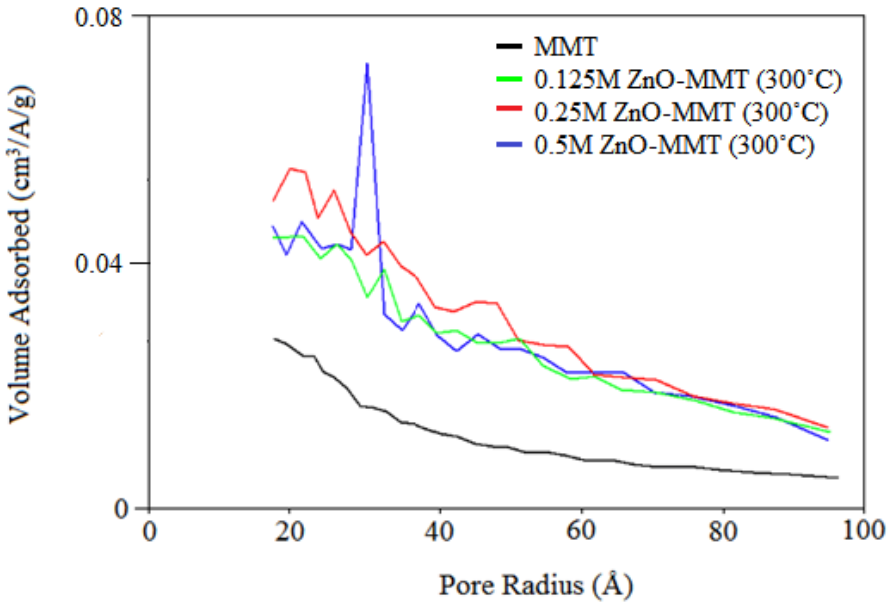


Figure 4.6. Pore size distribution plots of MMT and supported catalysts prepared at 300˚C.

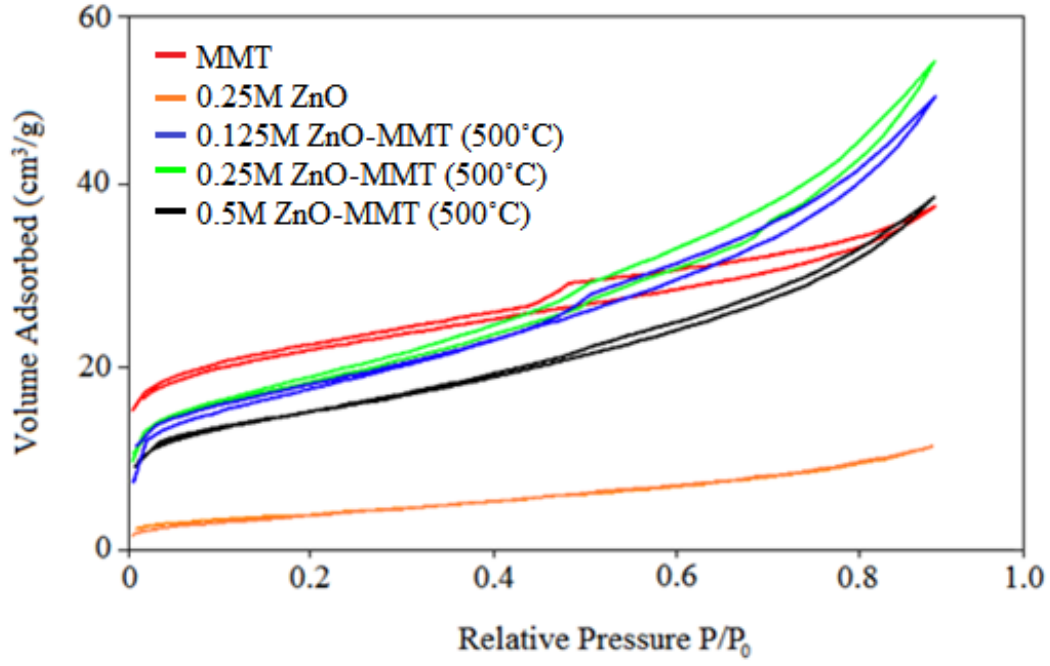


Figure 4.7. Nitrogen adsorption-desorption isotherms of MMT, 0.25M ZnO and supported catalysts prepared at 500˚C.

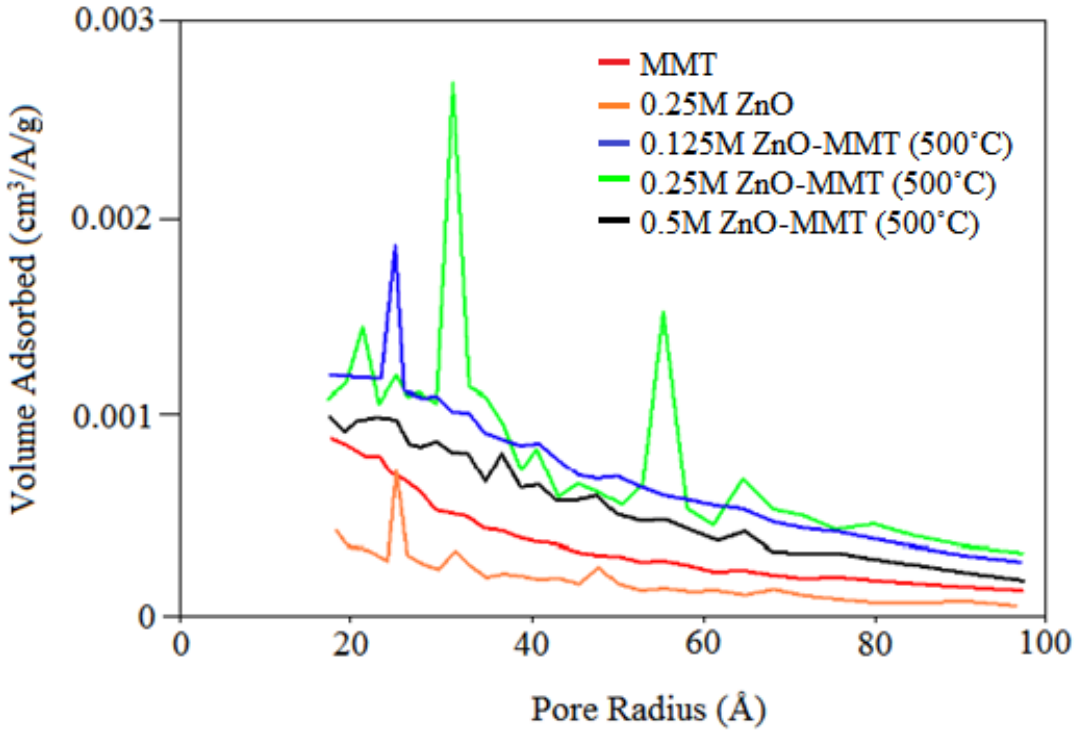


Figure 4.8. Pore size distribution plots of MMT and supported catalysts prepared at 500˚C.

4.1.4. UV-Vis DRS Analysis

UV Vis absorption spectras of the MMT and the supported catalysts are displayed in the Figure 4.9 and Figure 4.10. The inset in Figure 4.9 shows the absorption spectrum of 0.25M ZnO (500˚C). The bare MMT shows an extended absorption tail between 200 and 600 nm while 0.25 ZnO has a sharp absorption edge at the UV region. In the absorption spectras of supported catalysts the characteristic absorption edge of ZnO is detected. This edge becomes more observable and wider with the higher loading concentration of ZnO.

In addition the UV-Vis absorption spectra of the as prepared catalysts are transformed to the band-gap values (Equation 2.17) which are evaluated by linear extrapolation and taking the intercept on the x-axis gives the value of the band gap (Figure 4.11 and Figure 4.12). Accordingly, band gap energy of 0.25M ZnO (500˚C) is found as 3.12 eV (Figure 4.11 Inset). A slight decrease is observed for the supported catalysts in comparison to the 0.25M ZnO which may correspond an activity in the visible region.

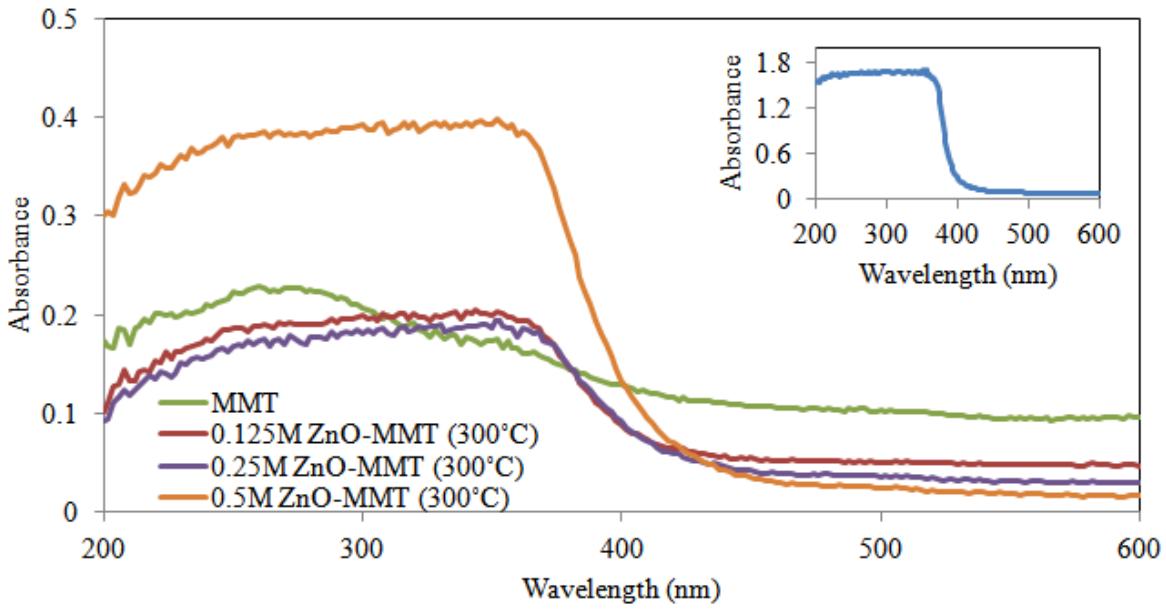


Figure 4.9. UV-Vis DRS spectra of MMT and supported catalysts prepared at 300˚C. Inset: UV-Vis DRS spectra of 0.25M ZnO (500˚C).

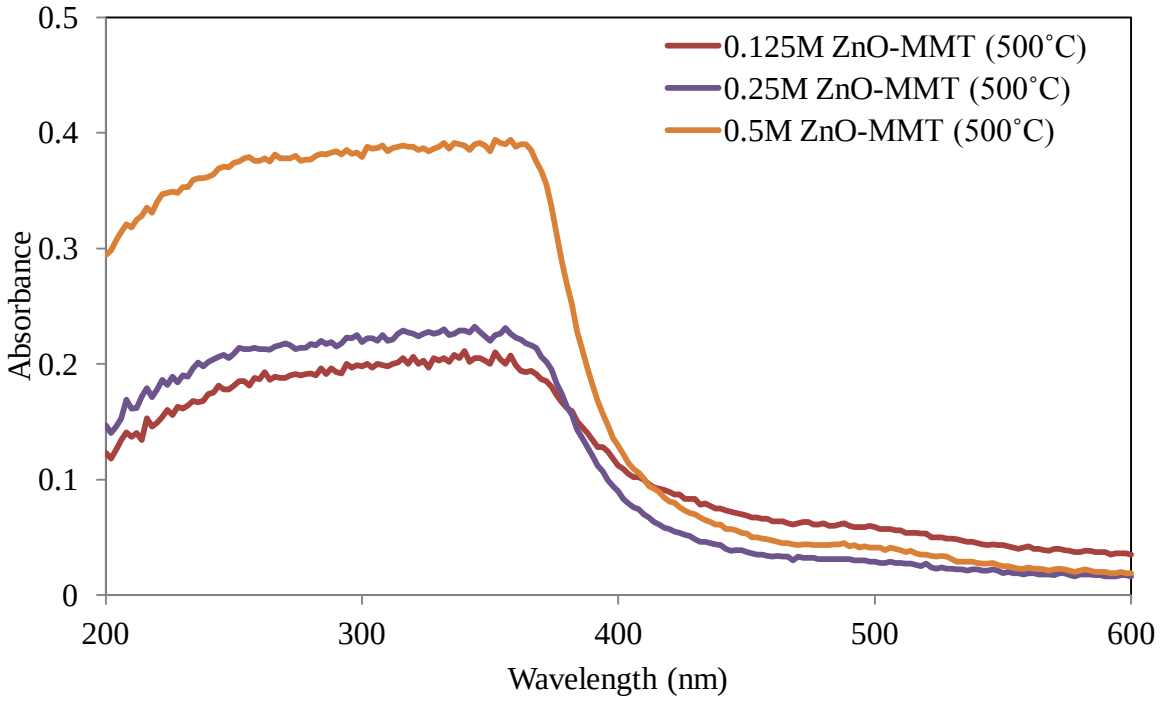


Figure 4.10. UV-Vis DRS spectra of supported catalysts prepared at 500˚C.

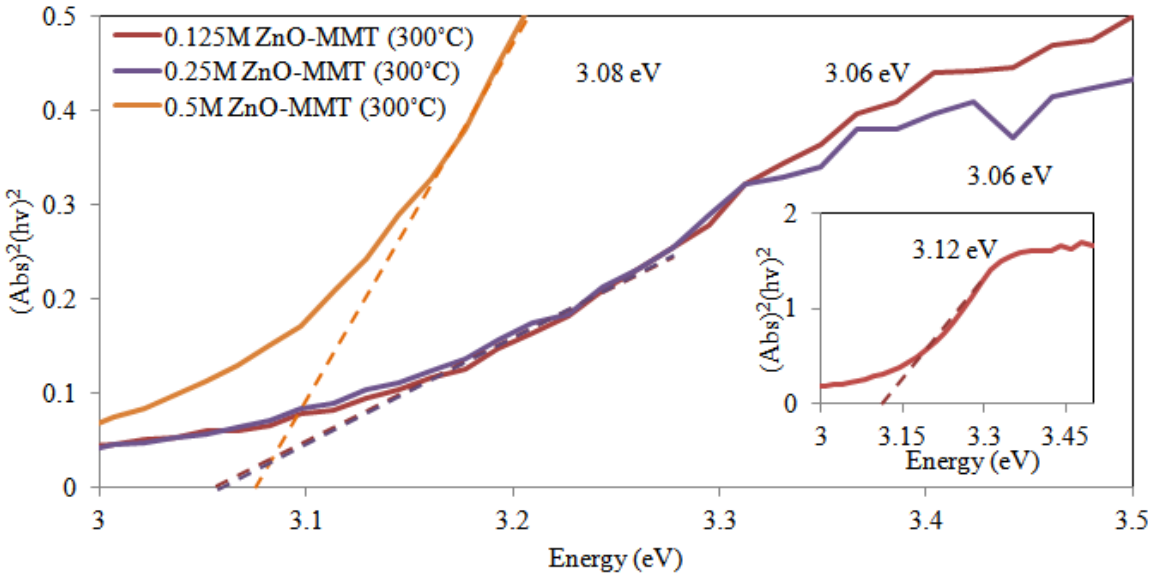


Figure 4.11. Band gap adsorption edges of supported catalysts. Inset: Band gap adsorption edges of 0.25M ZnO (500˚C).

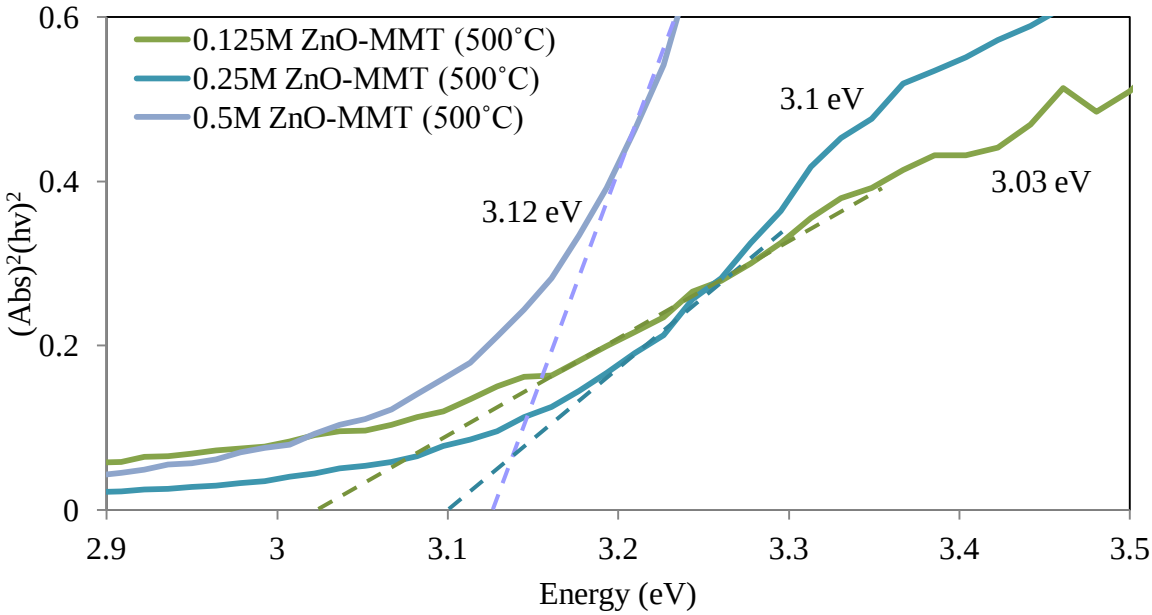


Figure 4.12. Band gap adsorption edges of supported catalysts.

4.2. Photoactivities of ZnO-MMT Catalysts

4.2.1. Control Experiments

Control experiments are set as two steps. In the first step, dark absorption capacities of MMT, 0.25M ZnO (500˚C), 0.25M ZnO-MMT (300˚C) and 0.25M ZnO-MMT (500˚C) are compared (Figure 4.13). For all samples, after 85 min mixing in the dark, no significant change is noticed in the MO concentrations. In the second set, photolysis of MO and photocatalytic activities of 0.25M ZnO (500˚C), 0.25M ZnO-MMT (300˚C) and 0.25M ZnO-MMT (500˚C) are examined (Figure 4.14). A negligible MO degradation is observed in the presence of UV light without any catalyst (Figure 4.14 Inset). The suspensions are stirred in the dark for 30 min to achieve adsorption/desorption equilibrium and thereafter exposed to illumination. Although, 0.25M ZnO (500˚C) shows a higher performance in comparison to the supported catalysts, the difficulties in the settlement of ZnO nanoparticles limit their applications in photocatalytic reactions. In the meantime, the activity of 0.25M ZnO-MMT (500˚C) is better than 0.25M ZnO-MMT (300˚C). Heat-induced growth of ZnO particles results in sharper and narrower X-ray peaks, contributes to the increase of crystallinity and hence increases the photoactivity [68].

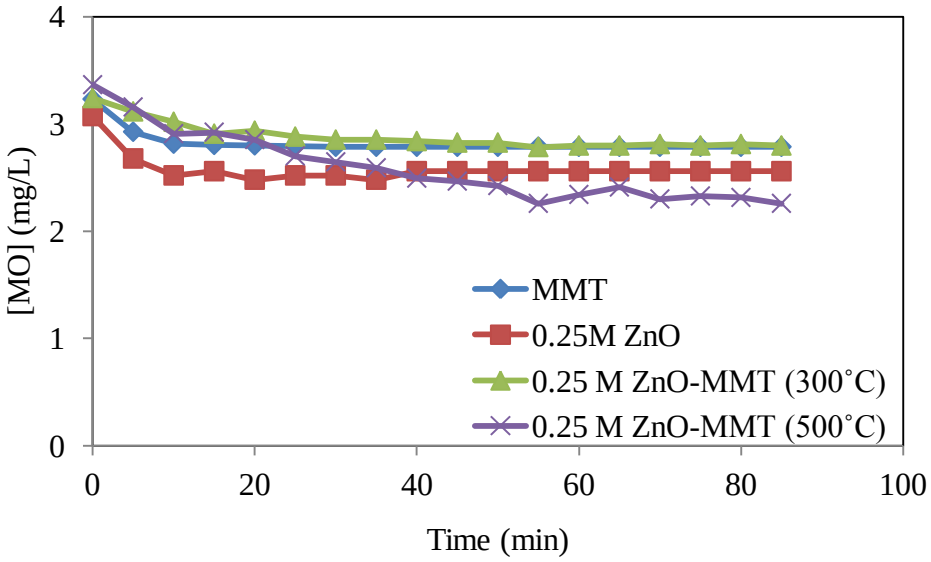


Figure 4.13. Control experiments in the dark. Conditions: pH: 6.5 (Natural), $[MO]_0$ = 3.27 mg/L, T = 298 K, Flow rate = 2000 rpm.

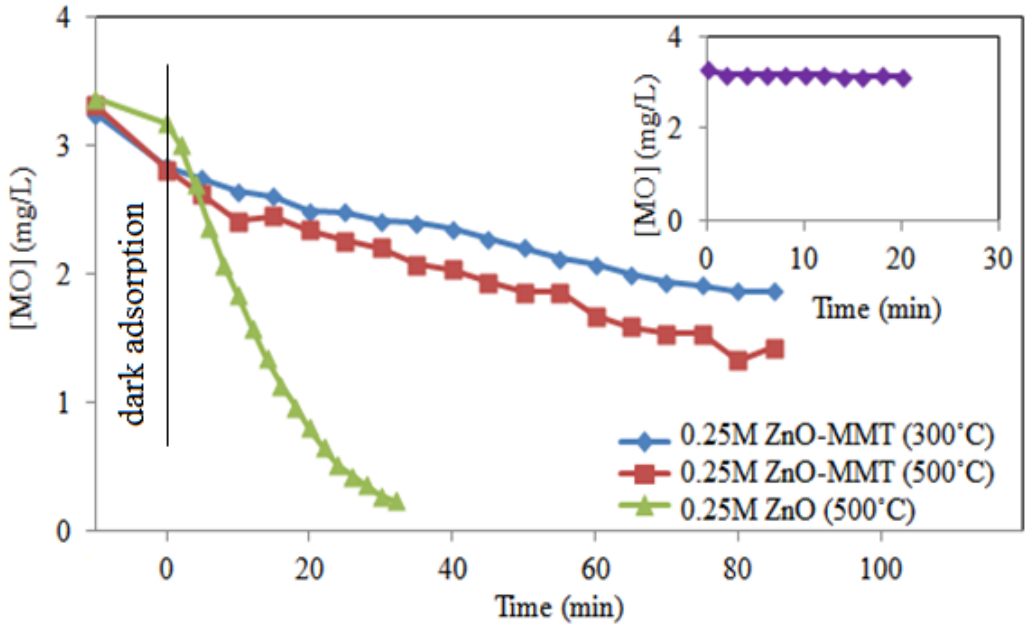


Figure 4.14. Control experiments under UV irradiation. Inset: Photolysis of MO. Conditions: pH: 6.5 (Natural), $[MO]_0$= 3.27 mg/L, T= 298K, Flow rate= 2000 rpm.

4.2.2. Dark Adsorption Experiments

4.2.2.1. Adsorption Kinetics. The dark adsorption details of MO (16.32 mg/L) over the 0.5M ZnO-MMT (300˚C) and 0.5M ZnO-MMT (500˚C) catalysts are investigated to

specify the adsorption kinetics in terms of pseudo first order and pseudo second order models.

Pseudo first order model is applied with respect to the slope of $\ln(q_e-q_t)$ versus t graph. The correlation coefficients are found as 0.9481 (degradation) and 0.9883 (decolorization) and for 0.5M ZnO-MMT (300˚C) and 0.8278 (degradation) and 0.9846 (decolorization) for 0.5M ZnO-MMT (500˚C) (Figure 4.15, Figure 4.16, Figure 4.17 and Figure 4.18).

In the case of pseudo second order model, correlation coefficients in the plots of t/q_t versus t are found as 0.9747 (degradation), 0.9910 (decolorization) for 0.5M ZnO-MMT (300˚C) and 0.4781 (degradation), 0.4549 (decolorization) for 0.5M ZnO-MMT (500˚C) (Figure 4.19, Figure 4.20, Figure 4.21 and Figure 4.22).

The higher values of the coefficients imply a better adsorption of MO. Accordingly, pseudo-second order model fits to the 0.5M ZnO-MMT (300˚C), while only a certain extent of adsorption seems to be possible by this model in the presence of 0.5M ZnO-MMT (500˚C).

4.2.2.2. Adsorption Isotherms. For the adsorption isotherms, Freundlich and Langmuir models are employed at four different initial concentrations of MO (3.27, 8.17, 16.32 and 24.55 mg/L) in the presence of 0.5M ZnO-MMT (300˚C) and 0.5M ZnO-MMT (500˚C).

Freundlich isotherms' line fittings in $\ln q_e$ versus $\ln C_e$ plots give correlations of 0.9725 (degradation) and 0.9778 (decolorization) for 0.5M ZnO-MMT (300˚C) and 0.9686 (degradation) and 0.9741 (decolorization) for 0.5M ZnO-MMT (500˚C) (Figure 4.23, Figure 4.24, Figure 4.25 and Figure 4.26).

Langmuir isotherms (q_t versus t plots) of the supported catalysts are illustrated in Figure 4.27, Figure 4.28, Figure 4.29, and Figure 4.30. The line fittings in C_e/q_e versus C_e graphs result in correlation coefficients of 0.9436 (degradation) and 0.9877 (decolorization) for 0.5M ZnO-MMT (300˚C) and 0.8786 (degradation) and 0.7247

(decolorization) for 0.5M ZnO-MMT (500˚C) (Figure 4.27, Figure 4.28, Figure 4.29 and Figure 4.30 Insets).

Thus, Freundlich isotherm model fits better to the supported catalysts with higher correlation coefficients.

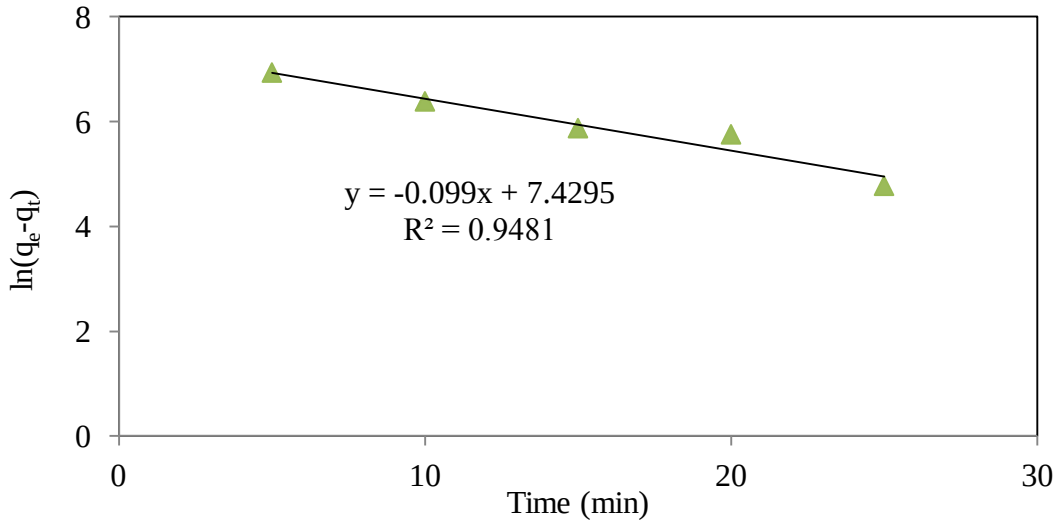


Figure 4.15. Pseudo first order kinetics for degradation of MO in the presence of 0.5M ZnO-MMT (300˚C). Conditions: pH= 6.5 (Natural), $[MO]_0$= 16.32 mg/L, T= 298 K, Flow rate= 2000 rpm.

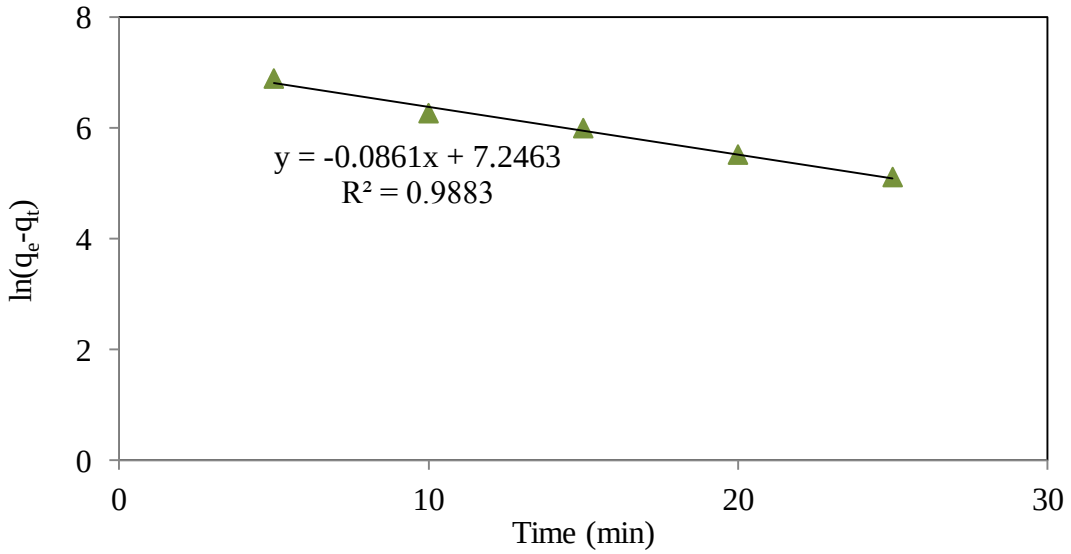


Figure 4.16. Pseudo first order kinetics for decolorization of MO in the presence of 0.5M ZnO-MMT (300˚C). Conditions: pH= 6.5 (Natural), $[MO]_0$= 16.32 mg/L, Calcination= 300˚C, T= 298 K; Flow rate= 2000 rpm.

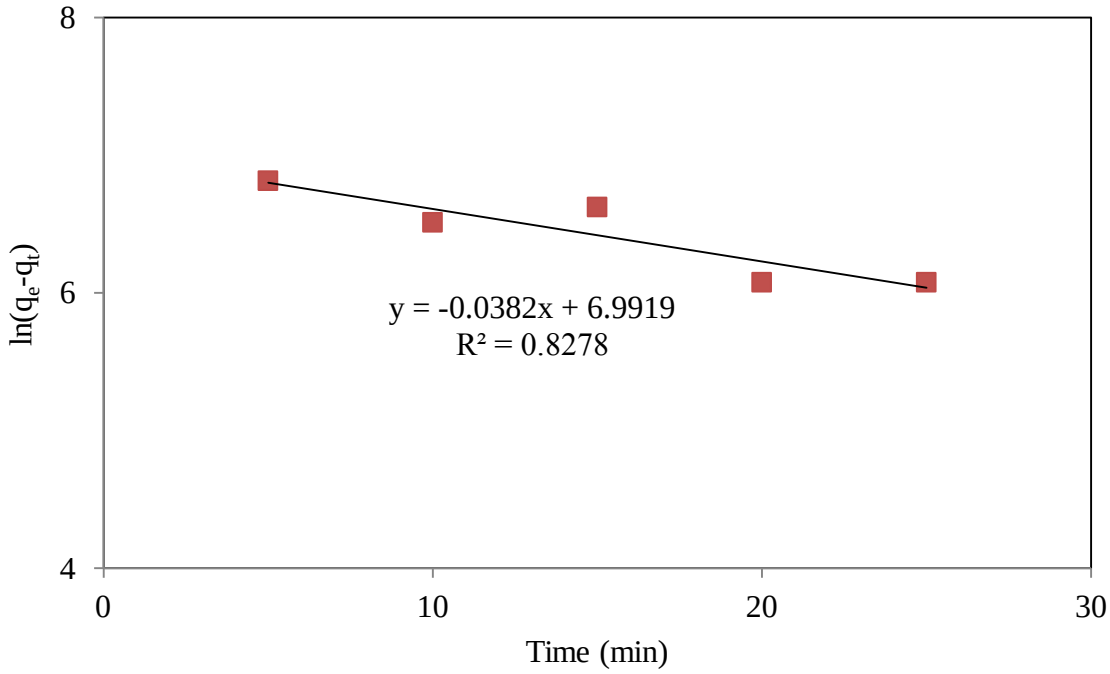


Figure 4.17. Pseudo first order kinetics for degradation of MO in the presence of 0.5M ZnO-MMT (500˚C). Conditions: pH= 6.5 (Natural), $[MO]_0$= 16.32 mg/L, T= 298 K, Flow rate= 2000 rpm.

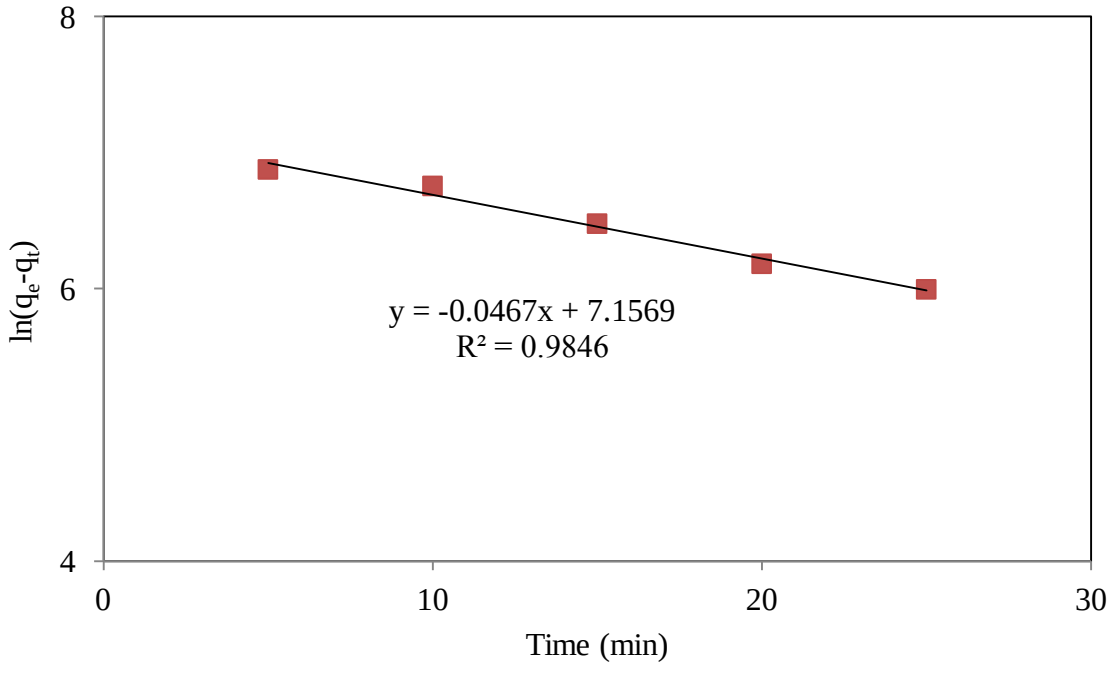


Figure 4.18. Pseudo first order kinetics for decolorization of MO in the presence of 0.5M ZnO-MMT (500˚C). Conditions: pH= 6.5 (Natural), $[MO]_0$= 16.32 mg/L, T= 298 K, Flow rate= 2000 rpm.

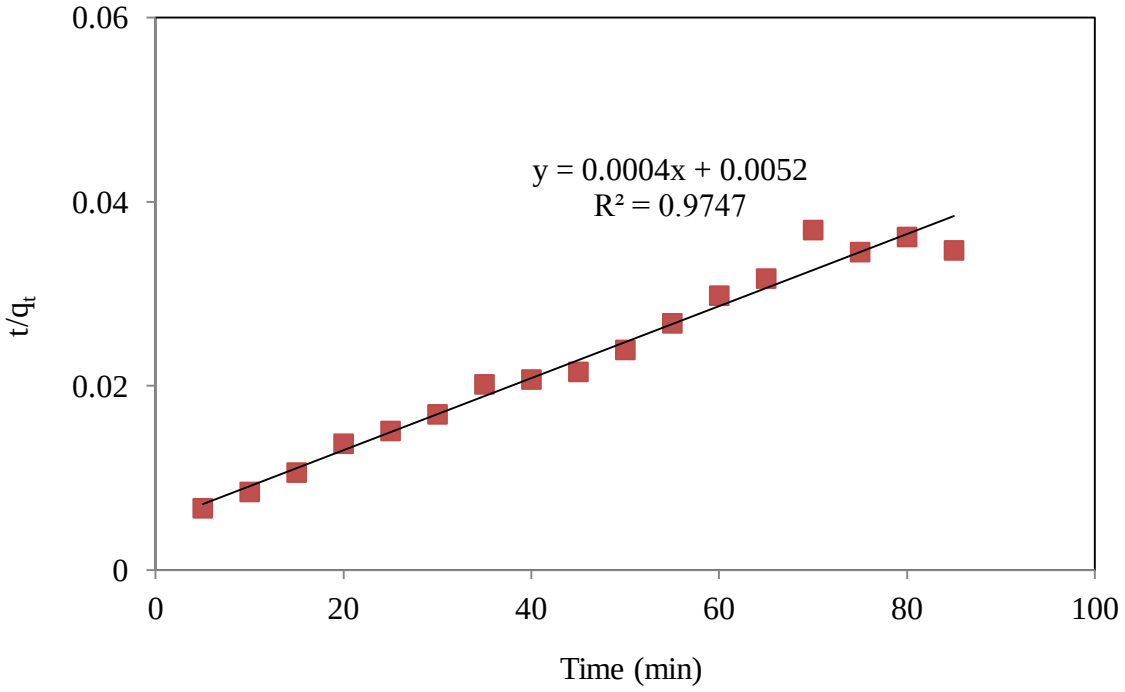


Figure 4.19. Pseudo second order kinetics for degradation of MO in the presence of 0.5M ZnO-MMT (300˚C). Conditions: pH=6.5 (Natural), $[MO]_0$= 16.32 mg/L, T= 298 K, Flow rate= 2000 rpm.

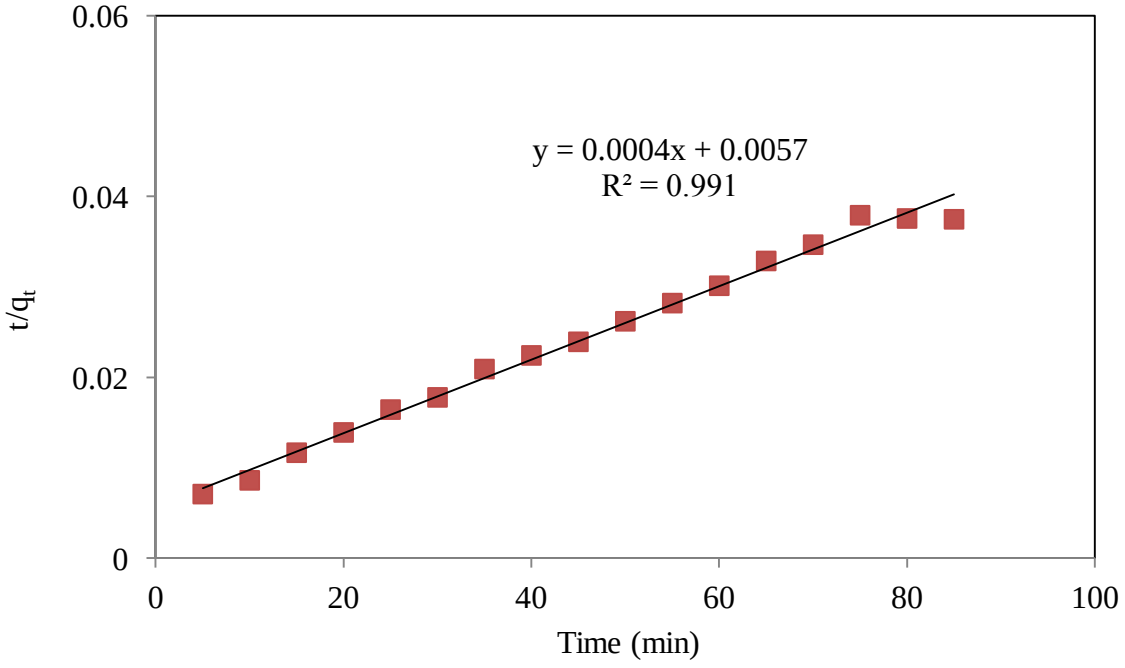


Figure 4.20. Pseudo second order kinetics for decolorization of MO in the presence of 0.5M ZnO-MMT (300˚C). Conditions: pH= 6.5 (Natural), $[MO]_0$= 16.32 mg/L, T= 298 K, Flow rate= 2000 rpm.

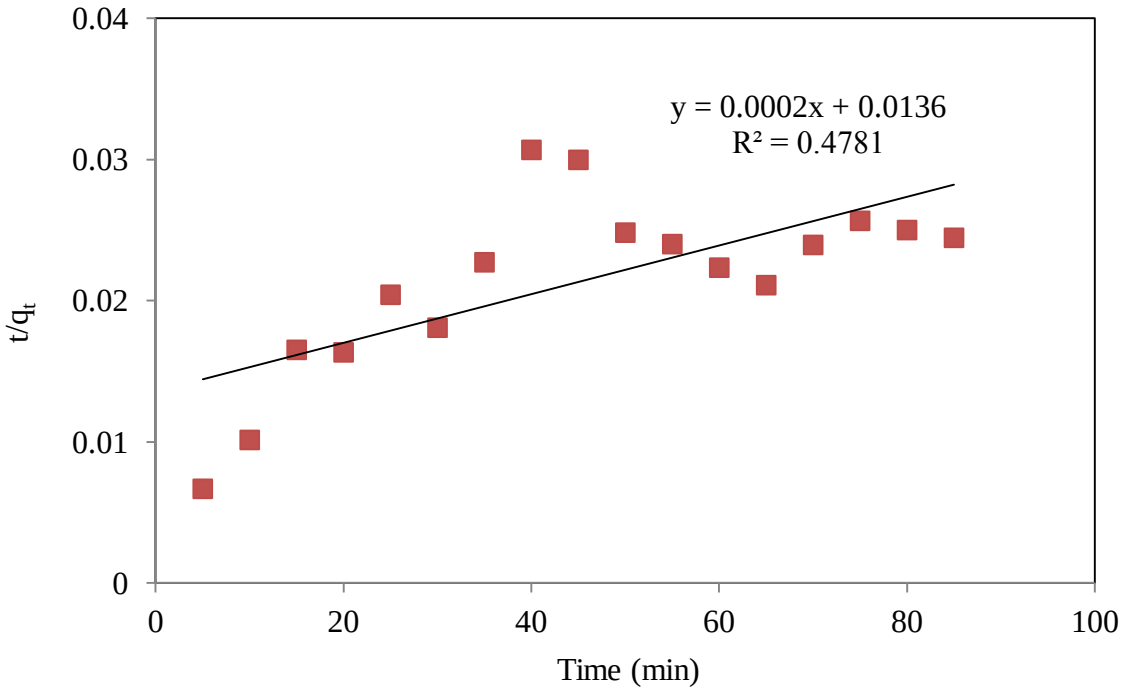


Figure 4.21. Pseudo second order kinetics for degradation of MO in the presence of 0.5M ZnO-MMT (500˚C). Conditions: pH= 6.5 (Natural), $[MO]_0$= 16.32 mg/L, T= 298 K, Flow rate= 2000 rpm.

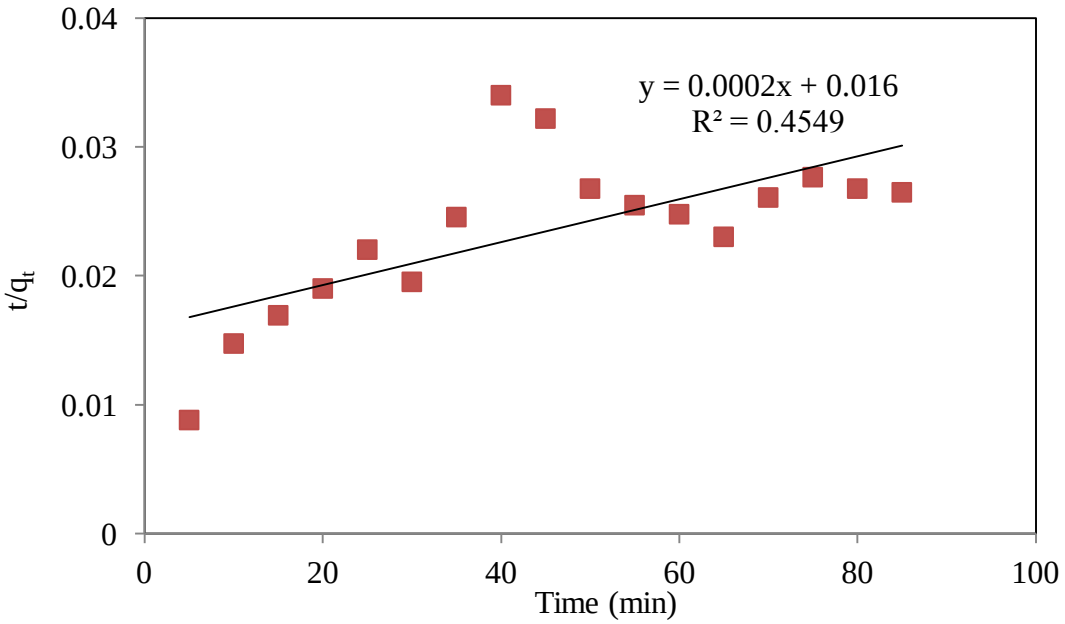


Figure 4.22. Pseudo second order kinetics for decolorization of MO in the presence of 0.5M ZnO-MMT (500˚C). Conditions: pH= 6.5 (Natural), $[MO]_0$= 16.32 mg/L, T= 298 K, Flow rate= 2000 rpm.

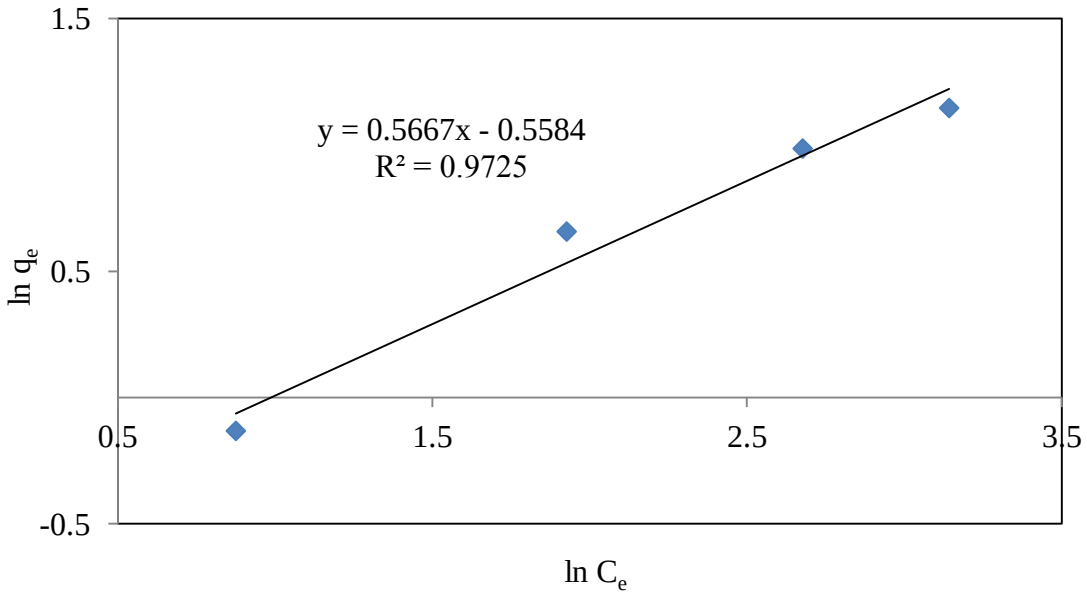


Figure 4.23. Freundlich adsorption isotherm for degradation of MO in the presence of 0.5M ZnO-MMT (300˚C). Conditions: pH= 6.5 (Natural), T= 298K, Flow rate= 2000 rpm.

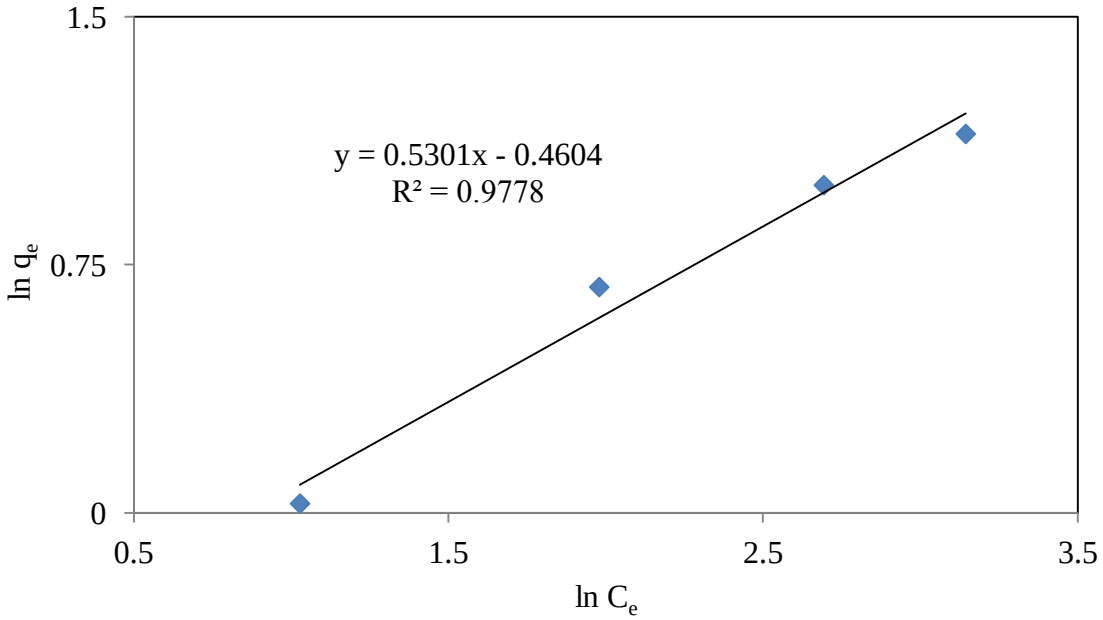


Figure 4.24. Freundlich adsorption isotherm for decolorization of MO in the presence of 0.5M ZnO-MMT (300˚C). Conditions: pH= 6.5 (Natural), T= 298K, Flow rate= 2000 rpm.

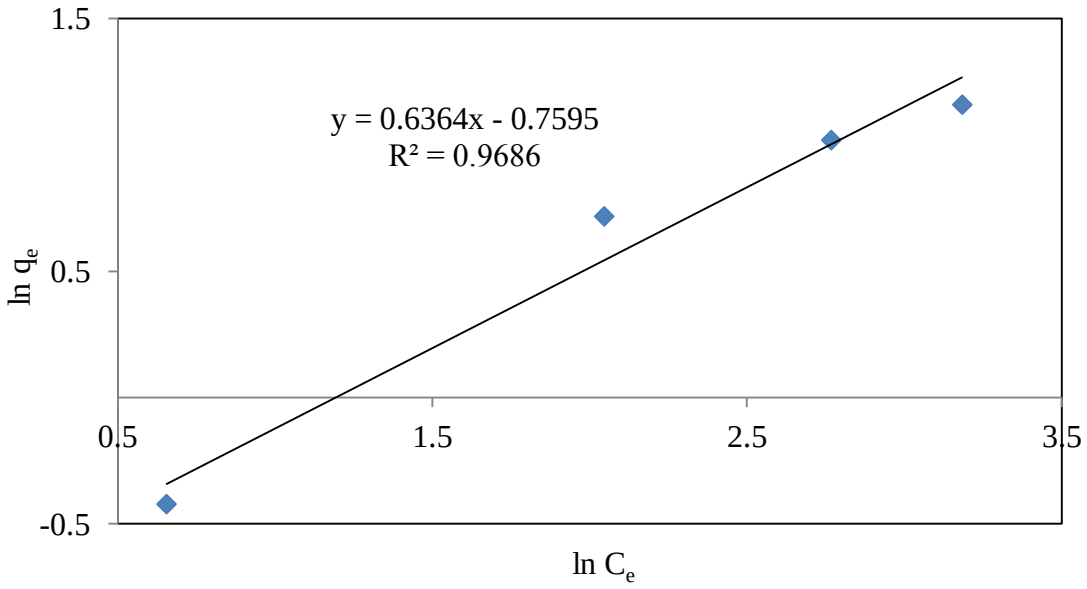


Figure 4.25. Freundlich adsorption isotherm for degradation of MO in the presence of 0.5M ZnO-MMT (500˚C). Conditions: pH= 6.5 (Natural), T= 298K, Flow rate= 2000 rpm.

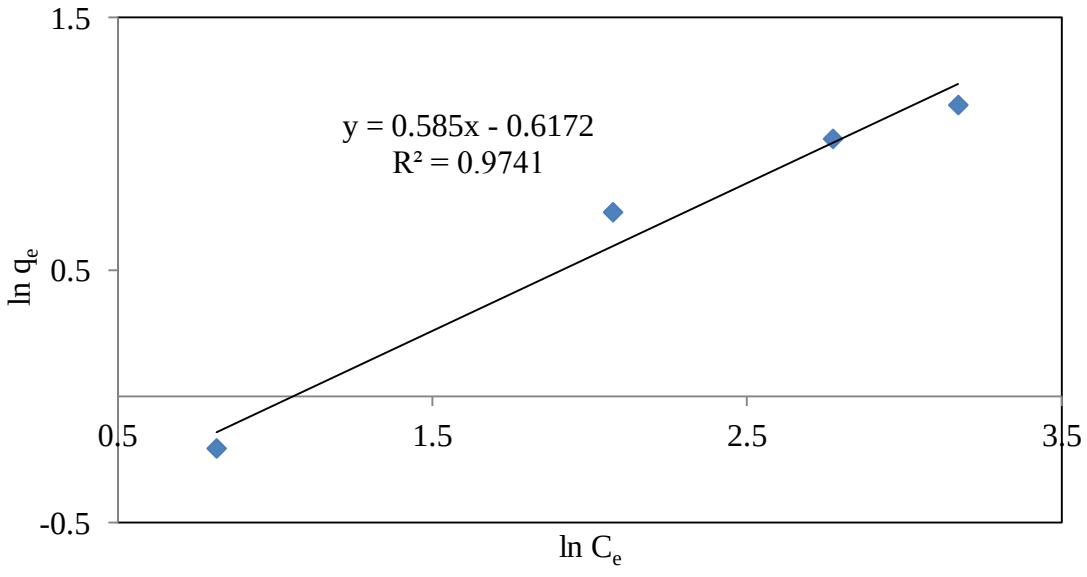


Figure 4.26. Freundlich adsorption isotherm for decolorization of MO in the presence of 0.5M ZnO-MMT (500˚C). Conditions: pH= 6.5 (Natural), T= 298K, Flow rate= 2000 rpm.

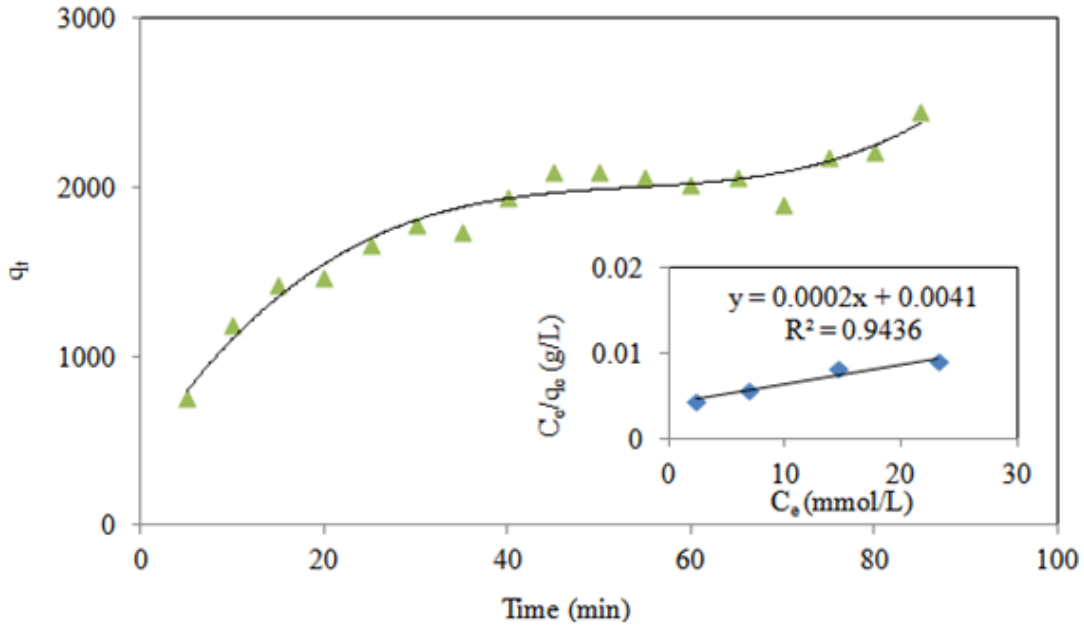


Figure 4.27. Langmuir adsorption isotherm for degradation of MO in the presence of 0.5M ZnO-MMT (300˚C). Inset: C_e/q_e vs. C_e plot. Conditions: pH= 6.5 (Natural), T= 298K, Flow rate= 2000 rpm.

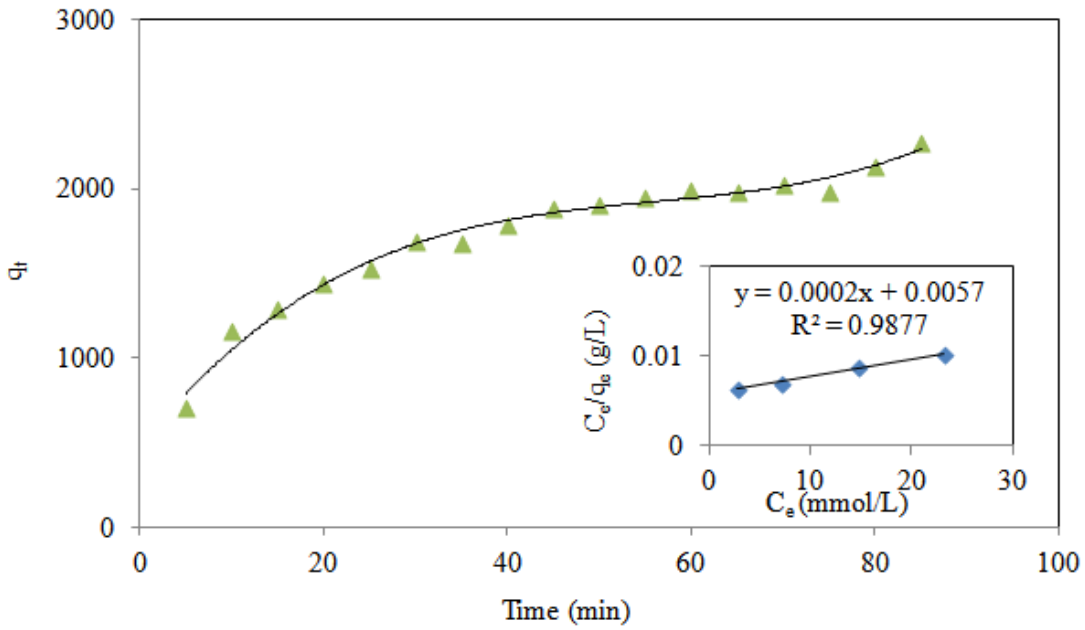


Figure 4.28. Langmuir adsorption isotherm for decolorization of MO in the presence of 0.5M ZnO-MMT (300˚C). Inset: C_e/q_e vs. C_e plot. Conditions: pH= 6.5 (Natural), T= 298K, Flow rate= 2000 rpm.

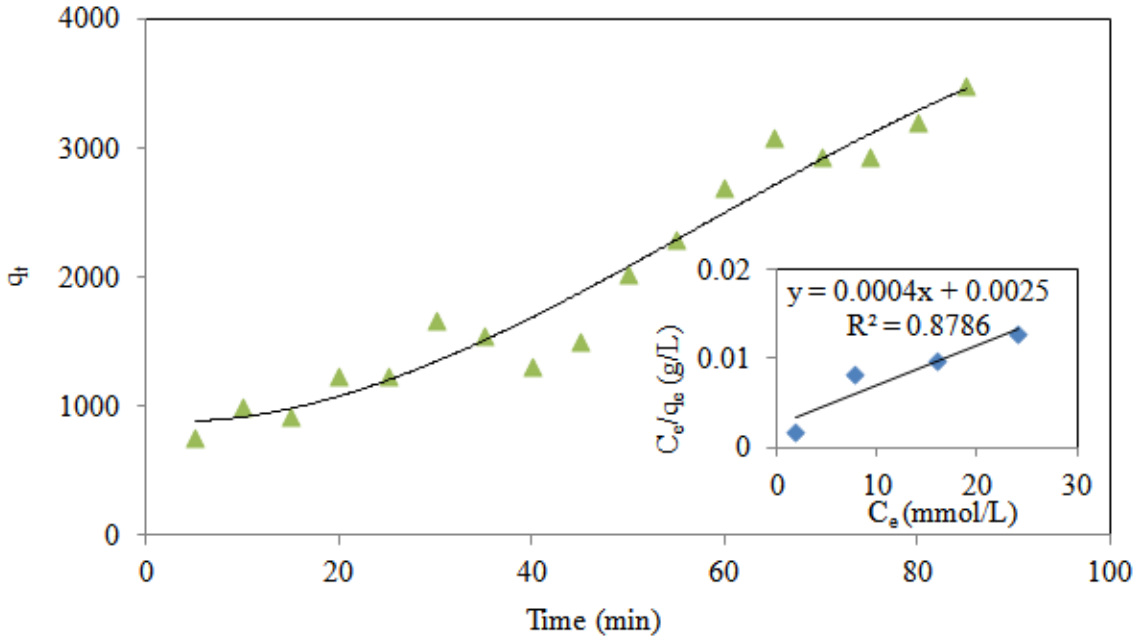


Figure 4.29. Langmuir adsorption isotherm for degradation of MO in the presence of 0.5M ZnO-MMT (500˚C). Inset: C_e/q_e vs. C_e plot. Conditions: pH= 6.5 (Natural), T= 298K, Flow rate= 2000 rpm.

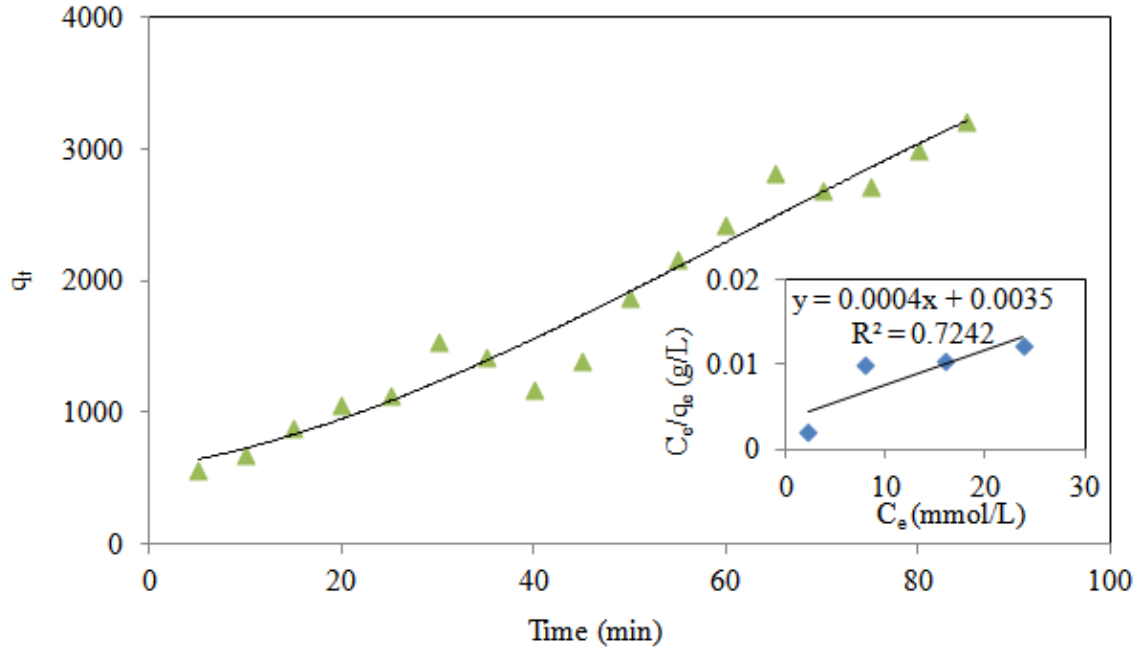


Figure 4.30. Langmuir adsorption isotherm for decolorization of MO in the presence of 0.5M ZnO-MMT (500˚C). Inset: C_e/q_e vs. C_e plot. Conditions: pH= 6.5 (Natural), T= 298K, Flow rate= 2000 rpm.

4.2.3. Photocatalytic Experiments

4.2.3.1. Effect of ZnO Loading. The photocatalytic reactions are carried out in the existence of supported catalysts loaded with different ZnO concentrations. Following 30 min dark experiments, the remaining concentrations of MO in solutions are controlled about 85 min (Figure 4.31, Figure 4.32, Figure 4.33 and Figure 4.34).

For both degradation and decolorization processes, ZnO loading concentrations do not possess a significant effect on the activities of the catalysts prepared at 300˚C (Figure 4.31 and Figure 4.32). Contrarily, the catalysts prepared at 500˚C reveals different performances upon loading amounts of ZnO nanoparticles (Figure 4.33 and Figure 4.34). The results of these experiments exhibit the following sequence for the efficiencies of these catalysts. 0.125M ZnO-MMT > 0.25M ZnO-MMT > 0.5M ZnO-MMT. This demonstrates the consistency with the XRD analysis where the highest crystalline order of ZnO nanoparticles is achieved in the presence of 0.5M ZnO-MMT (500˚C).

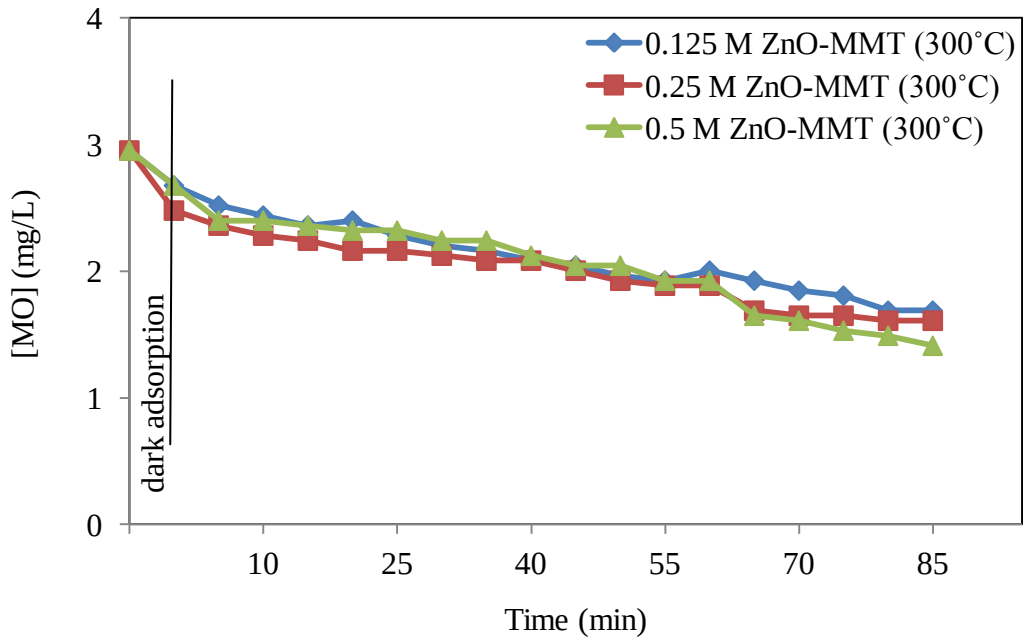


Figure 4.31. MO degradation in the presence of supported catalysts prepared at 300˚C. Conditions: pH= 6.5 (Natural), $[MO]_0$= 3.27 mg/L, T= 298 K, Flow rate= 2000 rpm.

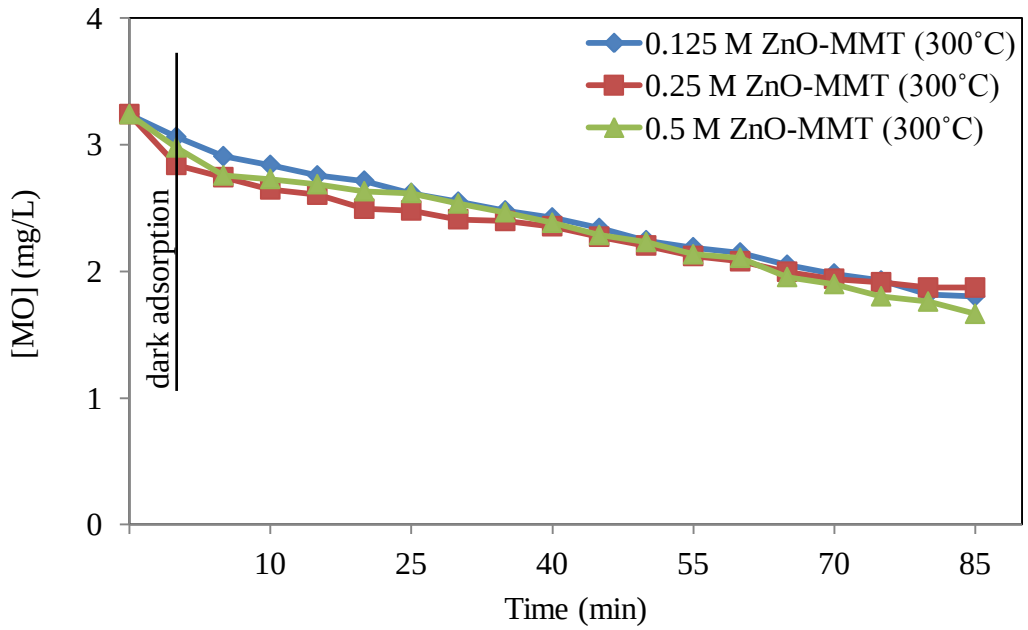


Figure 4.32. MO decolorization in the presence of supported catalysts prepared at 300˚C. Conditions: pH= 6.5 (Natural), $[MO]_0$= 3.27 mg/L, T= 298 K, Flow rate= 2000 rpm.

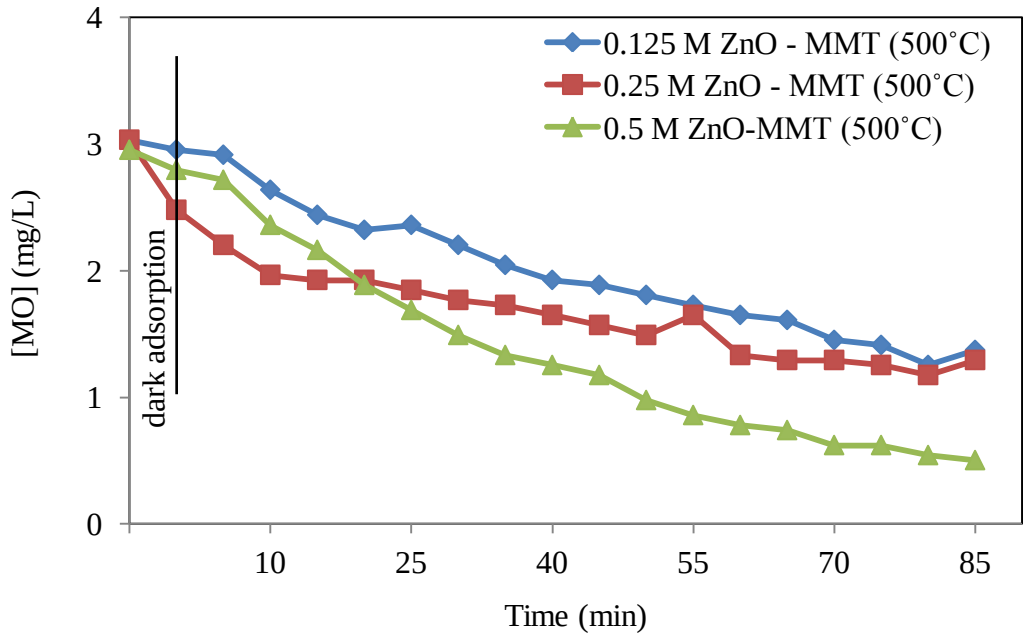


Figure 4.33. MO degradation in the presence of supported catalysts prepared at 500˚C. Conditions: pH= 6.5 (Natural), $[MO]_0$= 3.27 mg/L, T= 298 K, Flow rate= 2000 rpm.

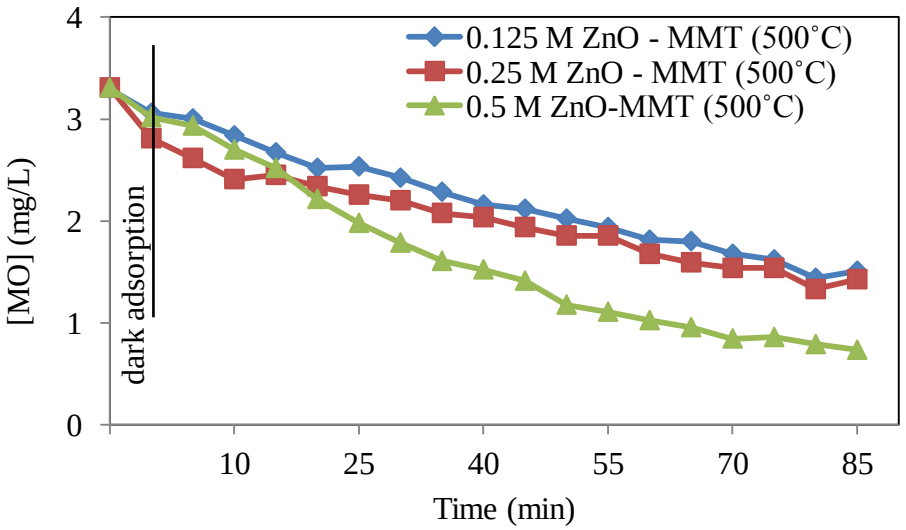


Figure 4.34. MO decolorization in the presence of supported catalysts prepared at 500˚C. Conditions: pH= 6.5 (Natural), $[MO]_0$= 3.27 mg/L, T= 298 K, Flow rate= 2000 rpm.

4.2.3.2. Effect of Initial MO Concentration. The influence of the initial MO concentration varying from 3.27 to 24.55 mg/L on the photocatalytic rates is also investigated in the presence of 0.5M ZnO-MMT (300˚C) and 0.5M ZnO-MMT (500˚C). For all concentrations, the best degradation and decolorization performances are obtained in the presence of 0.5M ZnO-MMT (500˚C) (Figure 4.35 and Figure 4.36). Pseudo first order kinetic model is confirmed according to the linearity noticed in the plots of ln (C_0/C) versus t (time) for all concentrations. (Figure 4.37, Figure 4.38, Figure 4.39 and Figure 4.40). As a general trend, the efficiency of both decolorization and degradation processes is found to decrease with increasing concentration of MO (Table 4.3 and Table 4.4). This can be a result of blocking of the photocatalytically active sites on the supported catalyst and reducing the interaction of photons with these sites.

Langmuir-Hinshelwood kinetic model analysis gives linearity in the plot of reciprocal rate (1/R) against reciprocal of MO concentrations (1/C_0) (Figure 4.37, Figure 4.38, Figure 4.39 and Figure 4.40 Inset).

In the presence of 0.5M ZnO-MMT (300˚C), the values of adsorption coefficient (K) and reaction rate constant (k) are found to be 0.013 L/mg and 0.047 mg/L min (degradation) and 0.010 L/mg and 0.070 mg/L min (decolorization). 0.5M ZnO-MMT (500˚C) gives higher K and k values. 0.030 L/mg and 0.254 mg/L min (degradation) and,

0.023 L/mg and 0.329 mg/L min (decolorization) demonstrating a higher adsorption capacity and hence degradation-decolorization ability.

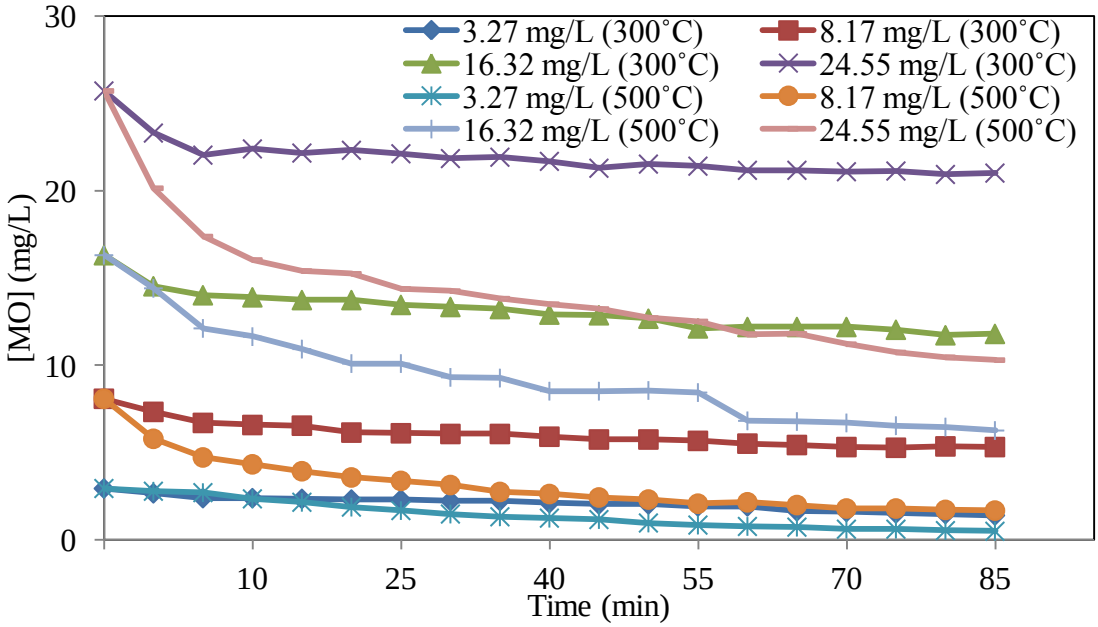


Figure 4.35. MO degradation at initial MO concentrations in the presence of 0.5M ZnO-MMT (300˚C) and 0.5M ZnO-MMT (500˚C). Conditions: pH=6.5 (Natural), T= 298 K, Flow rate= 2000 rpm.

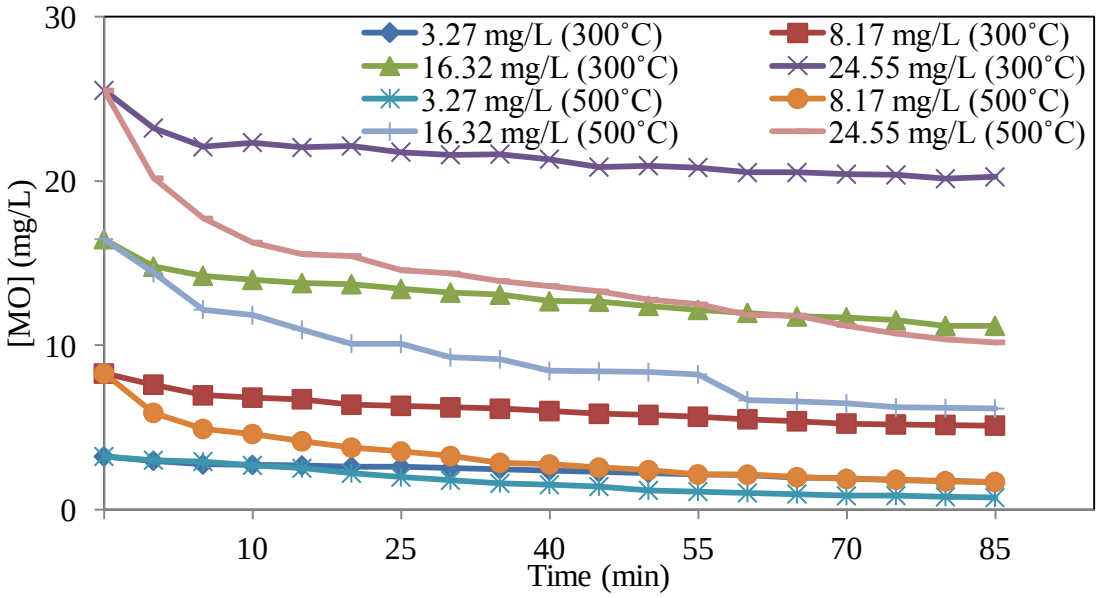


Figure 4.36. MO decolorization at initial MO concentrations in the presence of 0.5M ZnO-MMT (300˚C) and 0.5M ZnO-MMT (500˚C). Conditions: pH= 6.5 (Natural), T= 298 K, Flow rate= 2000 rpm.

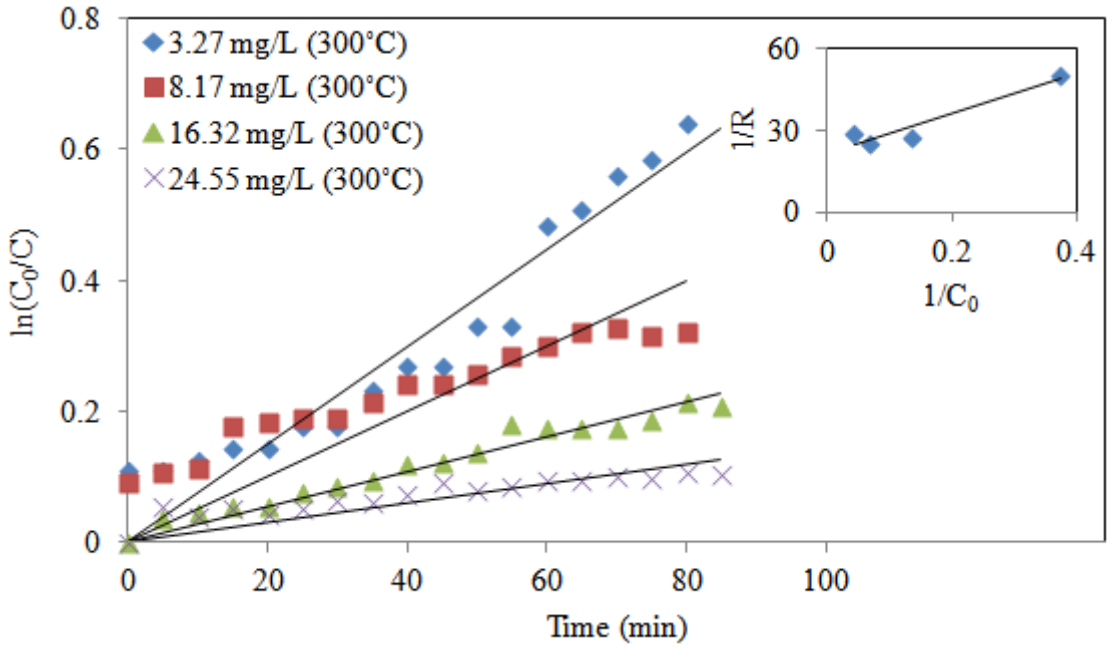


Figure 4.37. Pseudo-first order kinetics for degradation of MO in the presence of 0.5M ZnO-MMT (300˚C). Inset: Langmuir-Hinshelwood analysis. Conditions: pH= 6.5 (Natural), T= 298 K, Flow rate= 2000 rpm.

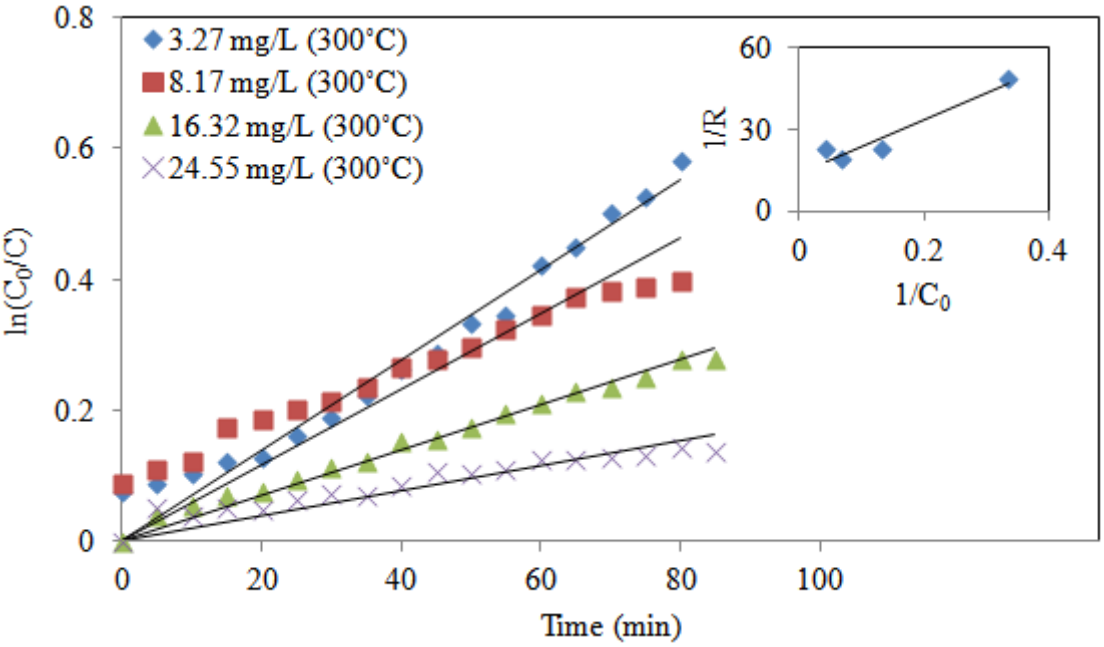


Figure 4.38. Pseudo-first order kinetics for decolorization of MO in the presence of 0.5M ZnO-MMT (300˚C). Inset: Langmuir-Hinshelwood analysis. Conditions: pH=6.5 (Natural), T= 298 K, Flow rate= 2000 rpm.

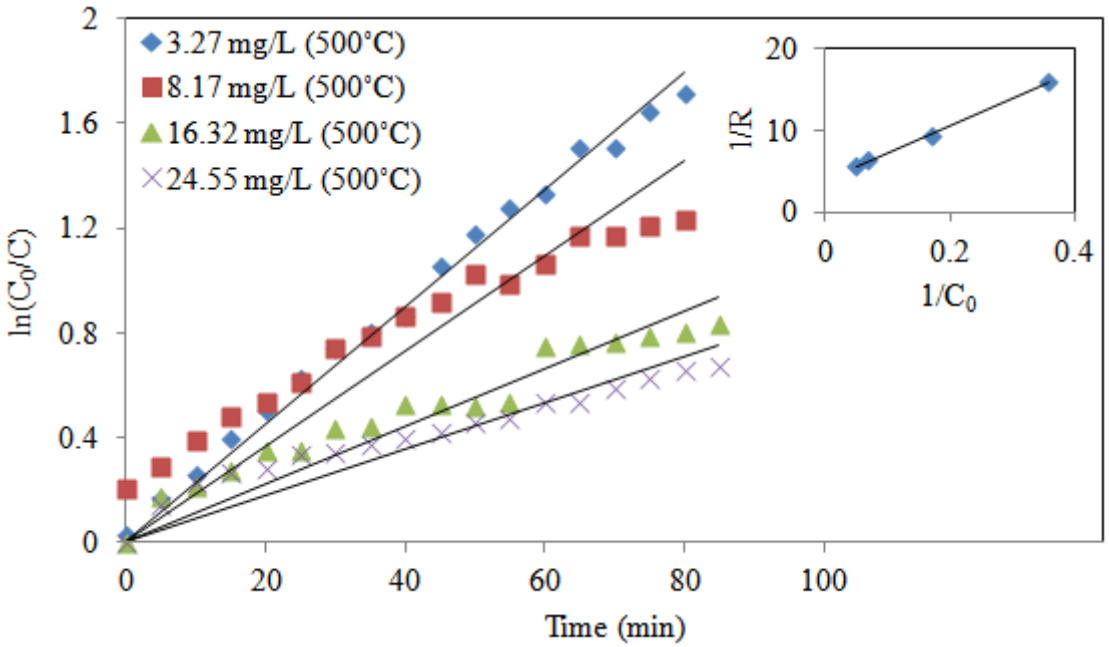


Figure 4.39. Pseudo-first order kinetics for degradation of MO in the presence of 0.5M ZnO-MMT (500˚C). Inset: Langmuir-Hinshelwood analysis. Conditions: pH= 6.5 (Natural), T= 298 K, Flow rate= 2000 rpm.

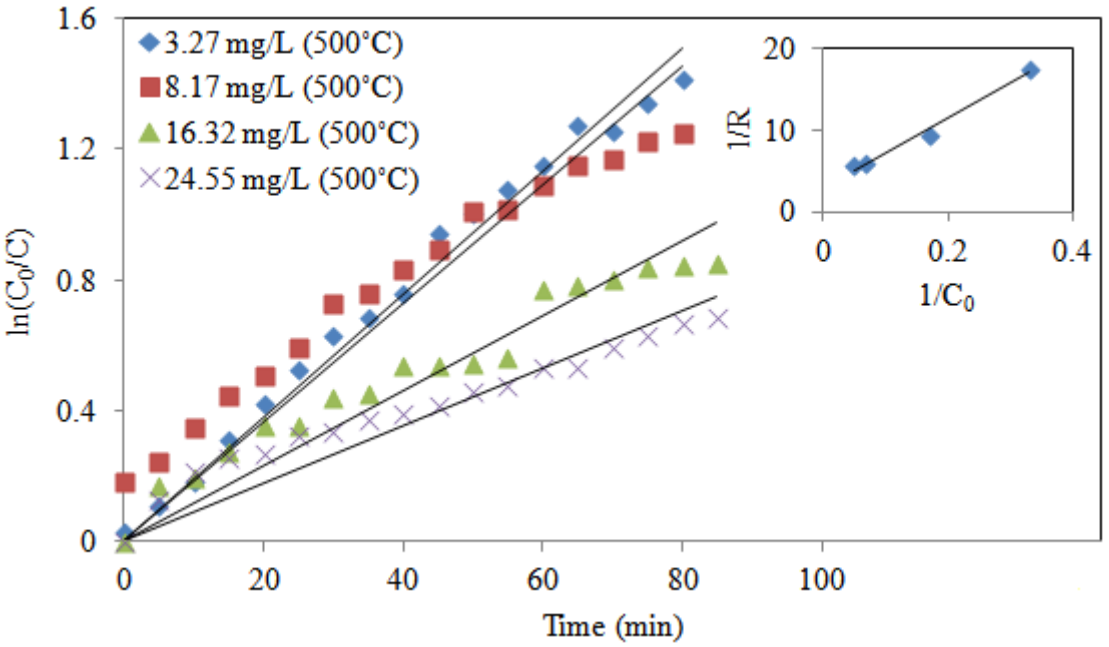


Figure 4.40. Pseudo-first order kinetics for decolorization of MO in the presence of 0.5M ZnO-MMT (500˚C). Inset: Langmuir-Hinshelwood analysis. Conditions: pH= 6.5 (Natural), T= 298 K, Flow rate= 2000 rpm.

Table 4.3. Rate constants (k) and linear regression values (R) for the degradation and decolorization processes of MO in the presence of 0.5M ZnO-MMT (300˚C).

	k (min^{-1})		**R**	
[MO] (mg/L)	**degradation**	**decolorization**	**degradation**	**decolorization**
24.55	0.0015	0.0019	0.5413	0.8221
16.32	0.0027	0.0035	0.9539	0.9830
8.17	0.0050	0.0058	0.4308	0.7234
3.27	0.0074	0.0069	0.9187	0.9672

Table 4.4. Rate constants (k) and linear regression values (R) for the degradation and decolorization processes of MO in the presence of 0.5M ZnO-MMT (500˚C).

	k (min^{-1})		**R**	
[MO] (mg/L)	**degradation**	**decolorization**	**degradation**	**decolorization**
24.55	0.0088	0.0088	0.8226	0.8673
16.32	0.0110	0.0115	0.8852	0.9096
8.17	0.0182	0.0181	0.7716	0.8474
3.27	0.0225	0.0189	0.9905	0.9859

4.3. Characterization Results of the ZnO-NC1 Catalysts

4.3.1. XRD Analysis

XRD spectrums of bare NC1, 0.125M ZnO-NC1 (300˚C), 0.25M ZnO-NC1 (300˚C), 0.5M ZnO-NC1 (300˚C), 0.125M ZnO-NC1 (500˚C), 0.25M ZnO-NC1 (500˚C) and 0.5M ZnO-NC1 (500˚C) catalysts are shown in Figure 4.41 and 4.42. Bare NC1, due to the organic modification, has the characteristic (001) reflection at 4.9˚ (2θ) with ad-spacing value of 18.17 Å. This value is relatively greater in comparison to that of MMT (12.8 Å), being in consistency with the study of Ha et al [69]. Also small (101) and (107) reflections of quartz and crystoballite are detected at 19.9˚ and 35.3˚ (2θ), respectively. [70, 71]. The characteristic peak at 4.9˚ (2θ) is lost in the presence of supported catalysts, indicating destruction of neat oriented layers. Nevertheless, there may be still space among

the layers. For the supported catalysts prepare at 300˚C, a new peak appears at 8.2˚ (2θ). This peak refers to the formation of tactoids (clay particles), suggesting an immiscible dispersion of destructed layers [72]. The characteristic ZnO peak (101) is observed at 36.4^{o} (2θ). Other ZnO reflections of (100), (002), (102), (110), (103) and (200) are detected at 31.9˚, 34.6˚, 47.7˚, 56.7˚, 63.1˚, and 66.6˚ (2θ), respectively. The extinction of intensities at the NC1 diffraction peaks with the increment in the reflections of ZnO peaks suggests that ZnO nanoparticles uniformly distributed on the NC1 surface.

The crystalline sizes of ZnO nanoparticles (D_{ZnO}), based on the broadening of the most intense (101) diffraction at 36.4˚ (2θ) are calculated by employing the Scherrer's equation (Table 4.5). For the catalysts calcinated at 300^{o}C, similar crystal sizes are obtained. However, for the catalysts calcinated at 500^{o}C, crystal sizes increase regularly upon loading concentration of ZnO. This also suggests that the adsorption of ZnO nanoparticles and/or coagulation is much more probable on the surface of NC1 in the absence of tactoids.

Table 4.5. Crystalline sizes (D), surface areas (BET), pore volumes (V_{pore}) and pore radius (r_{pore}) of 0.25M ZnO, NC1 (500 ^{o}C) and supported catalysts.

Catalyst	**2θ (˚)**	**D (nm)**	**BET (m^2/g)**	**V_{pore} (cm^3/g)**	**r_{pore} (Å)**
0.25M ZnO (500˚C)	36.4	15.20	7.6	0.013	17.8
NC1	4.9	-	4.5	0.010	51.8
0.125M ZnO-NC1 (300˚C)	36.4	13.92	25.5	0.046	16.4
0.25M ZnO-NC1 (300˚C)	36.4	13.23	26.7	0.048	15.7
0.5M ZnO- NC1 (300˚C)	36.4	14.90	28.7	0.057	14.9
0.125M ZnO- NC1 (500˚C)	36.4	13.13	27.5	0.042	14.9
0.25M ZnO- NC1 (500˚C)	36.4	16.95	26.1	0.043	16.4
0.5M ZnO- NC1 (500˚C)	36.4	21.77	19.6	0.031	22.6

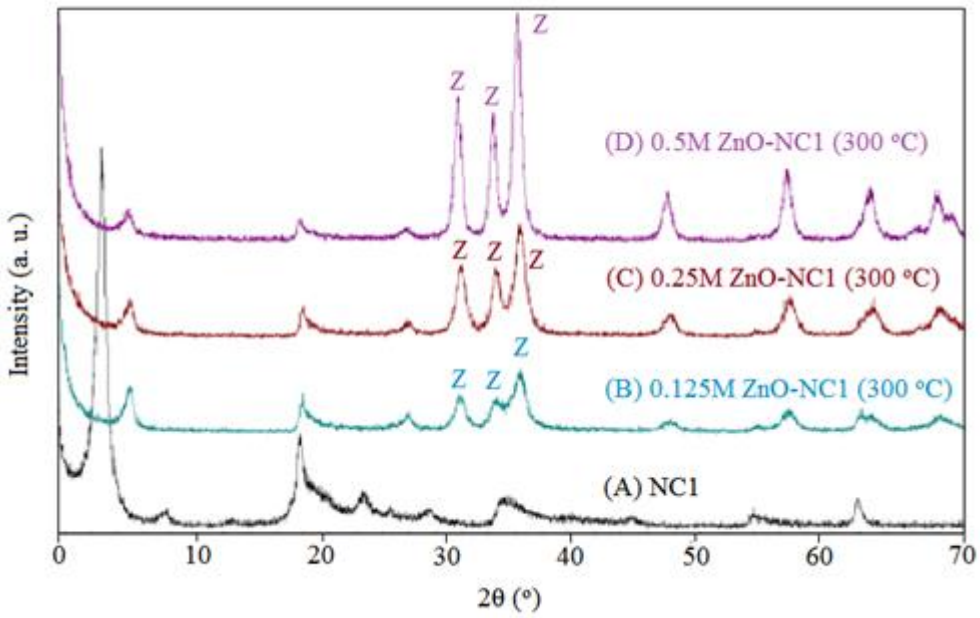


Figure4.41. XRD patterns of NC1 (A) and supported catalysts (300 ^{o}C) (B-D). (Z: ZnO).

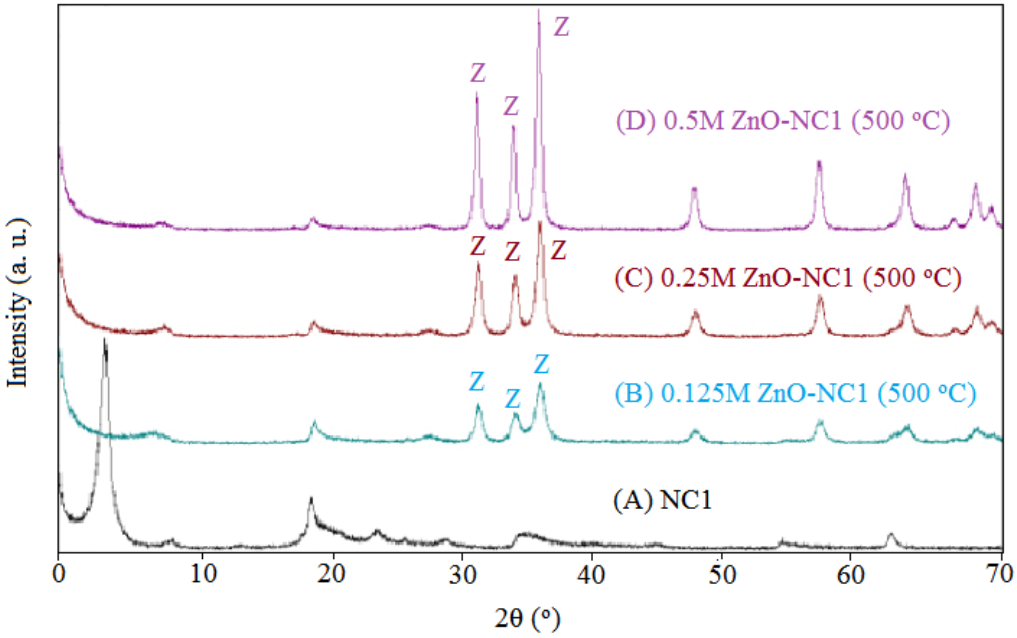


Figure 4.42. XRD patterns of NC1 (A) and supported catalysts (500 ^{o}C) (B-D). (Z: ZnO).

4.3.2. SEM-EDX Analysis

Surface morphologies of the bare NC1 and 0.25M ZnO-NC1 (500˚C) are investigated by SEM (EDX) analysis. Bare NC1 has a clear curly flake-like structure

(Figure 4.43) and based on the EDX analysis it consists of major Si, Al, O elements and minor Fe, Mg, K, Na, K and Ca elements (Table 4.6). For 0.25M ZnO-NC1 (500˚C), Zn and O elemental compositions are noticeable.

SEM micrograph and mapping images of the 0.25M ZnO-NC1 (500˚C) are shown in the Figure 4.44. Although the structure of NC1 is retained following the ZnO treatment, homogenously distributed ZnO nanoparticles over the surface of the support are detected. This is also evidenced in the EDX data (Table 4.6). Moreover, NC1 has no Zn while 0.25M ZnO-NC1 (500˚C) shows 61.28% Zn component. The reduction in the silica and alumina percentages may also correspond to the location of ZnO nanoparticles within the silica matrix of the clay.

Table 4.6. Elemental composition of NC1 and 0.25M ZnO-NC1 (500˚C).

	0.25M ZnO	**NC1**	**0.25M ZnO-NC1 (500˚C)**
Components	**Wt %**	**Wt %**	**Wt %**
Zn	88.79	-	61.28
Si	-	44.46	14.16
O	11.21	29.15	16.21
Al	-	16.94	6.69
Fe	-	4.70	-
Mg	-	3.07	1.66
Na	-	1.07	-
K	-	0.22	-
Ca	-	0.40	-

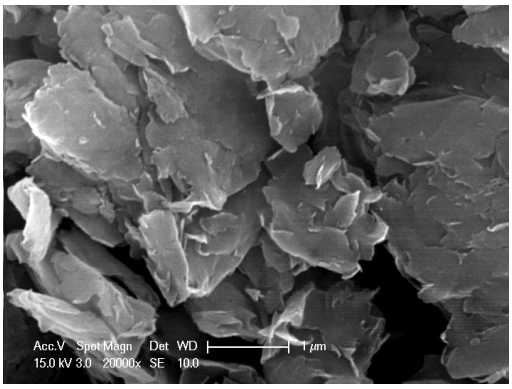


Figure 4.43. SEM image of NC1.

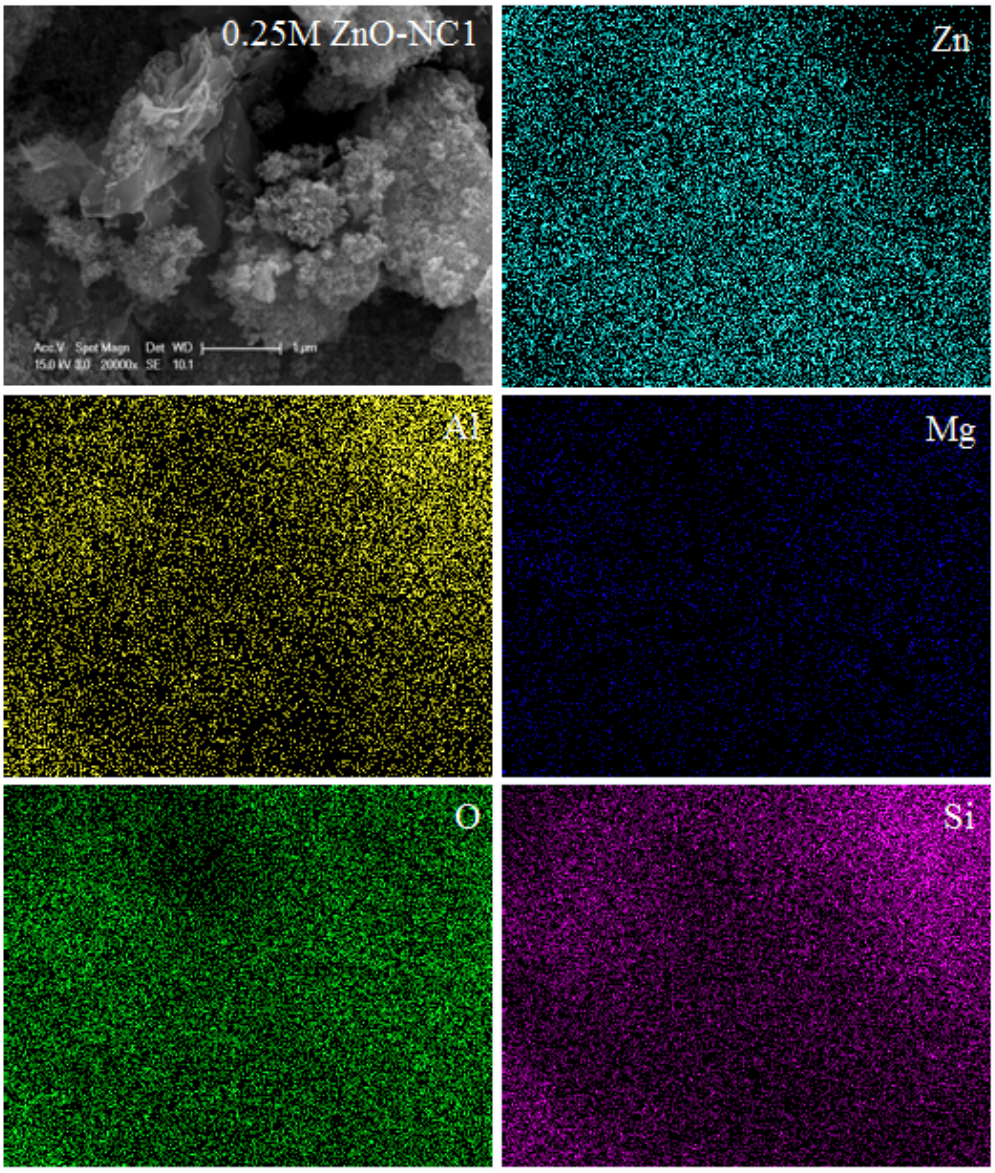


Figure 4.44. SEM image of 0.25M ZnO-NC1 (500 ^{o}C) and mapping images of 0.25M ZnO-NC1, Zn, Al, Mg, O and Si.

4.3.3. Nitrogen Adsorption-Desorption Isotherms

Nitrogen adsorption-desorption isotherms and pore size distribution plots of the NC1 and supported catalysts are illustrated in Figure 4.45, Figure 4.46, Figure 4.47 and Figure 4.48. NC1 and supported catalysts exhibits Type IV isotherms, owing to their mesoporous structure. On the other hand, the increment in the loading concentration of ZnO narrows the hysteresis loops. The pore size distribution curves display that the pores of the supported catalysts exist in the typical mesoporous region of 20-40 Å (Figure 4.45 and Figure 4.46). In comparison to the bare NC1, supported catalysts have larger surface area and pore volumes (Table 4.5). The decrease in the surface area and pore volume of 0.5M ZnO-NC1 (500˚C) can be explained with excess ZnO loading on the clay surface. This creates smoother areas on the catalyst surface which covers the porous structure.

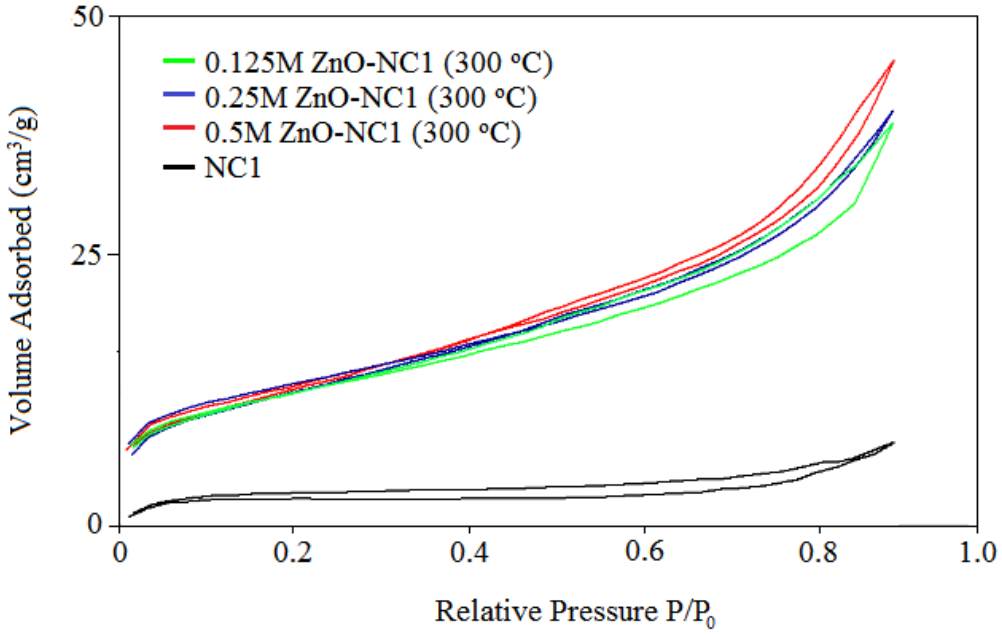


Figure 4.45. Nitrogen adsorption-desorption isotherms of NC1 and supported catalysts prepared at 300˚C.

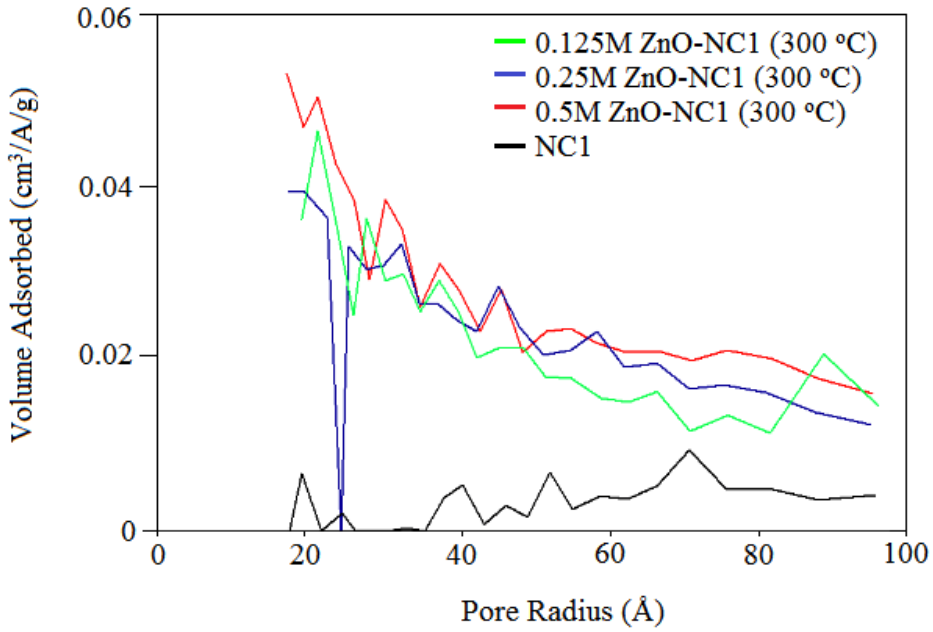


Figure 4.46. Pore size distribution plots of NC1 and supported catalysts prepared at 300˚C.

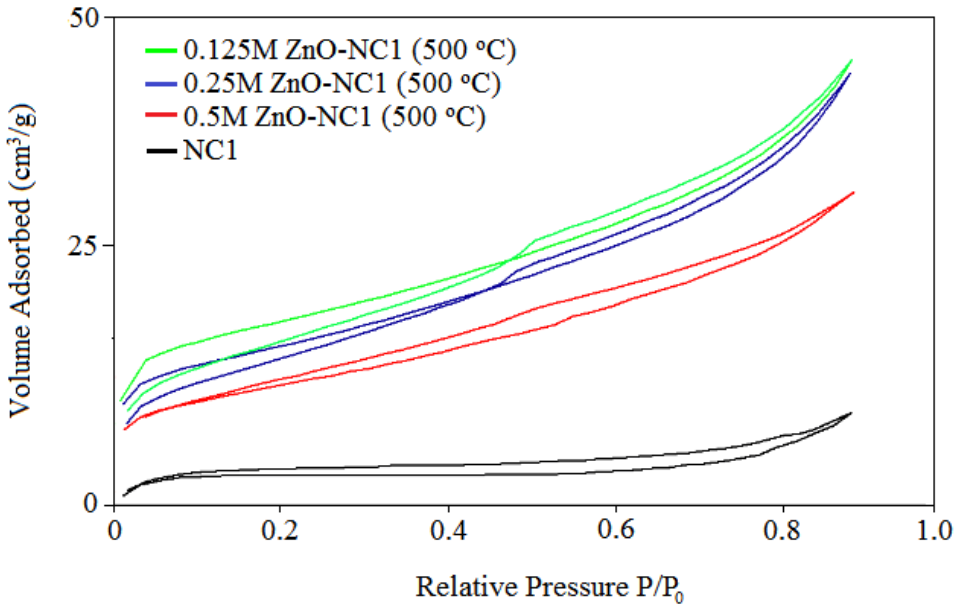


Figure 4.47. Nitrogen adsorption-desorption isotherms of NC1 and supported catalysts prepared at 500˚C.

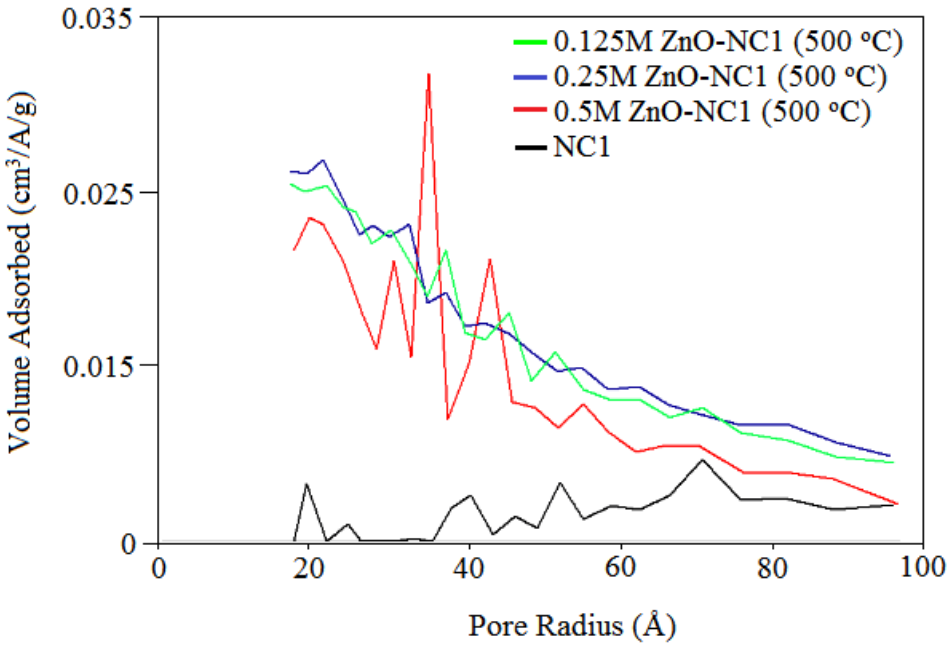


Figure 4.48. Pore size distribution plots of NC1 and supported catalysts prepared at 300˚C.

4.3.4. UV-Vis DRS Analysis

Figure 4.49 and Figure 4.50 present the UV-Vis absorption spectroscopy of the NC1, 0.25M ZnO and the supported catalysts. The bare NC1 shows an extended absorption tail between 200 and 600 nm while 0.25M ZnO has a sharp absorption edge at the UV region. In the absorption spectra of the supported catalysts, the characteristic absorption edge of ZnO is detected. This edge becomes more observable and wider with the higher loading concentration of ZnO.

In addition the UV-Vis absorption spectra of the as prepared catalysts are transformed to the band-gap values (Equation 2.17) which are evaluated by linear extrapolation and taking the intercept on the x-axis gives the value of the band gap (Figure 4.51 and Figure 4.52). Accordingly, band gap energy of 0.25M ZnO (500˚C) is found as 3.12 eV (Figure 4.51 Inset). A slight decrease is observed for the supported catalysts, in comparison to the 0.25M ZnO which may correspond an activity in the visible region.

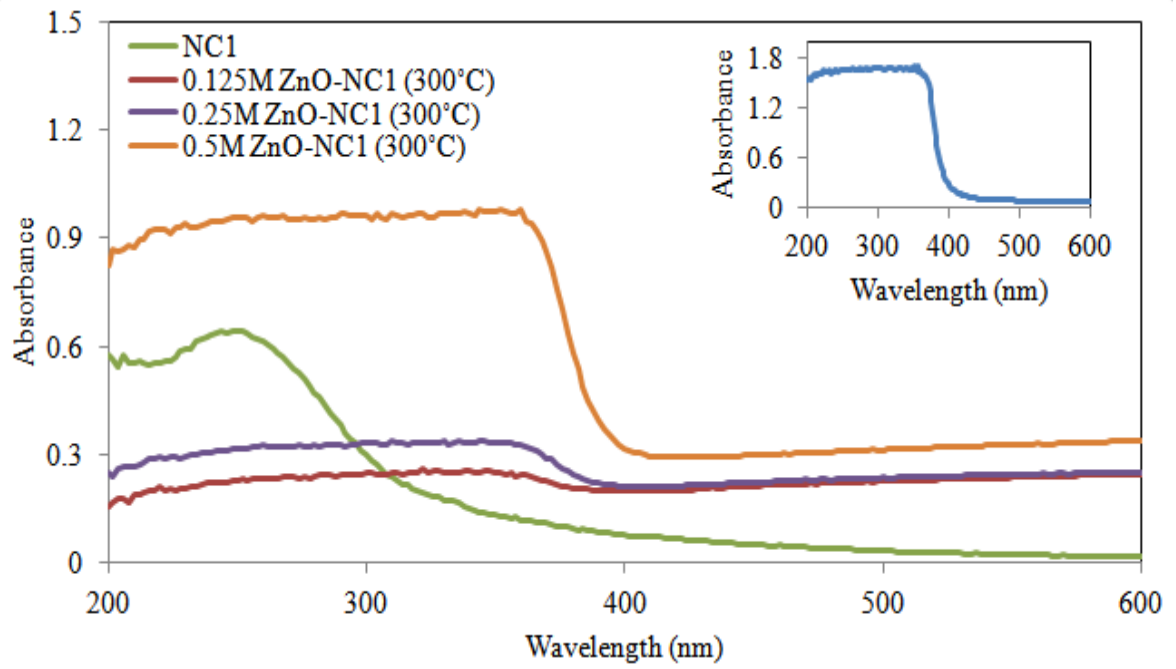


Figure 4.49. UV-Vis DRS spectra of NC1 and supported catalysts prepared at 300˚C. Inset: UV-Vis DRS spectra of 0.25M ZnO (500˚C).

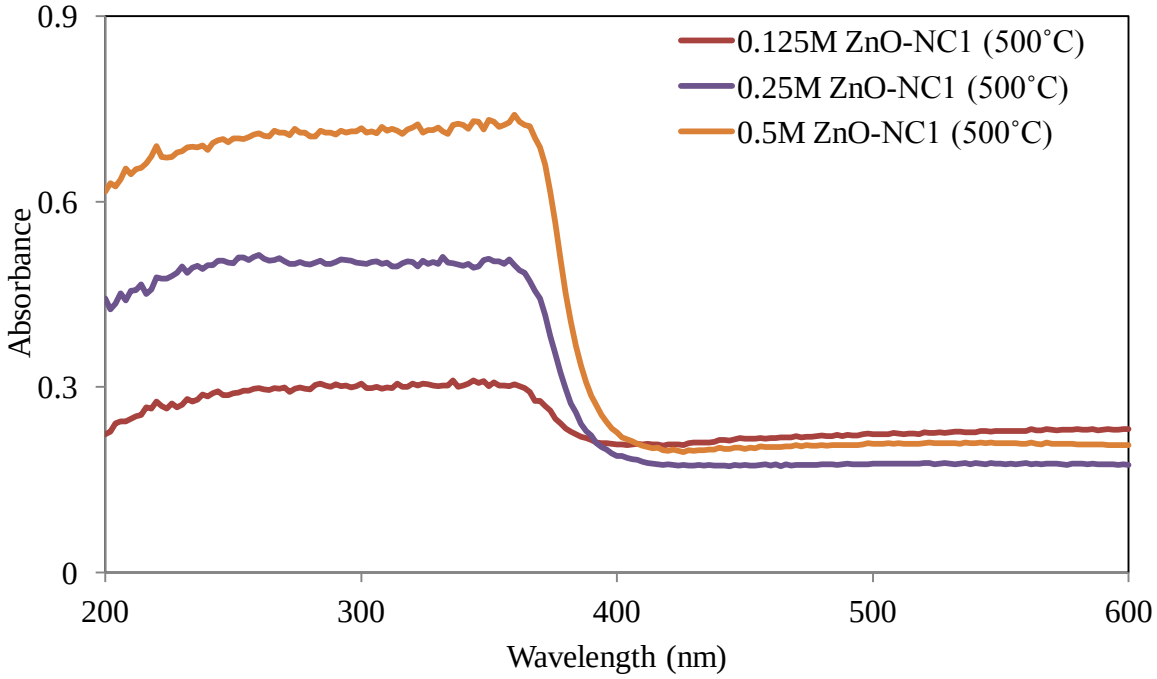


Figure 4.50. UV-Vis DRS spectra of supported catalysts prepared at 500˚C.

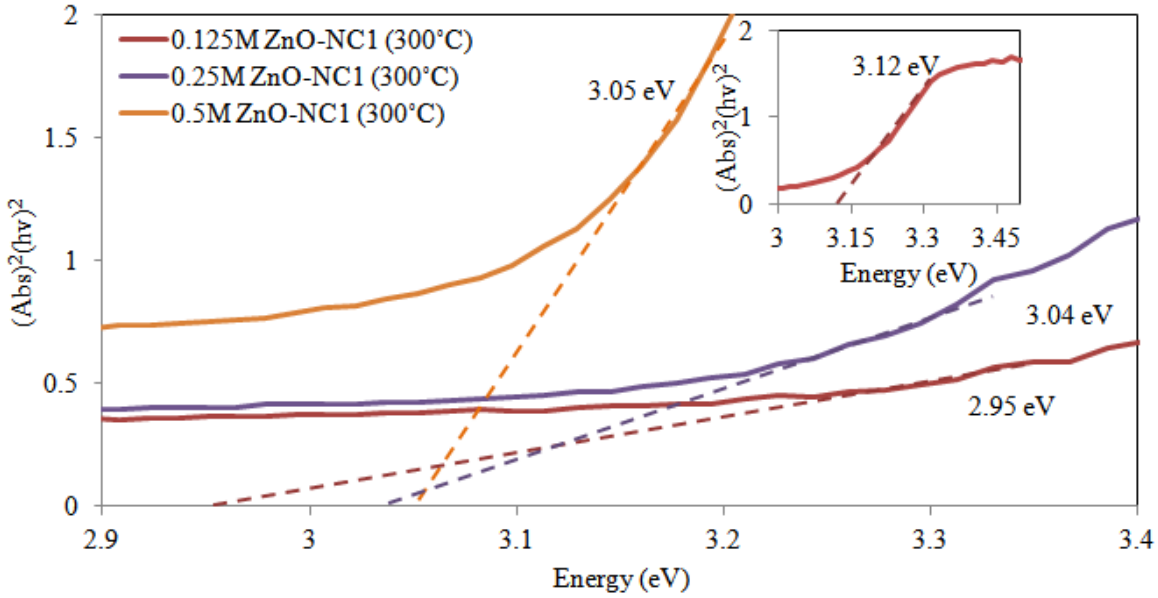


Figure 4.51. Band gap adsorption edges of supported catalysts. Inset: Band gap adsorption edges of 0.25M ZnO (500˚C).

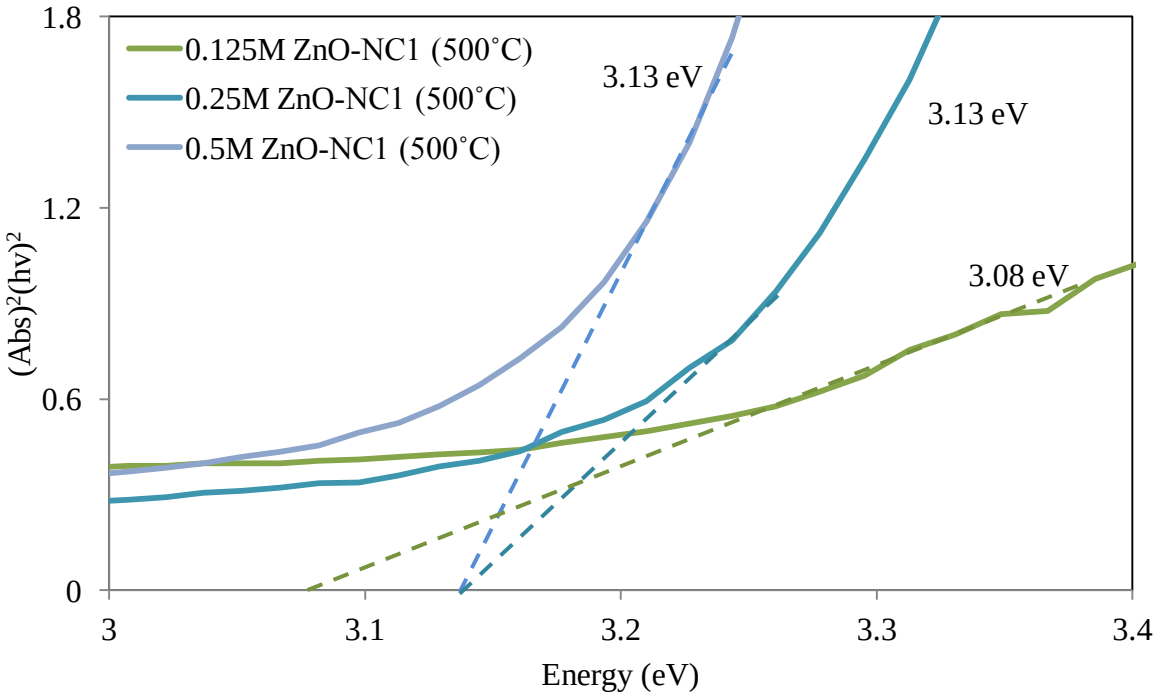


Figure 4.52. Band gap adsorption edges of supported catalysts.

4.4. Photoactivities of ZnO-NC1 Catalysts

4.4.1. Control Experiments

Control experiments are set as two steps. In the first step, dark absorption capacities of NC1, 0.25M ZnO, 0.25 M ZnO-NC1 (300˚C) and 0.25 M ZnO-NC1 (500˚C) are compared (Figure 4.53). For 0.25M ZnO and 0.25M ZnO-NC1 (300˚C), after 85 min mixing in the dark, no significant change is noticed in the MO concentrations. On the other hand the raw NC1 shows excellent adsorption property due to higher basal spacing. Also 0.25 M ZnO-NC1 (500˚C) can absorb dye compound, owing to decomposition of modification material between the layers at this temperature. In the second set photolysis of MO and photocatalytic activities of 0.25M ZnO (500˚C), 0.25 M ZnO-NC1 (300˚C) and 0.25 M ZnO-NC1 (500˚C) are examined (Figure 4.54). A negligible MO degradation is observed in the presence of UV light without any catalyst (Figure 4.54 Inset). The suspensions are stirred in the dark for 30 min to achieve adsorption/desorption equilibrium and thereafter exposed to illumination. Although, 0.25M ZnO (500˚C) shows a higher performance in comparison to the supported catalysts, the difficulties in the settlement of ZnO nanoparticles limit their applications in photocatalytic reactions. In the meantime, the activity of 0.25M ZnO-NC1 (500˚C) is better than 0.25M ZnO-NC1 (300˚C). Heat-induced growth of ZnO particles results in sharper and narrower X-ray peaks, contributes to the increase of crystallinity and hence increases the photoactivity.

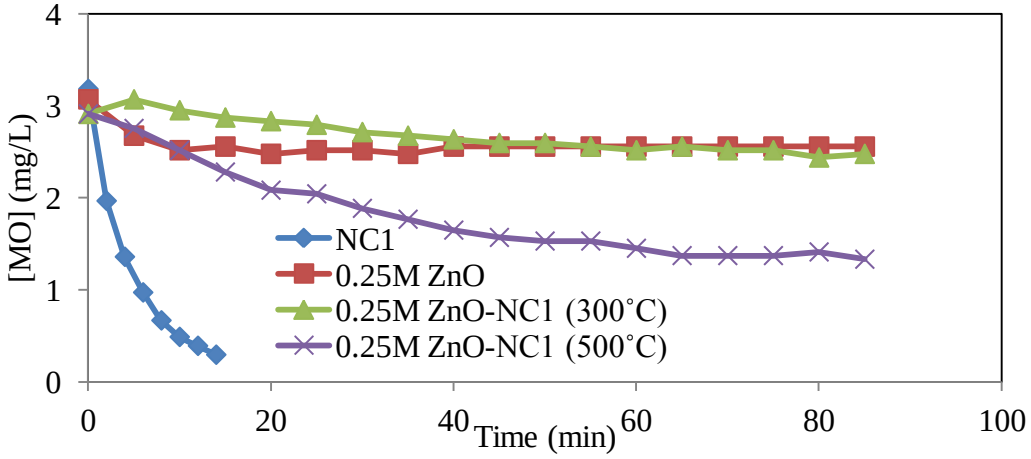


Figure 4.53. Control experiments in the dark. Conditions: pH: 6.5 (Natural), $[MO]_0$ = 3.27 mg/L, T = 298 K, Flow rate = 2000 rpm.

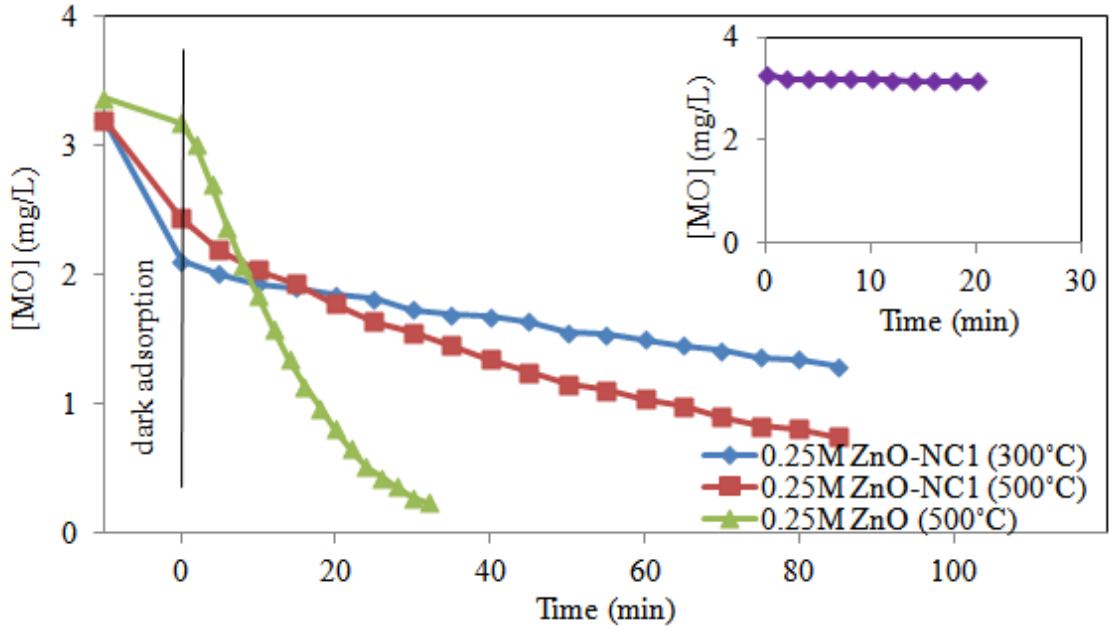


Figure 4.54. Control experiments under UV irradiation. Inset: Photolysis of MO. Conditions: pH: 6.5 (Natural), $[MO]_0$= 3.27 mg/L, T= 298K, Flow rate= 2000 rpm.

4.4.2. Dark Adsorption Experiments

4.4.2.1. Adsortion Kinetics. The dark adsorption details of MO (8.17 mg/L) over the 0.5M ZnO-NC1 (300˚C) and 0.5M ZnO-NC1 (500˚C) catalysts are investigated to specify the adsorption kinetics in terms of pseudo first order and pseudo second order models.

Pseudo first order model is applied with respect to the slope of $\ln(q_e-q_t)$ versus t graph. The correlation coefficients are found as 0.9368 (degradation) and 0.6576 (decolorization) and for 0.5M ZnO-NC1 (300˚C) and 0.9669 (degradation) and 0.9874 (decolorization) for 0.5M ZnO-NC1 (500˚C) (Figure 4.55, Figure 4.56, Figure 4.57 and Figure 4.58).

However, in the case of pseudo second order model, correlation coefficients in the plots of t/q_t versus t are found as 0.9756 (degradation), 0.9614 (decolorization) for 0.5M ZnO-NC1 (300˚C) and 0.7018 (degradation), 0.6600 (decolorization) for 0.5M ZnO-NC1 (500˚C) (Figure 4.59, Figure 4.60, Figure 4.61 and Figure 4.62).

The higher values of the coefficients imply a better adsorption of MO. Accordingly, pseudo-second order model fits to the 0.5M ZnO-NC1 (300˚C), while only a certain extent of adsorption seems to be possible by this model in the presence of 0.5M ZnO-NC1 (500˚C).

4.4.2.2. Adsorption Isotherms. For the adsorption isotherms, Freundlich and Langmuir isotherm models are employed at four different initial concentrations of MO (3.27, 8.17, 16.32 and 24.55 mg/L) in the presence of 0.5M ZnO-NC1 (300˚C) and 0.5M ZnO-NC1 (500˚C).

Freundlich isotherms' line fittings of ln q_e versus ln C_e in plots give correlations of 0.9993 (degradation), 0.9998 (decolorization) for 0.5M ZnO-NC1 (300˚C) and 0.9885 (degradation) and 0.9993 (decolorization) for 0.5M ZnO-NC1 (500˚C) (Figure 4.63, Figure 4.64, Figure 4.65 and Figure 4.66).

Langmuir isotherms (q_t versus t plots) of the supported catalysts are illustrated in Figure 4.66, Figure 4.67, Figure 4.68 and Figure 4.69. The line fittings in C_e/q_e versus C_e graphs result in correlation coefficients of 0.9627 (degradation), 0.9627 (decolorization) for 0.5M ZnO-NC1 (300˚C) and 0.9342 (degradation) and 0.9706 (decolorization) for 0.5M ZnO-NC1 (500˚C) (Figure 4.67, Figure 4.68, Figure 4.69 and Figure 4.70 Insets).

Consequently, Freundlich isotherm model fits better to the supported catalysts with higher correlation coefficients.

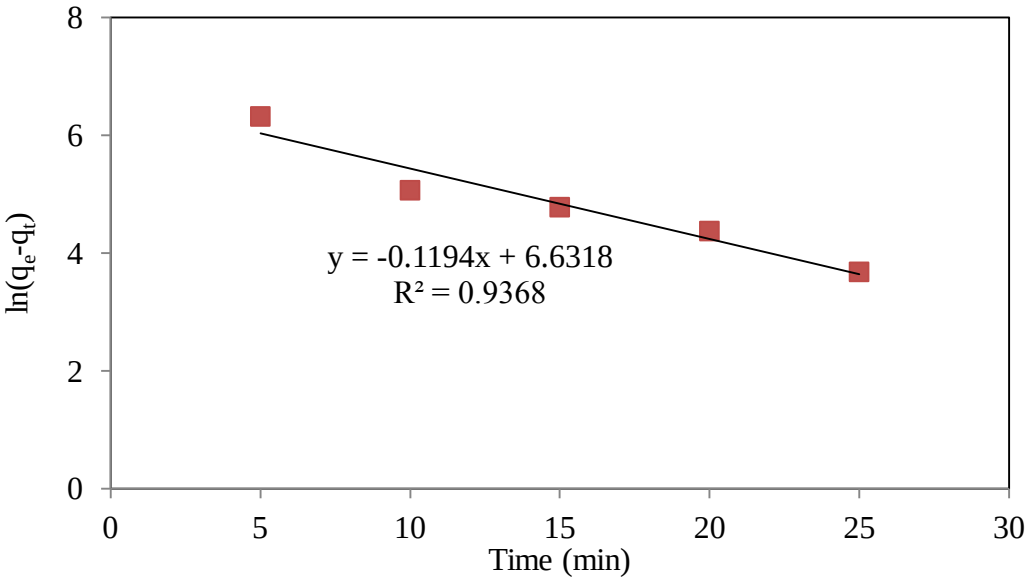


Figure 4.55. Pseudo first order kinetics for degradation of MO in the presence of 0.5M ZnO-NC1 (300˚C). Conditions: pH= 6.5 (Natural), $[MO]_0$= 8.17 mg/L, T= 298 K, Flow rate= 2000 rpm.

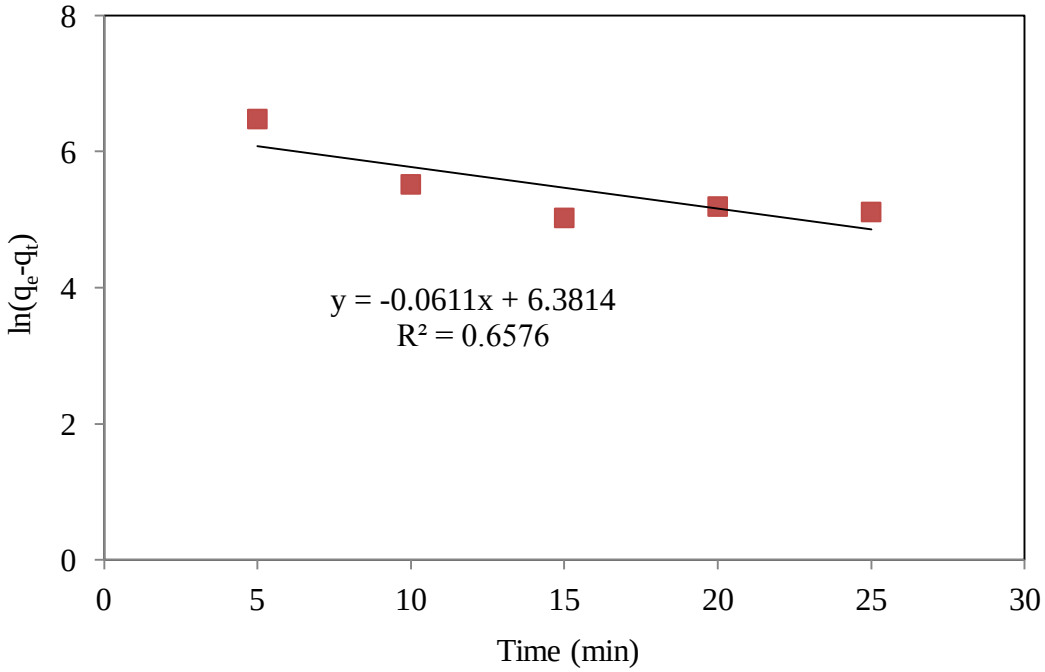


Figure 4.56. Pseudo first order kinetics for decolorization of MO in the presence of 0.5M ZnO-NC1 (300˚C). Conditions: pH= 6.5 (Natural), $[MO]_0$= 8.17 mg/L, T= 298 K, Flow rate= 2000 rpm.

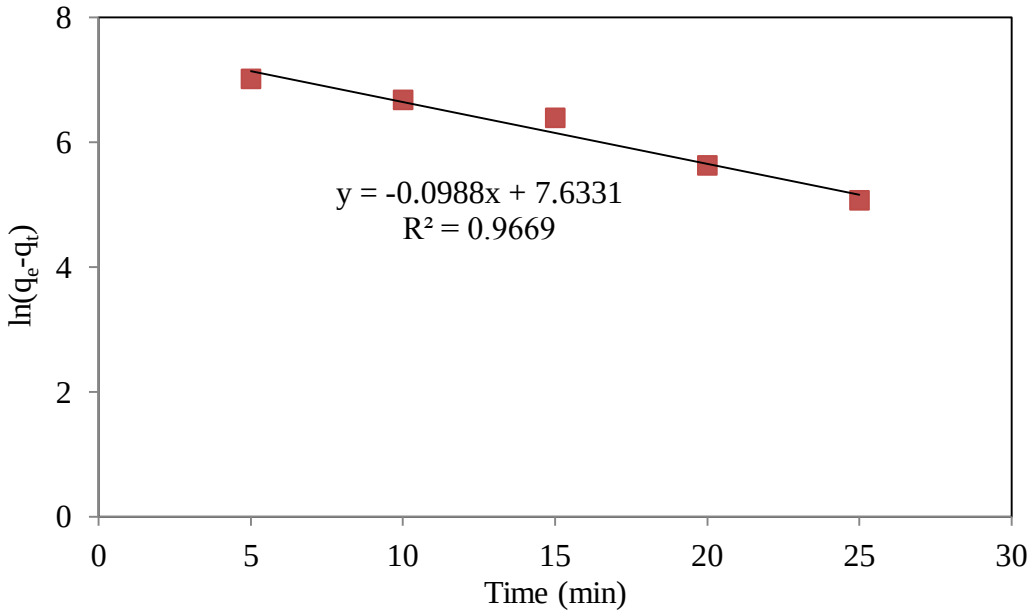


Figure 4.57. Pseudo first order kinetics for degradation of MO in the presence of 0.5M ZnO-NC1 (500˚C). Conditions: pH= 6.5 (Natural), $[MO]_0$= 8.17 mg/L, T= 298 K, Flow rate= 2000 rpm.

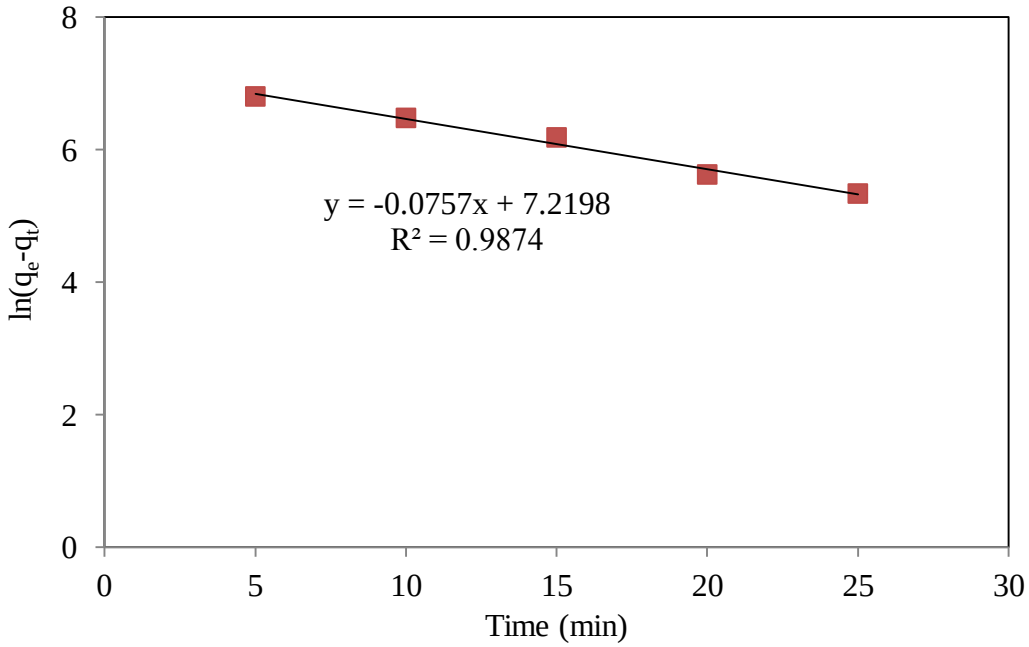


Figure 4.58. Pseudo first order kinetics for decolorization of MO in the presence of 0.5M ZnO-NC1 (500˚C). Conditions: pH= 6.5 (Natural), $[MO]_0$= 8.17 mg/L, T= 298 K, Flow rate= 2000 rpm.

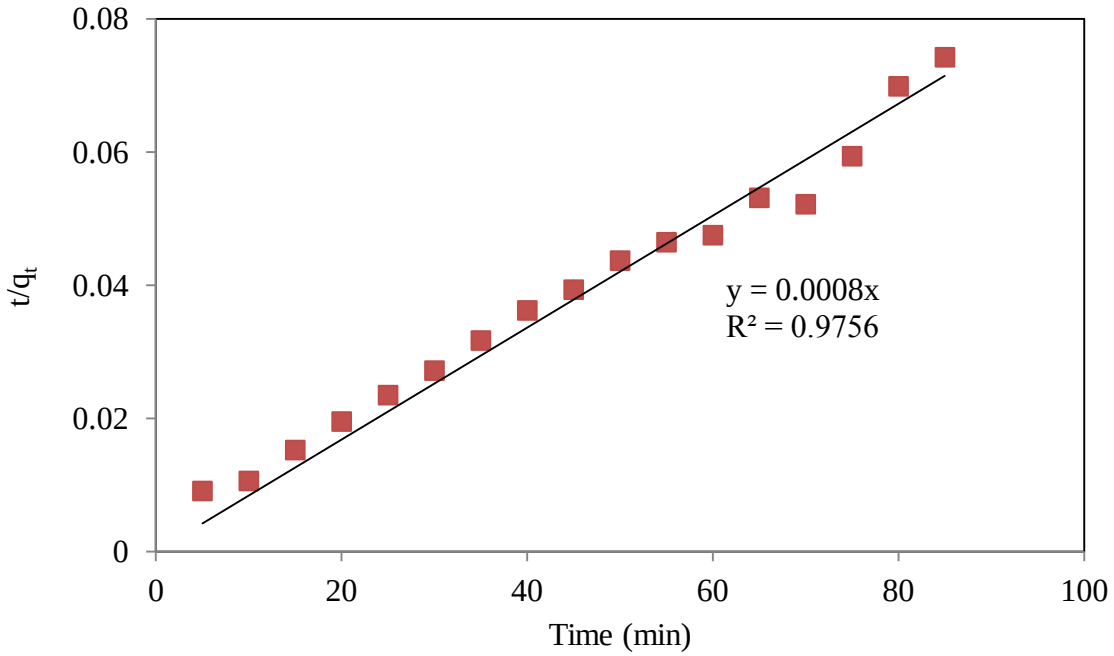


Figure 4.59. Pseudo second order kinetics for degradation of MO in the presence of 0.5M ZnO-NC1 (300˚C). Conditions: pH= 6.5 (Natural), $[MO]_0$= 8.17 mg/L, T= 298 K, Flow rate= 2000 rpm.

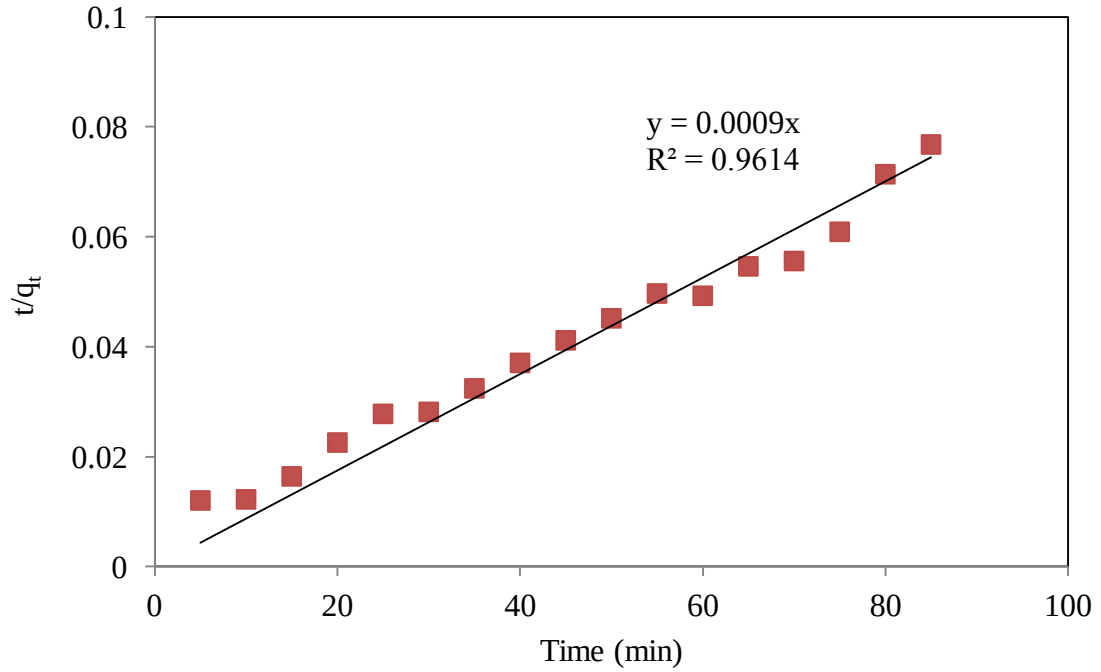


Figure 4.60. Pseudo second order kinetics for decolorization of MO in the presence of 0.5M ZnO-NC1 (300˚C). Conditions: pH= 6.5 (Natural), $[MO]_0$= 8.17 mg/L, T= 298 K, Flow rate= 2000 rpm.

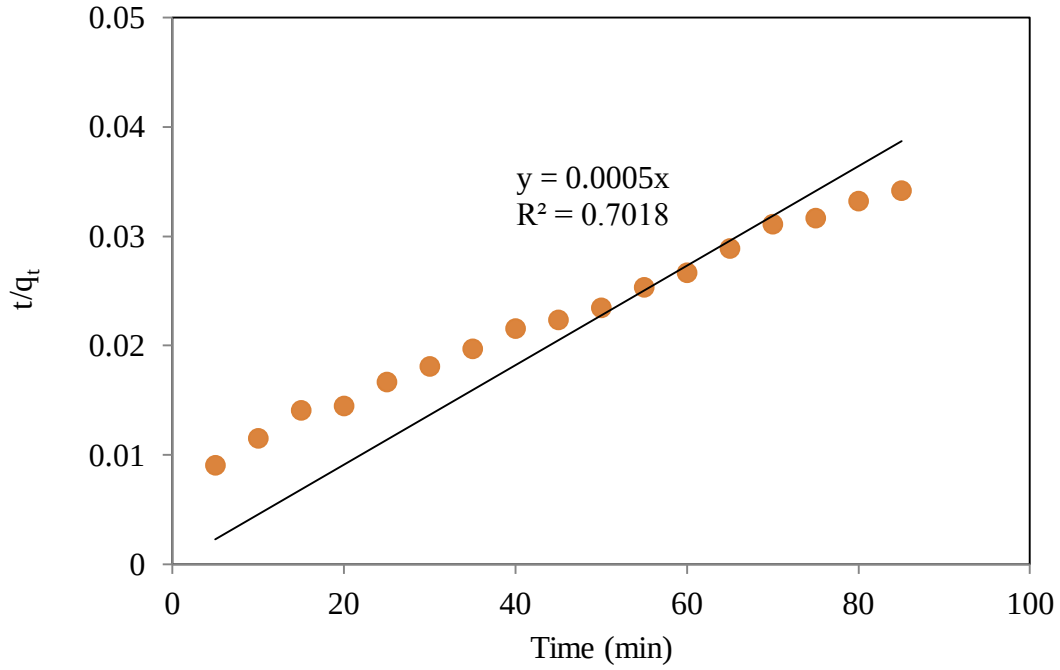


Figure 4.61. Pseudo second order kinetics for degradation of MO in the presence of 0.5M ZnO-NC1 (500˚C). Conditions: pH= 6.5 (Natural), $[MO]_0$= 8.17 mg/L, T= 298 K, Flow rate= 2000 rpm.

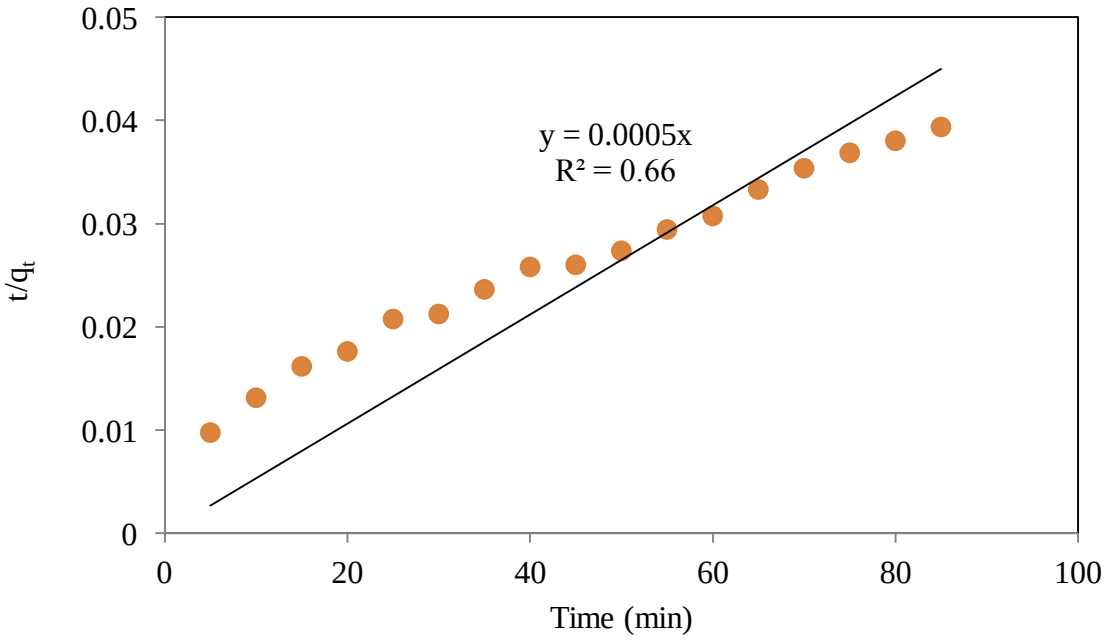


Figure 4.62. Pseudo second order kinetics for decolorization of MO in the presence of 0.5M ZnO-NC1 (500˚C). Conditions: pH= 6.5 (Natural), $[MO]_0$= 8.17 mg/L, T= 298 K, Flow rate= 2000 rpm.

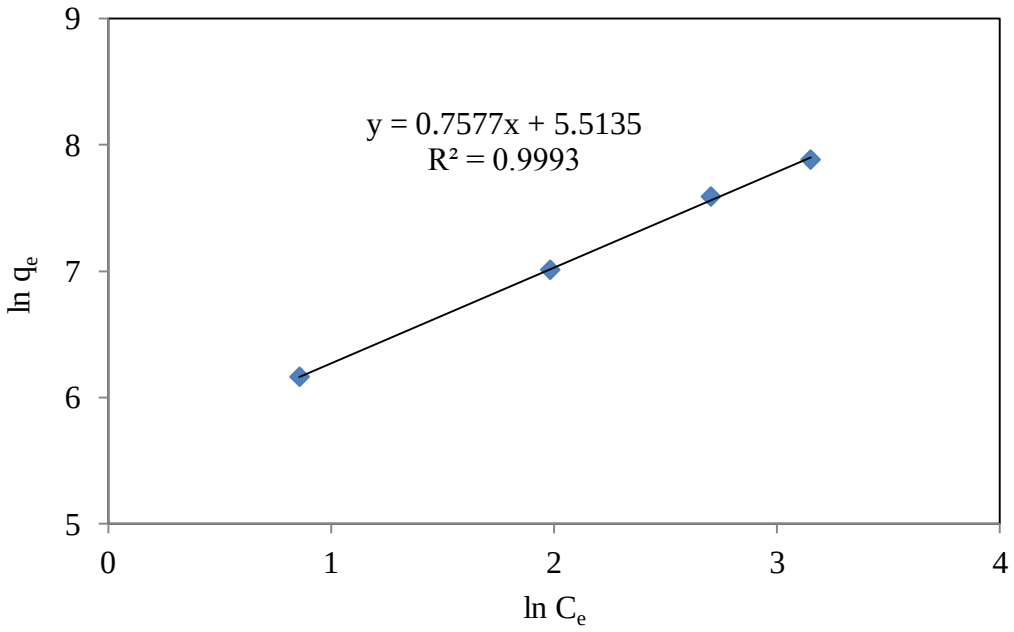


Figure 4.63. Freundlich adsorption isotherm for degradation of MO in the presence of 0.5M ZnO-NC1 (300˚C). Conditions: pH= 6.5 (Natural), T= 298K, Flow rate= 2000 rpm.

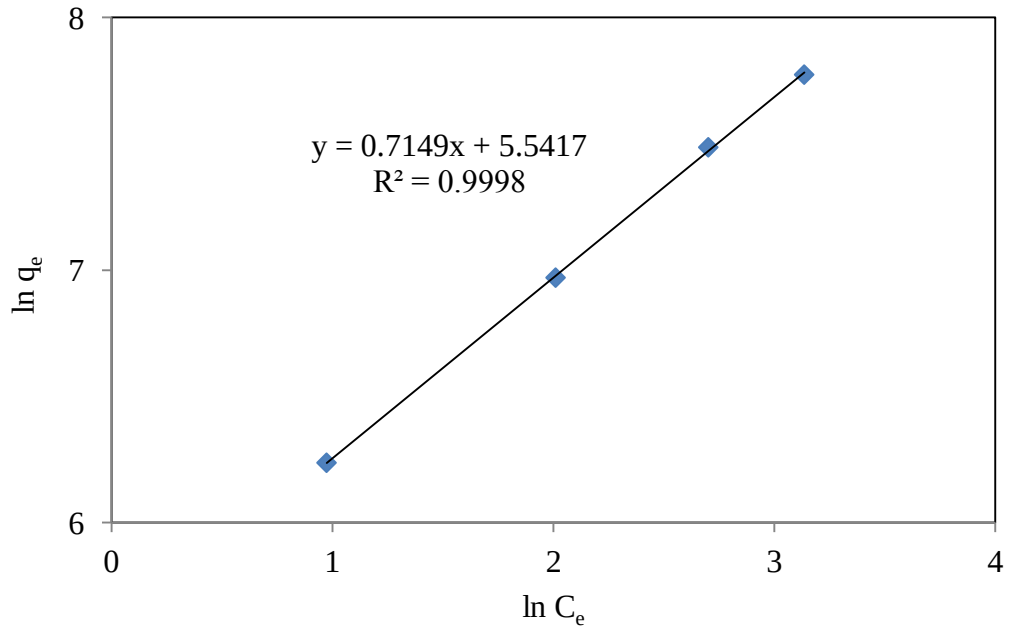


Figure 4.64. Freundlich adsorption isotherm for decolorization of MO in the presence of 0.5M ZnO-NC1 (300˚C). Conditions: pH= 6.5 (Natural), T= 298K, Flow rate= 2000 rpm.

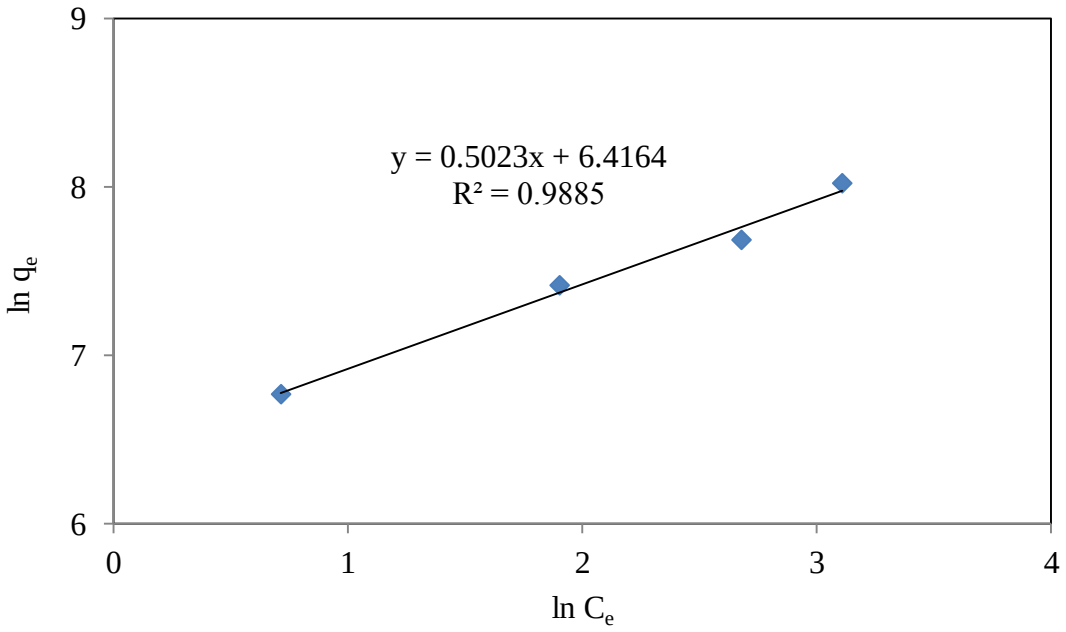


Figure 4.65. Freundlich adsorption isotherm for degradation of MO in the presence of 0.5M ZnO-NC1 (500˚C). Conditions: pH= 6.5 (Natural), T= 298K, Flow rate= 2000 rpm.

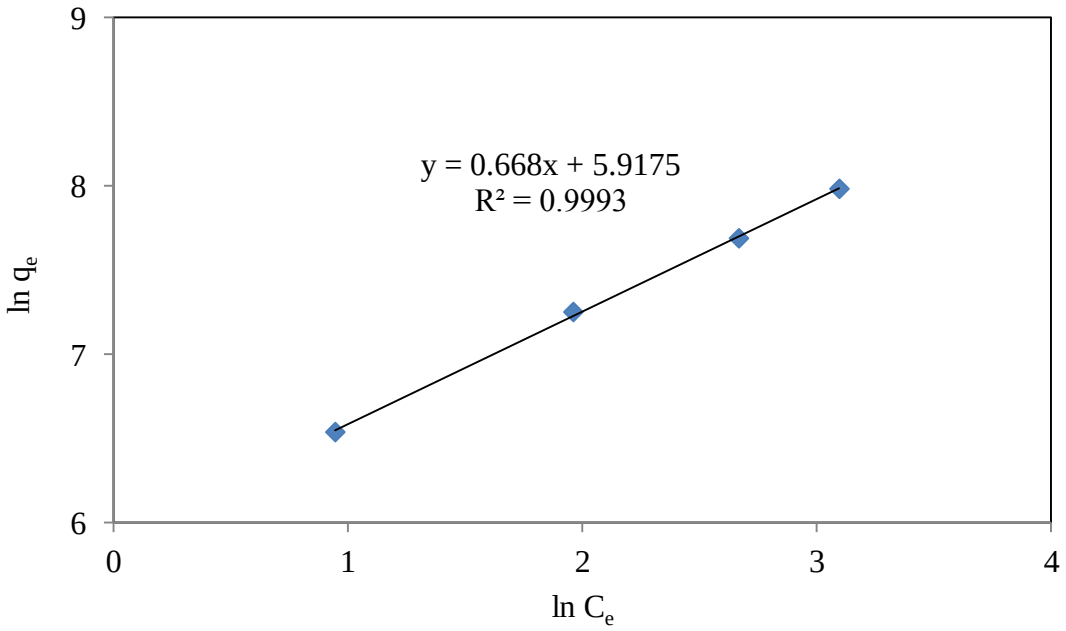


Figure 4.66. Freundlich adsorption isotherm for decolorization of MO in the presence of 0.5M ZnO-NC1 (500˚C). Conditions: pH= 6.5 (Natural), T= 298K, Flow rate= 2000 rpm.

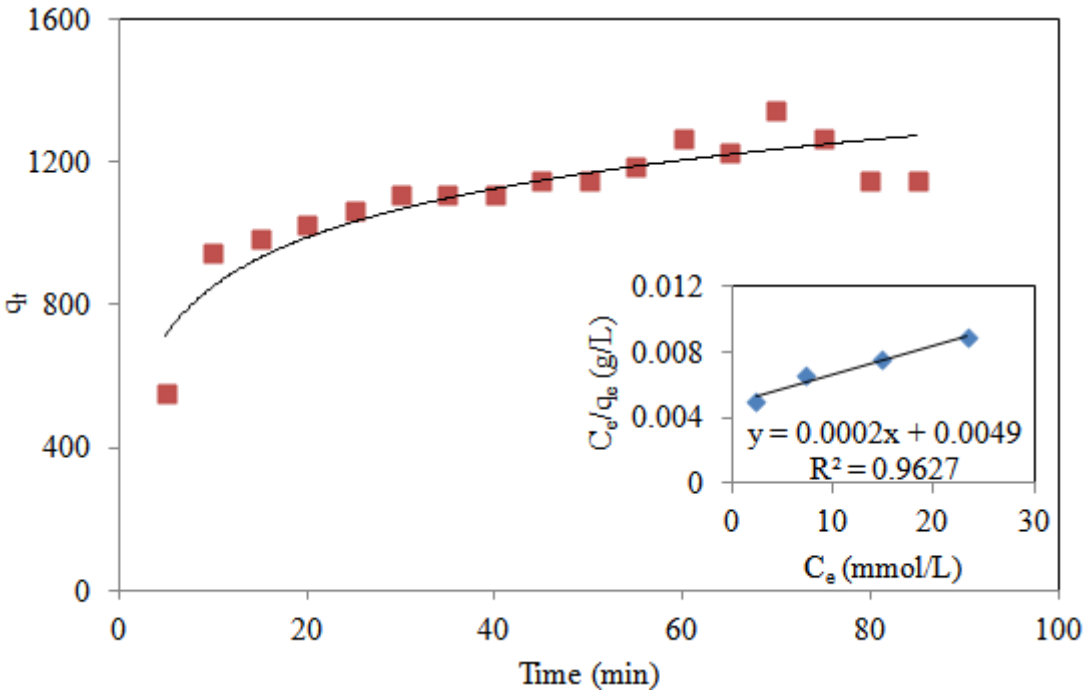


Figure 4.67. Langmuir adsorption isotherm for degradation of MO in the presence of 0.5M ZnO-NC1 (300˚C). Inset: C_e/q_e vs. C_e plot. Conditions: pH= 6.5 (Natural), T= 298K, Flow rate= 2000 rpm.

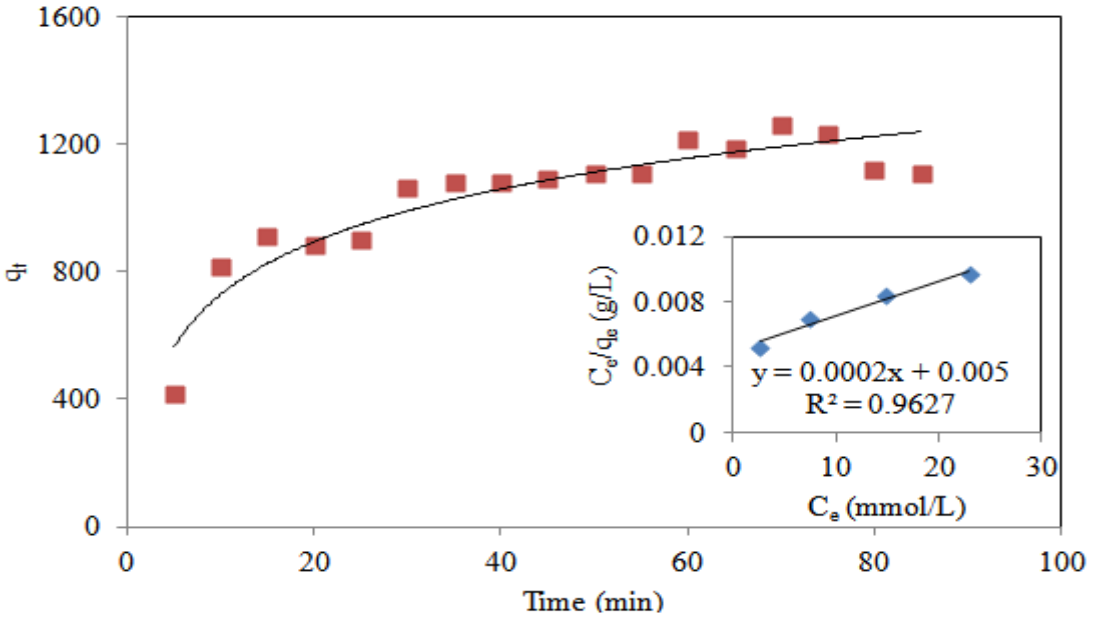


Figure 4.68. Langmuir adsorption isotherm for decolorization of MO in the presence of 0.5M ZnO-NC1 (300˚C). Inset: C_e/q_e vs. C_e plot. Conditions: pH= 6.5 (Natural), T= 298K, Flow rate= 2000 rpm.

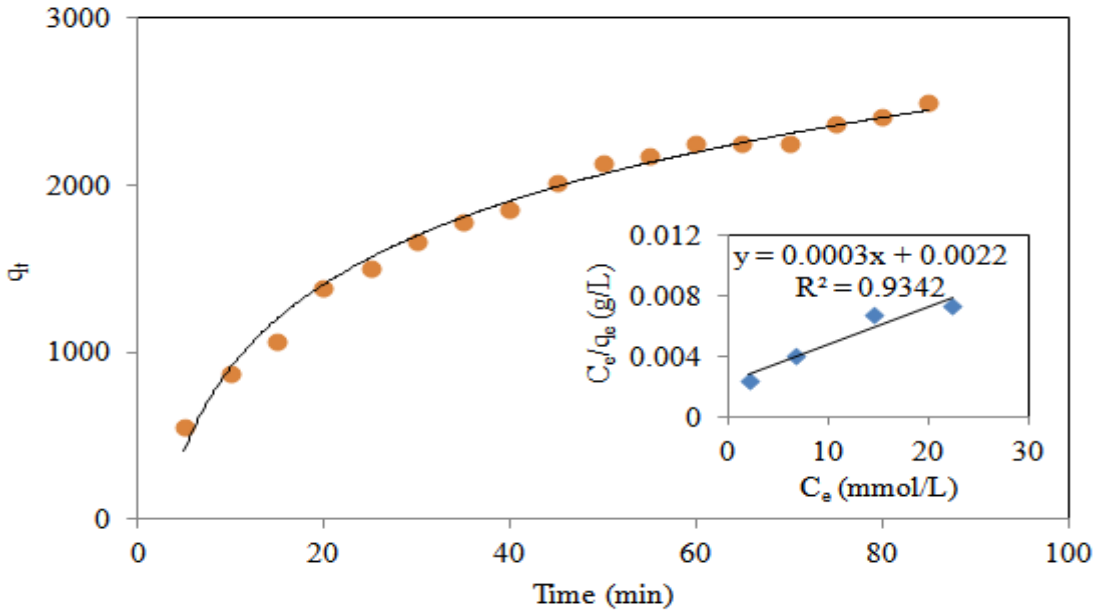


Figure 4.69. Langmuir adsorption isotherm for degradation of MO in the presence of 0.5M ZnO-NC1 (500˚C). Inset: C_e/q_e vs. C_e plot. Conditions: pH= 6.5 (Natural), T= 298K, Flow rate= 2000 rpm.

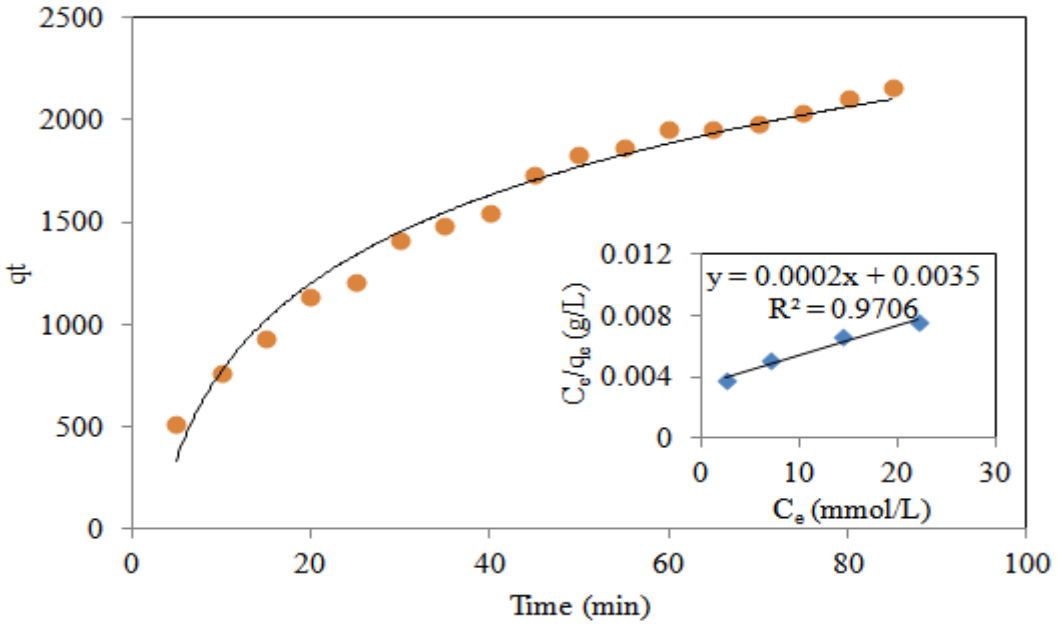


Figure 4.70. Langmuir adsorption isotherm for decolorization of MO in the presence of 0.5M ZnO-NC1 (500˚C). Inset: C_e/q_e vs. C_e plot. Conditions: pH= 6.5 (Natural), T= 298K, Flow rate= 2000 rpm.

4.4.3. Photocatalytic Experiments

4.4.3.1. Effect of ZnO Loading. The photocatalytic reactions are carried out in the existence of supported catalysts loaded with different ZnO concentrations. Following 30 min dark experiments, the remaining concentrations of MO in solutions are controlled about 85 min (Figure 4.71, Figure 4.72, Figure 4.73 and Figure 4.74).

For both degradation and decolorization processes, ZnO loading concentrations positively affect the photocatalytic activity of the supported catalysts (Figure 4.71, Figure 4.72, Figure 4.73 and Figure 4.74). 0.5M ZnO-NC1 (500˚C) shows the best activity and this demonstrates the consistency with the XRD analysis where the highest crystalline order of ZnO nanoparticles is achieved in the presence of 0.5M ZnO-NC1 (500˚C).

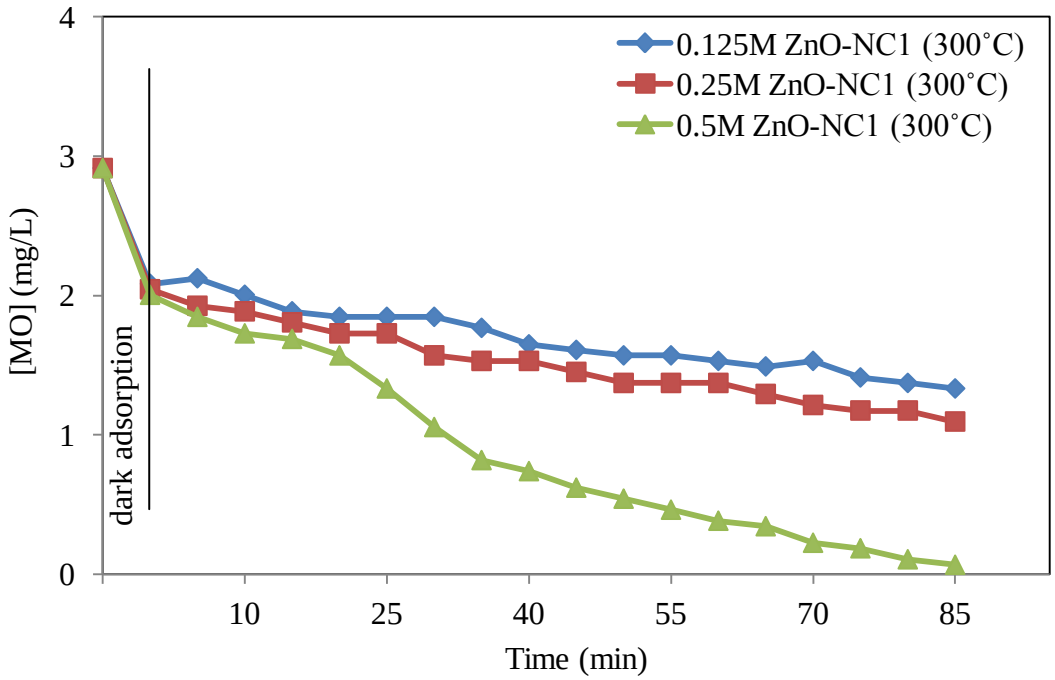


Figure 4.71. MO degradation in the presence of supported catalysts prepared at 300˚C. Conditions: pH= 6.5 (Natural), $[MO]_0$= 3.27 mg/L, T= 298 K, Flow rate= 2000 rpm.

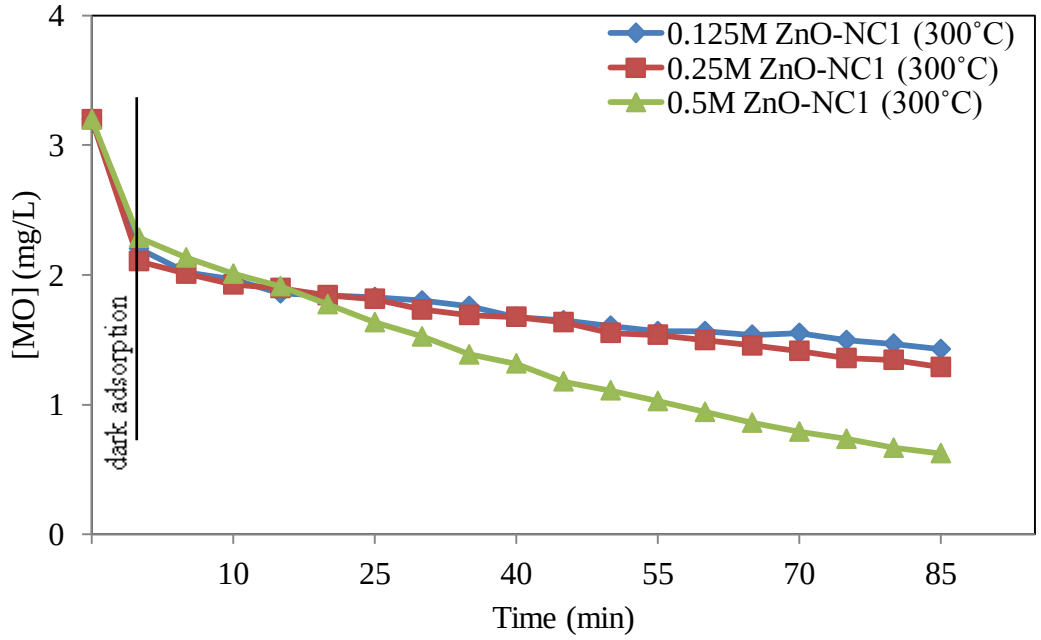


Figure 4.72. MO decolorization in the presence of supported catalysts prepared at 300˚C. Conditions: pH= 6.5 (Natural), $[MO]_0$= 3.27 mg/L, T= 298 K, Flow rate= 2000 rpm.

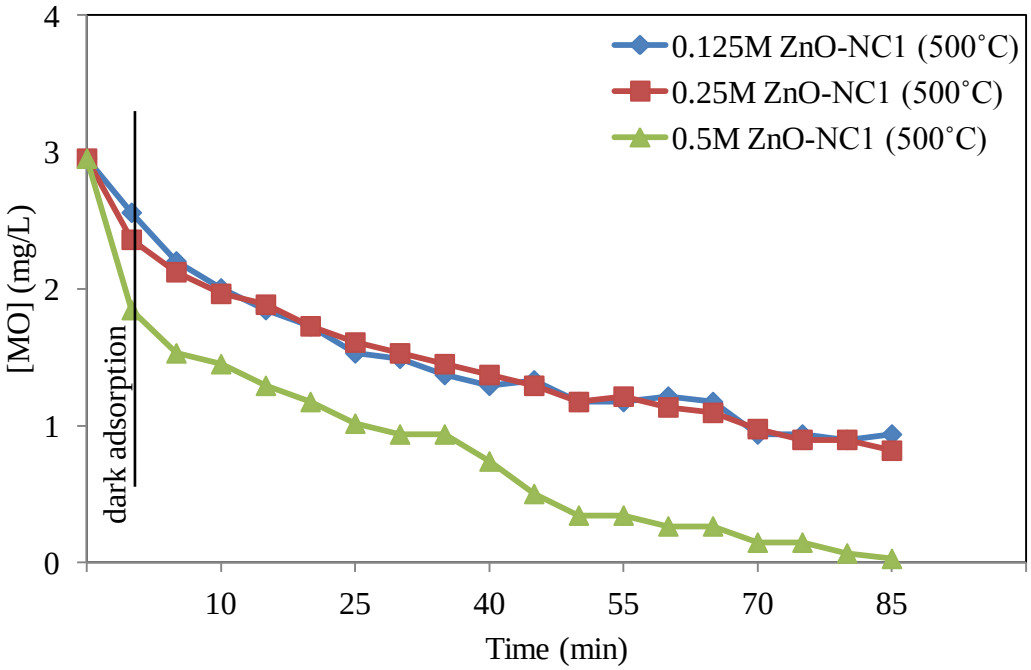


Figure 4.73. MO degradation in the presence of supported catalysts prepared at 500˚C. Conditions: pH= 6.5 (Natural), $[MO]_0$= 3.27 mg/L, T= 298 K, Flow rate= 2000 rpm.

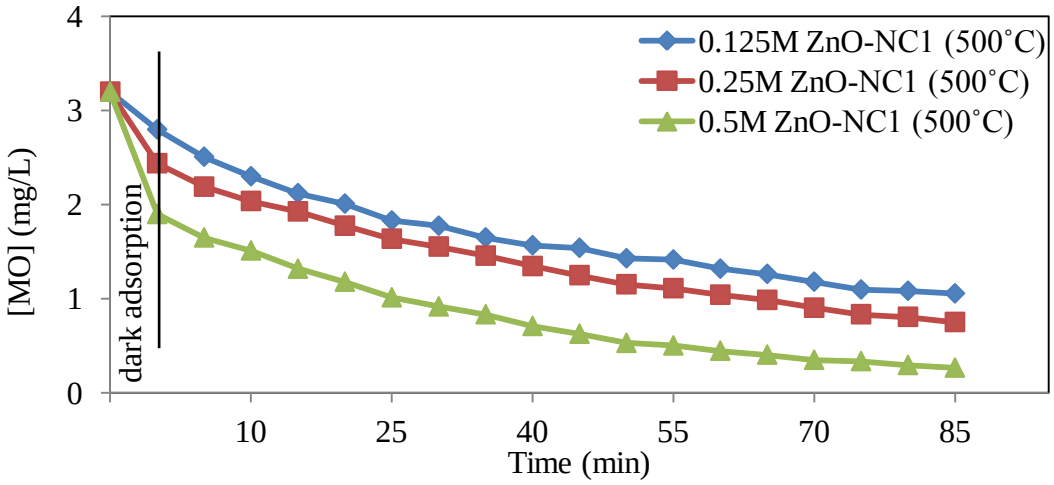


Figure 4.74. MO decolorization in the presence of supported catalysts prepared at 500˚C. Conditions: pH= 6.5 (Natural), $[MO]_0$= 3.27 mg/L, T= 298 K, Flow rate= 2000 rpm.

4.4.3.2. Effect of Initial MO Concentration. The influence of the initial MO concentration varying from 3.27 to 24.55 mg/L on the photocatalytic rates is also investigated in the presence of 0.5M ZnO-NC1 (300˚C) and 0.5M ZnO-NC1 (500˚C). For all concentrations, the best degradation and decolorization performances are obtained in the presence of 0.5M ZnO-NC1 (500˚C) (Figure 4.75 and Figure 4.76). Pseudo first order kinetic model is confirmed according to the linearity noticed in the plots of ln (C_0/C) versus t (time) for all concentrations. (Figure 4.77, Figure 4.78, Figure 4.79 and Figure 4.80). As a general trend, the efficiency of both decolorization and degradation processes is found to decrease with increasing concentration of MO (Table 4.7 and Table 4.8). This can be a result of blocking of the photocatalytically active sites on the supported catalyst and reducing the interaction of photons with these sites.

Langmuir-Hinshelwood kinetic model analysis gives linearity in the plot of reciprocal rate (1/R) against reciprocal of MO concentrations (1/C_0) (Figure 4.77, Figure 4.78, Figure 4.79 and Figure 4.80 Inset).

In the presence of 0.5M ZnO-NC1 (300˚C), the values of adsorption coefficient (K) and reaction rate constant (k) are found to be 0.038 L/mg and 0.074 mg/L min (degradation) and 0.025 L/mg and 0.089 mg/L min (decolorization). 0.5M ZnO-NC1 (500˚C) gives higher K and k values. 0.154 L/mg and 0.085 mg/L min (for degradation)

and, 0.042 L/mg and 0.096 mg/L min (for decolorization) demonstrating a higher adsorption capacity and hence degradation-decolorization ability.

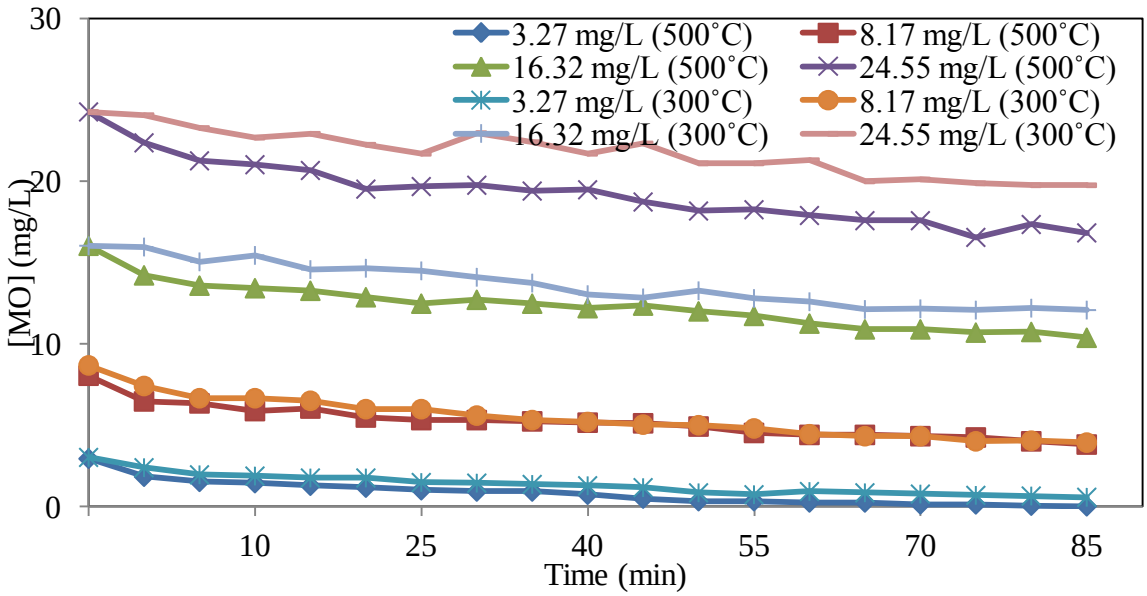


Figure 4.75. MO degradation at initial MO concentrations in the presence of 0.5M ZnO-NC1 (300˚C) and 0.5M ZnO-NC1 (500˚C).Conditions: pH=6.5 (Natural), T= 298 K, Flow rate= 2000 rpm.

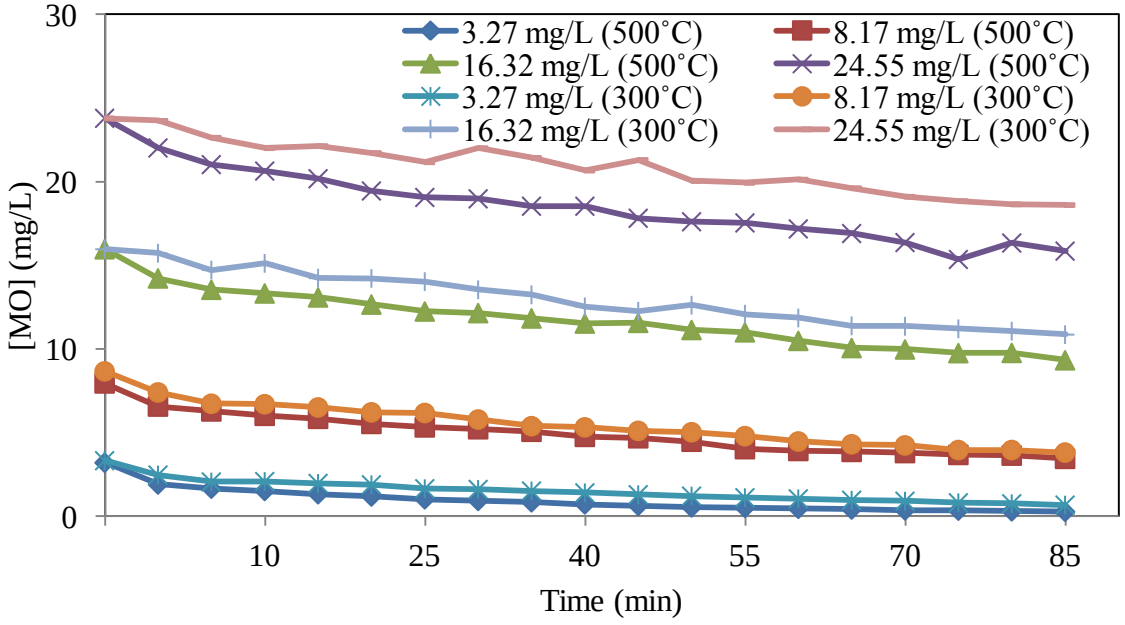


Figure 4.76. MO decolorization at initial MO concentrations in the presence of 0.5M ZnO-NC1 (300˚C) and 0.5M ZnO-NC1 (500˚C).Conditions: pH= 6.5 (Natural), T= 298 K, Flow rate= 2000 rpm.

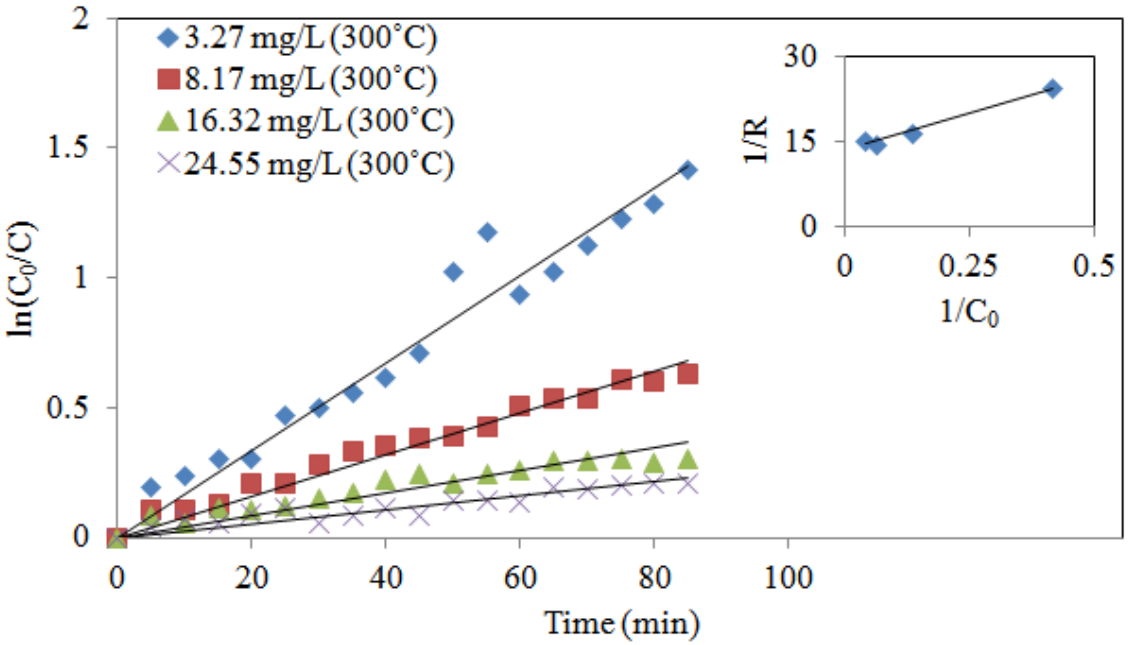


Figure 4.77. Pseudo-first order kinetics for degradation of MO in the presence of 0.5M ZnO-NC1 (300˚C). Inset: Langmuir-Hinshelwood analysis. Conditions: pH= 6.5 (Natural), T= 298 K, Flow rate= 2000 rpm.

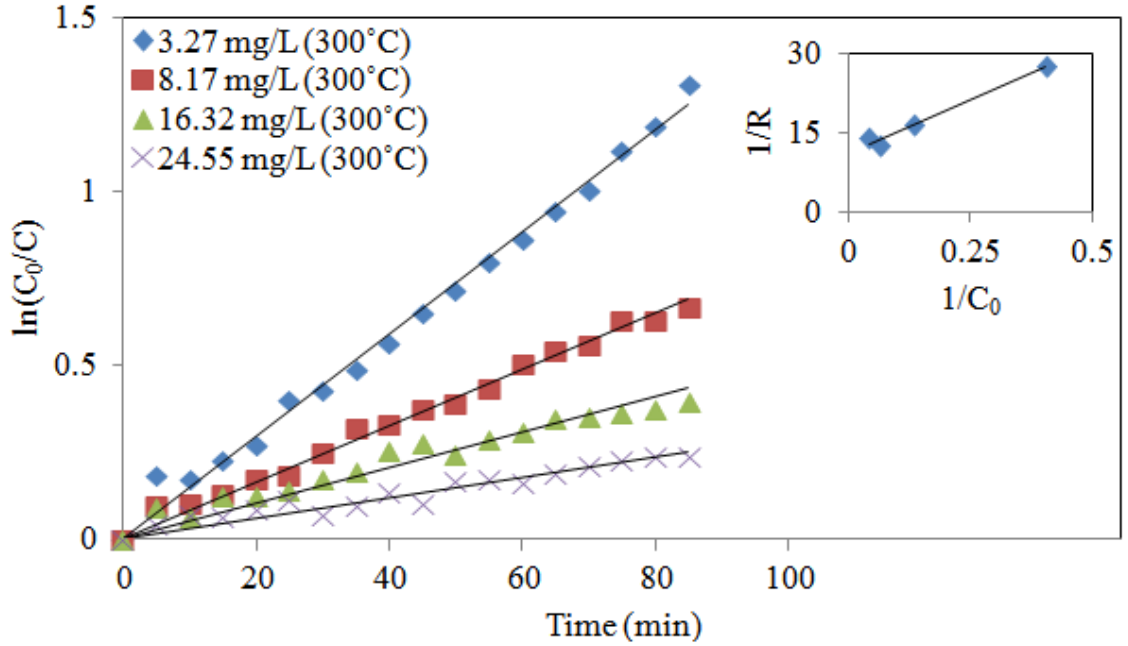


Figure 4.78. Pseudo-first order kinetics for decolorization of MO in the presence of 0.5M ZnO-NC1 (300˚C). Inset: Langmuir-Hinshelwood analysis. Conditions: pH=6.5 (Natural), T= 298 K, Flow rate= 2000 rpm.

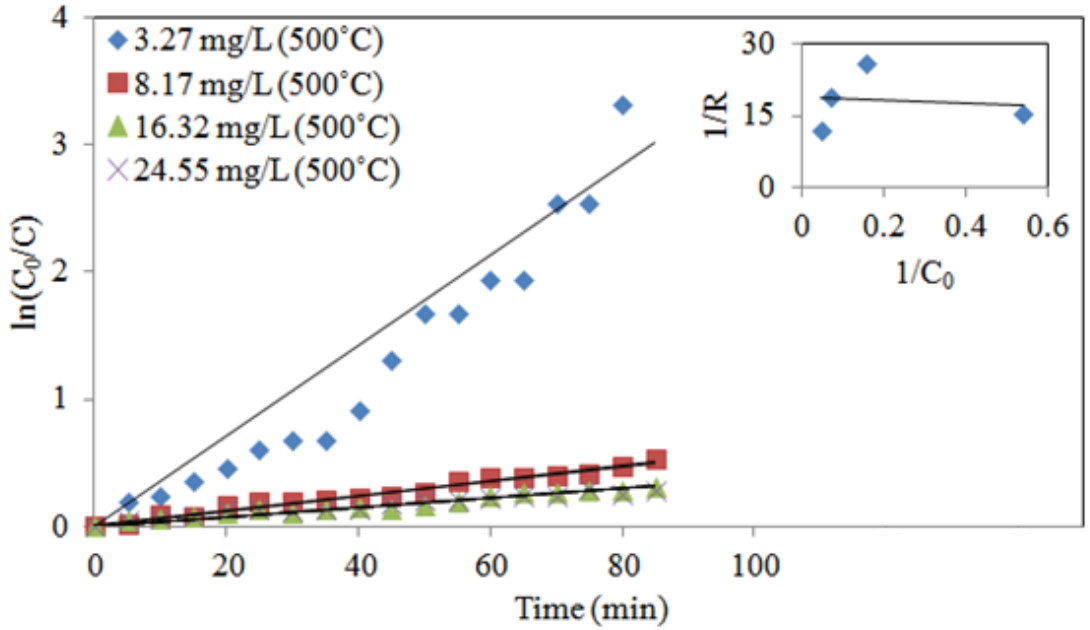


Figure 4.79. Pseudo-first order kinetics for degradation of MO in the presence of 0.5M ZnO-NC1 (500˚C). Inset: Langmuir-Hinshelwood analysis. Conditions: pH= 6.5 (Natural), T= 298 K, Flow rate= 2000 rpm.

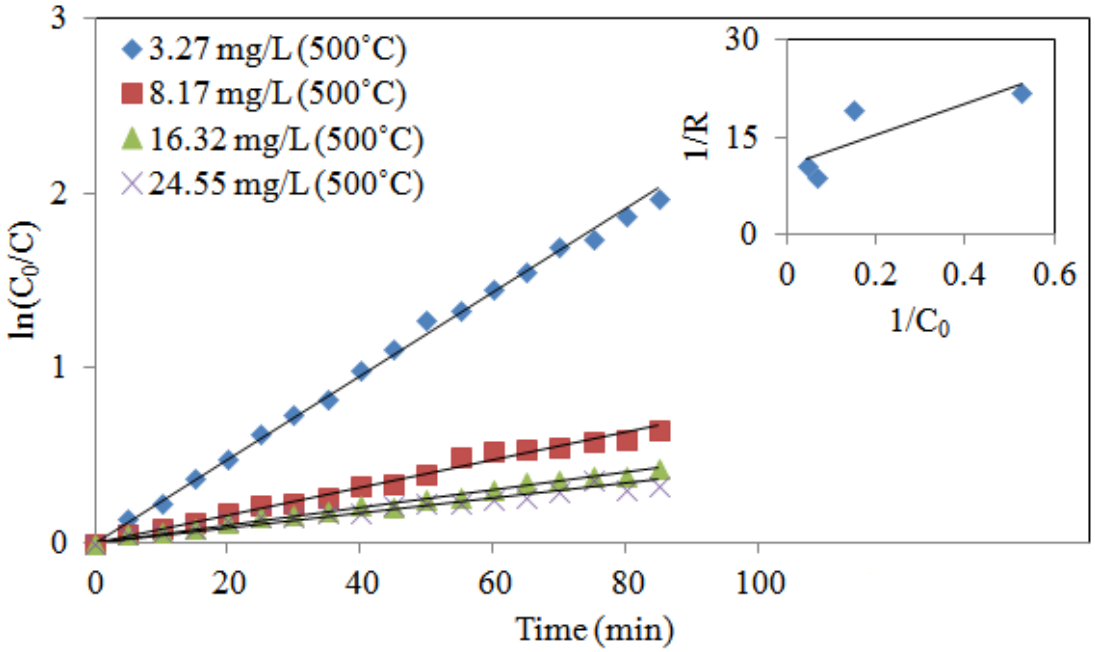


Figure 4.80. Pseudo-first order kinetics for decolorization of MO in the presence of 0.5M ZnO-NC1 (500˚C). Inset: Langmuir-Hinshelwood analysis. Conditions: pH= 6.5 (Natural), T= 298 K, Flow rate= 2000 rpm.

Table 4.7. Rate constants (k) and linear regression values (R) for the degradation and decolorization processes of MO in the presence of 0.5M ZnO-NC1 (300˚C).

	k (min^{-1})		**R**	
[MO] (mg/L)	**degradation**	**decolorization**	**degradation**	**decolorization**
24.55	0.0027	0.0030	0.840	0.915
16.32	0.0043	0.0051	0.858	0.935
8.17	0.0081	0.0081	0.969	0.989
3.27	0.0169	0.0147	0.954	0.992

Table 4.8. Rate constants (k) and linear regression values (R) for the degradation and decolorization processes of MO in the presence of 0.5M ZnO-NC1 (500˚C).

	k (min^{-1})		**R**	
[MO] (mg/L)	**degradation**	**decolorization**	**degradation**	**decolorization**
24.55	0.0037	0.0043	0.902	0.997
16.32	0.0037	0.0050	0.963	0.988
8.17	0.0060	0.0079	0.972	0.986
3.27	0.0354	0.0238	0.877	0.938

4.5. Characterization Results of the ZnO-NC2 Catalysts

4.5.1. XRD Analysis

XRD spectrums of bare NC2, 0.125M ZnO-NC2 (300˚C), 0.25M ZnO-NC2 (300˚C), 0.5M ZnO-NC2 (300˚C), 0.125M ZnO-NC2 (500˚C), 0.25M ZnO-NC2 (500˚C) and 0.5M ZnO-NC2 (500˚C) catalysts are shown in Figure 4.81 and 4.82. Bare NC2, due to the organic modification, the characteristic (001) reflection is observed at 4.2˚ (2θ) with d-spacing value of. 21.22 Å. This value is relatively higher than that of MMT (12.8 Å) [73]. Also small (101) and (107) reflections of quartz and crystoballite are detected at 19.9˚ and 35.3˚ (2θ), respectively. [74, 75]. The characteristic peak at NC2 (4.2˚ (2θ)) is not detected in the existence of supported catalysts similar to the ZnO-NC1 systems. Generation of tactoids for the catalysts prepared at 300˚C with the peak at 8.2˚ (2θ) suggesting an immiscible dispersion of destructed layers [76]. The distinctive ZnO peak (101) is observed at 36.4^{o} (2θ) and other reflections of (100), (002), (102), (110), (103) and (200) are detected at 31.9˚, 34.6˚, 47.7˚, 56.7˚, 63.1˚, and 66.6˚ (2θ) respectively. As the loading concentrations of ZnO increases the intensities of NC2 peaks decrease, pointing out uniform distribution of ZnO nanoparticles on the NC2 surface.

The crystalline size of ZnO nanoparticles (D_{ZnO}), based on the broadening of the most intense (101) diffraction at 36.4˚ (2θ) are calculated by employing Scherrer's equation (Table 4.9). Similar to the NC1-ZnO systems, ZnO crystal sizes do not vary with the ZnO loading concentration for the catalysts prepared at 300˚C. However, for the catalysts calcined at 500˚C, ZnO crystal sizes increase regularly due to the aggregation of ZnO nanoparticles on the surface of NC2.

.

Table 4.9. Crystalline sizes (D), surface areas (BET), pore volumes (V_{pore}) and pore radius (r_{pore}).of 0.25M ZnO and supported catalysts.

Catalyst	**2θ (˚)**	**D (nm)**	**BET (m^2/g)**	**V_{pore} (cm^3/g)**	**r_{pore} (Å)**
0.25M ZnO (500°C)	36.4	15.2	7.6	0.013	17.8
NC2	4.2	-	12.6	0.028	15.8
0.125M ZnO-NC2 (300°C)	36.4	14.04	31.0	0.056	16.4
0.25M ZnO-NC2 (300°C)	36.4	13.23	29.9	0.053	14.9
0.5M ZnO-NC2 (300°C)	36.4	13.75	31.9	0.060	14.9
0.125M ZnO-NC2 (500°C)	36.4	14.34	36.2	0.061	15.6
0.25M ZnO-NC2 (500°C	36.4	15.76	31.0	0.052	16.4
0.5M ZnO-NC2 (500°C)	36.4	20.64	22.5	0.034	15.8

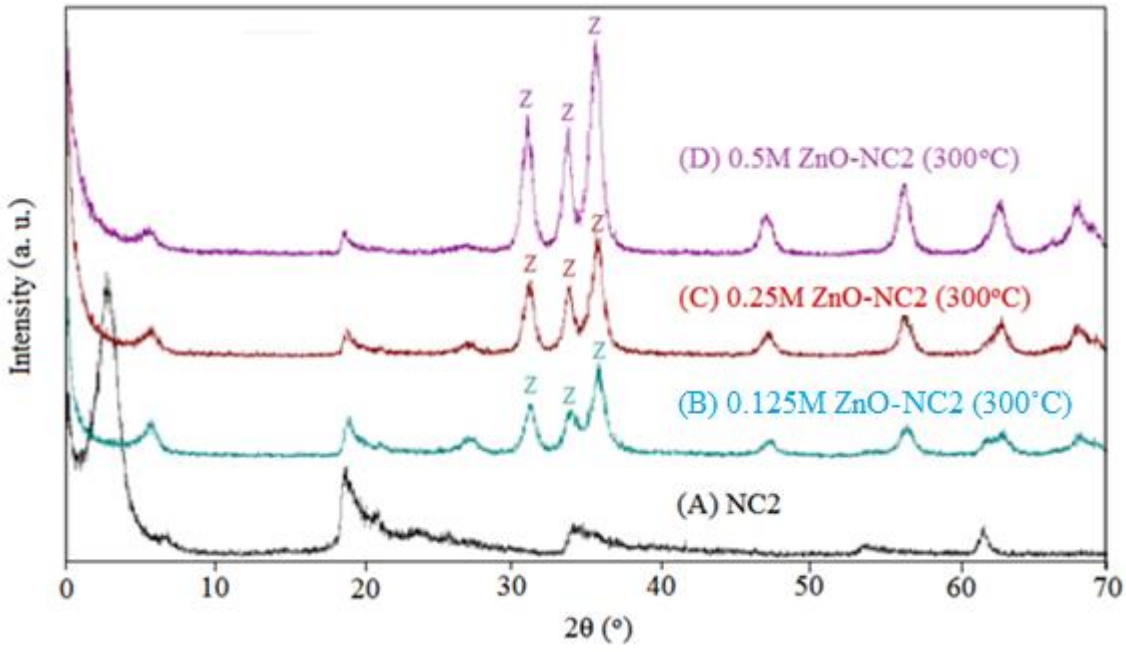


Figure 4.81. XRD patterns of NC2 (A) and supported catalysts (300˚C) (B-D). (Z: ZnO).

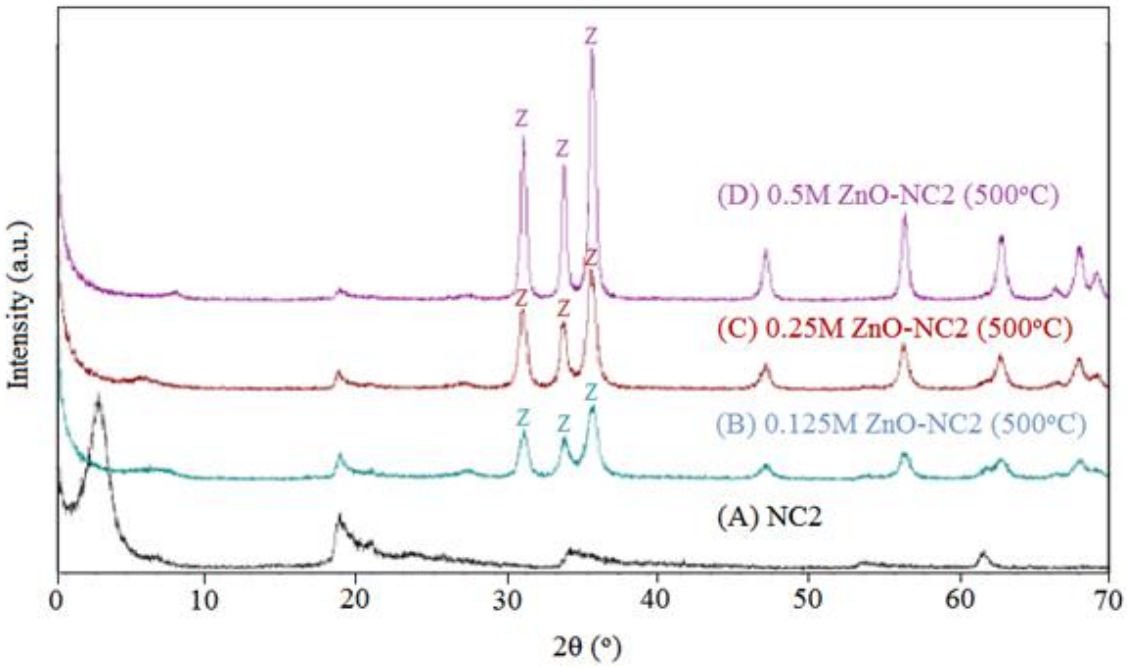


Figure 4.82. XRD patterns of NC2 (A) and supported catalysts (500˚C) (B-D). (Z: ZnO).

4.5.2. SEM-EDX Analysis

Surface morphologies of the bare NC2 and 0.25M ZnO-NC2 (500˚C) are investigated by SEM (EDX) analysis. Bare NC2 has a clear curly flake-like structure (Figure 4.83) and based on the EDX analysis it consists of major Si, Al, O elements and minor Fe, Mg, K, Na, K and Ca elements (Table 4.10). For 0.25M ZnO-NC2 (500˚C), Zn and O elemental compositions are noticeable.

SEM micrograph and mapping images of the 0.25M ZnO-NC2 (500˚C) are shown in the Figure 4.84. Although the structure of NC2 is retained following the ZnO treatment, homogenously distributed ZnO nanoparticles over the surface of the support are detected. This is also evidenced in the EDX data (Table 4.10). Moreover, NC2 has no Zn, whereas 0.25M ZnO-NC2 (500˚C) shows 73.64% Zn component. The reduction in the silica and alumina percentages may also correspond to the location of ZnO nanoparticles in the silica matrix of the clay.

Table 4.10. Elemental composition of NC2 and 0.25M ZnO-NC2 (500˚C).

	0.25M ZnO	**NC2**	**0.25M ZnO-NC2 (500˚C)**
Components	**Wt %**	**Wt %**	**Wt %**
Zn	88.79	-	73.65
Si	-	45.91	8.15
O	11.21	28.45	13.12
Al	-	15.13	3.52
Fe	-	5.35	-
Mg	-	3.21	1.55
Cl	-	1.11	-
Na	-	0.40	-
K	-	0.39	-
Ca	-	0.07	-

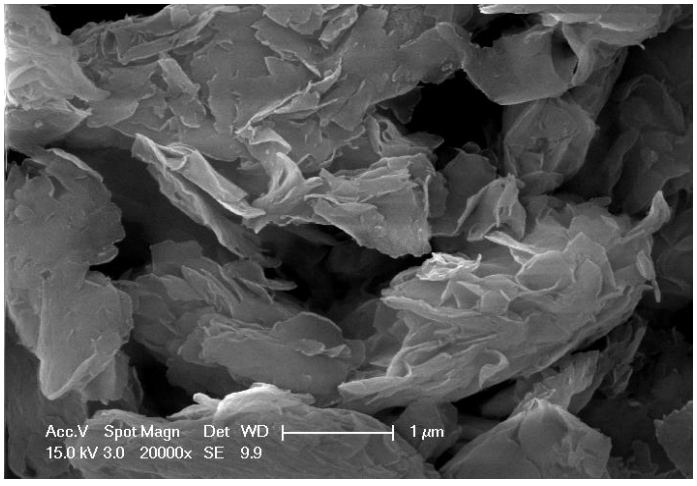


Figure 4.83. SEM image of NC2.

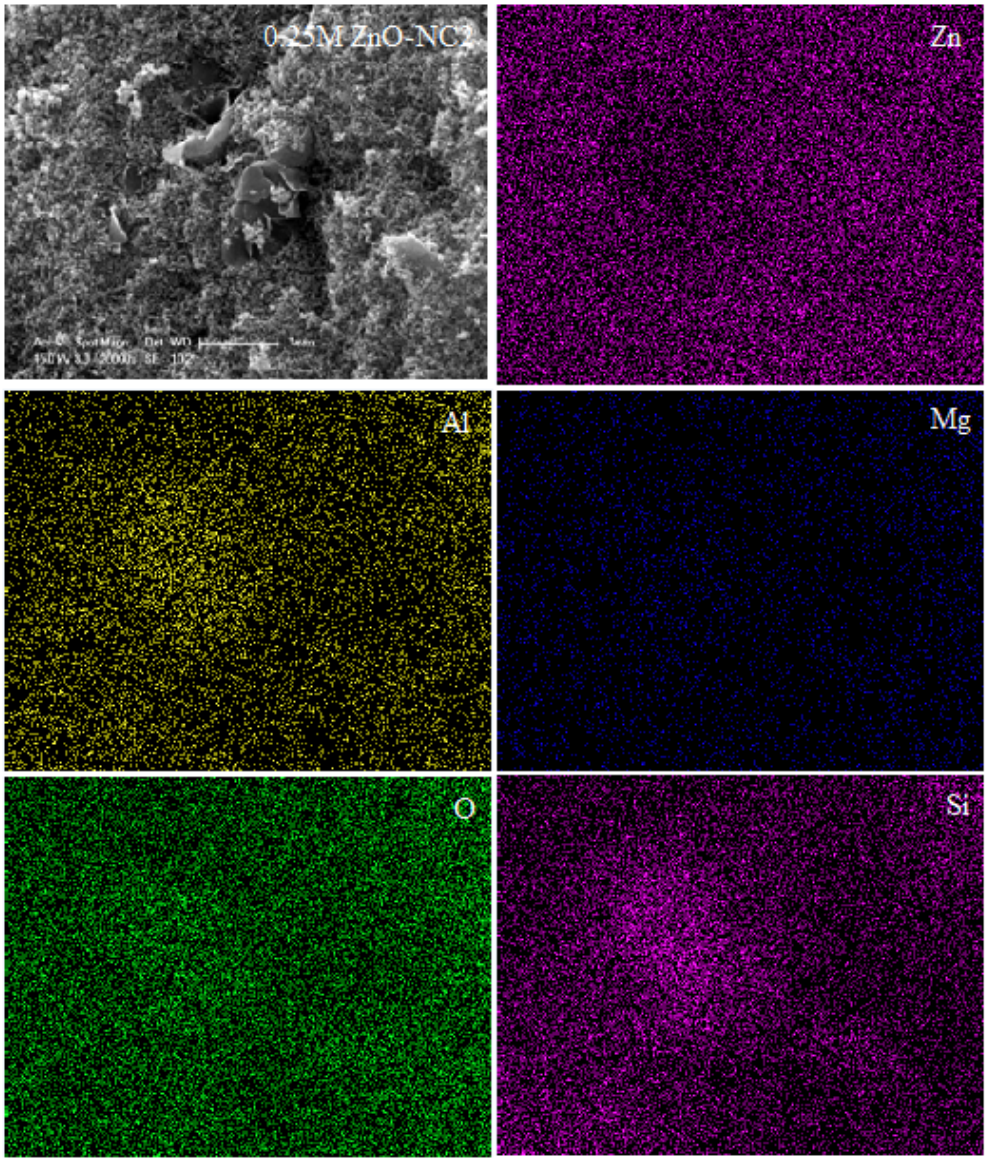


Figure 4.84. SEM image of 0.25M ZnO-NC2 (500˚C) and mapping images of 0.25M ZnO-NC2 (500˚C), Zn, Al, Mg, O and Si.

4.5.3. Nitrogen Adsorption-Desorption Isotherms

Nitrogen adsorption-desorption isotherms and pore size distribution plots of the NC2 and supported catalysts are illustrated in Figure 4.85, Figure 4.86, Figure 4.87 and Figure 4.88. NC2 and supported catalysts exhibits Type IV isotherms, owing to their mesoporous structure. On the other hand, the increment in the loading concentration of ZnO narrows the hysteresis loops. The pore size distribution curves display that the pores of the supported catalysts exist in the typical mesoporous region of 20-40 Å (Figure 4.85 and Figure 4.86). In comparison to the raw NC2, supported catalysts have larger surface

area and pore volumes (Table 4.9). The relative decrease in the surface area and pore volume of 0.5M ZnO-NC2 (500˚C) can be explained with excess ZnO loading on the clay surface. This creates smoother areas on the catalyst surface which covers the porous structure.

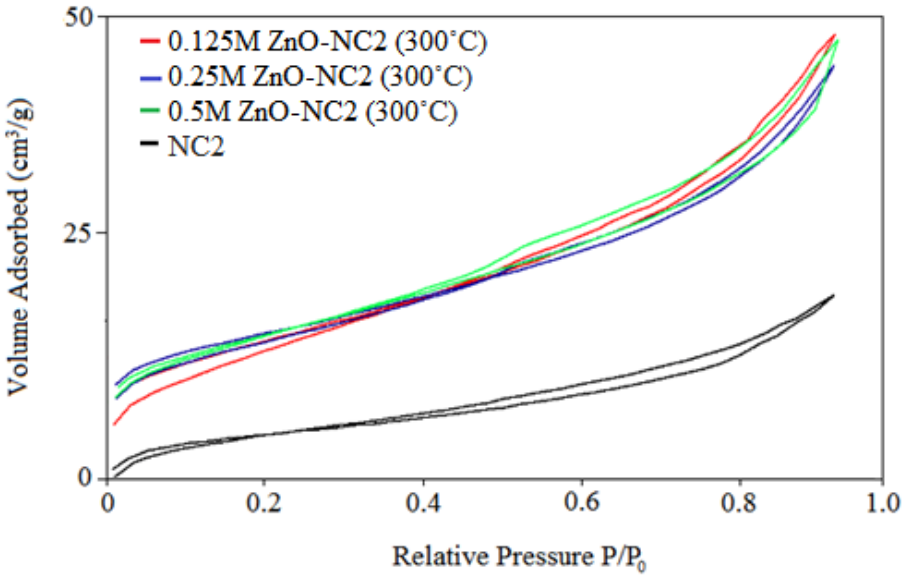


Figure 4.85. Nitrogen adsorption-desorption isotherms of NC2 and supported catalysts prepared at 300˚C.

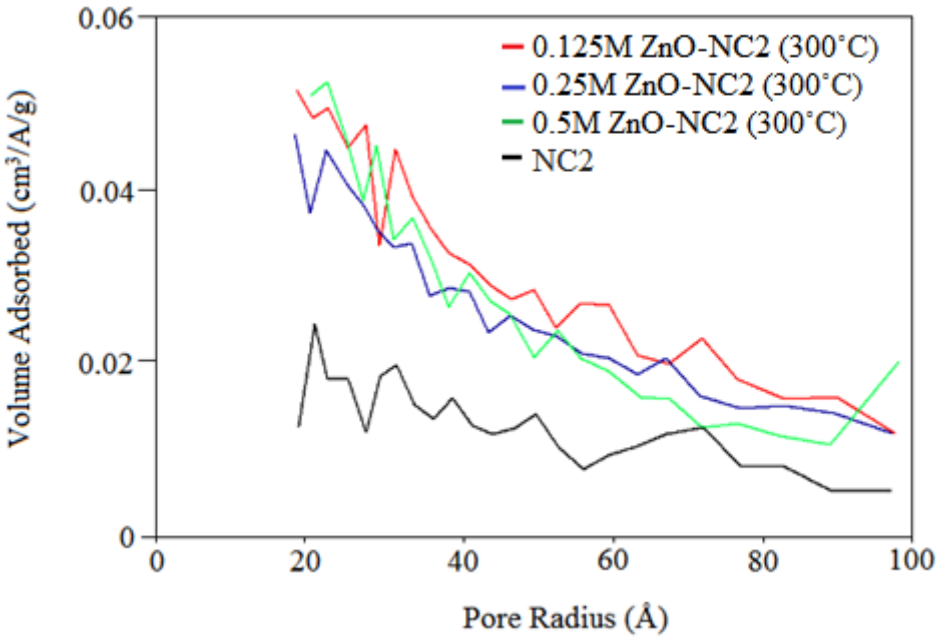


Figure 4.86. Pore size distribution plots of NC2 and supported catalysts prepared at 300˚C.

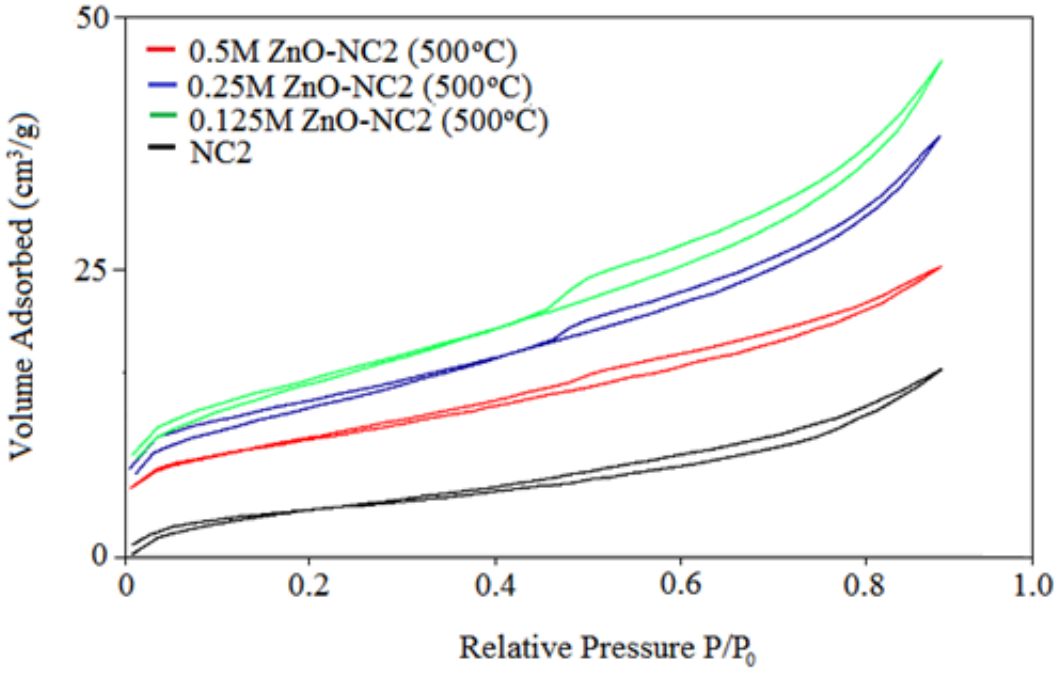


Figure 4.87. Nitrogen adsorption-desorption isotherms of NC2 and supported catalysts prepared at 500˚C.

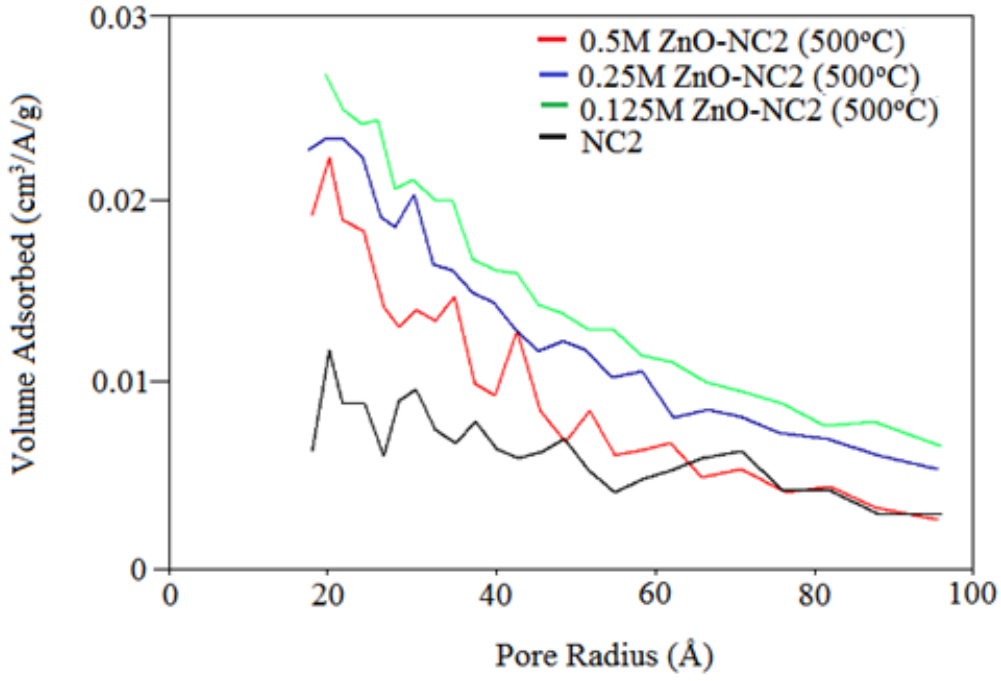


Figure 4.88. Pore size distribution plots of NC2 and supported catalysts prepared at 500˚C.

4.5.4. UV-Vis DRS Analysis

Figure 4.89 and Figure 4.90 present the UV-Vis absorption spectroscopy of the NC2, 0.25M ZnO and the supported catalysts. The bare NC2 shows an extended absorption tail between 200 and 600 nm while 0.25M ZnO has a sharp absorption edge at the UV region. In the absorption spectra of the supported catalysts, the characteristic absorption edge of ZnO is detected. This edge becomes more observable and wider with the higher loading concentration of ZnO.

In addition the UV-Vis absorption spectra of the as prepared catalysts are transformed to the band-gap values (Equation 2.17) which are evaluated by linear extrapolation and taking the intercept on the x-axis gives the value of the band gap (Figure 4.91 and Figure 4.92). Accordingly, band gap energy of 0.25M ZnO (500˚C) is found as 3.12 eV (Figure 4.91 Inset). A slight decrease is observed for the supported catalysts, in comparison to the 0.25M ZnO which may correspond an activity in the visible region.

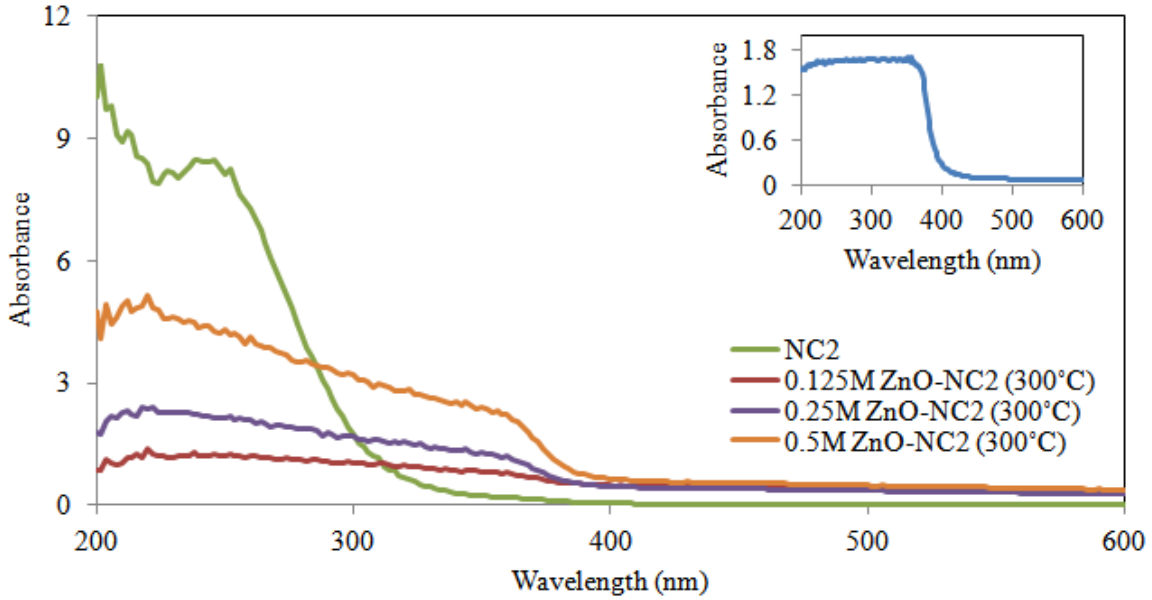


Figure 4.89. UV UV-Vis DRS spectra of NC2 and supported catalysts prepared at 300˚C. Inset: UV-Vis DRS spectra of 0.25M ZnO (500˚C).

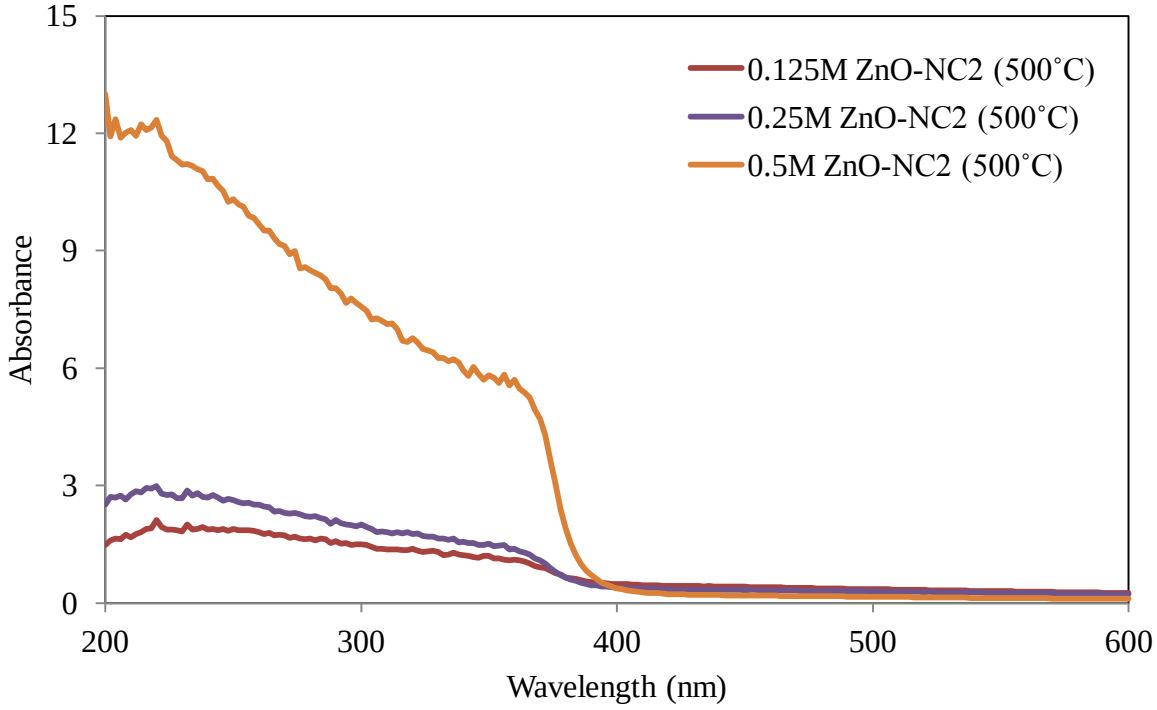


Figure 4.90. UV-Vis DRS spectra of supported catalysts prepared at 500˚C.

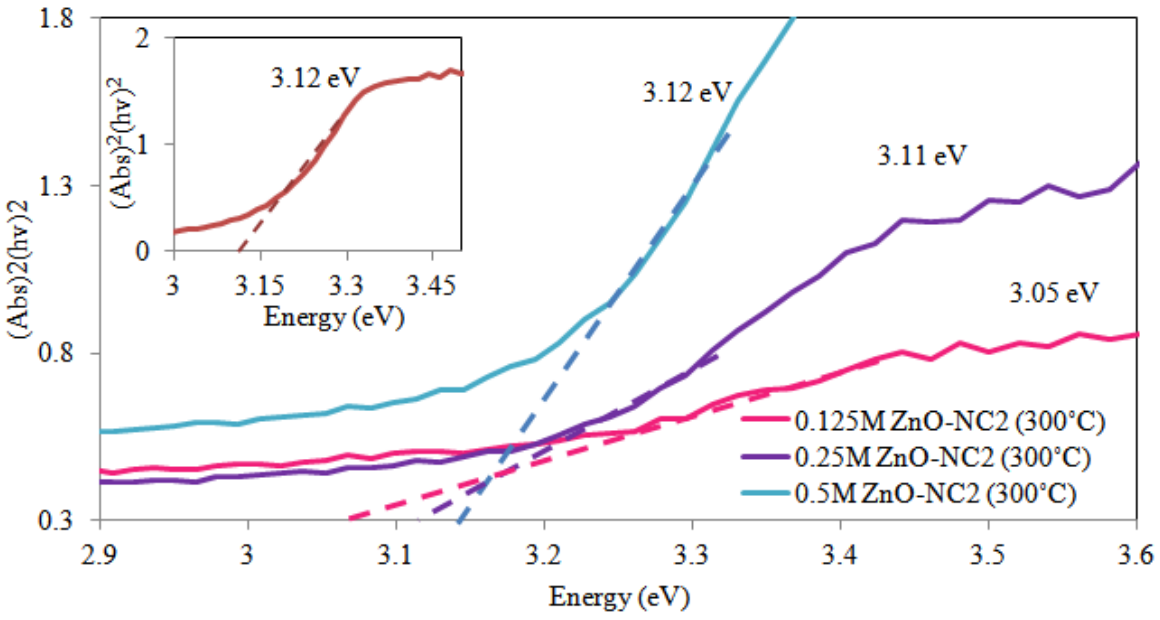


Figure 4.91. Band gap adsorption edges of supported catalysts. Inset: Band gap adsorption edges of 0.25M ZnO (500˚C).

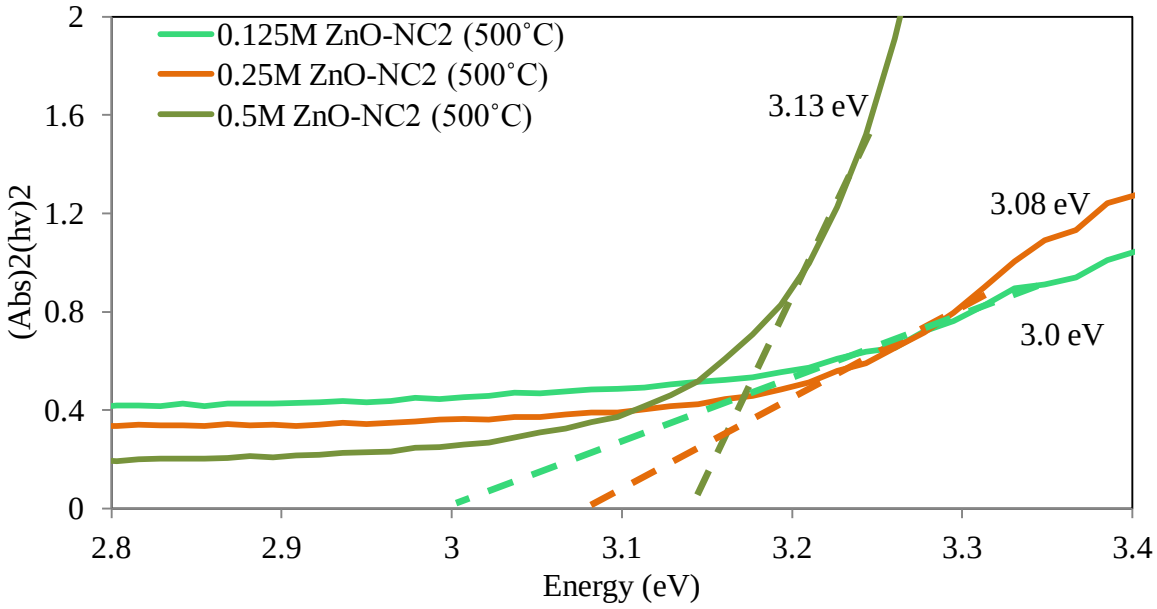


Figure 4.92. Band gap adsorption edges of supported catalysts.

4.6. Photoactivities of ZnO-NC2 Catalysts

4.6.1. Control Experiments

Control experiments are set as two steps. In the first step, dark absorption capacities of NC2, 0.25M ZnO, 0.25 M ZnO-NC2 (300˚C) and 0.25 M ZnO-NC2 (500˚C) are compared (Figure 4.93). For 0.25M ZnO and 0.25M ZnO-NC2 (300˚C), after 85 min mixing in the dark, no significant change is noticed in the MO concentrations. On the other hand the raw NC2 shows excellent adsorption property due to higher basal spacing. Also 0.25 M ZnO-NC2 (500˚C) can absorb dye compound, owing to decomposition of modification material between the layers at this temperature. In the second set photolysis of MO and photocatalytic activities of 0.25M ZnO (500˚C), 0.25 M ZnO-NC2 (300˚C) and 0.25 M ZnO-NC2 (500˚C) are examined (Figure 4.94). A negligible MO degradation is observed in the presence of UV light without any catalyst (Figure 4.94 Inset). The suspensions are stirred in the dark for 30 min to achieve adsorption/desorption equilibrium and thereafter exposed to illumination. Although, 0.25M ZnO (500˚C) shows a higher performance in comparison to the supported catalysts, the difficulties in the settlement of ZnO nanoparticles limit their applications in photocatalytic reactions. In the meantime, the activity of 0.25M ZnO-NC2 (500˚C) is better than 0.25M ZnO-NC2 (300˚C). Heat-induced

growth of ZnO particles results in sharper and narrower X-ray peaks, contributes to the increase of crystallinity and hence increases the photoactivity

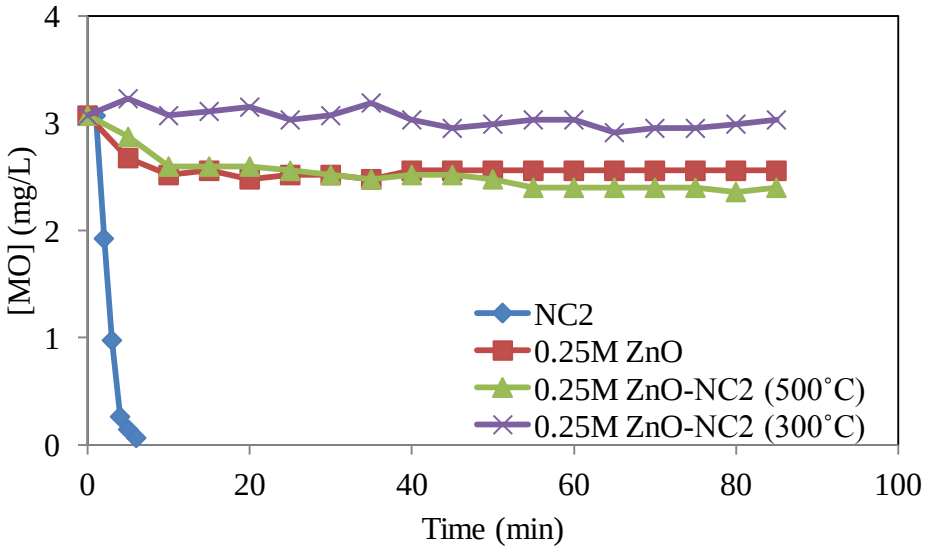


Figure 4.93. Control experiments in the dark. Conditions: pH: 6.5 (Natural), $[MO]_0$ = 3.27 mg/L, T = 298 K, Flow rate = 2000 rpm.

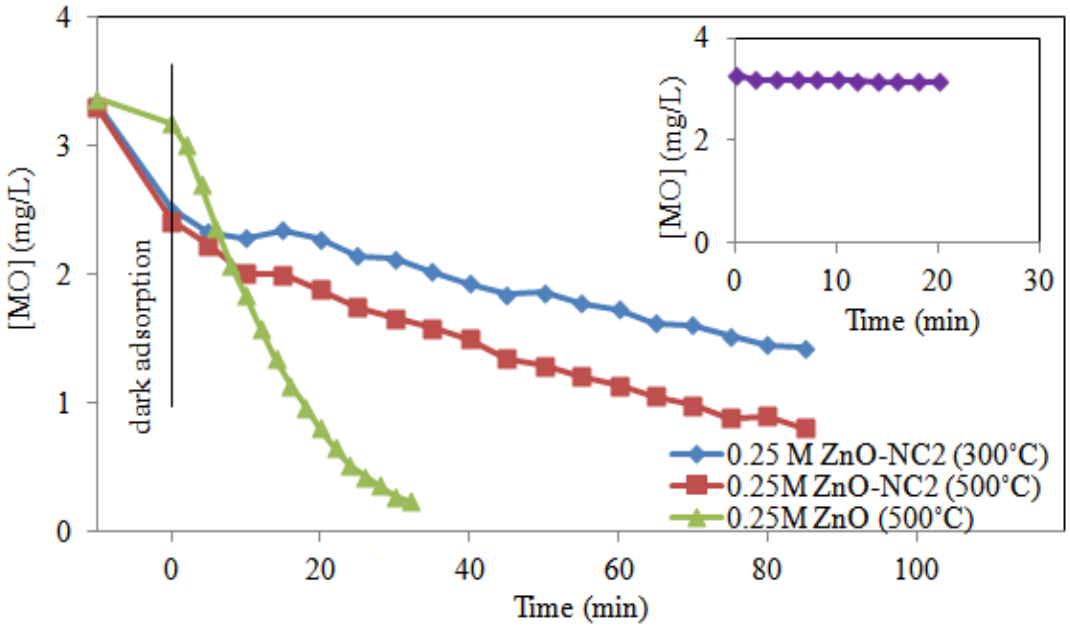


Figure 4.94. Control experiments under UV irradiation. Inset: Photolysis of MO. Conditions: pH: 6.5 (Natural), $[MO]_0$= 3.27 mg/L, T= 298K, Flow rate= 2000 rpm.

4.6.2. Dark Adsorption Experiments

4.6.2.1. Adsorption Kinetics. The dark adsorption details of MO (8.17 mg/L) over the 0.5M ZnO-NC2 (300˚C) and 0.5M ZnO-NC2 (500˚C) catalysts are investigated to specify the adsorption kinetics in terms of pseudo first order and pseudo second order models.

Pseudo first order model is applied with respect to the slope of $\ln(q_e-q_t)$ versus t graph. The correlation coefficients are found as 0.8447 (degradation) and 0.6555 (decolorization) and for 0.5M ZnO-NC2 (300˚C) and 0.9424 (degradation) and 0.9620 (decolorization) for 0.5M ZnO-NC2 (500˚C) (Figure 4.95, Figure 4.96, Figure 4.97 and Figure 4.98).

However, in the case of pseudo second order model, correlation coefficients in the plots of t/q_t versus t are found as 0.2074 (degradation), 0.9823 (decolorization) for 0.5M ZnO-NC2 (300˚C) and 0.9470 (degradation), 0.9207 (decolorization) for 0.5M ZnO-NC2 (500˚C) (Figure 4.99, Figure 4.100, Figure 4.101 and Figure 4.102).

The higher values of the coefficients imply a better adsorption of MO. Accordingly, pseudo-second order model fits to the 0.5M ZnO-NC2 (300˚C), while only a certain extent of adsorption seems to be possible by this model in the presence of 0.5M ZnO-NC2 (500˚C).

4.6.2.2. Adsorption Isotherms. For the adsorption isotherms, Freundlich and Langmuir isotherm models are employed at four different initial concentrations of MO (3.27, 8.17, 16.32 and 24.55 mg/L) in the presence of 0.5M ZnO-NC2 (300˚C) and 0.5M ZnO-NC2 (500˚C).

Freundlich isotherms' line fittings of $\ln q_e$ versus $\ln C_e$ in plots give correlations of 0.8334 (degradation), 0.9117 (decolorization) for 0.5M ZnO-NC2 (300˚C) and 0.9913 (degradation) and 0.9859 (decolorization) for 0.5M ZnO-NC2 (500˚C) (Figure 4.103, Figure 4.104, Figure 4.105 and Figure 4.106).

Langmuir isotherms (q_t versus t plots) of the supported catalysts are illustrated in Figure 4.106, Figure 4.107, Figure 4.108 and Figure 4.109. The line fittings in C_e/q_e versus C_e graphs result in correlation coefficients of 0.0538 (degradation), 0.3795 (decolorization) for 0.5M ZnO-NC2 (300˚C) and 0.4264 (degradation) and 0.7117 (decolorization) for 0.5M ZnO-NC2 (500˚C) (Figure 4.107, Figure 4.108, Figure 4.199 and Figure 4.110 Insets).

Consequently, Freundlich isotherm model fits better to the supported catalysts with higher correlation coefficients.

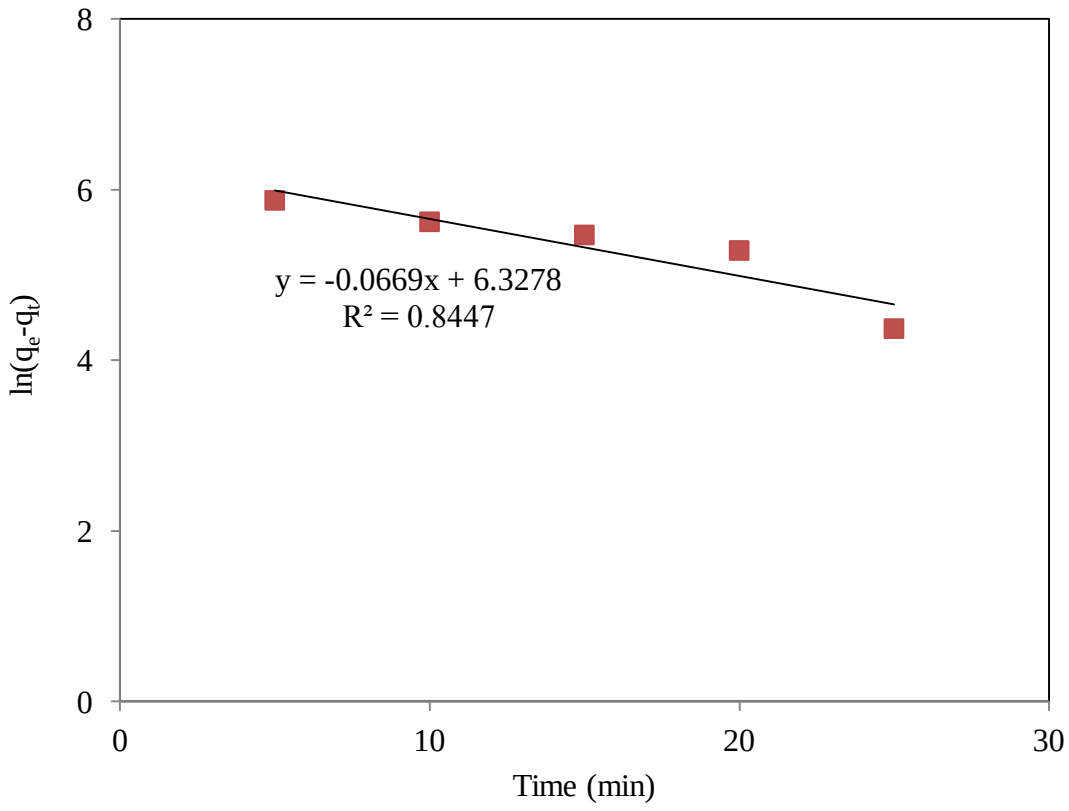


Figure 4.95. Pseudo first order kinetics for degradation of MO in the presence of 0.5M ZnO-NC2 (300˚C). Conditions: pH= 6.5 (Natural), $[MO]_0$= 8.17 mg/L, T= 298 K, Flow rate= 2000 rpm.

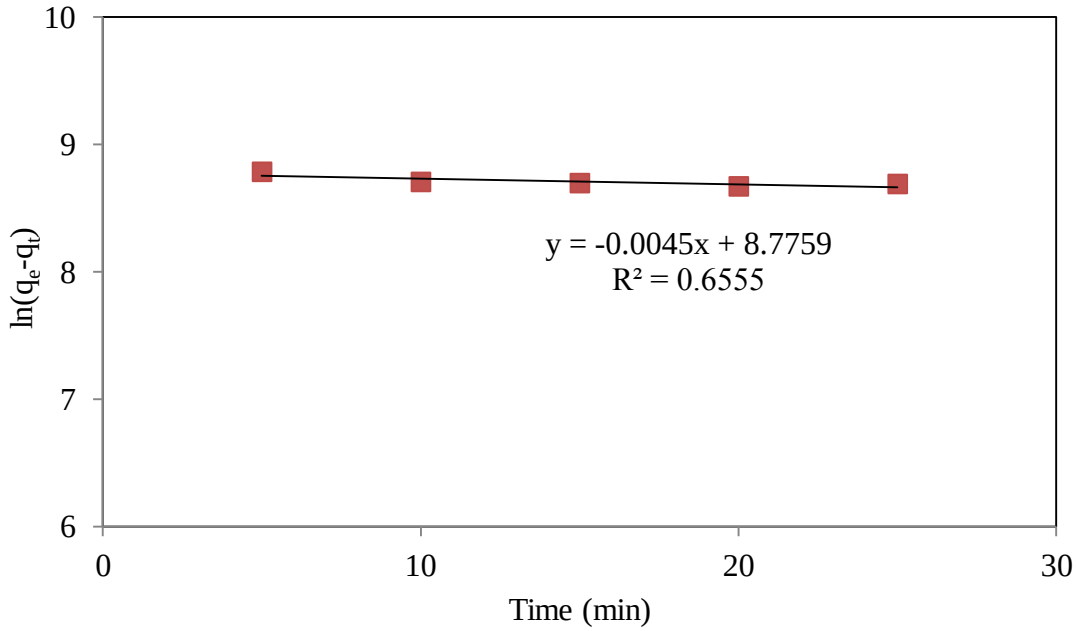


Figure 4.96. Pseudo first order kinetics for decolorization of MO in the presence of 0.5M ZnO-NC2 (300˚C). Conditions: pH= 6.5 (Natural), $[MO]_0$= 8.17 mg/L, T= 298 K, Flow rate= 2000 rpm.

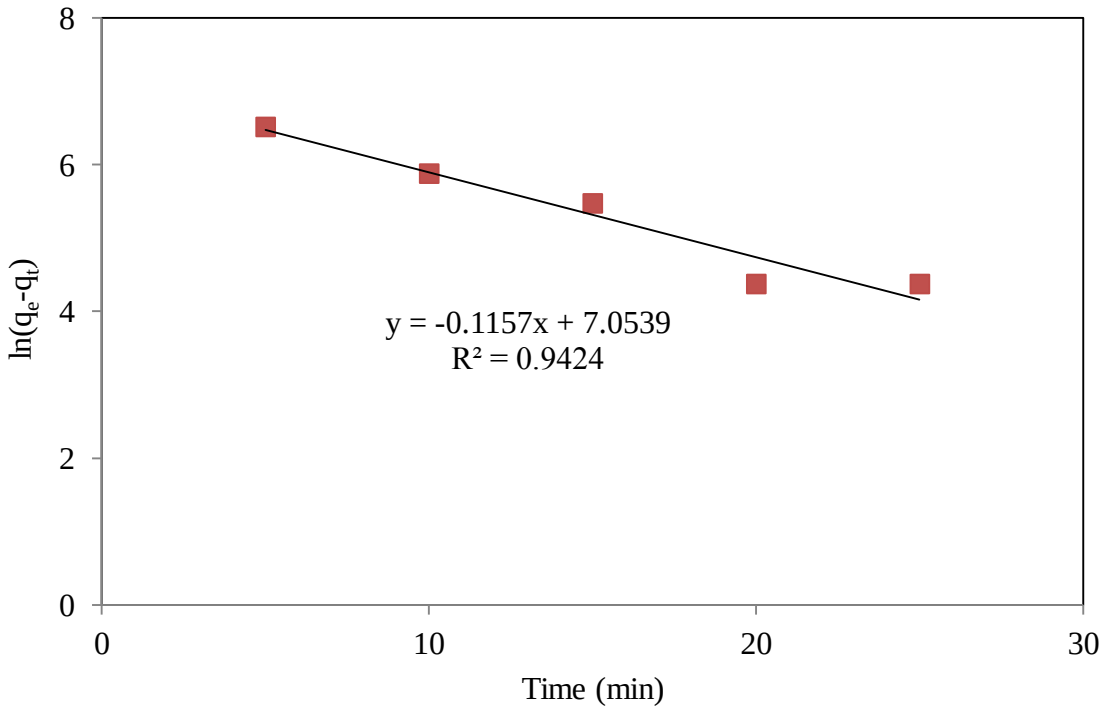


Figure 4.97. Pseudo first order kinetics for degradation of MO in the presence of 0.5M ZnO-NC2 (500˚C). Conditions: pH= 6.5 (Natural), $[MO]_0$= 8.17 mg/L, T= 298 K, Flow rate= 2000 rpm.

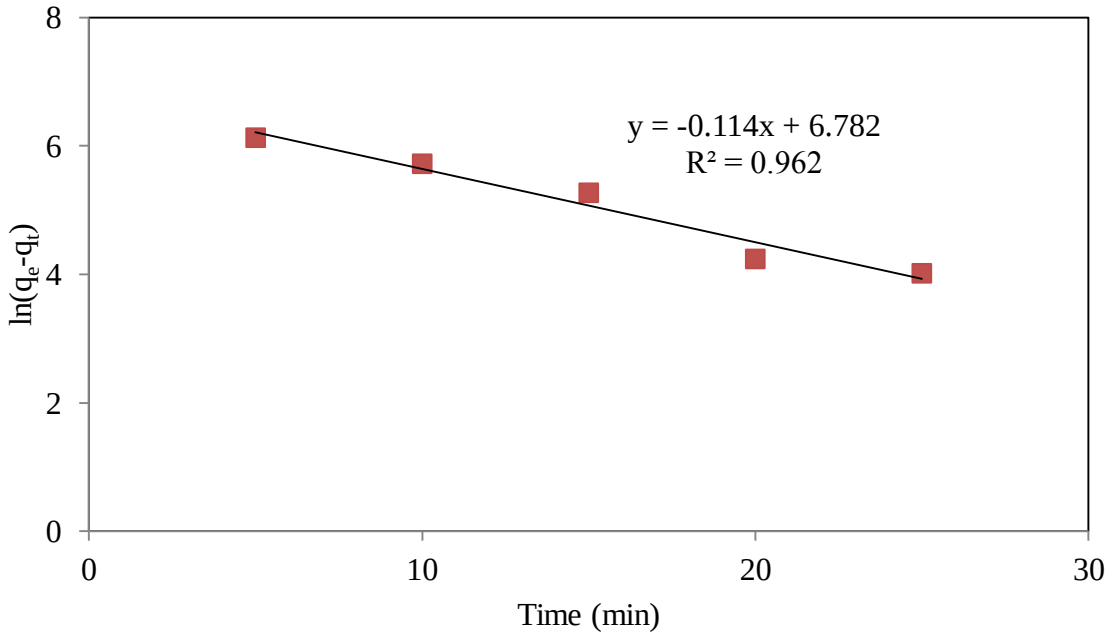


Figure 4.98. Pseudo first order kinetics for decolorization of MO in the presence of 0.5M ZnO-NC2 (500˚C). Conditions: pH= 6.5 (Natural), $[MO]_0$= 8.17 mg/L, T= 298 K, Flow rate= 2000 rpm.

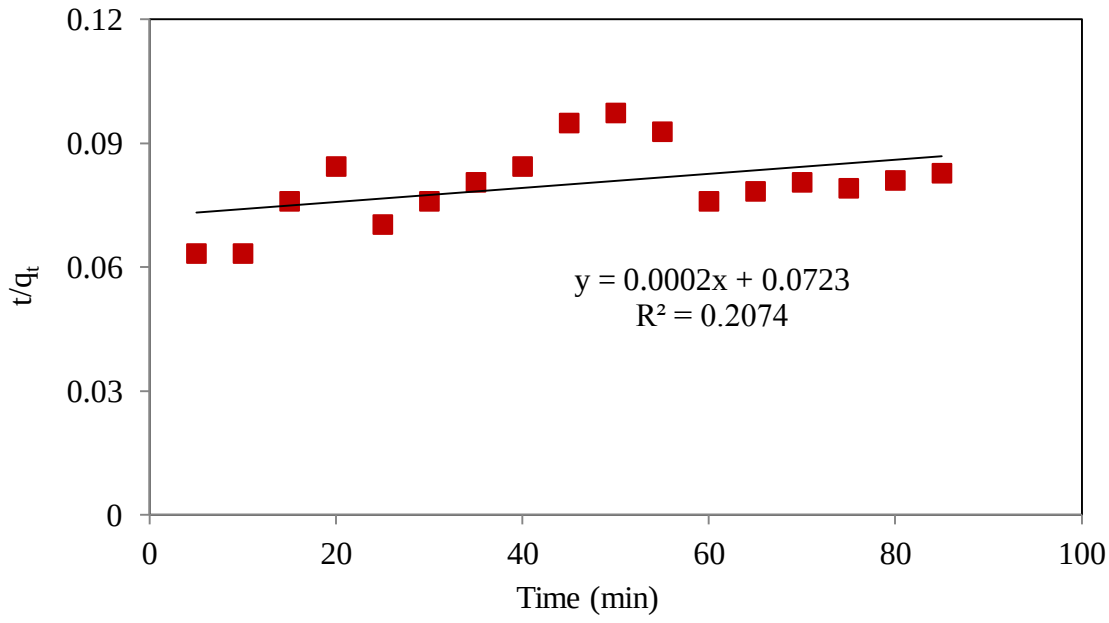


Figure 4.99. Pseudo second order kinetics for degradation of MO in the presence of 0.5M ZnO-NC2 (300˚C). Conditions: pH= 6.5 (Natural), $[MO]_0$= 8.17 mg/L, T= 298 K, Flow rate= 2000 rpm.

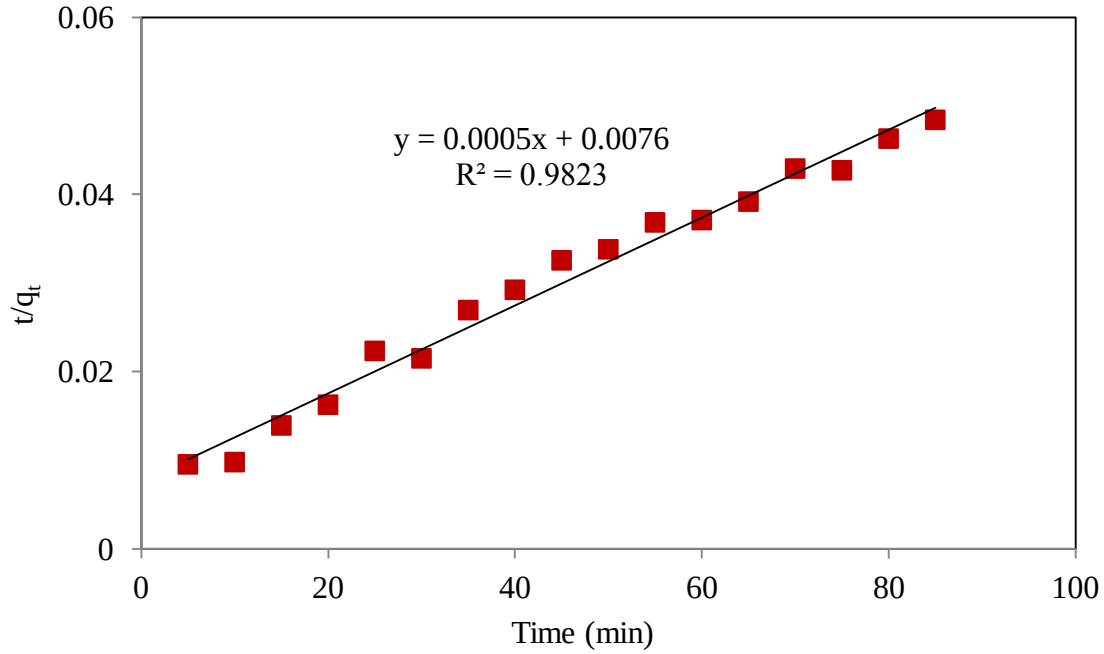


Figure 4.100. Pseudo second order kinetics for decolorization of MO in the presence of 0.5M ZnO-NC2 (300˚C). Conditions: pH= 6.5 (Natural), $[MO]_0$= 8.17 mg/L, T= 298 K, Flow rate= 2000 rpm.

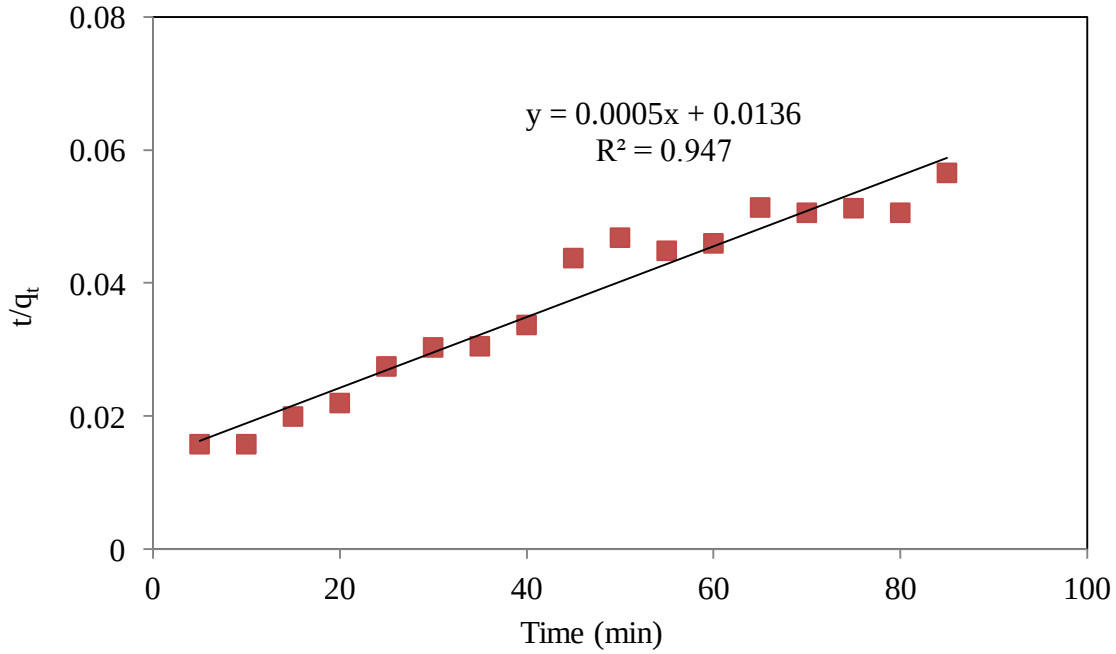


Figure 4.101. Pseudo second order kinetics for degradation of MO in the presence of 0.5M ZnO-NC2 (500˚C). Conditions: pH= 6.5 (Natural), $[MO]_0$= 8.17 mg/L, T= 298 K, Flow rate= 2000 rpm.

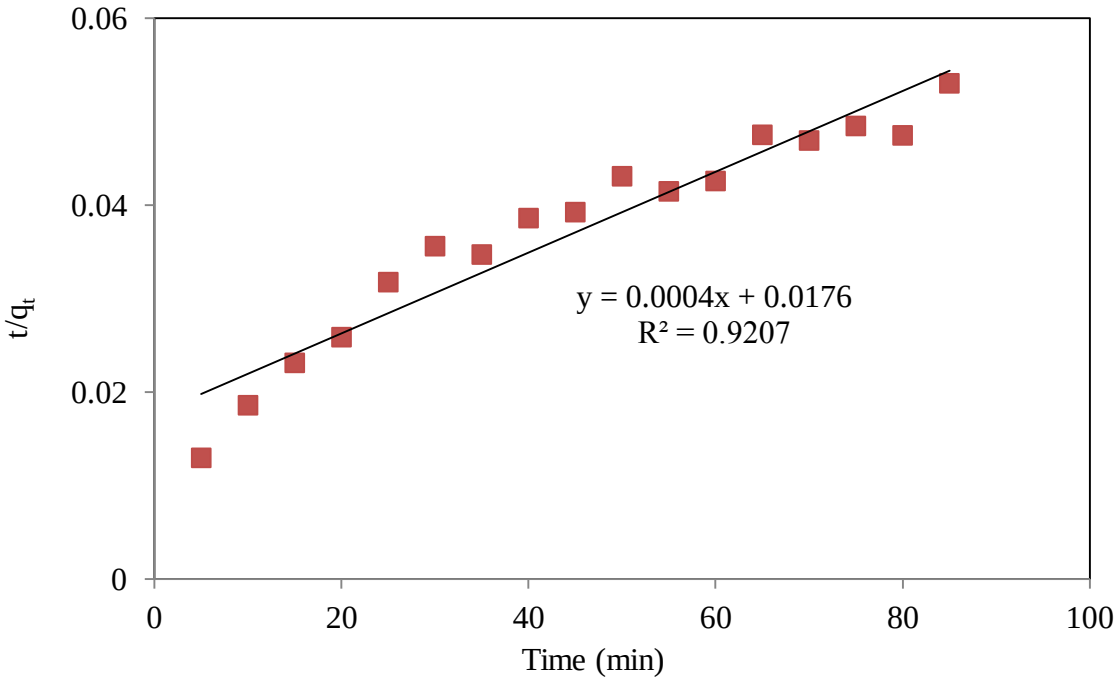


Figure 4.102. Pseudo second order kinetics for decolorization of MO in the presence of 0.5M ZnO-NC2 (500˚C). Conditions: pH= 6.5 (Natural), $[MO]_0$= 8.17 mg/L, T= 298 K, Flow rate= 2000 rpm.

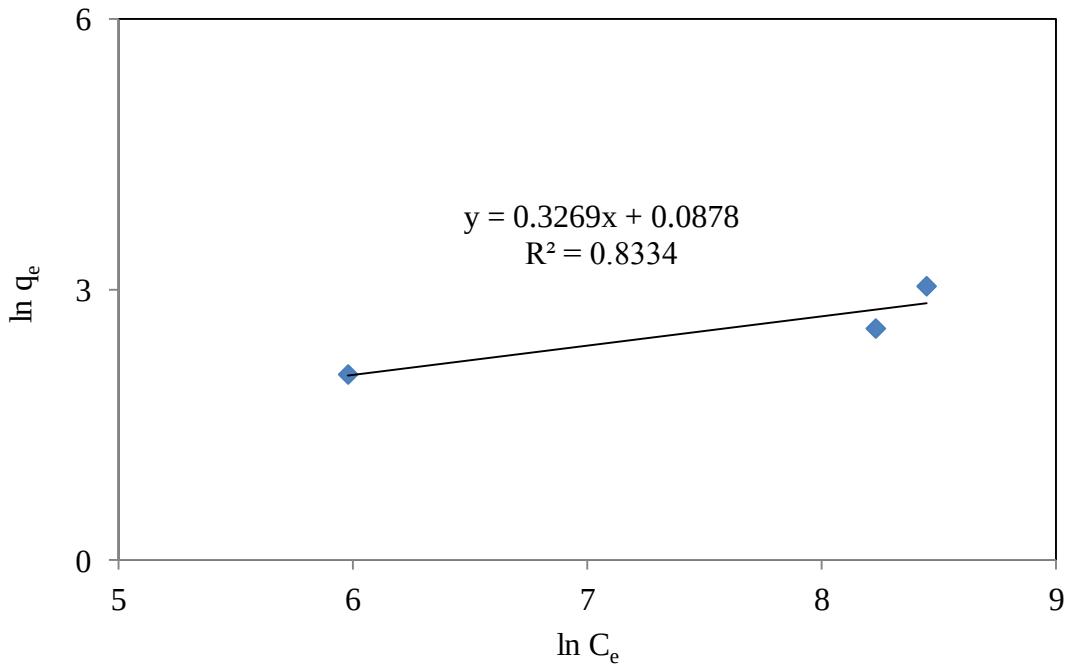


Figure 4.103. Freundlich adsorption isotherm for degradation of MO in the presence of 0.5M ZnO-NC2 (300˚C). Conditions: pH= 6.5 (Natural), T= 298K, Flow rate= 2000 rpm.

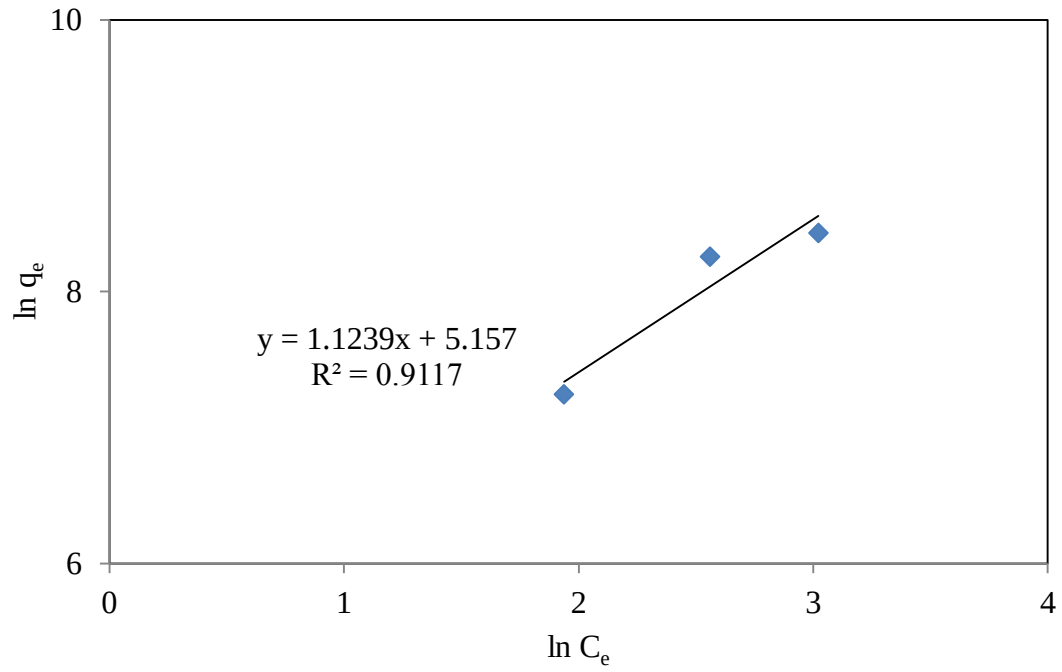


Figure 4.104. Freundlich adsorption isotherm for decolorization of MO in the presence of 0.5M ZnO-NC2 (300˚C). Conditions: pH= 6.5 (Natural), T= 298K, Flow rate= 2000 rpm.

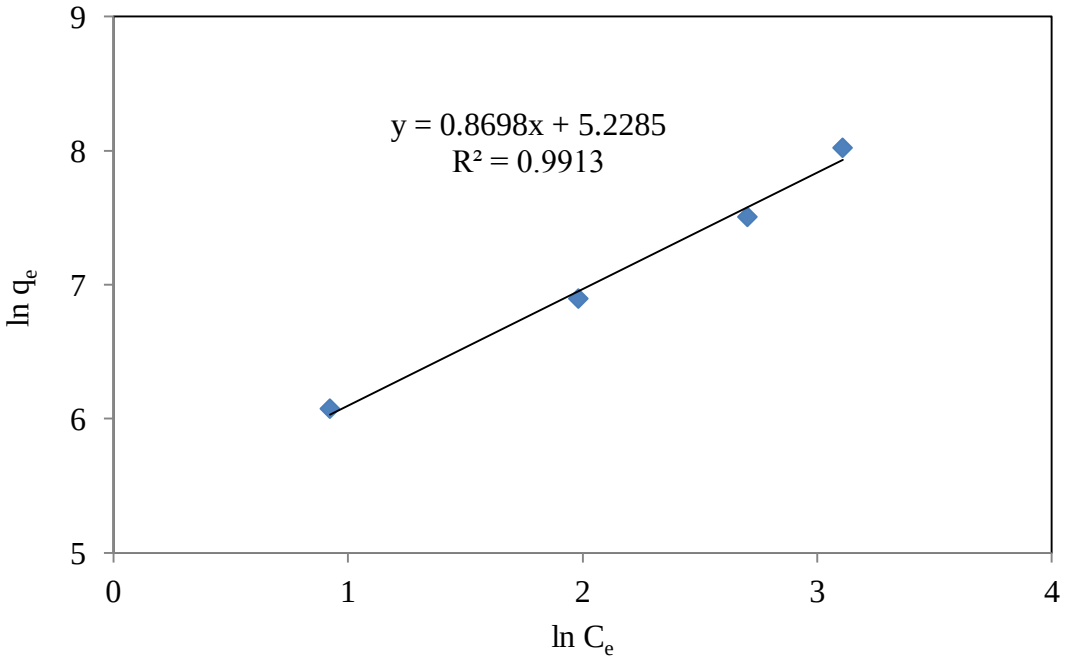


Figure 4.105. Freundlich adsorption isotherm for degradation of MO in the presence of 0.5M ZnO-NC2 (500˚C). Conditions: pH= 6.5 (Natural), T= 298K, Flow rate= 2000 rpm.

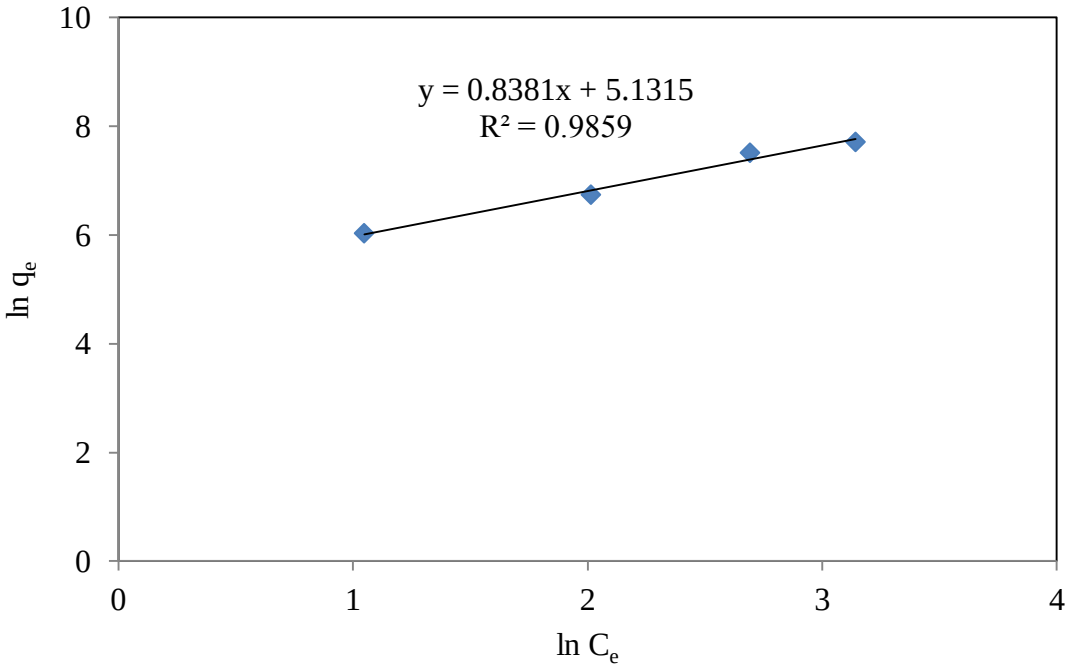


Figure 4.106. Freundlich adsorption isotherm for decolorization of MO in the presence of 0.5M ZnO-NC2 (500˚C). Conditions: pH= 6.5 (Natural), T= 298K, Flow rate= 2000 rpm.

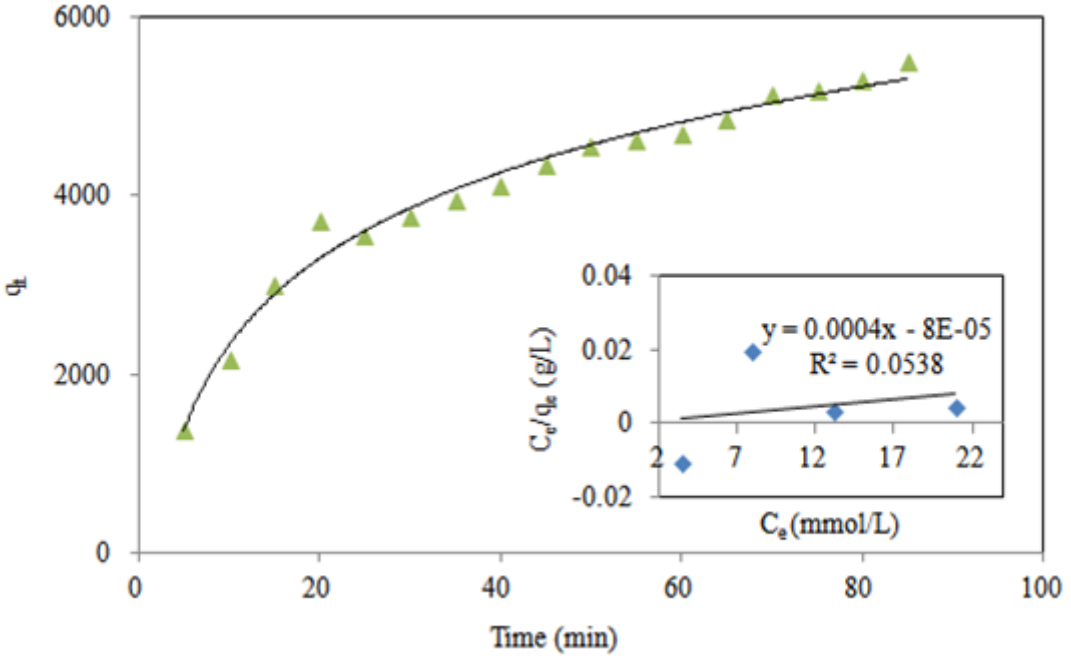


Figure 4.107. Langmuir adsorption isotherm for degradation of MO in the presence of 0.5M ZnO-NC2 (300˚C). Inset: C_e/q_e vs. C_e plot. Conditions: pH= 6.5 (Natural), T= 298K, Flow rate= 2000 rpm.

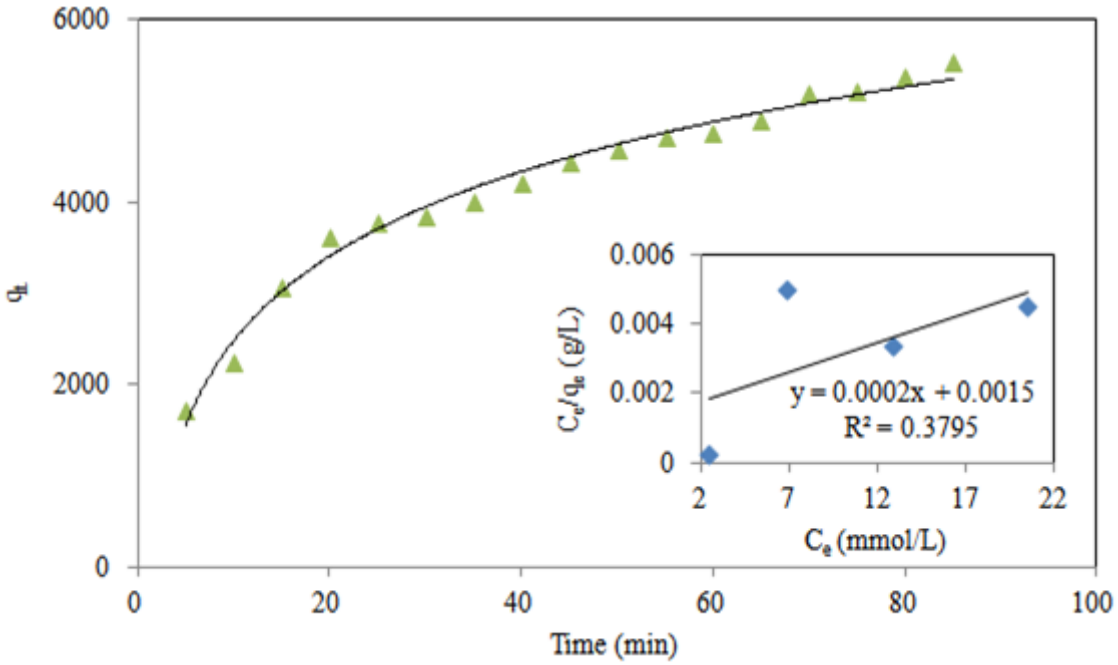


Figure 4.108. Langmuir adsorption isotherm for decolorization of MO in the presence of 0.5M ZnO-NC2 (500˚C). Inset: C_e/q_e vs. C_e plot. Conditions: pH= 6.5 (Natural), T= 298K, Flow rate= 2000 rpm.

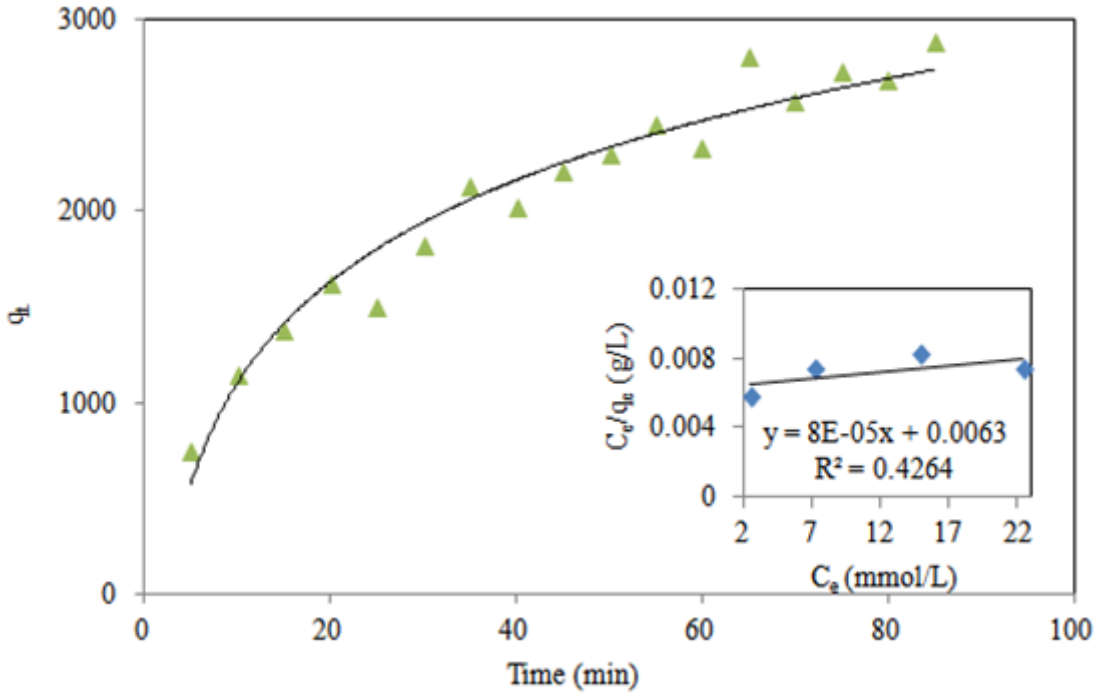


Figure 4.109. Langmuir adsorption isotherm for degradation of MO in the presence of 0.5M ZnO-NC2 (500˚C). Inset: C_e/q_e vs. C_e plot. Conditions: pH= 6.5 (Natural), T= 298K, Flow rate= 2000 rpm.

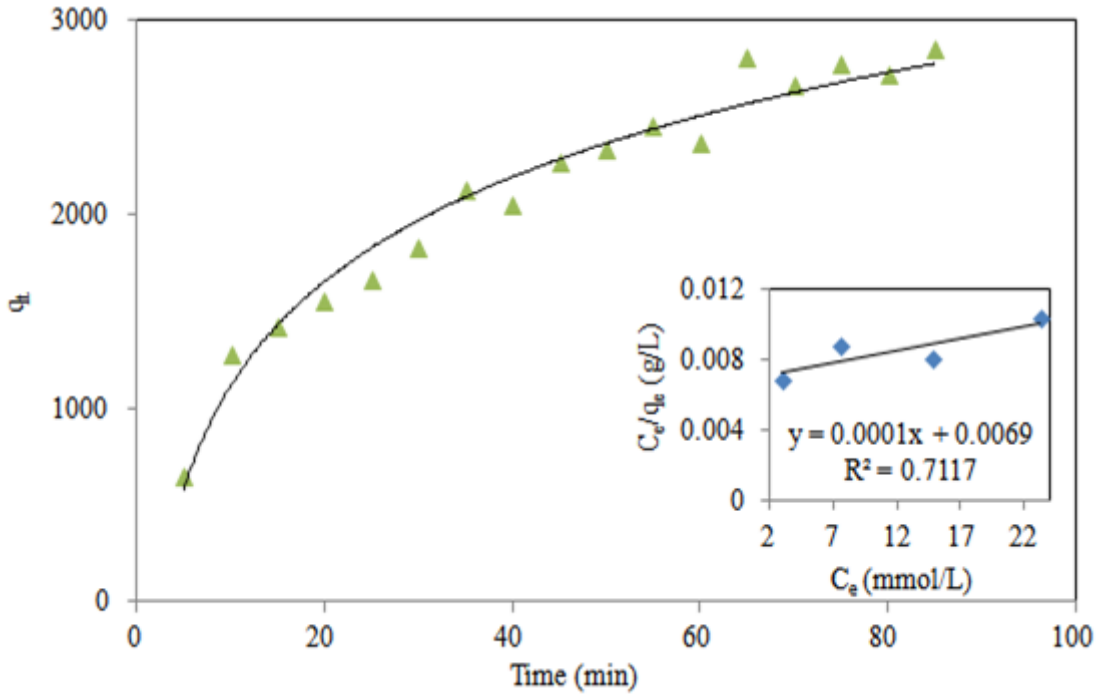


Figure 4.110. Langmuir adsorption isotherm for decolorization of MO in the presence of 0.5M ZnO-NC2 (500˚C). Inset: C_e/q_e vs. C_e plot. Conditions: pH= 6.5 (Natural), T= 298K, Flow rate= 2000 rpm.

4.6.3. Photocatalytic Experiments

4.6.3.1. Effect of ZnO Loading. The photocatalytic reactions are carried out in the existence of supported catalysts loaded with different ZnO concentrations. Following 30 min dark experiments, the remaining concentrations of MO in solutions are controlled about 85 min (Figure 4.111, Figure 4.112, Figure 4.113 and Figure 4.114).

For both degradation and decolorization processes, ZnO loading concentrations negatively affect the photocatalytic activity of the supported catalysts prepared at 300˚C, due to reduction of adsorption capability (Figure 4.111 and Figure 4.112). On the other hand, for both degradation and decolorization processes, ZnO loading concentrations positively affect the photocatalytic activity of the supported catalysts prepared at 500˚C (Figure 4.113 and Figure 4.114). 0.5M ZnO-NC2 (500˚C) shows the best activity and this demonstrates the consistency with the XRD analysis where the highest crystalline order of ZnO nanoparticles is achieved in the presence of 0.5M ZnO-NC2 (500˚C).

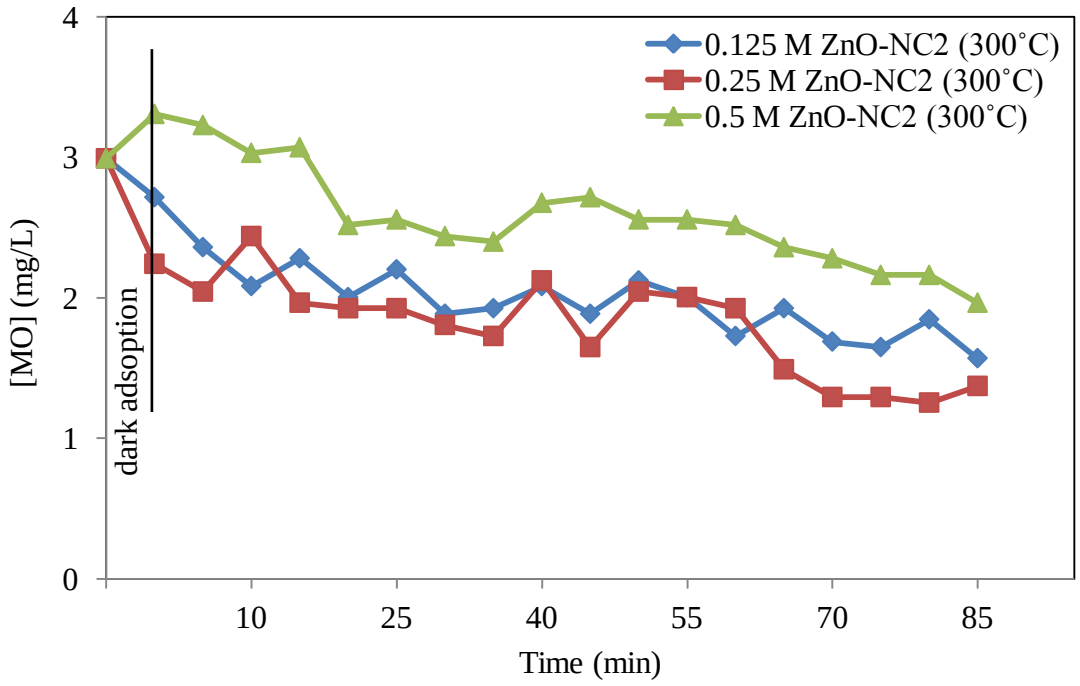


Figure 4.111. MO degradation in the presence of supported catalysts prepared at 300˚C. Conditions: pH= 6.5 (Natural), $[MO]_0$= 3.27 mg/L, T= 298 K, Flow rate= 2000 rpm.

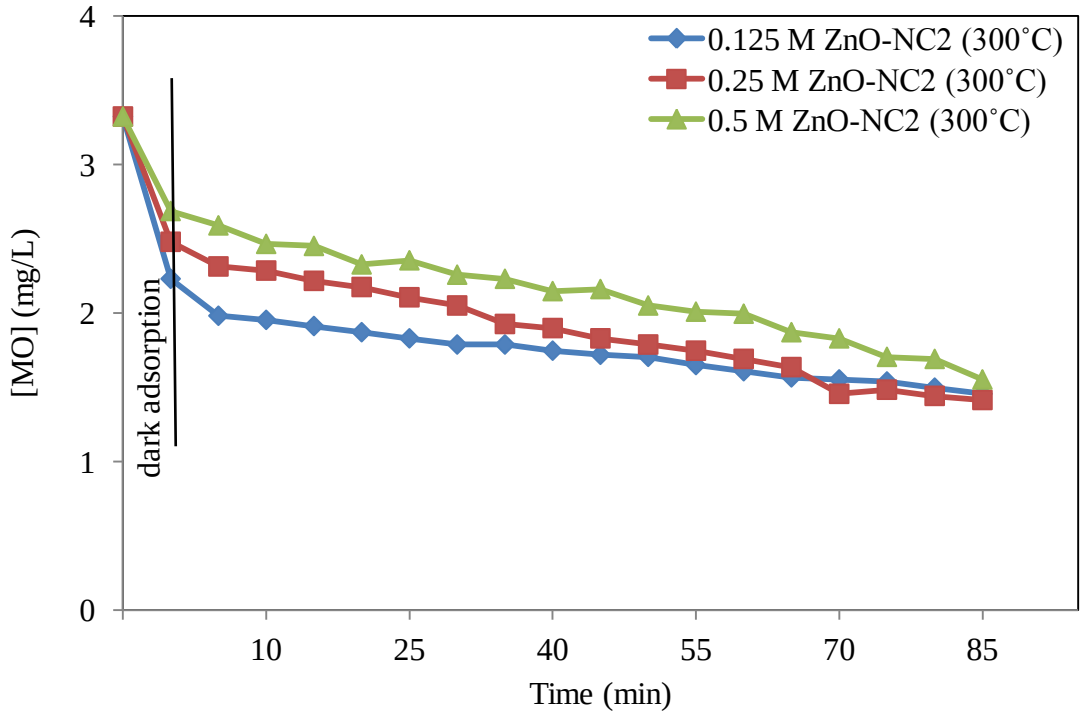


Figure 4.112. MO decolorization in the presence of supported catalysts prepared at 300˚C. Conditions: pH= 6.5 (Natural), $[MO]_0$= 3.27 mg/L, T= 298 K, Flow rate= 2000 rpm.

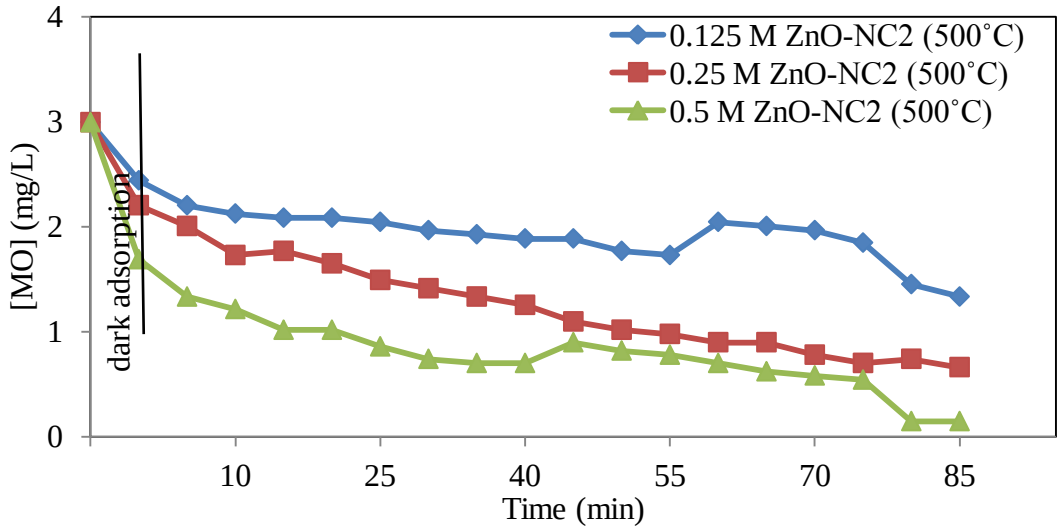


Figure 4.113. MO degradation in the presence of supported catalysts prepared at 500˚C. Conditions: pH= 6.5 (Natural), $[MO]_0$= 3.27 mg/L, T= 298 K, Flow rate= 2000 rpm.

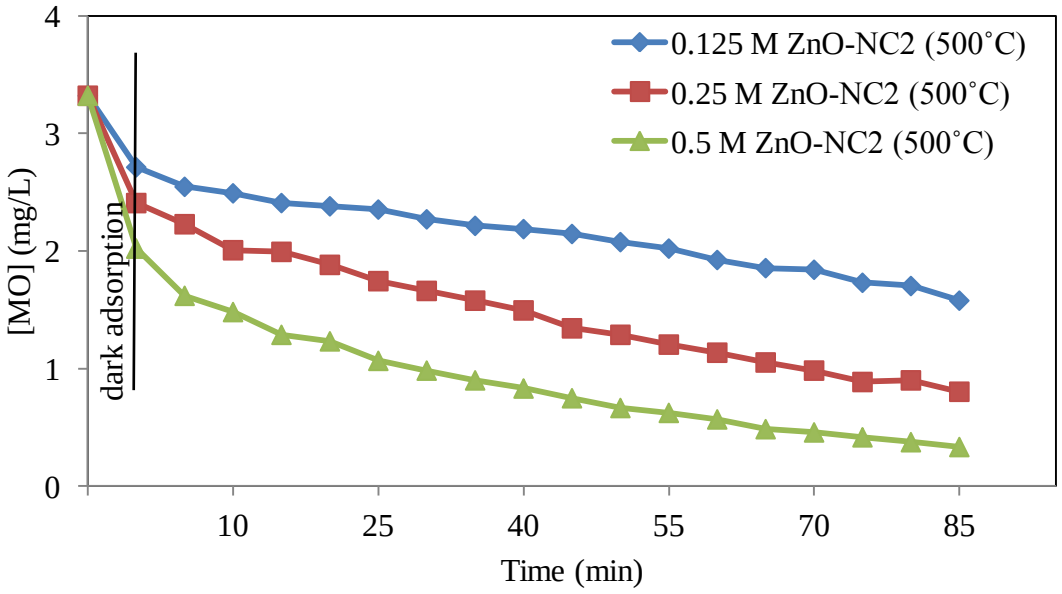


Figure 4.114. MO decolorization in the presence of supported catalysts prepared at 500˚C. Conditions: pH= 6.5 (Natural), $[MO]_0$= 3.27 mg/L, T= 298 K, Flow rate= 2000 rpm.

4.6.3.2. Effect of Initial MO Concentration. The influence of the initial MO concentration varying from 3.27 to 24.55 mg/L on the photocatalytic rates is also investigated in the presence of 0.5M ZnO-NC2 (300˚C) and 0.5M ZnO-NC2 (500˚C). For all concentrations, the best degradation and decolorization performances are obtained in the presence of 0.5M ZnO-NC2 (500˚C) (Figure 4.115 and Figure 4.116). Pseudo first order kinetic model is confirmed according to the linearity noticed in the plots of ln (C_0/C) versus t (time) for all

concentrations. (Figure 4.117, Figure 4.118, Figure 4.119 and Figure 4.120). As a general trend, the efficiency of both decolorization and degradation processes is found to decrease with increasing concentration of MO (Table 4.11 and Table 4.12). This can be a result of blocking of the photocatalytically active sites on the supported catalyst and reducing the interaction of photons with these sites.

Langmuir-Hinshelwood kinetic model analysis gives linearity in the plot of reciprocal rate (1/R) against reciprocal of MO concentrations ($1/C_0$) (Figure 4.117, Figure 4.118, Figure 4.119 and Figure 4.120 Inset).

In the presence of 0.5M ZnO-NC2 (300˚C), the values of adsorption coefficient (K) and reaction rate constant (k) are found to be 0.016 L/mg and 0.041 mg/L min (degradation) and 0.011 L/mg and 0.050 mg/L min (decolorization). 0.5M ZnO-NC2 (500˚C) gives higher K and k values. 0.061 L/mg and 0.053 mg/L min (for degradation) and, 0.056 L/mg and 0.069 mg/L min (for decolorization) demonstrating a higher adsorption capacity and hence degradation-decolorization ability.

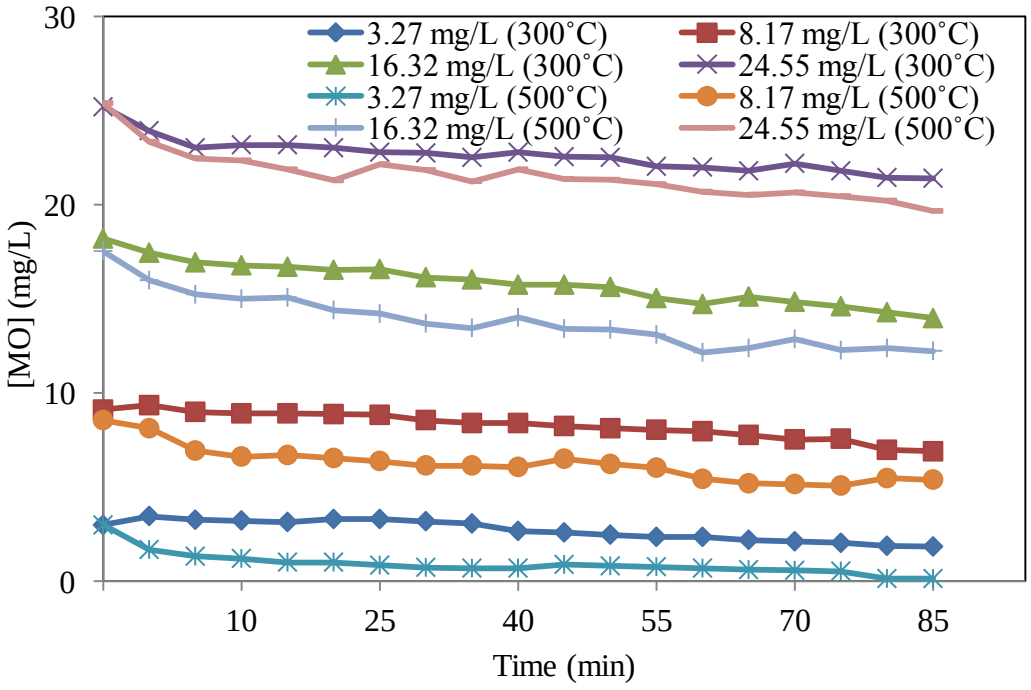


Figure 4.115. MO degradation at initial MO concentrations in the presence of 0.5M ZnO-NC2 (300˚C) and 0.5M ZnO-NC2 (500˚C).Conditions: pH=6.5 (Natural), T= 298 K, Flow rate= 2000 rpm.

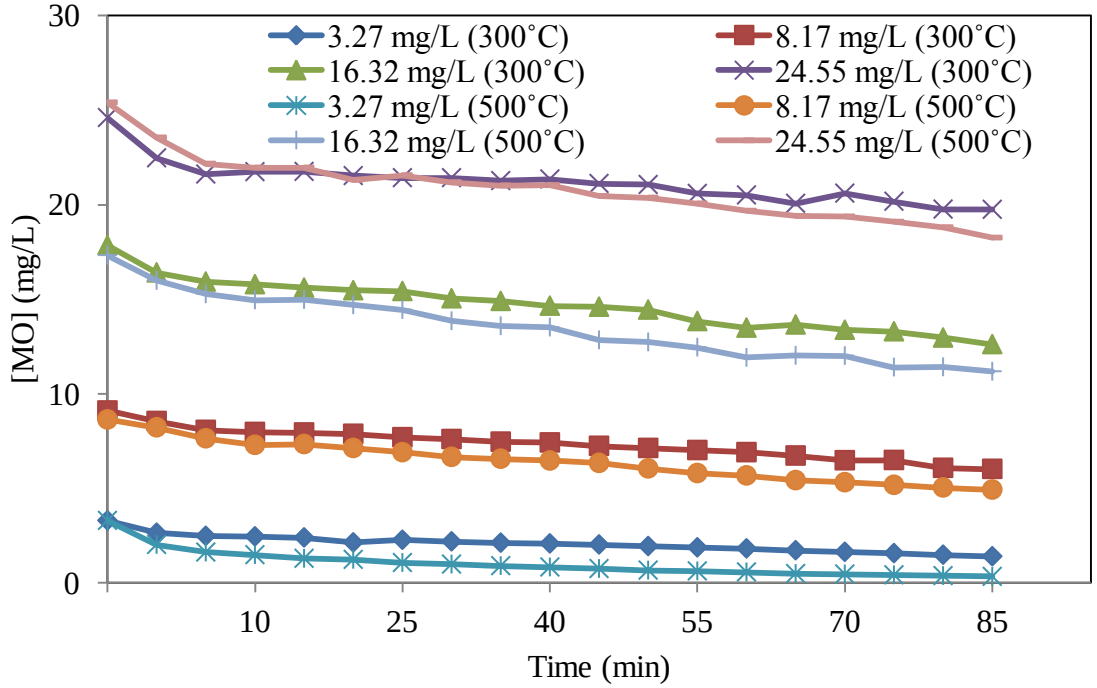


Figure 4.116. MO decolorization at initial MO concentrations in the presence of 0.5M ZnO-NC2 (300˚C) and 0.5M ZnO-NC2 (500˚C).Conditions: pH= 6.5 (Natural), T= 298 K, Flow rate= 2000 rpm.

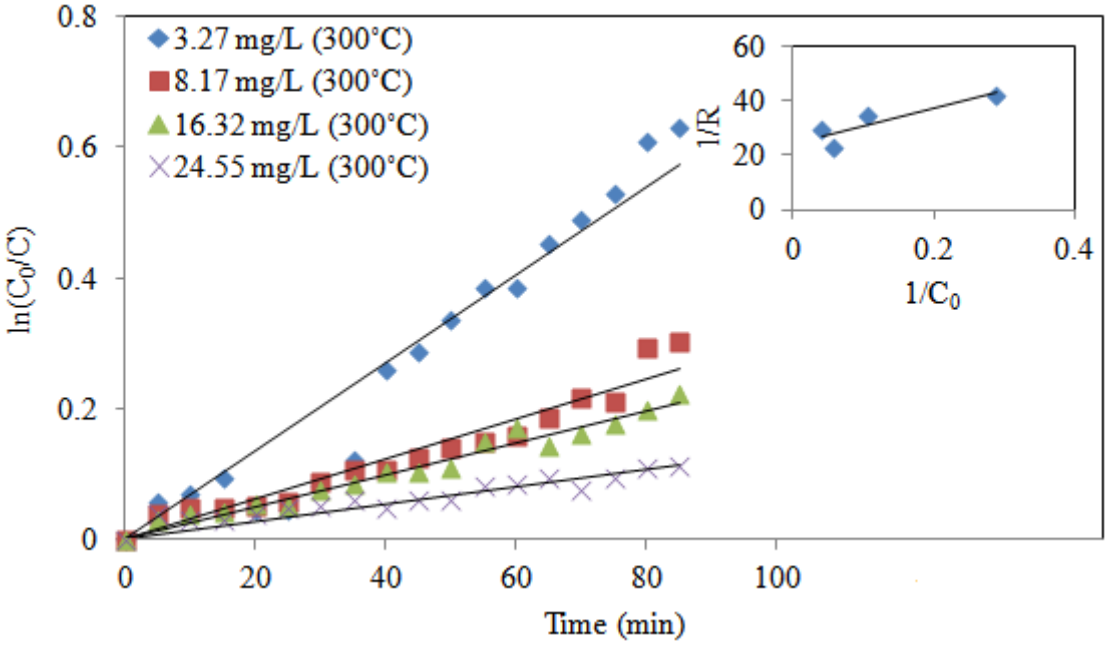


Figure 4.117. Pseudo-first order kinetics for degradation of MO in the presence of 0.5M ZnO-NC2 (300˚C). Inset: Langmuir-Hinshelwood analysis. Conditions: pH= 6.5 (Natural), T= 298 K, Flow rate= 2000 rpm.

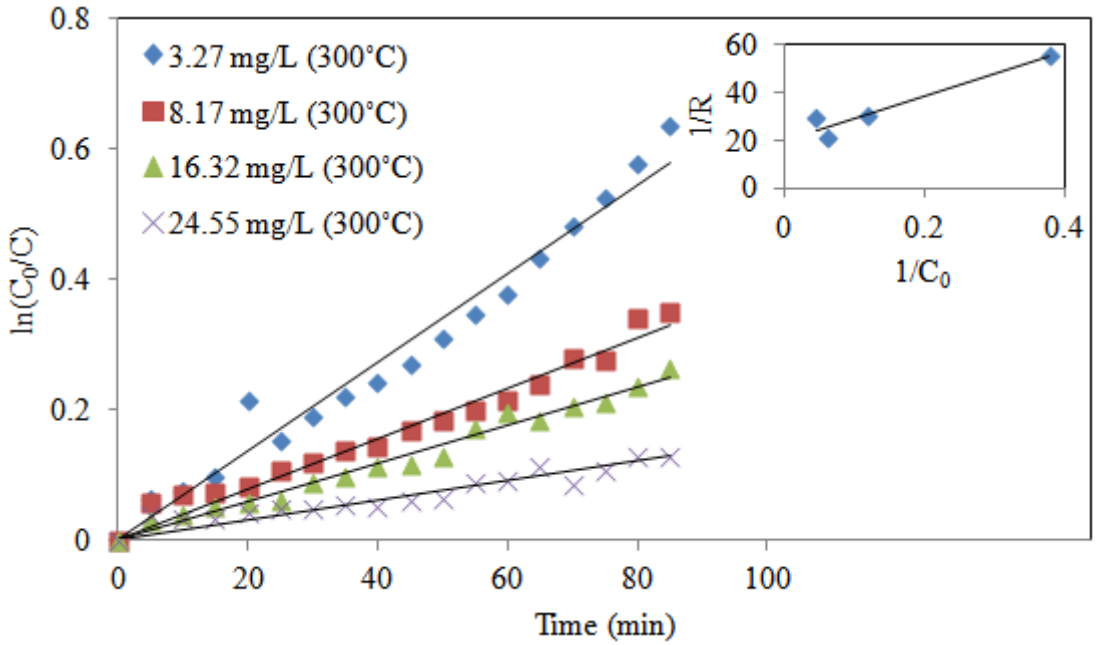


Figure 4.118. Pseudo-first order kinetics for decolorization of MO in the presence of 0.5M ZnO-NC2 (300˚C). Inset: Langmuir-Hinshelwood analysis. Conditions: pH=6.5 (Natural), T= 298 K, Flow rate= 2000 rpm.

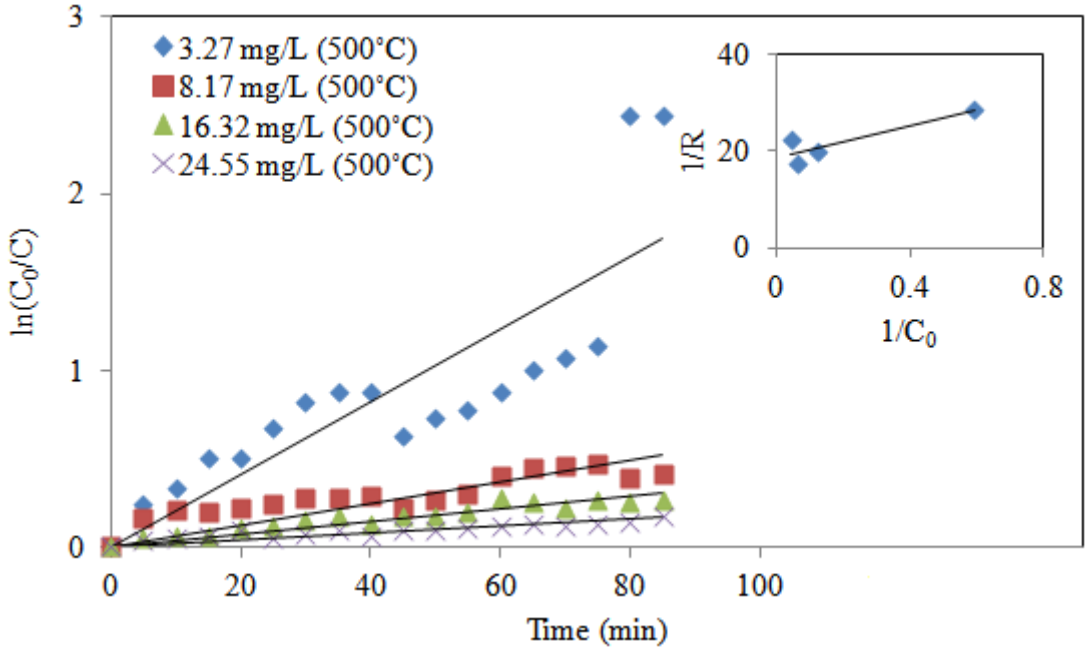


Figure 4.119. Pseudo-first order kinetics for degradation of MO in the presence of 0.5M ZnO-NC2 (500˚C). Inset: Langmuir-Hinshelwood analysis. Conditions: pH= 6.5 (Natural), T= 298 K, Flow rate= 2000 rpm.

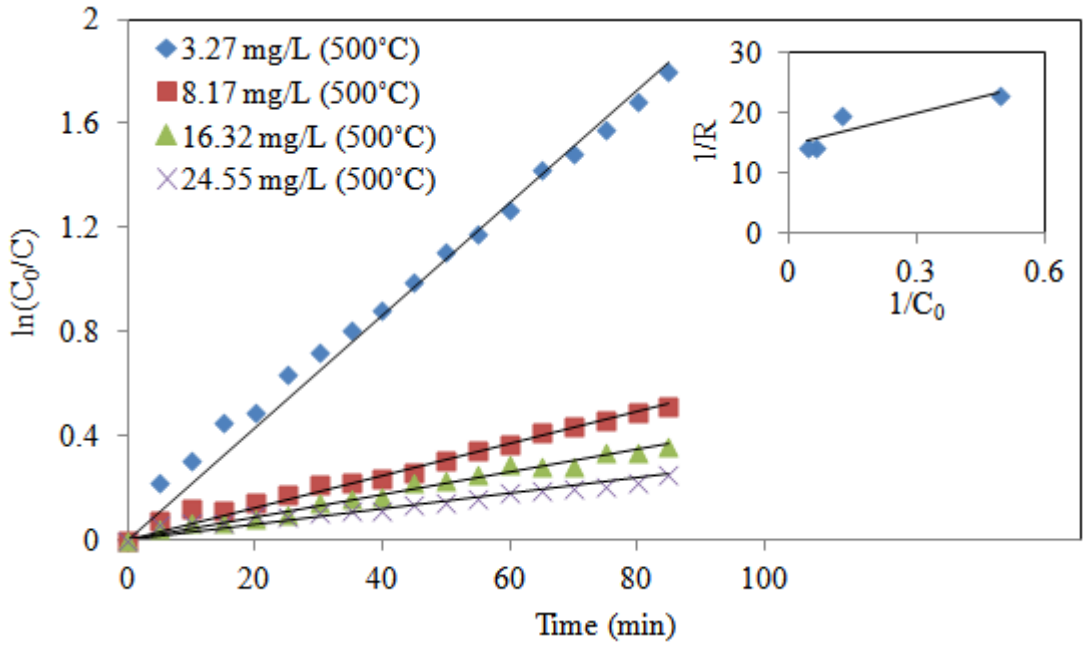


Figure 4.120. Pseudo-first order kinetics for decolorization of MO in the presence of 0.5M ZnO-NC2 (500˚C). Inset: Langmuir-Hinshelwood analysis. Conditions: pH= 6.5 (Natural), T= 298 K, Flow rate= 2000 rpm.

Table 4.11. Rate constants (k) and linear regression values (R) for the degradation and decolorization processes of the different initial concentrations of MO in the presence of 0.5M ZnO-NC2 (300˚C).

	k (min^{-1})		**R**	
[MO] (mg/L)	**degradation**	**decolorization**	**degradation**	**decolorization**
24.55	0.0014	0.0015	0.815	0.883
16.32	0.0025	0.0029	0.968	0.981
8.17	0.0031	0.0039	0.942	0.967
3.27	0.0068	0.0068	0.921	0.969

Table 4.12. Rate constants (k) and linear regression values (R) for the degradation and decolorization processes of the different initial concentrations of MO in the presence of 0.5M ZnO-NC2 (500˚C).

	k (min^{-1})		**R**	
[MO] (mg/L)	**degradation**	**decolorization**	**degradation**	**decolorization**
24.55	0.0019	0.0030	0.773	0.905
16.32	0.0036	0.0044	0.871	0.982
8.17	0.0061	0.0062	0.563	0.980
3.27	0.0206	0.0216	0.689	0.986

4.7. Characterization Results of the ZnO-MMT2 Catalysts

4.7.1. XRD Analysis

XRD spectrums of bare MMT2, 0.125M ZnO-MMT2 (300˚C), 0.25M ZnO-MMT2 (300˚C), 0.5M ZnO-MMT2 (300˚C), 0.125M ZnO-MMT2 (500˚C), 0.25M ZnO-MMT2 (500˚C) and 0.5M ZnO-MMT2 (500˚C) catalysts are shown in Figure 4.121 and 4.122. Bare MMT2, due to the organic modification, shows the characteristic (001) reflection at 2.6˚ (2θ) with a d-spacing value 34.2 Å. This value is increased in comparison to the MMT's d-spacing (12.8 Å) noticed at 7.04˚ (2θ) being in consistency with the study of Ha et. al. [77]. Also small (101) and (107) reflections of quartz and crystoballite are detected at 19.9˚ and 35.3˚ (2θ), respectively.[78, 79]. In the XRD patterns of supported catalysts, characteristic reflection peak of MMT2 (2.6˚ (2θ)) is not detected. This may imply destruction of neat oriented layers. Nevertheless, there can be still space among the layers. For the catalysts prepared at 300˚C, the peak at 8.2˚ (2θ) refers to the formation of tactoids, suggesting an immiscible dispersion of destructed layers [80]. The distinctive ZnO peak (101) is observed at 36.4^{o} (2θ). Also other reflections of (100), (002), (102), (110), (103) and (200) are detected at 31.9˚, 34.6˚, 47.7˚, 56.7˚, 63.1˚, and 66.6˚ (2θ) respectively. The extinction of intensities at the MMT2 diffraction peaks with the increment in the

reflections of ZnO peaks suggests that ZnO nanoparticles uniformly distributed on the MMT2 surface.

The crystalline sizes of ZnO nanoparticles (D_{ZnO}), based on the broadening of the most intense (101) diffraction at 36.4˚ (2θ), are calculated by employing Scherrer's equation (Table 4.13). For the catalysts calcinated at 300^{o}C, ZnO crystal sizes are almost similar. For the catalysts calcinated at 500˚C, tactoid formation is not detected. This may enhance the adsorption possibility and hence, accumulation of ZnO nanoparticles on the surface of the MMT2 support. Accordingly, ZnO crystal sizes increase from 0.125M ZnO-MMT2 (500˚C) to 0.5M ZnO-MMT2 (500˚C).

Table 4.13. Crystalline sizes (D), surface areas (BET), pore volumes (V_{pore}) and pore radius (r_{pore}).of 0.25M ZnO and supported catalysts.

Catalyst	**2θ (˚)**	**D (nm)**	**BET (m^2/g)**	**V_{pore} (cm^3/g)**	**r_{pore} (Å)**
0.25M ZnO (500^{o}C)	36.4	15.2	7.6	0.013	17.8
MMT2	2.6	-	7.7	0.018	15.8
0.125M ZnO-MMT2 (300^{o}C)	36.4	15.1	30.0	0.051	15.7
0.25M ZnO-MMT2 (300^{o}C)	36.4	15.2	31.6	0.054	16.4
0.5M ZnO-MMT2 (300^{o}C)	36.4	15.5	30.7	0.052	15.9
0.125M ZnO-MMT2 (500^{o}C)	36.4	17.5	32.1	0.040	15.0
0.25M ZnO-MMT2 (500^{o}C	36.4	19.3	25.3	0.033	14.9
0.5M ZnO-MMT2 (500^{o}C)	36.4	22.6	11.8	0.012	15.1

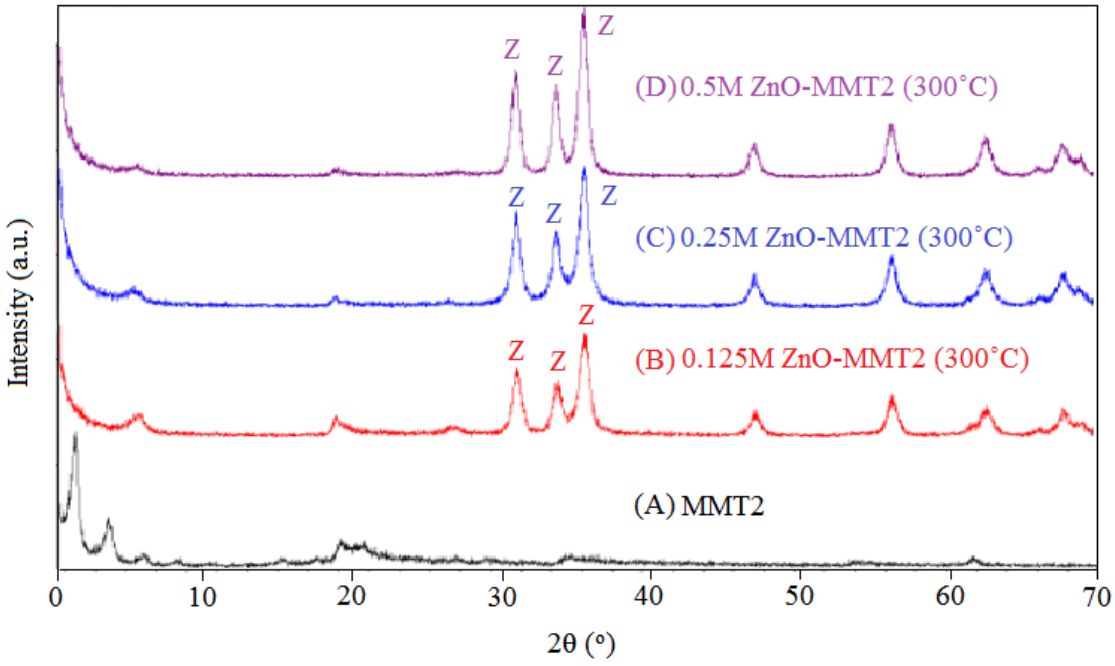


Figure 4.121. XRD patterns of MMT2 (A) and supported catalysts (300˚C) (B-D). (Z: ZnO).

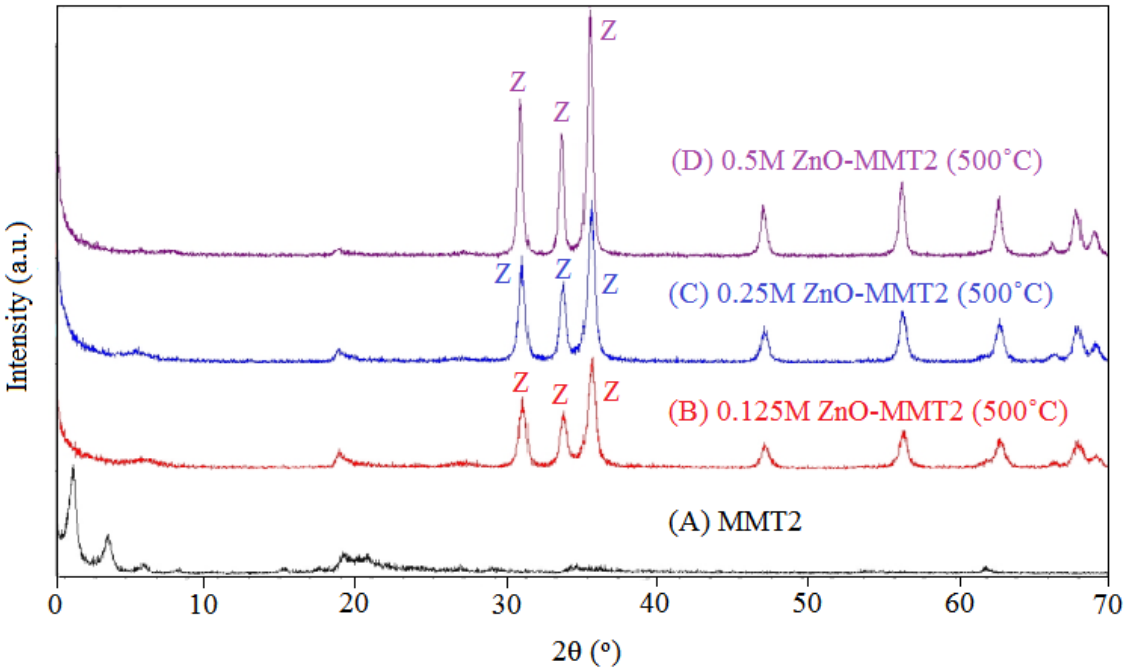


Figure 4.122. XRD patterns of MMT2 (A) and supported catalysts (500˚C) (B-D). (Z: ZnO).

4.7.2. SEM-EDX Analysis

Surface morphologies of the bare MMT2 and 0.25M ZnO-MMT2 (500˚C) are investigated by SEM (EDX) analysis. Bare MMT2 has a clear curly flake-like structure (Figure 4.123) and based on the EDX analysis it consists of major Si, Al, O elements and minor Fe, Mg, K, Na, K and Ca elements (Table 4.14). For 0.25M ZnO-MMT2 (500˚C), Zn and O elemental compositions are noticeable.

SEM micrograph and mapping images of the 0.25M ZnO-MMT2 (500˚C) are shown in the Figure 4.124. Although the structure of MMT2 is retained following the ZnO treatment, homogenously distributed ZnO nanoparticles over the surface of the support are detected. This is also evidenced in the EDX data (Table 4.14). Moreover, MMT2 has no Zn, 0.25M ZnO-MMT2 (500˚C) shows 41.83% Zn component. The reduction in the silica and alumina percentages may also correspond to the location of ZnO nanoparticles in the silica matrix of the clay.

Table 4.14. Elemental composition of MMT2 and 0.25M ZnO-MMT2 (500˚C).

	0.25M ZnO	**MMT2**	**0.25M ZnO-MMT2 (500˚C)**
Components	**Wt %**	**Wt %**	**Wt %**
Zn	88.79	-	41.83
Si	-	39.27	22.08
O	11.21	27.73	21.65
Al	-	22.38	8.75
Mg	-	5.76	4.20
Fe	-	3.08	1.49
Na	-	1.79	-

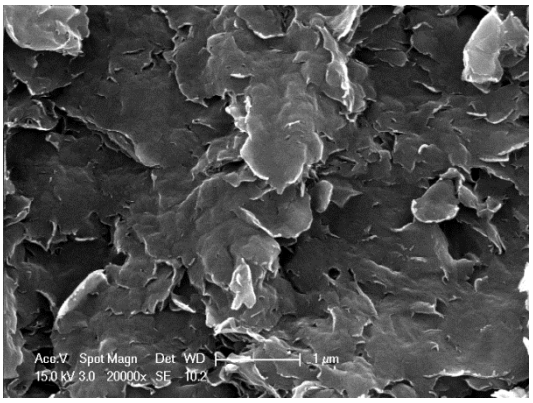


Figure 4.123. SEM image of MMT2.

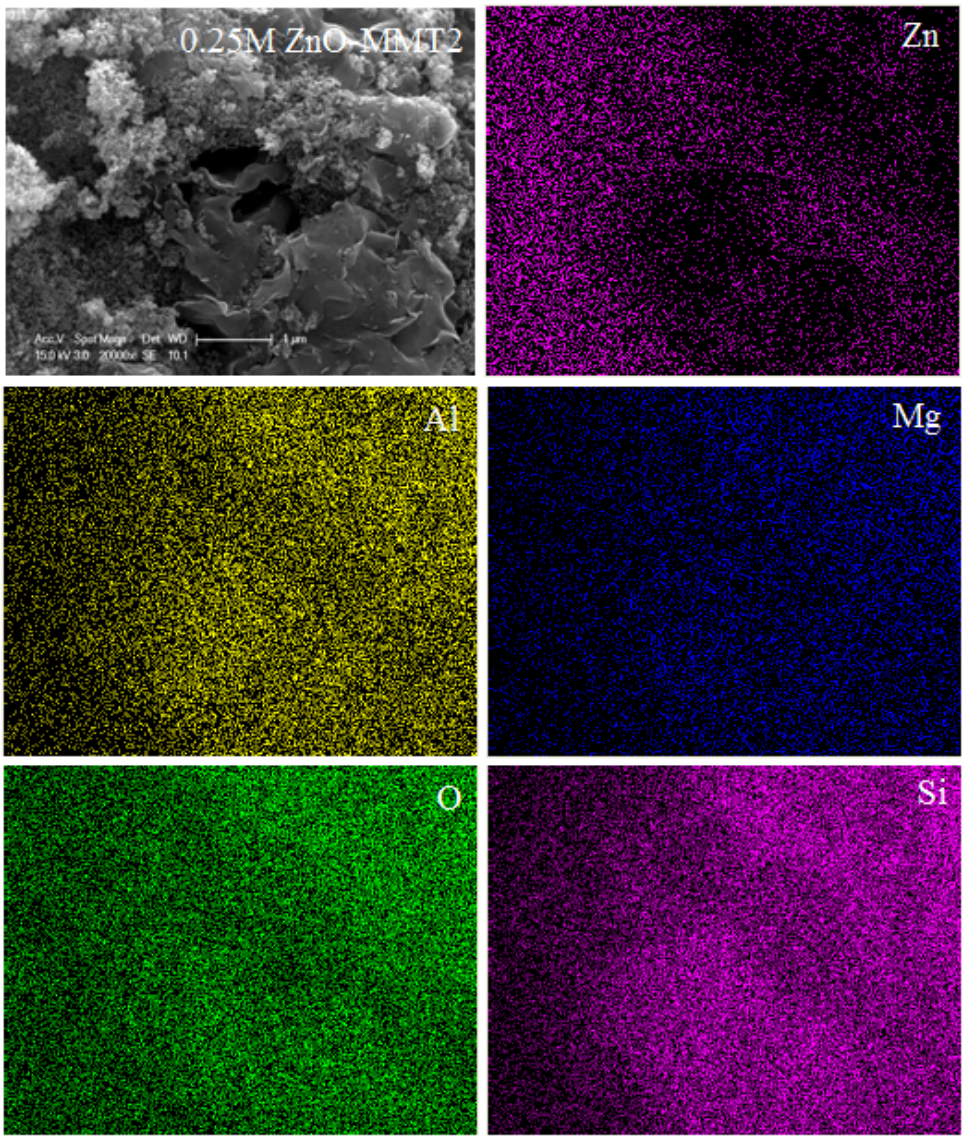


Figure 4.124. SEM image of 0.25M ZnO-MMT2 (500˚C) and mapping images of 0.25M ZnO-MMT2 (500˚C), Zn, Al, Mg, O and Si.

4.7.3. Nitrogen Adsorption-Desorption Isotherms

Nitrogen adsorption-desorption isotherms and pore size distribution plots of the MMT2 and supported catalysts are illustrated in Figure 4.125, Figure 4.126, Figure 4.127 and Figure 4.128. MMT2 and supported catalysts exhibits Type IV isotherms, owing to their mesoporous structure. On the other hand, the increment in the loading concentration of ZnO narrows the hysteresis loops. The pore size distribution curves display that the pores of the supported catalysts exist in the typical mesoporous region of 20-40 Å (Figure 4.125 and Figure 4.126). In comparison to the raw MMT2, supported catalysts have larger surface area and pore volumes (Table 4.13). The relative decrease in the surface area and pore volume of 0.5M ZnO-MMT2 (500˚C) can be explained with excess ZnO loading on the clay surface. This creates smoother areas on the catalyst surface which covers the porous structure.

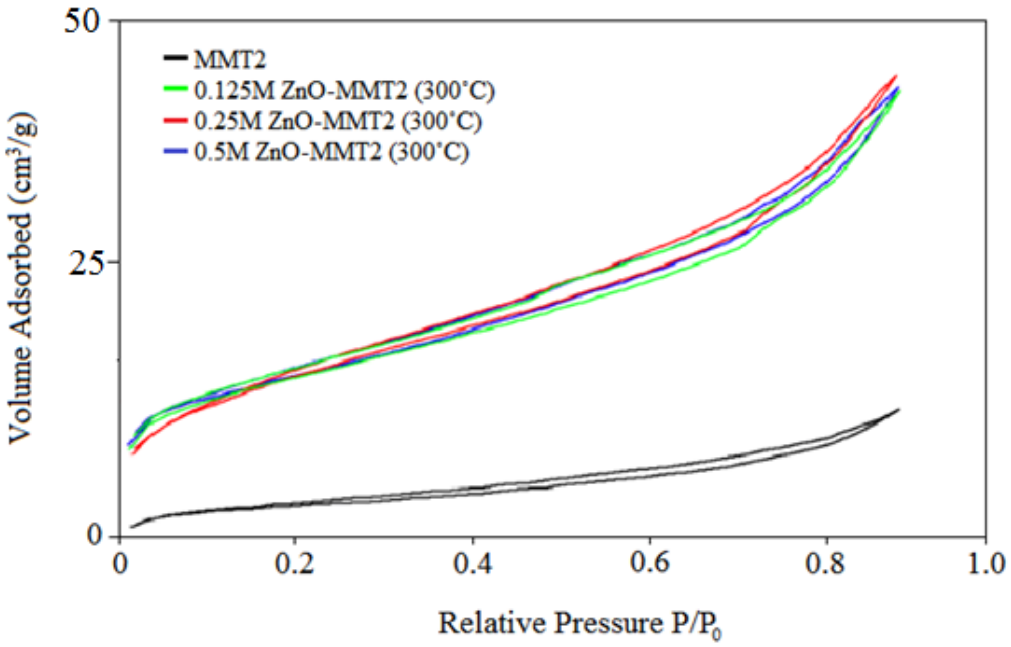


Figure 4.125. Nitrogen adsorption-desorption isotherms of MMT2 and supported catalysts prepared at 300˚C.

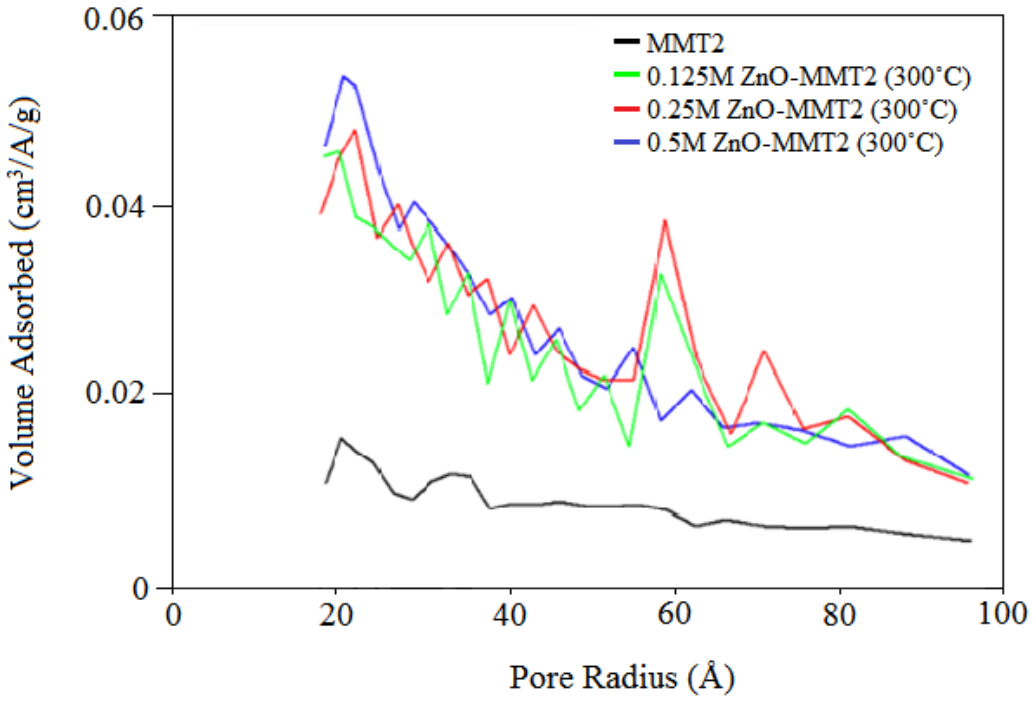


Figure 4.126. Pore size distribution plots of MMT2 and supported catalysts prepared at 300˚C.

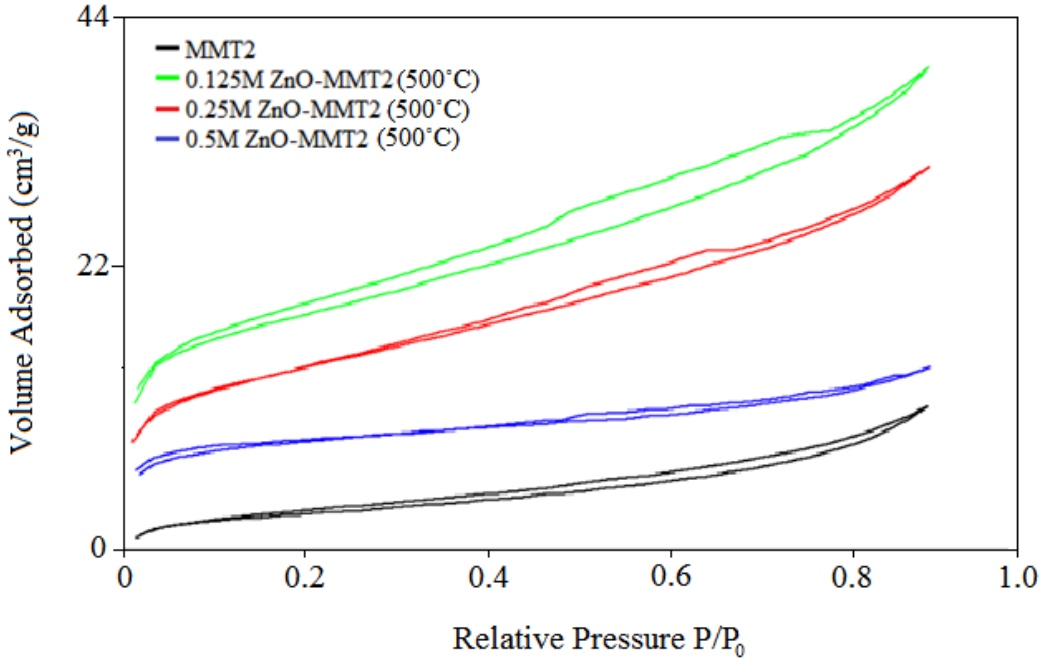


Figure 4.127. Nitrogen adsorption-desorption isotherms of MMT2 and supported catalysts prepared at 500˚C.

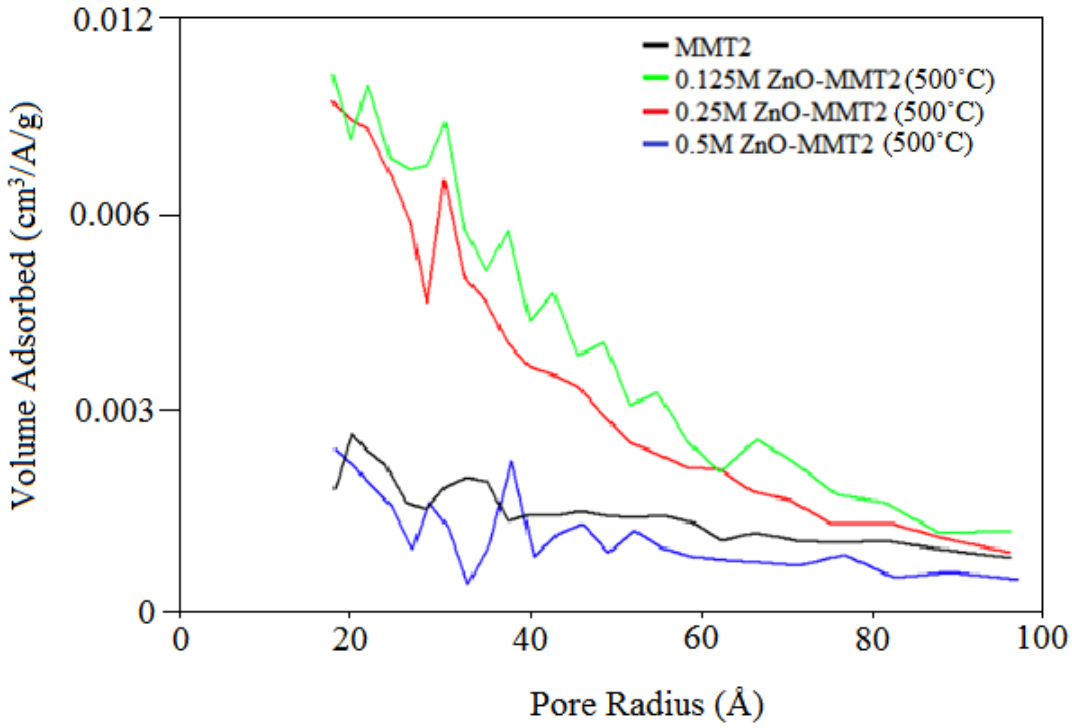


Figure 4.128. Pore size distribution plots of MMT2 and supported catalysts prepared at 500˚C.

4.7.4. UV-Vis DRS Analysis

Figure 4.129 and Figure 4.130 present the UV-Vis absorption spectroscopy of the MMT2, 0.25M ZnO and the supported catalysts. The bare MMT2 do not show an extended absorption tail between 200 and 600 nm, on the other hand 0.25M ZnO has a sharp absorption edge at the UV region. In the absorption spectra of the supported catalysts, the characteristic absorption edge of ZnO is detected. This edge becomes more observable and wider with the higher loading concentration of ZnO.

In addition the UV-Vis absorption spectra of the as prepared catalysts are transformed to the band-gap values (Equation 2.17) which are evaluated by linear extrapolation and taking the intercept on the x-axis gives the value of the band gap (Figure 4.131 and Figure 4.132). Accordingly, band gap energy of 0.25M ZnO (500˚C) is found as 3.12 eV (Figure 4.131 Inset). A slight decrease is observed for the supported catalysts, in comparison to the 0.25M ZnO which may correspond an activity in the visible region.

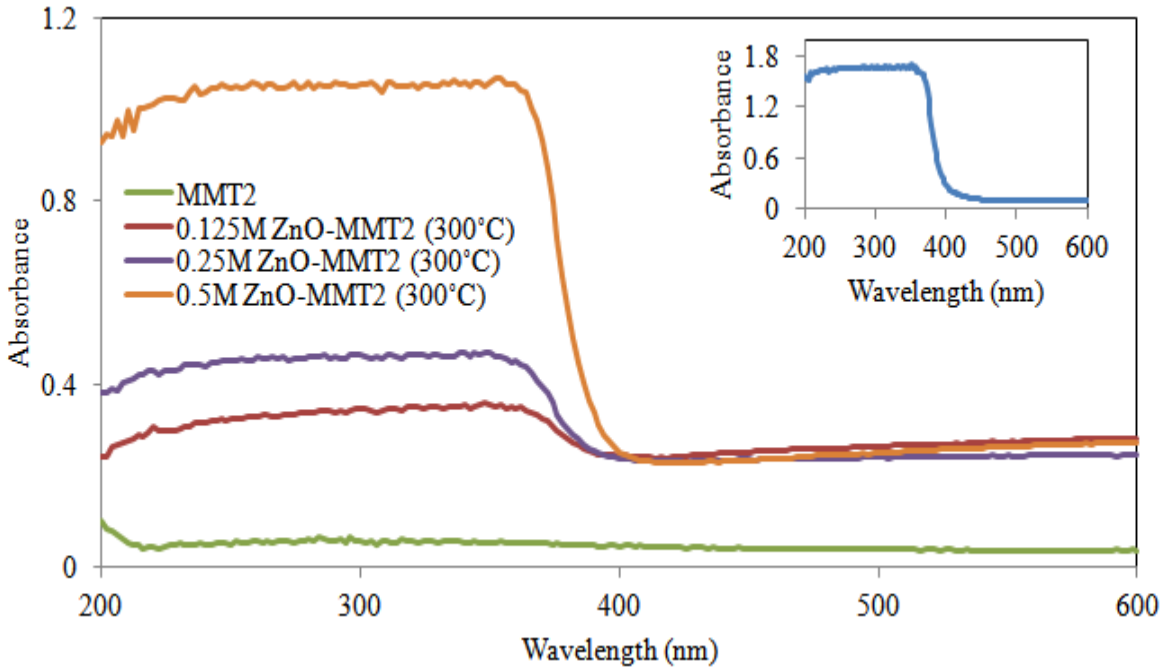


Figure 4.129. UV-Vis DRS spectra of MMT2 and supported catalysts prepared at 300˚C. Inset: UV-Vis DRS spectra of 0.25M ZnO (500˚C).

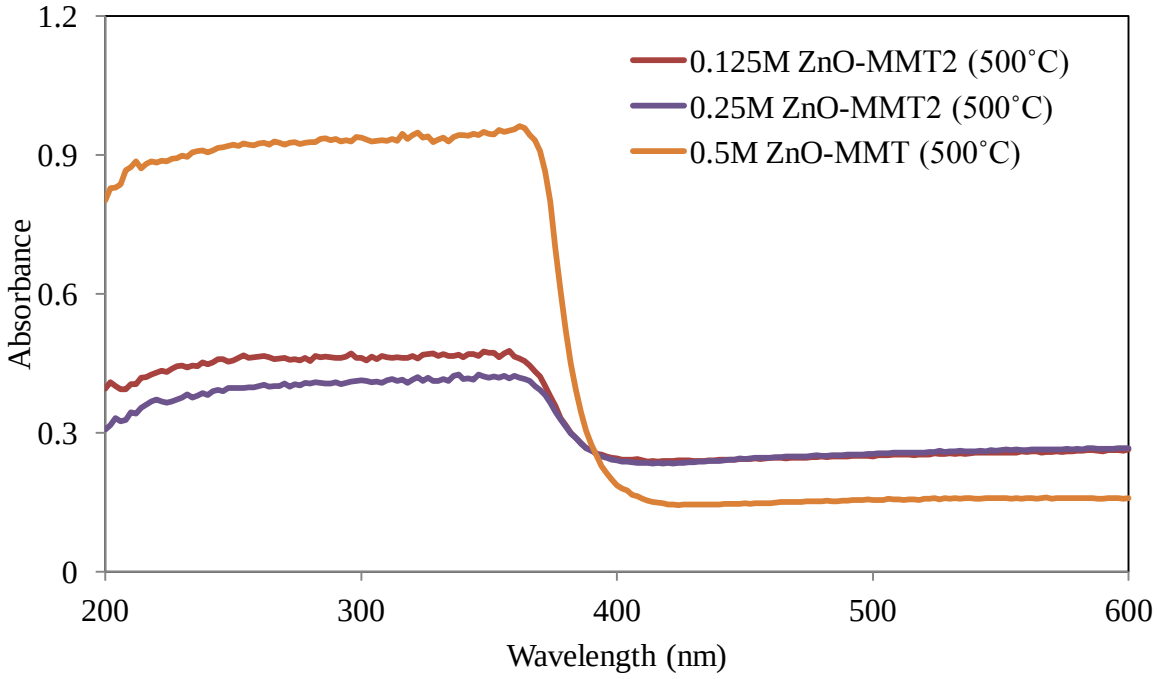


Figure 4.130. UV-vis DRS spectra of supported catalysts prepared at 500˚C.

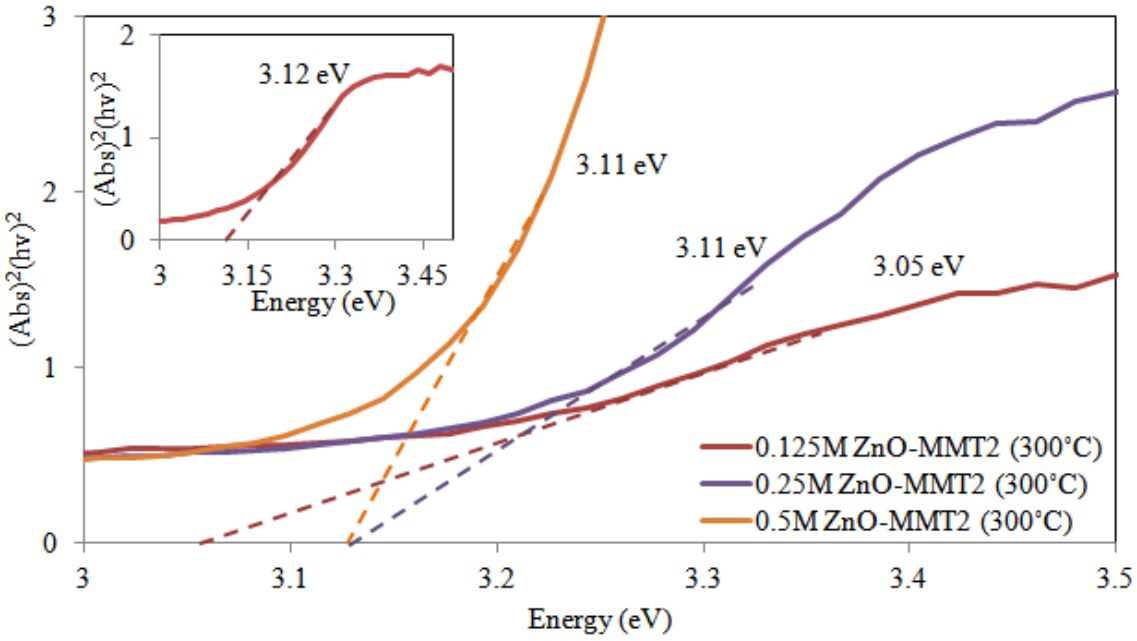


Figure 4.131. Band gap adsorption edges of supported catalysts. Inset: Band gap adsorption edges of 0.25M ZnO (500˚C).

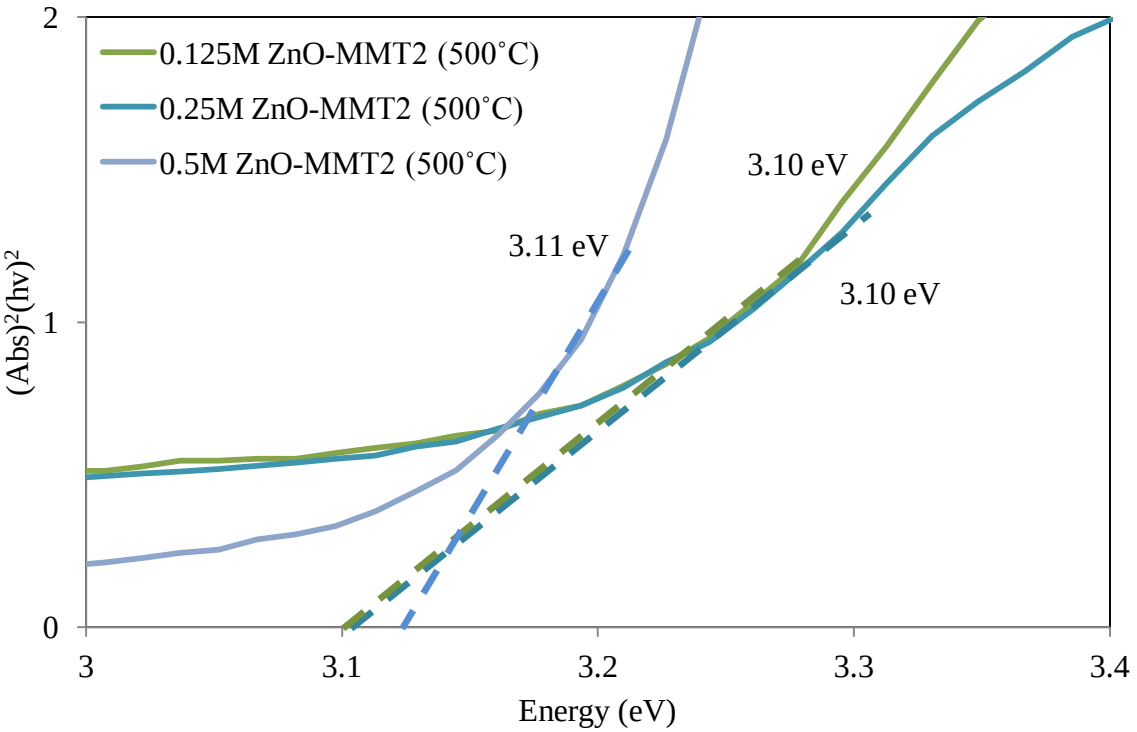


Figure 4.132. Band gap adsorption edges of supported catalysts.

4.8. Photoactivities of ZnO-MMT2 Catalysts

4.8.1. Control Experiments

Control experiments are set as two steps. In the first step, dark absorption capacities of MMT2, 0.25M ZnO, 0.25 M ZnO-MMT2 (300˚C) and 0.25 M ZnO-MMT2 (500˚C) are compared (Figure 4.133). For 0.25M ZnO and 0.25M ZnO-MMT2 (500˚C), after 85 min mixing in the dark, no significant change is noticed in the MO concentrations. On the other hand the raw MMT2 and 0.25M ZnO-MMT2 (300˚C) show excellent adsorption property due to higher basal spacing. In the second set photolysis of MO and photocatalytic activities of 0.25M ZnO (500˚C), 0.25 M ZnO-MMT2 (300˚C) and 0.25 M ZnO-MMT2 (500˚C) are examined (Figure 4.134). A negligible MO degradation is observed in the presence of UV light without any catalyst (Figure 4.134 Inset). The suspensions are stirred in the dark for 30 min to achieve adsorption/desorption equilibrium and thereafter exposed to illumination. Although, 0.25M ZnO (500˚C) shows a higher performance in comparison to the supported catalysts, the difficulties in the settlement of ZnO nanoparticles limit their applications in photocatalytic reactions. In the meantime, the activity of 0.25M ZnO-MMT2 (300˚C) is better than 0.25M ZnO-MMT2 (500˚C), because of the better adsorption capability.

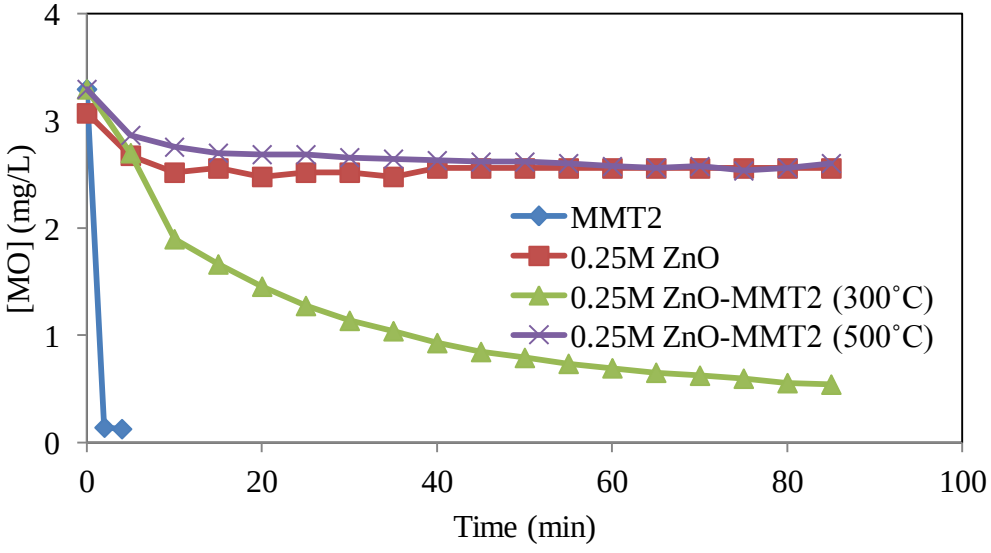


Figure 4.133. Control experiments in the dark. Conditions: pH: 6.5 (Natural), $[MO]_0$ = 3.27 mg/L, T = 298 K, Flow rate = 2000 rpm.

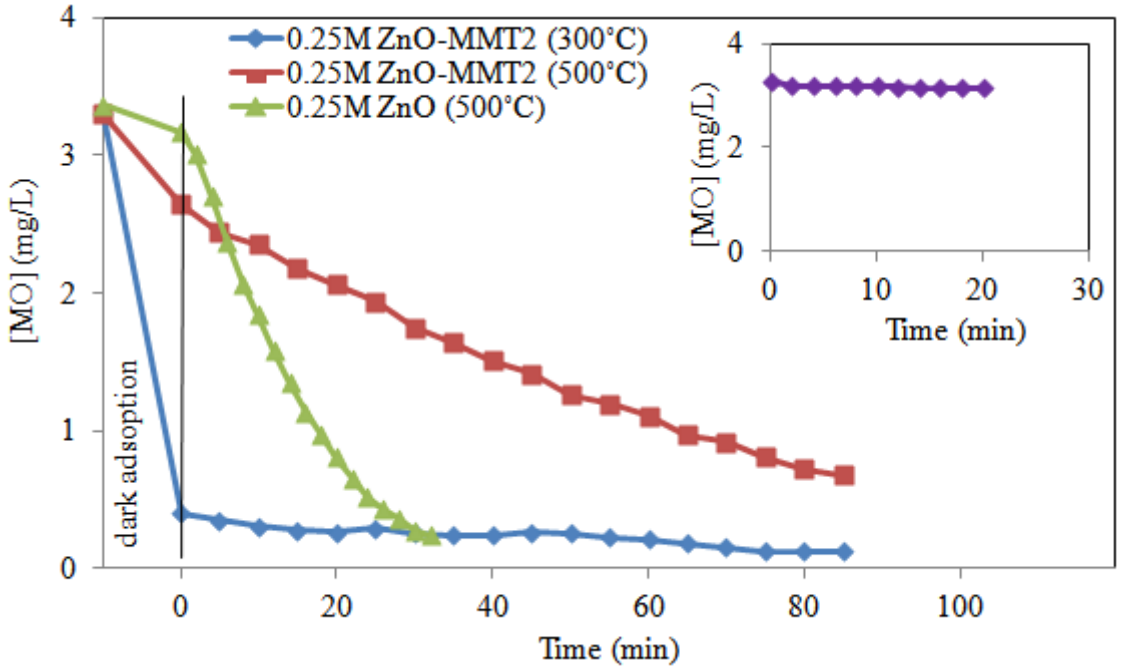


Figure 4.134. Control experiments under UV irradiation. Inset: Photolysis of MO. Conditions: pH: 6.5 (Natural), $[MO]_0$= 3.27 mg/L, T= 298K, Flow rate= 2000 rpm.

4.8.2. Dark Adsorption Experiments

4.8.2.1. Adsortion Kinetics. The dark adsorption details of MO (8.17 mg/L) over the 0.5M ZnO-MMT2 (300˚C) and 0.5M ZnO-MMT2 (500˚C) catalysts are investigated to specify the adsorption kinetics in terms of pseudo first order and pseudo second order models.

Pseudo first order model is applied with respect to the slope of $\ln(q_e-q_t)$ versus t graph. The correlation coefficients are found as 0.6282 (degradation) and 0.9068 (decolorization) and for 0.5M ZnO-MMT2 (300˚C) and 0.9949 (degradation) and 0.9226 (decolorization) for 0.5M ZnO-MMT2 (500˚C) (Figure 4.135, Figure 4.136, Figure 4.137 and Figure 4.138).

However, in the case of pseudo second order model, correlation coefficients in the plots of t/q_t versus t are found as 0.8445 (degradation), 0.9697 (decolorization) for 0.5M ZnO-MMT2 (300˚C) and 0.9388 (degradation), 0.9287 (decolorization) for 0.5M ZnO-MMT2 (500˚C) (Figure 4.139, Figure 4.140, Figure 4.141 and Figure 4.142).

The higher values of the coefficients imply a better adsorption of MO. Accordingly, pseudo-second order model fits to the 0.5M ZnO-MMT2 (300˚C), while only a certain extent of adsorption seems to be possible by this model in the presence of 0.5M ZnO-MMT2 (500˚C).

4.8.2.2. Adsorption Isotherms. For the adsorption isotherms, Freundlich and Langmuir isotherm models are employed at four different initial concentrations of MO (3.27, 8.17, 16.32 and 24.55 mg/L) in the presence of 0.5M ZnO-MMT2 (300˚C) and 0.5M ZnO-MMT2 (500˚C).

Freundlich isotherms' line fittings of ln q_e versus ln C_e in plots give correlations of 0.9513 (degradation), 0.9522 (decolorization) for 0.5M ZnO-MMT2 (300˚C) and 0.9813 (degradation) and 0.9088 (decolorization) for 0.5M ZnO-MMT2 (500˚C) (Figure 4.143, Figure 4.144, Figure 4.145 and Figure 4.146).

Langmuir isotherms (q_t versus t plots) of the supported catalysts are illustrated in Figure 4.147, Figure 4.148, Figure 4.149 and Figure 4.150. The line fittings in C_e/q_e versus C_e graphs result in correlation coefficients of 0.6988 (degradation), 0.7239 (decolorization) for 0.5M ZnO-MMT2 (300˚C) and 0.5227 (degradation) and 0.5227 (decolorization) for 0.5M ZnO-MMT2 (500˚C) (Figure 4.147, Figure 4.148, Figure 4.149 and Figure 4.150 Insets).

Consequently, Freundlich isotherm model fits better to the supported catalysts with higher correlation coefficients.

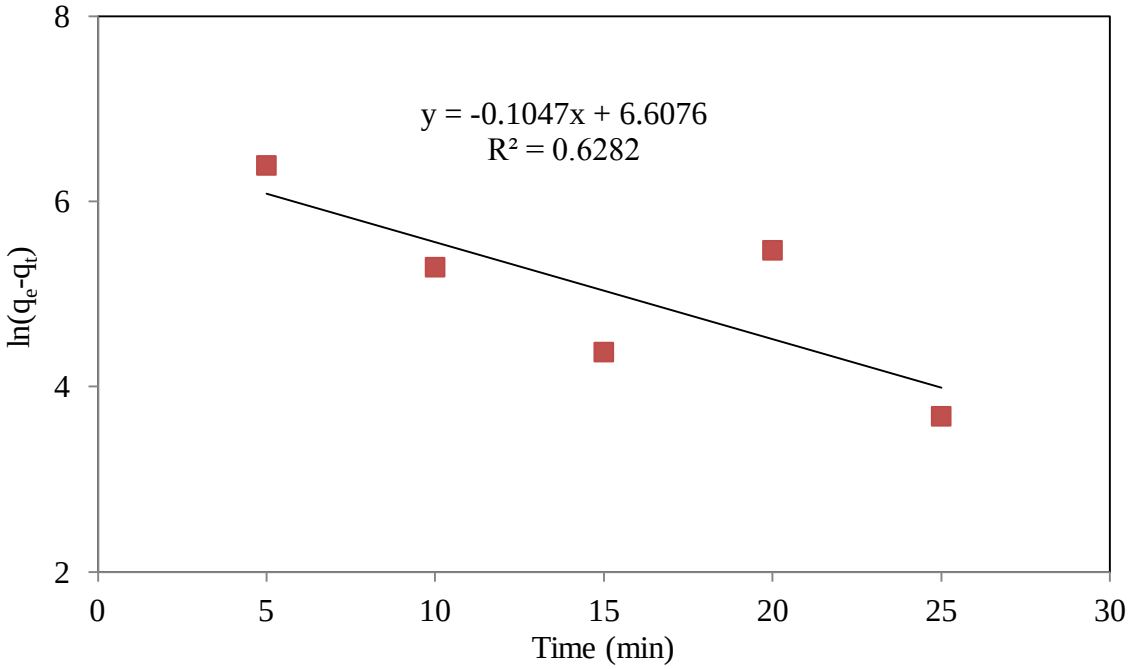


Figure 4.135. Pseudo first order kinetics for degradation of MO in the presence of 0.5M ZnO-MMT2 (300˚C). Conditions: pH= 6.5 (Natural), $[MO]_0$= 8.17 mg/L, T= 298 K, Flow rate= 2000 rpm.

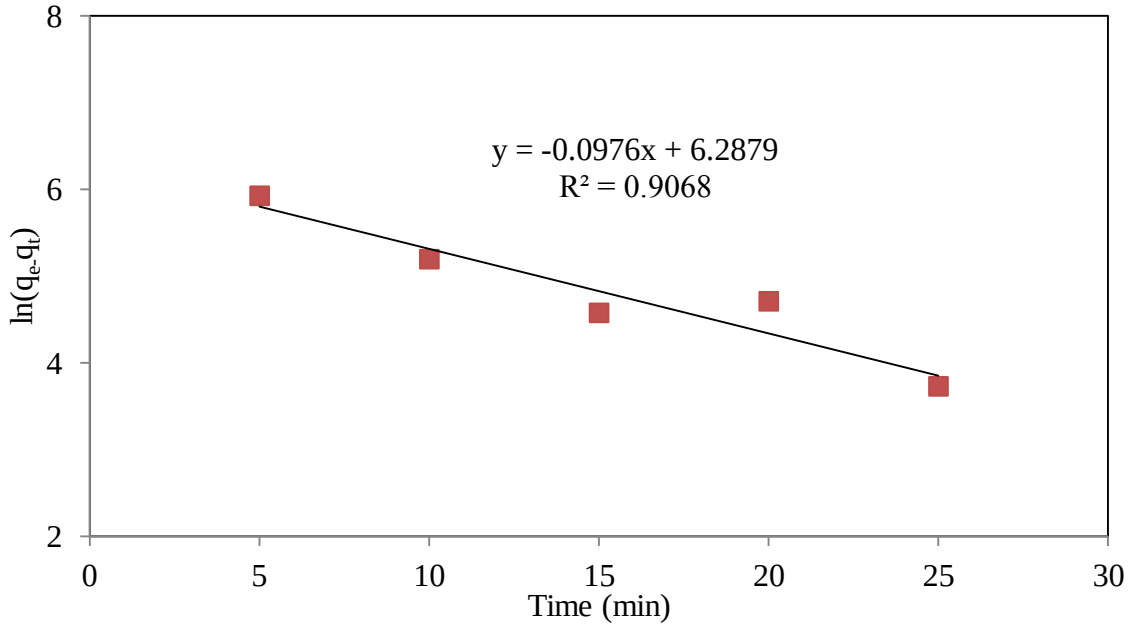


Figure 4.136. Pseudo first order kinetics for decolorization of MO in the presence of 0.5M ZnO-MMT2 (300˚C). Conditions: pH= 6.5 (Natural), $[MO]_0$= 8.17 mg/L, T= 298 K, Flow rate= 2000 rpm.

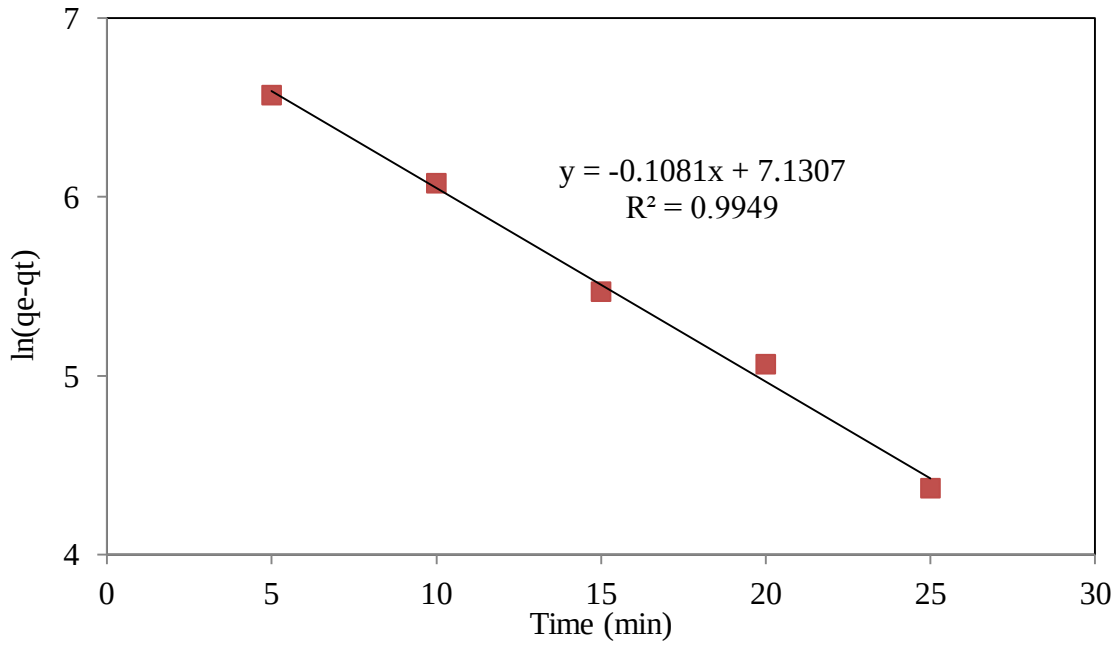


Figure 4.137. Pseudo first order kinetics for degradation of MO in the presence of 0.5M ZnO-MMT2 (500˚C). Conditions: pH= 6.5 (Natural), $[MO]_0$= 8.17 mg/L, T= 298 K, Flow rate= 2000 rpm.

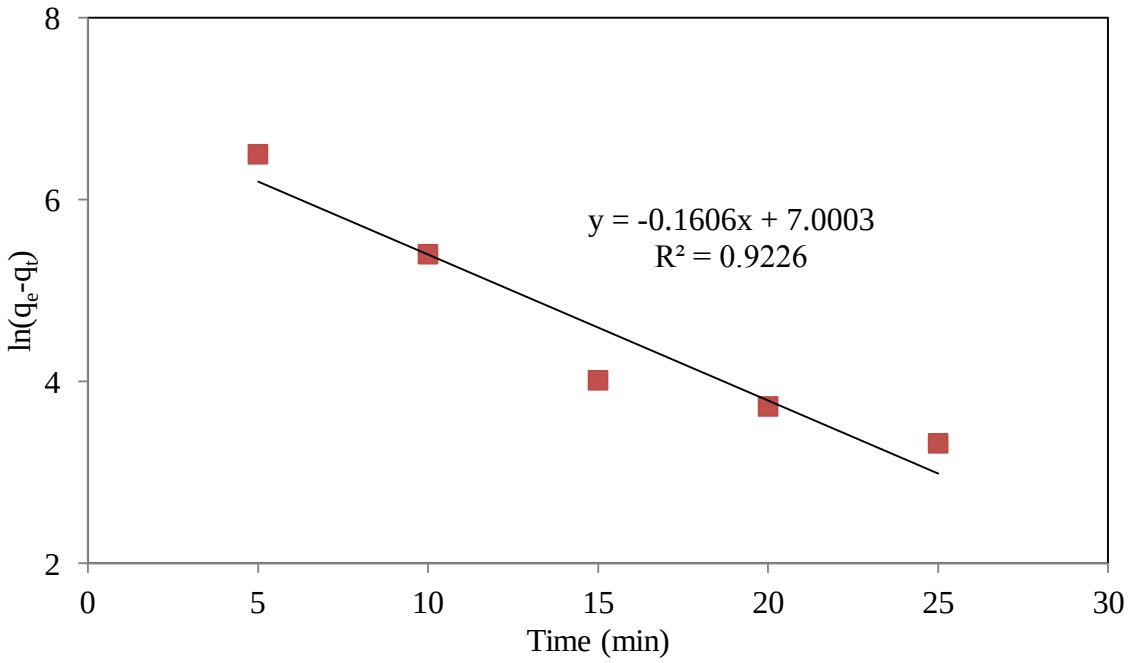


Figure 4.138. Pseudo first order kinetics for decolorization of MO in the presence of 0.5M ZnO-MMT2 (500˚C). Conditions: pH= 6.5 (Natural), $[MO]_0$= 8.17 mg/L, T= 298 K, Flow rate= 2000 rpm.

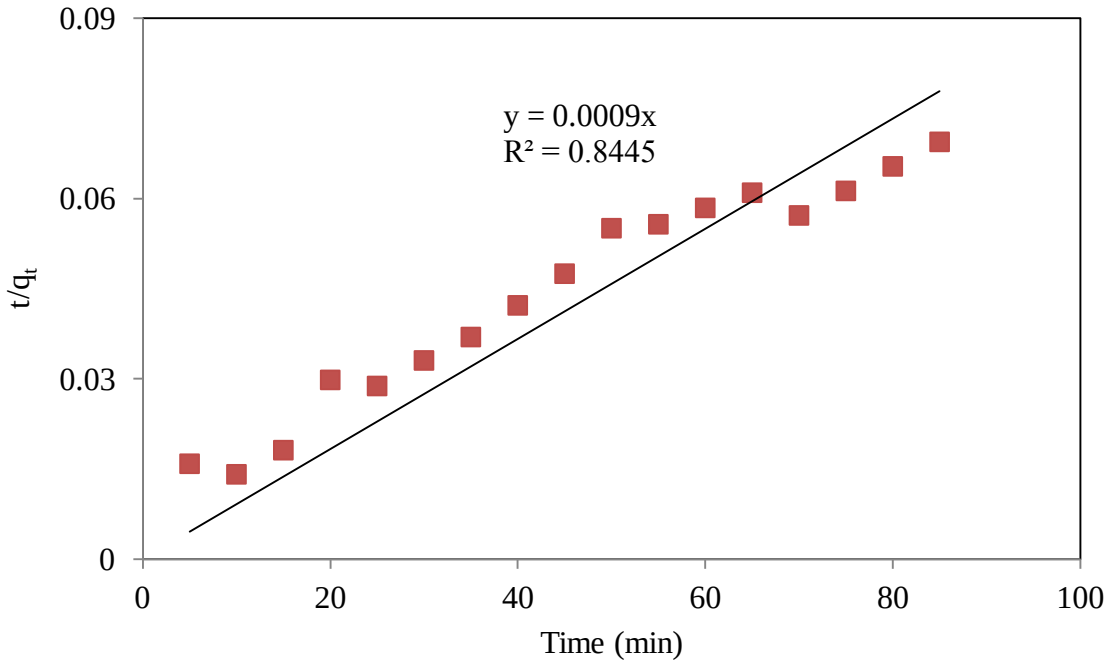


Figure 4.139. Pseudo second order kinetics for degradation of MO in the presence of 0.5M ZnO-MMT2 (300˚C). Conditions: pH=6.5 (Natural), $[MO]_0$= 8.17 mg/L, T= 298 K, Flow rate= 2000 rpm.

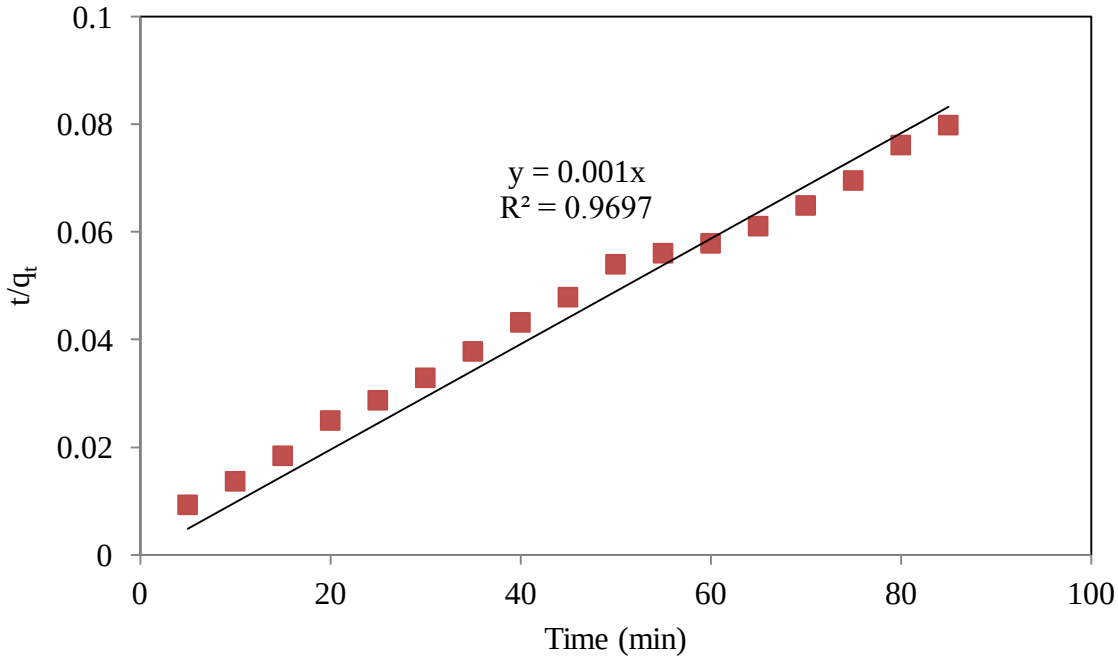


Figure 4.140. Pseudo second order kinetics for decolorization of MO in the presence of 0.5M ZnO-MMT2 (300˚C). Conditions: pH= 6.5 (Natural), $[MO]_0$= 8.17 mg/L, T= 298 K, Flow rate= 2000 rpm.

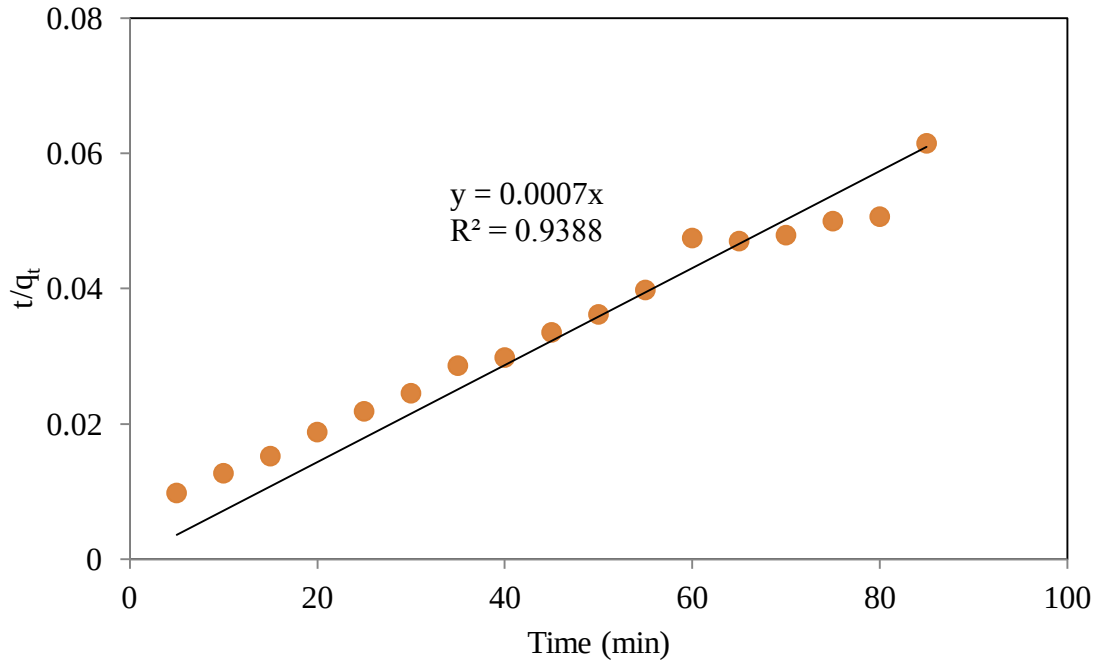


Figure 4.141. Pseudo second order kinetics for degradation of MO in the presence of 0.5M ZnO-MMT2 (500˚C). Conditions: pH= 6.5 (Natural), $[MO]_0$= 8.17 mg/L, T= 298 K, Flow rate= 2000 rpm.

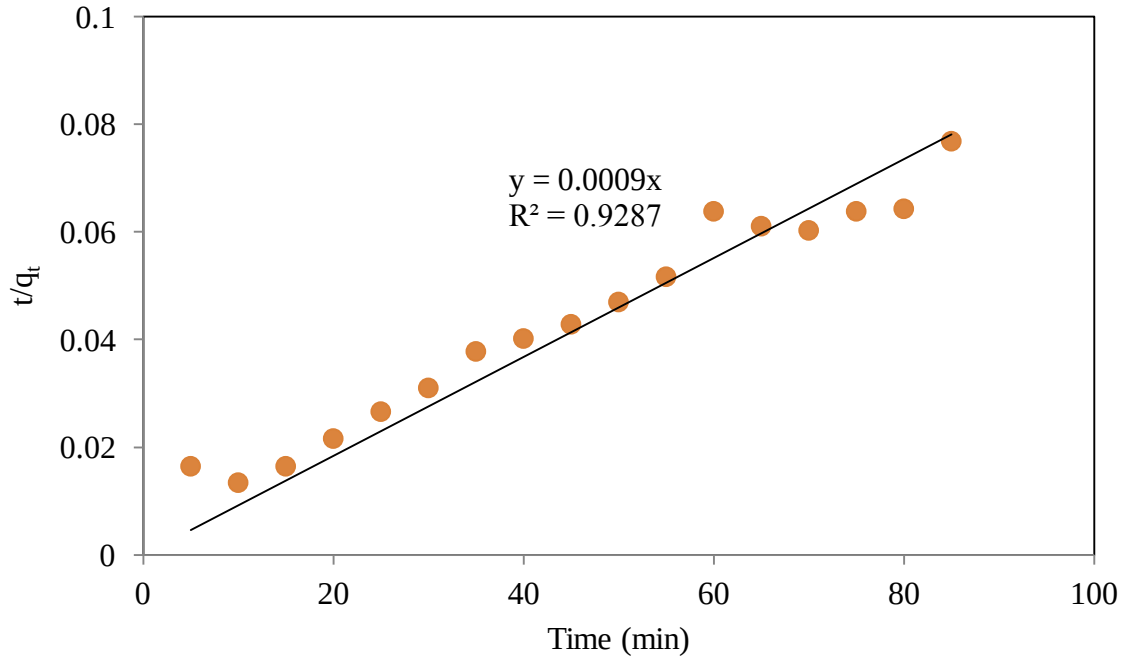


Figure 4.142. Pseudo second order kinetics for decolorization of MO in the presence of 0.5M ZnO-MMT2 (500˚C). Conditions: pH= 6.5 (Natural), $[MO]_0$= 8.17 mg/L, T= 298 K, Flow rate= 2000 rpm.

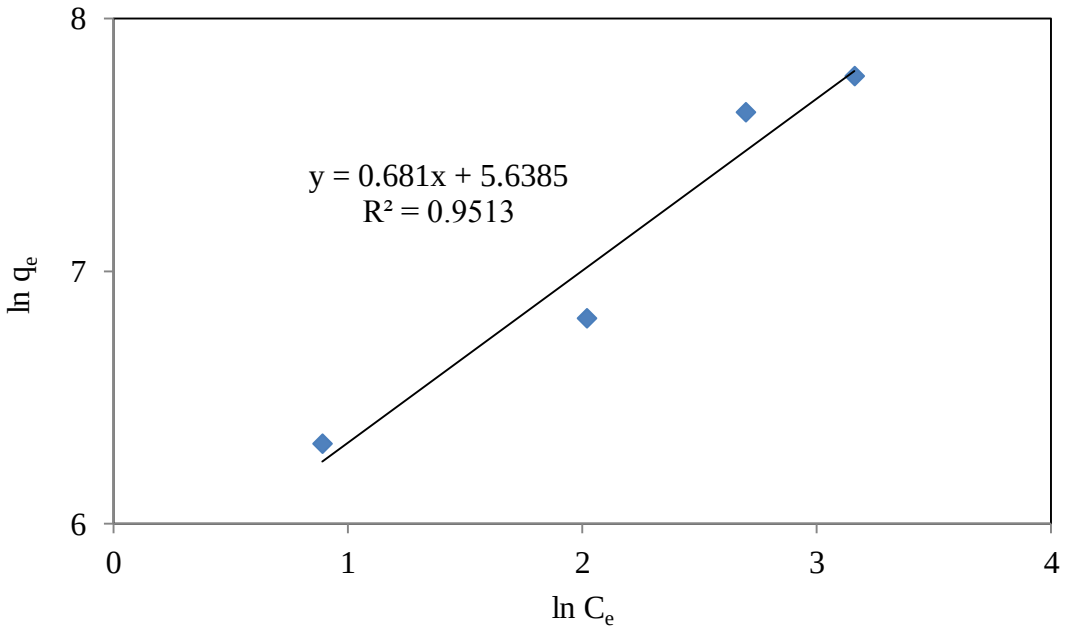


Figure 4.143. Freundlich adsorption isotherm for degradation of MO in the presence of 0.5M ZnO-MMT2 (300˚C). Conditions: pH= 6.5 (Natural), T= 298K, Flow rate= 2000 rpm.

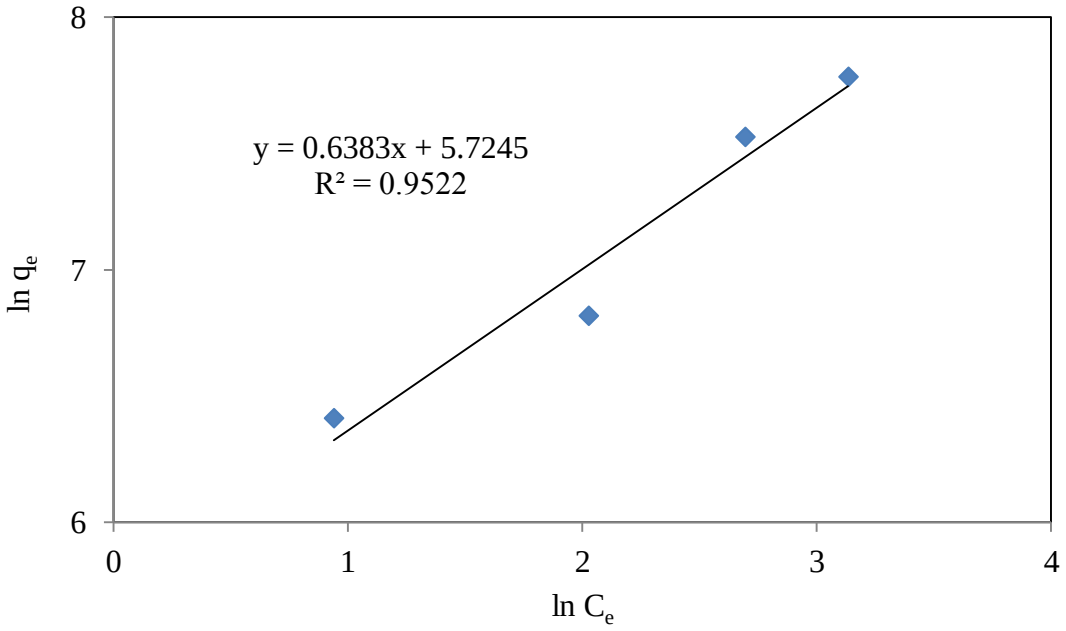


Figure 4.144. Freundlich adsorption isotherm for decolorization of MO in the presence of 0.5M ZnO-MMT2 (300˚C). Conditions: pH= 6.5 (Natural), T= 298K, Flow rate= 2000 rpm.

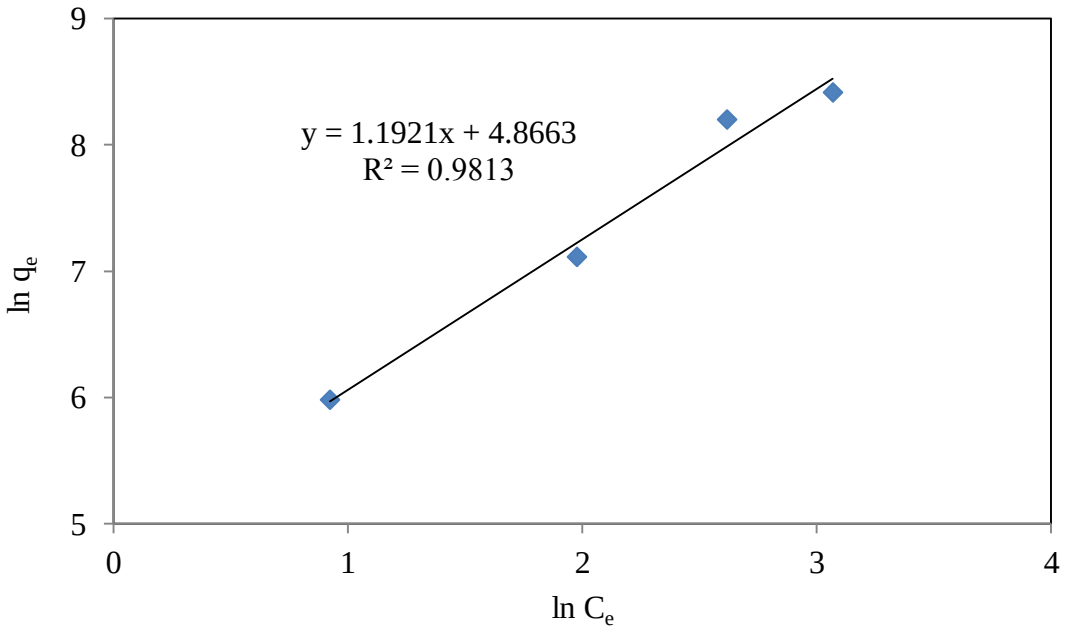


Figure 4.145. Freundlich adsorption isotherm for degradation of MO in the presence of 0.5M ZnO-MMT2 (500˚C). Conditions: pH= 6.5 (Natural), T= 298K, Flow rate= 2000 rpm.

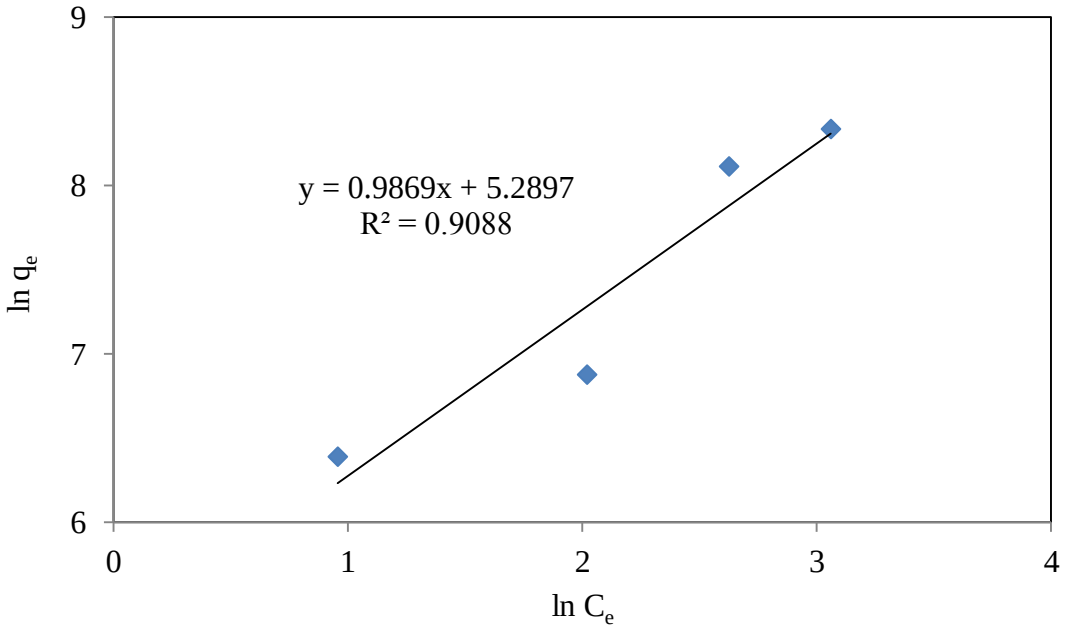


Figure 4.146. Freundlich adsorption isotherm for decolorization of MO in the presence of 0.5M ZnO-MMT2 (500˚C). Conditions: pH= 6.5 (Natural), T= 298K, Flow rate= 2000 rpm.

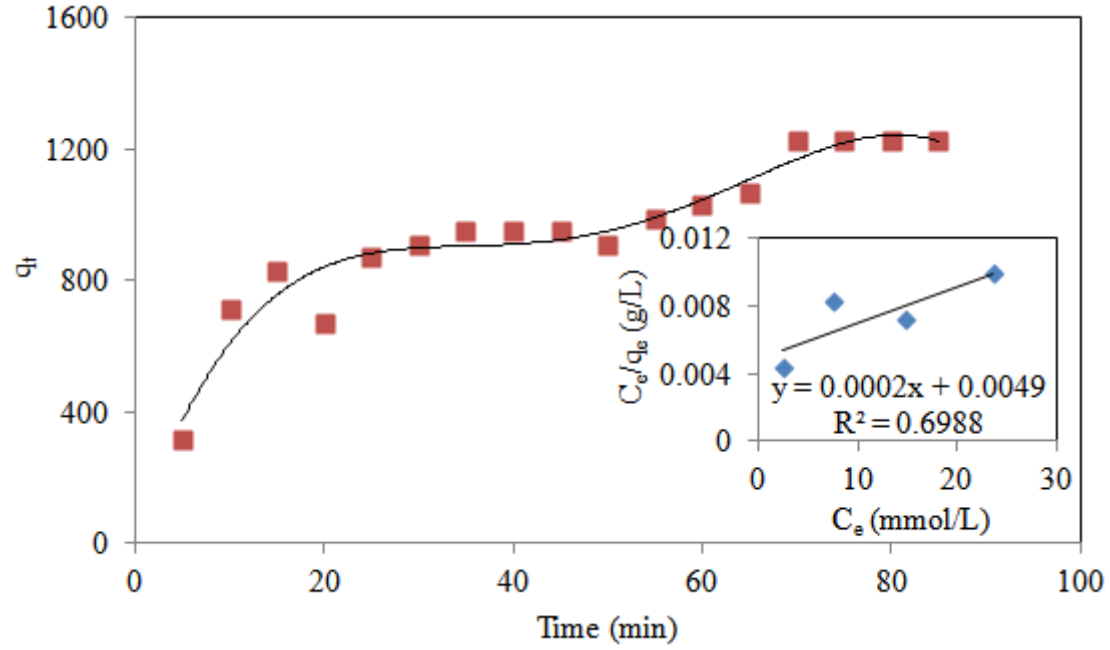


Figure 4.147. Langmuir adsorption isotherm for degradation of MO in the presence of 0.5M ZnO-MMT2 (300˚C). Inset: C_e/qe vs. C_e plot. Conditions: pH= 6.5 (Natural), T= 298K, Flow rate= 2000 rpm.

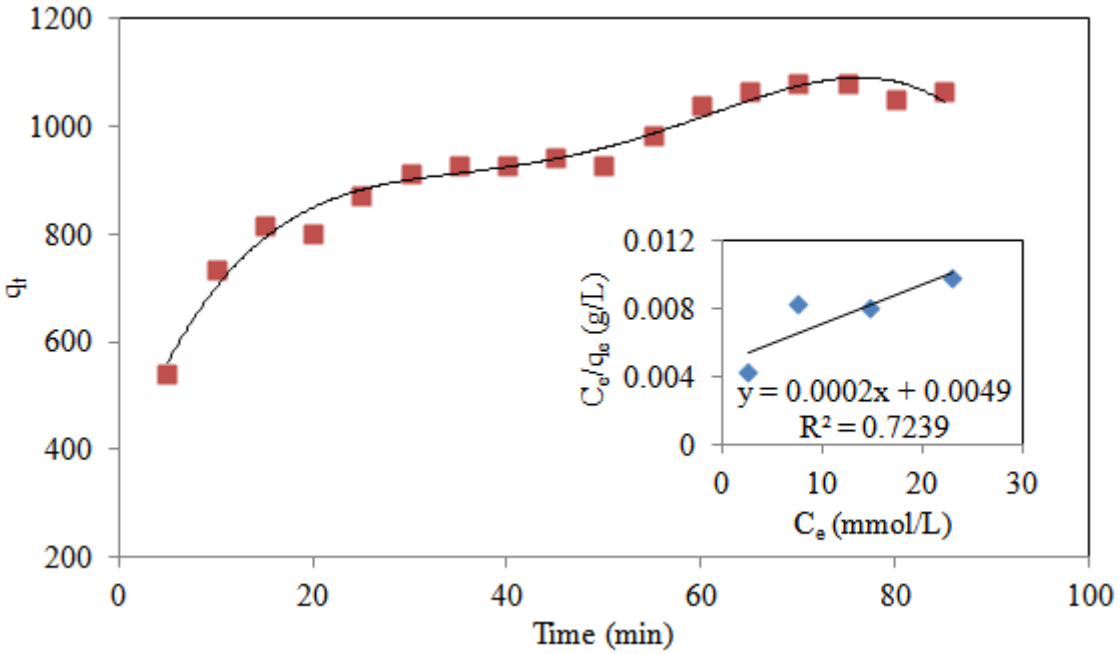


Figure 4.148. Langmuir adsorption isotherm for decolorization of MO in the presence of 0.5M ZnO-MMT2 (300˚C). Inset: C_e/q_e vs. C_e plot. Conditions: pH= 6.5 (Natural), T= 298K, Flow rate= 2000 rpm.

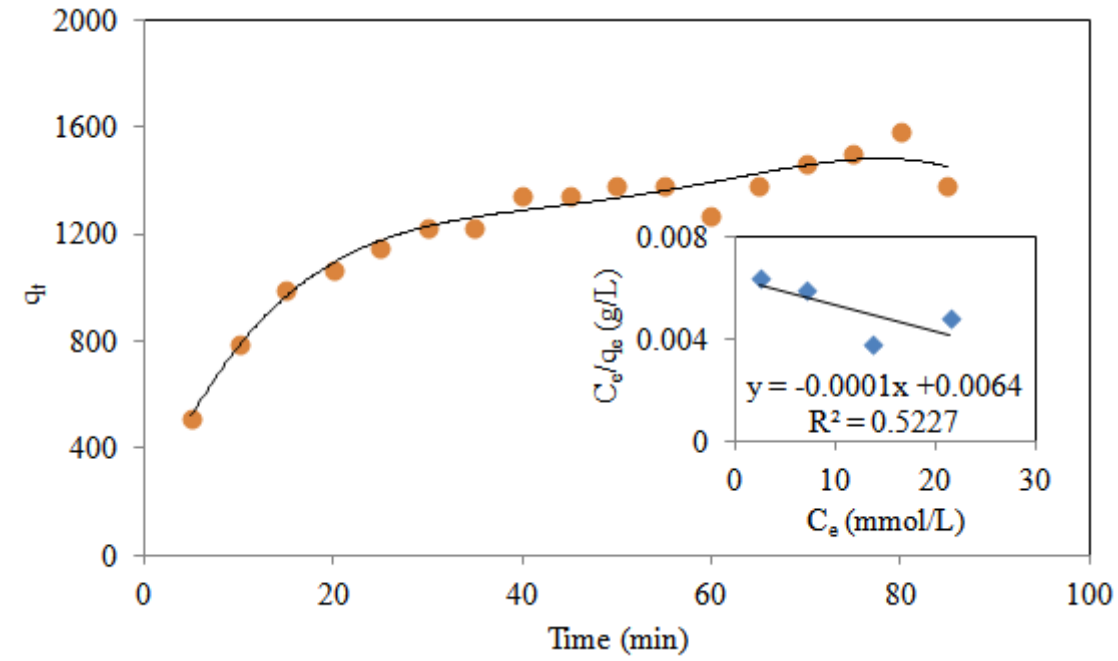


Figure 4.149. Langmuir adsorption isotherm for degradation of MO in the presence of 0.5M ZnO-MMT2 (500˚C). Inset: C_e/q_e vs. C_e plot. Conditions: pH= 6.5 (Natural), T= 298K, Flow rate= 2000 rpm.

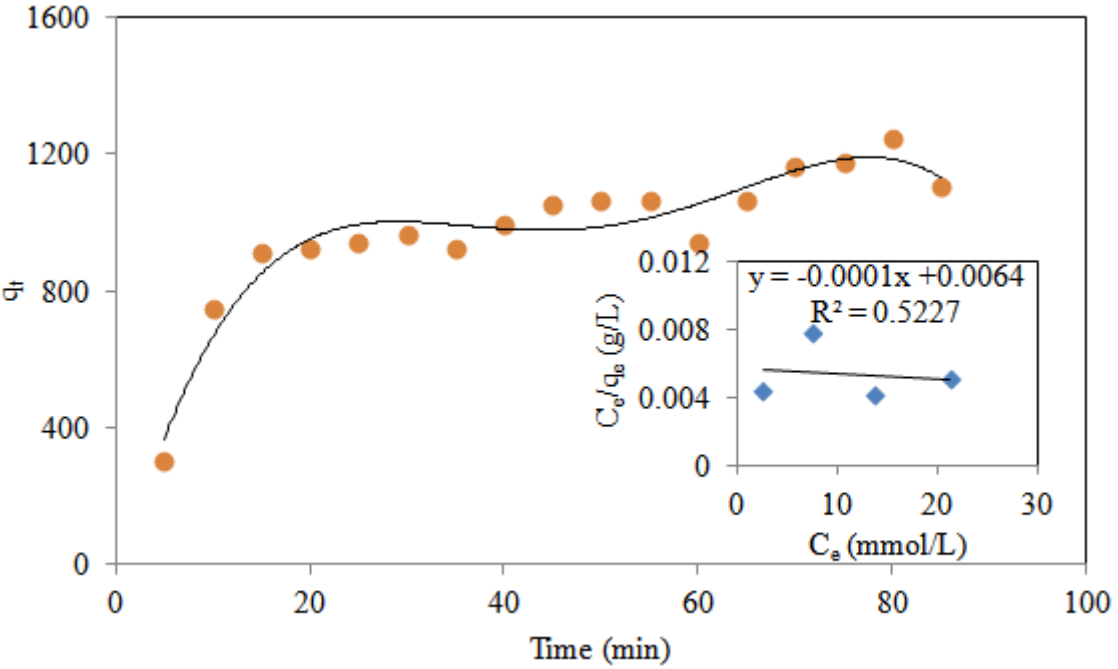


Figure 4.150. Langmuir adsorption isotherm for decolorization of MO in the presence of 0.5M ZnO-MMT2 (500˚C). Inset: C_e/q_e vs. C_e plot. Conditions: pH= 6.5 (Natural), T= 298K, Flow rate= 2000 rpm.

4.8.3. Photocatalytic Experiments

4.8.3.1. Effect of ZnO Loading. The photocatalytic reactions are carried out in the existence of supported catalysts loaded with different ZnO concentrations. Following 30 min dark experiments, the remaining concentrations of MO in solutions are controlled about 85 min (Figure 4.151, Figure 4.152, Figure 4.153 and Figure 4.154).

For both degradation and decolorization processes, ZnO loading concentrations negatively affect the photocatalytic activity of the supported catalysts (Figure 4.151, Figure 4.152, Figure 4.153 and Figure 4.154). 0.25M ZnO-MMT2 (300˚C) and 0.125M ZnO-MMT2 (500˚C) show better activity than other catalysts due to the better adsorption capability of the catalysts.

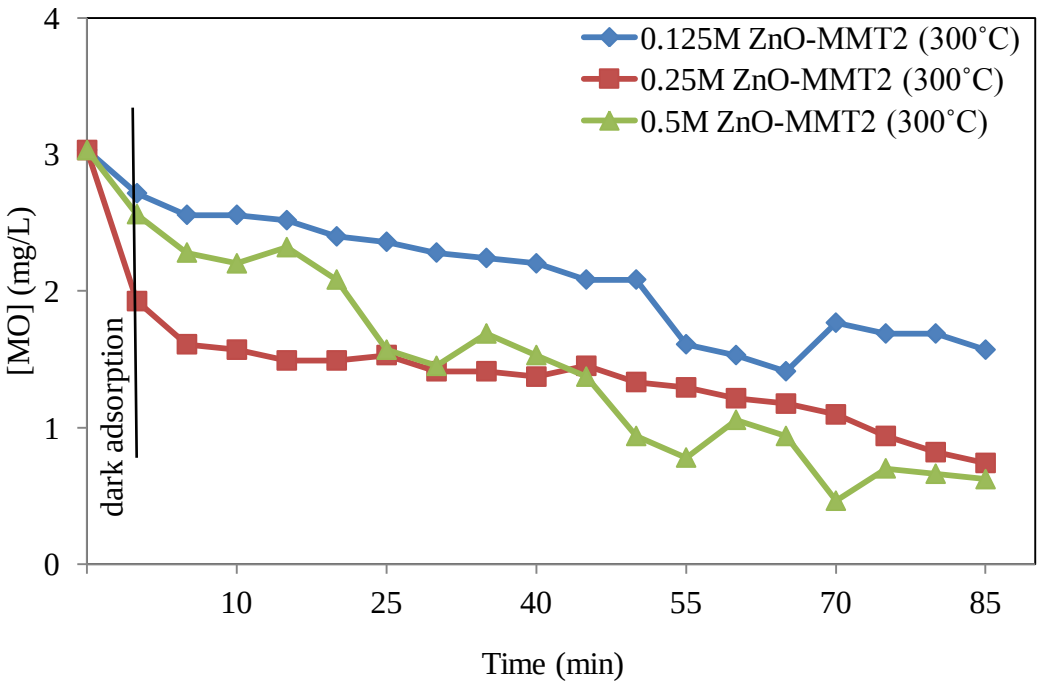


Figure 4.151. MO degradation in the presence of supported catalysts prepared at 300˚C. Conditions: pH= 6.5 (Natural), $[MO]_0$= 3.27 mg/L, T= 298 K, Flow rate= 2000 rpm.

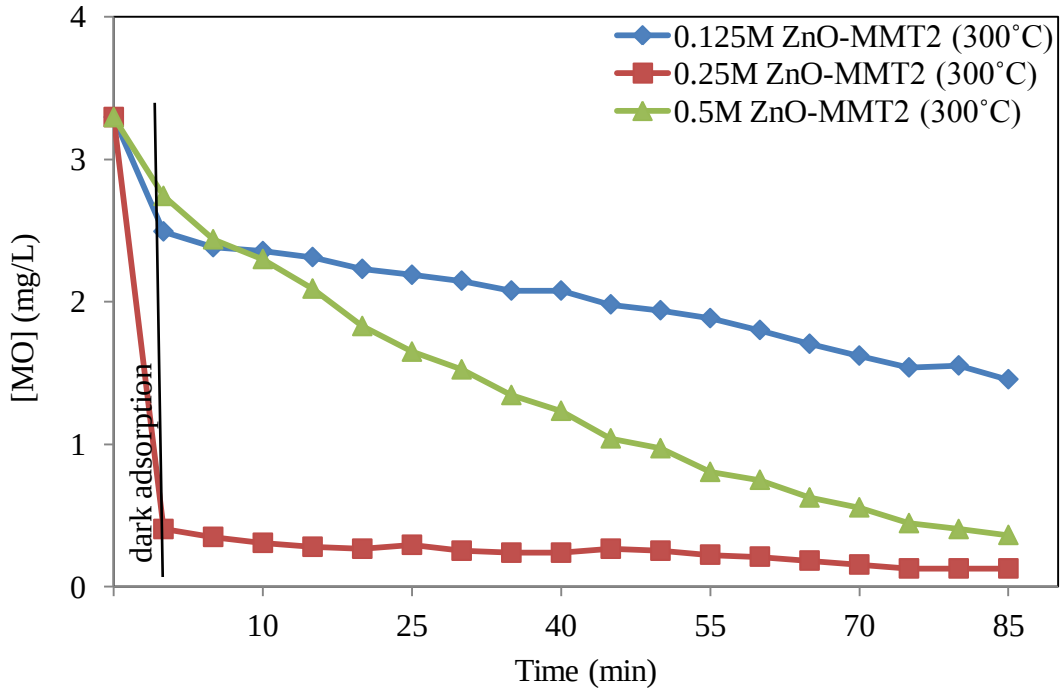


Figure 4.152. MO decolorization in the presence of supported catalysts prepared at 300˚C. Conditions: pH= 6.5 (Natural), $[MO]_0$= 3.27 mg/L, T= 298 K, Flow rate= 2000 rpm.

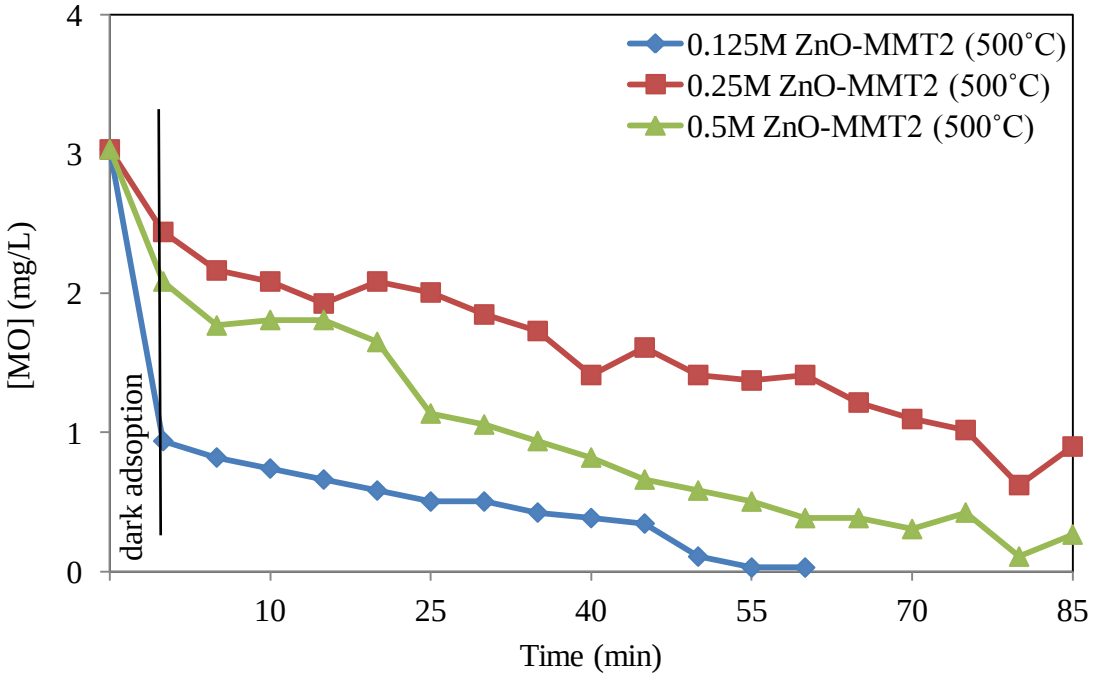


Figure 4.153. MO degradation in the presence of supported catalysts prepared at 500˚C. Conditions: pH= 6.5 (Natural), $[MO]_0$= 3.27 mg/L, T= 298 K, Flow rate= 2000 rpm.

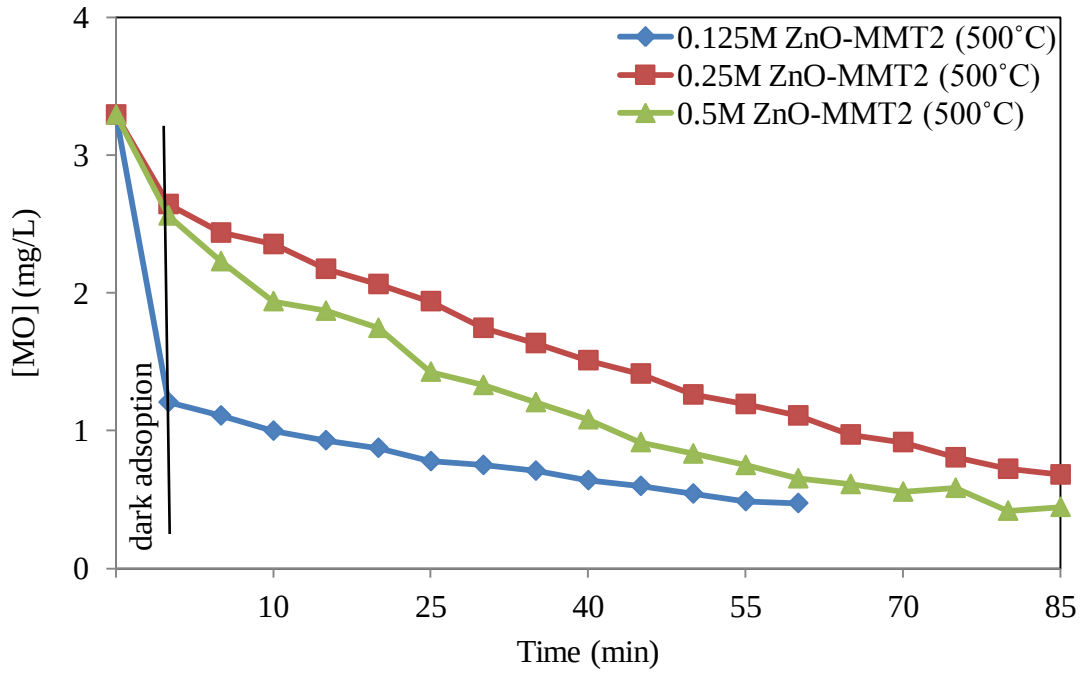


Figure 4.154. MO decolorization in the presence of supported catalysts prepared at 500˚C. Conditions: pH= 6.5 (Natural), $[MO]_0$= 3.27 mg/L, T= 298 K, Flow rate= 2000 rpm.

4.8.3.2. Effect of Initial MO Concentration. The influence of the initial MO concentration varying from 3.27 to 24.55 mg/L on the photocatalytic rates is also investigated in the presence of 0.5M ZnO-MMT2 (300˚C) and 0.5M ZnO-MMT2 (500˚C). For all concentrations, the best degradation and decolorization performances are obtained in the presence of 0.5M ZnO-MMT2 (300˚C) (Figure 4.155 and Figure 4.156). Pseudo first order kinetic model is confirmed according to the linearity noticed in the plots of ln (C_0/C) versus t (time) for all concentrations. (Figure 4.157, Figure 4.158, Figure 4.159 and Figure 4.160). As a general trend, the efficiency of both decolorization and degradation processes is found to decrease with increasing concentration of MO (Table 4.15 and Table 4.16). This can be a result of blocking of the photocatalytically active sites on the supported catalyst and reducing the interaction of photons with these sites.

Langmuir-Hinshelwood kinetic model analysis gives linearity in the plot of reciprocal rate (1/R) against reciprocal of MO concentrations ($1/C_0$) (Figure 4.167, Figure 4.168, Figure 4.169 and Figure 4.170 Inset).

In the presence of 0.5M ZnO-MMT2 (500˚C), the values of adsorption coefficient (K) and reaction rate constant (k) values are found to be 0.134 L/mg and 0.068 mg/L min (for degradation) and, 0.044 L/mg and 0.103 mg/L min (for decolorization) demonstrating a higher adsorption capacity and hence degradation-decolorization ability. 0.5M ZnO-MMT2 (300˚C) gives higher K and k values. 0.049 L/mg and 0.102 mg/L min (for degradation) and 0.041 L/mg and 0.140 mg/L min (for decolorization) demonstrating a higher adsorption capacity and hence degradation-decolorization ability.

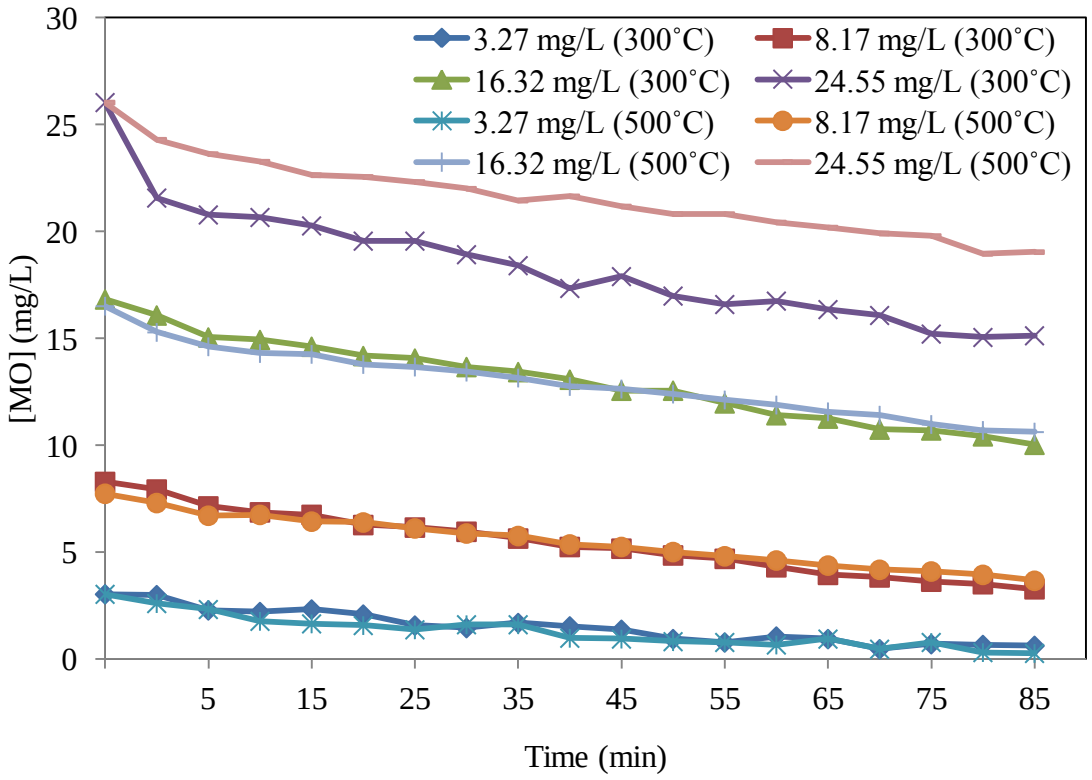


Figure 4.155. MO degradation at initial MO concentrations in the presence of 0.5M ZnO-MMT2 (300˚C) and 0.5M ZnO-MMT2 (500˚C). Conditions: pH=6.5 (Natural), T= 298 K, Flow rate= 2000 rpm.

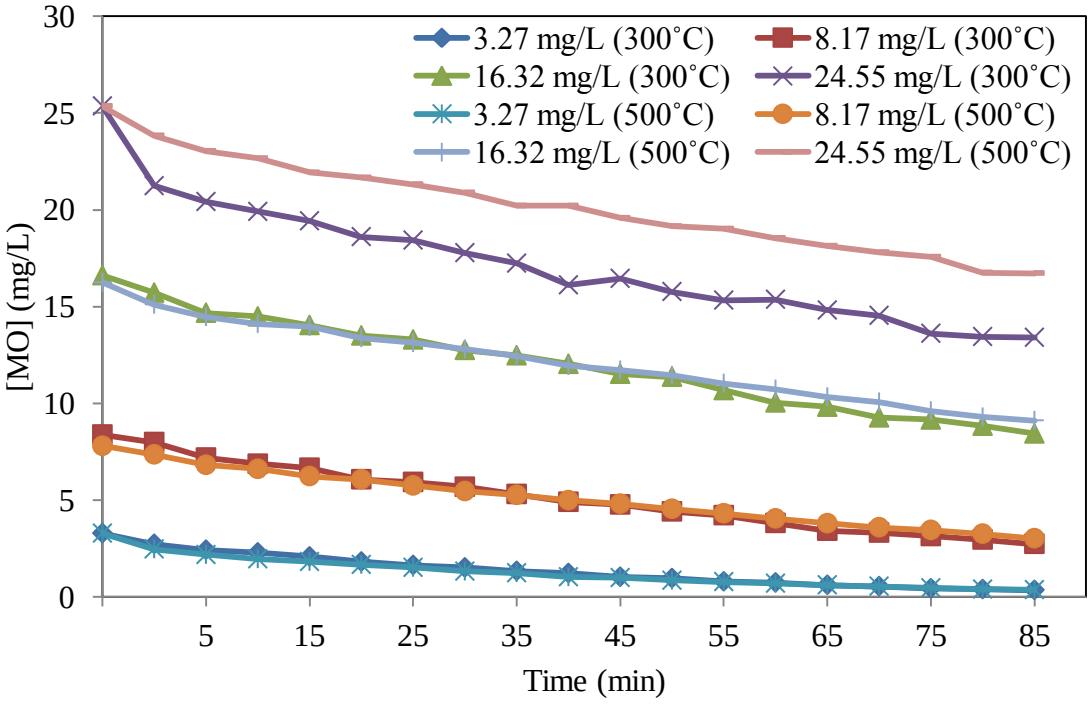


Figure 4.156. MO decolorization at initial MO concentrations in the presence of 0.5M ZnO-MMT2 (300˚C) and 0.5M ZnO-MMT2 (500˚C). Conditions: pH= 6.5 (Natural), T= 298 K, Flow rate= 2000 rpm.

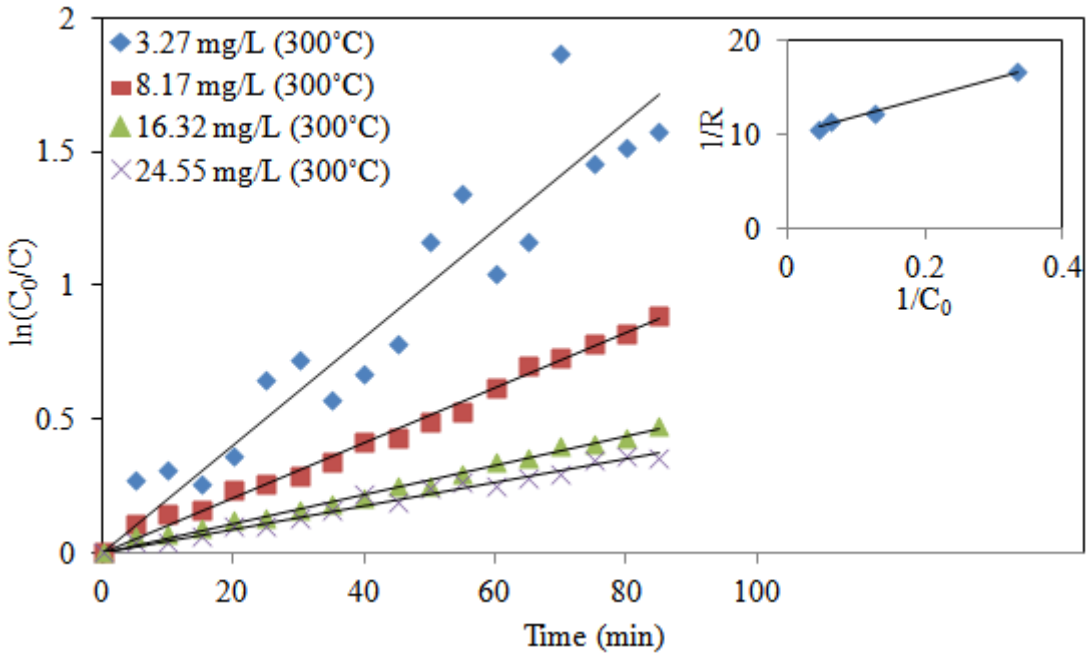


Figure 4.157. Pseudo-first order kinetics for degradation of MO in the presence of 0.5M ZnO-MMT2 (300˚C). Inset: Langmuir-Hinshelwood analysis. Conditions: pH= 6.5 (Natural), T= 298 K, Flow rate= 2000 rpm.

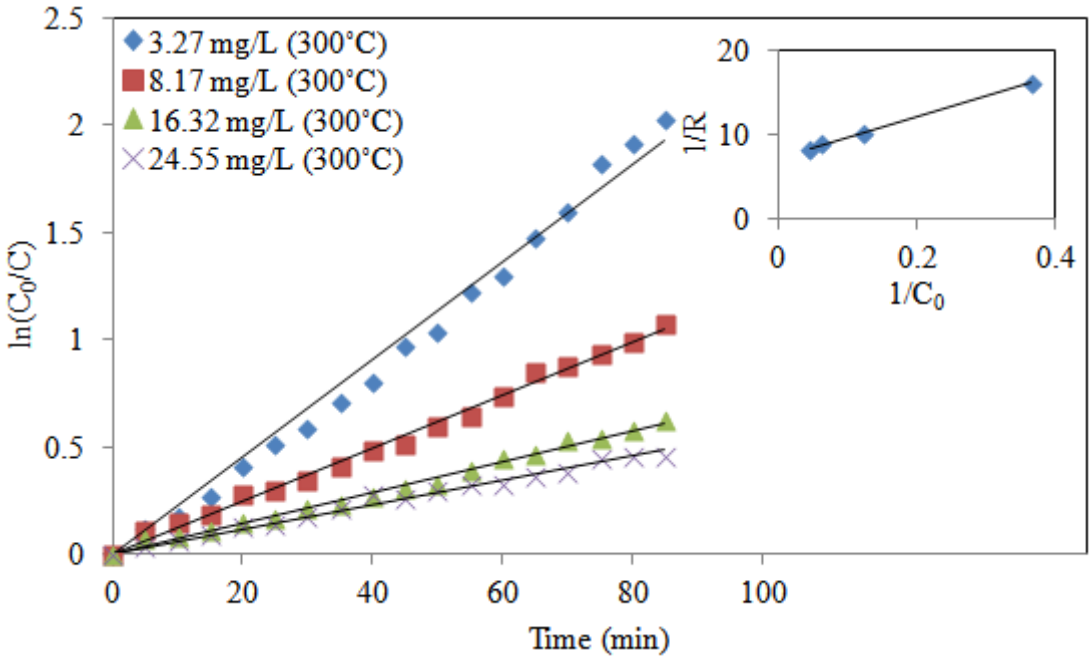


Figure 4.158. Pseudo-first order kinetics for decolorization of MO in the presence of 0.5M ZnO-MMT2 (300˚C). Inset: Langmuir-Hinshelwood analysis. Conditions: pH=6.5 (Natural), T= 298 K, Flow rate= 2000 rpm.

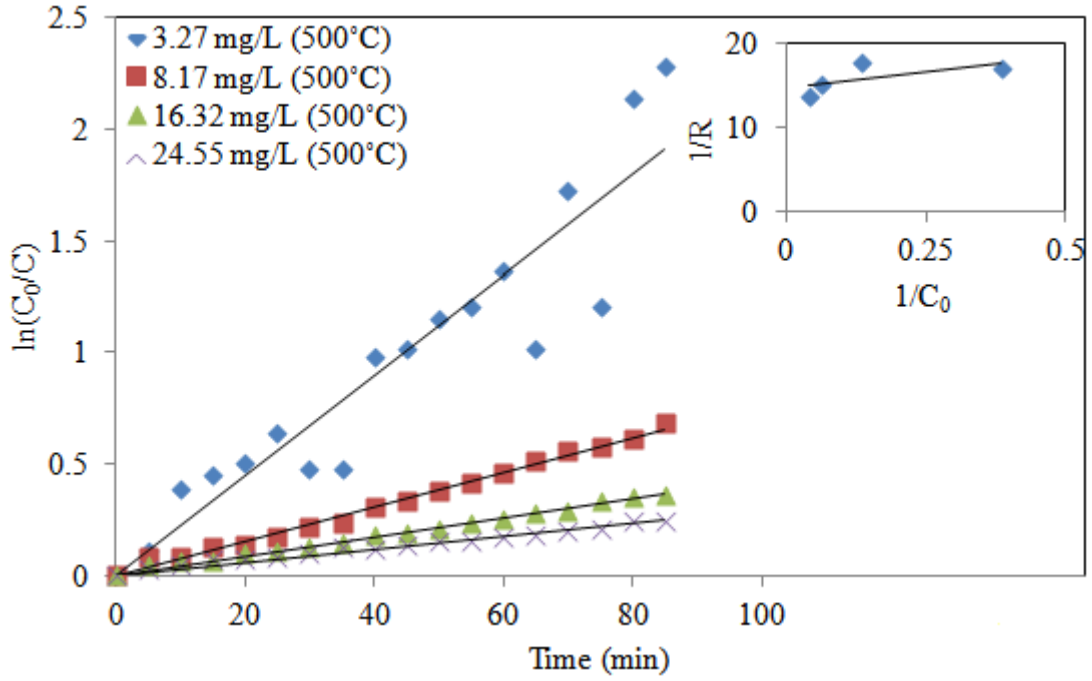


Figure 4.159. Pseudo-first order kinetics for degradation of MO in the presence of 0.5M ZnO-MMT2 (500˚C). Inset: Langmuir-Hinshelwood analysis. Conditions: pH= 6.5 (Natural), T= 298 K, Flow rate= 2000 rpm.

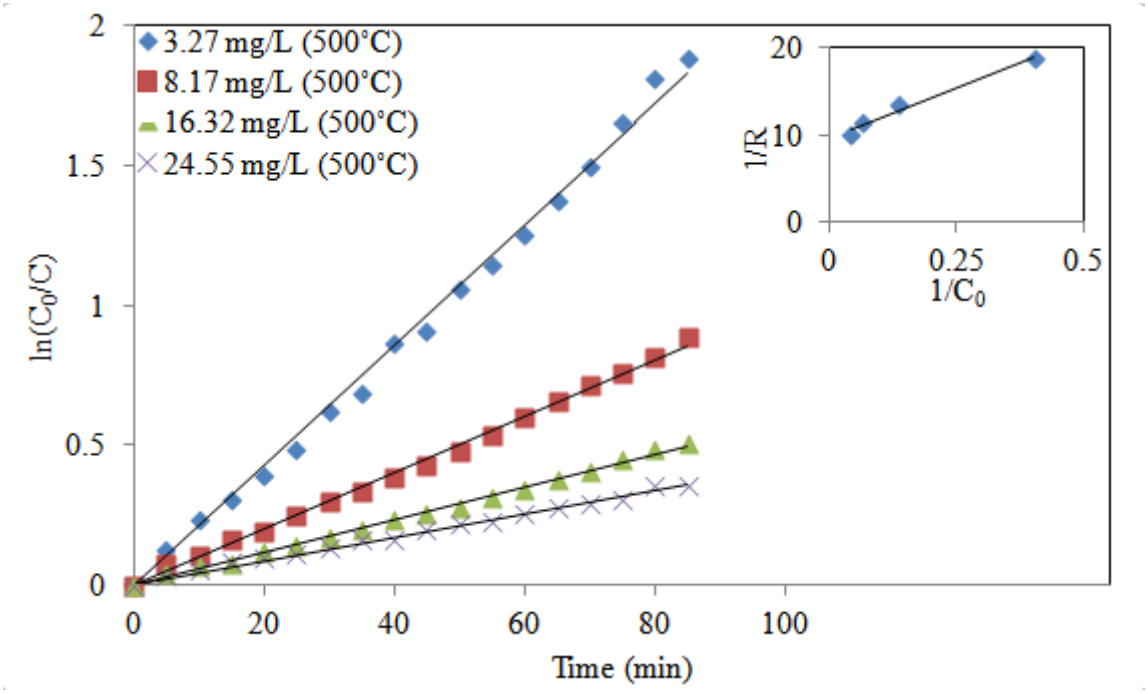


Figure 4.160. Pseudo-first order kinetics for decolorization of MO in the presence of 0.5M ZnO-MMT2 (500˚C). Inset: Langmuir-Hinshelwood analysis. Conditions: pH= 6.5 (Natural), T= 298 K, Flow rate= 2000 rpm.

Table 4.15. Rate constants (k) and linear regression values (R) for the degradation and decolorization processes of the different initial concentrations of MO in the presence of 0.5M ZnO-MMT2 (300˚C).

	k (min^{-1})		**R**	
[MO] (mg/L)	**degradation**	**decolorization**	**degradation**	**decolorization**
24.55	0.0044	0.0057	0.9811	0.9864
16.32	0.0055	0.0072	0.9883	0.9923
8.17	0.0103	0.124	0.9910	0.9936
3.27	0.0202	0.0227	0.8984	0.9873

Table 4.16. Rate constants (k) and linear regression values (R) for the degradation and decolorization processes of the different initial concentrations of MO in the presence of 0.5M ZnO-MMT2 (500˚C).

	k (min^{-1})		**R**	
[MO] (mg/L)	**degradation**	**decolorization**	**degradation**	**decolorization**
24.55	0.0030	0.0042	0.0695	0.9917
16.32	0.0043	0.0058	0.9906	0.9962
8.17	0.0077	0.0100	0.9916	0.9963
3.27	0.0225	0.0215	0.8730	0.9947

4.9. Reuse Properties of Supported Catalysts

The stabilities of 0.5M ZnO-MMT (300˚C), 0.5M ZnO-MMT (500˚C), 0.5M ZnO-NC1 (300˚C), 0.5M ZnO-NC1 (500˚C), 0.5M ZnO-NC2 (300˚C), 0.5M ZnO-NC2 (500˚C), 0.5M ZnO-MMT2 (300˚C) and 0.5M ZnO-MMT2 (500˚C) catalysts are tested with four recycling experiments. For each cycle, the photocatalysts are filtered, washed and calcinated at 300˚C or 500˚C for 2 hours by keeping the other reaction conditions constant. After four cycles, both decolorization and degradation processes. The increment in the concentrations of MO among the cycle may be explained by the formation of by-products and their accumulation on the active surface sites of the catalysts. Also, heat treatment may cause catalyst aggregation, decrease part of the catalysts surface for both photon absorption and MO adsorption [81].

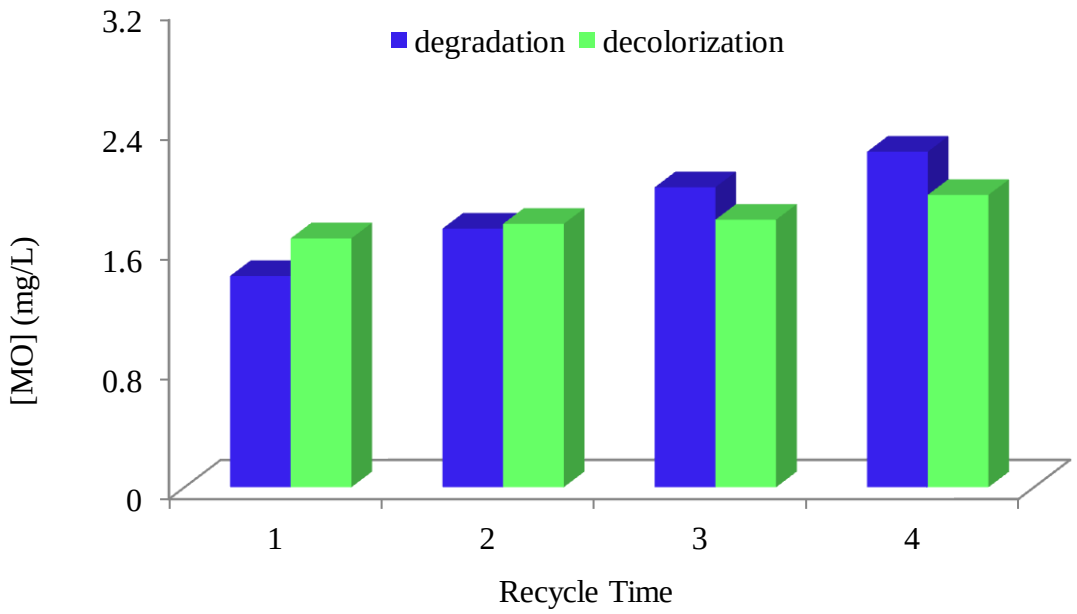


Figure 4.161. Results of recycling studies in the presence of 0.5M ZnO-MMT (300˚C). Conditions: pH: 6.5 (Natural), $[MO]_0$= 3.27 mg/L, T=298 K, Flow rate= 2000 rpm.

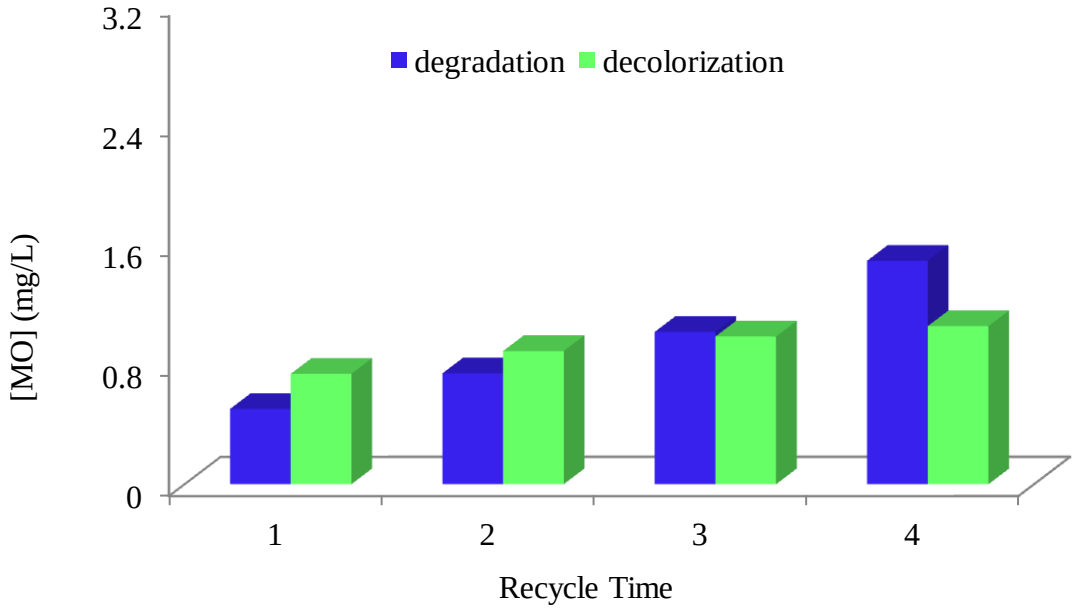


Figure 4.162. Results of recycling studies in the presence of 0.5M ZnO-MMT (500˚C). Conditions: pH: 6.5 (Natural), $[MO]_0$= 3.27 mg/L, T=298 K, Flow rate= 2000 rpm.

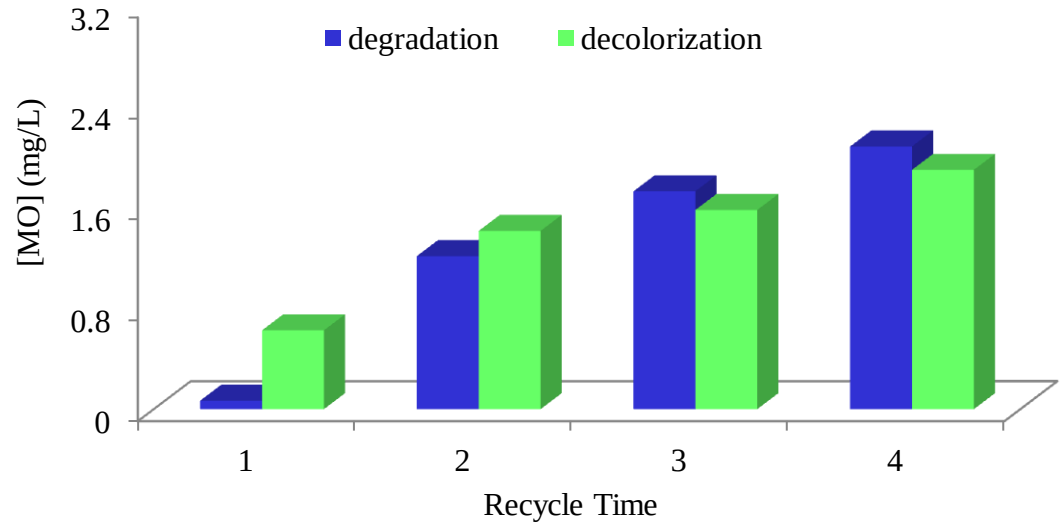


Figure 4.163. Results of recycling studies in the presence of 0.5M ZnO-NC1 (300˚C). Conditions: pH: 6.5 (Natural), $[MO]_0$= 3.27 mg/L, T=298 K, Flow rate= 2000 rpm.

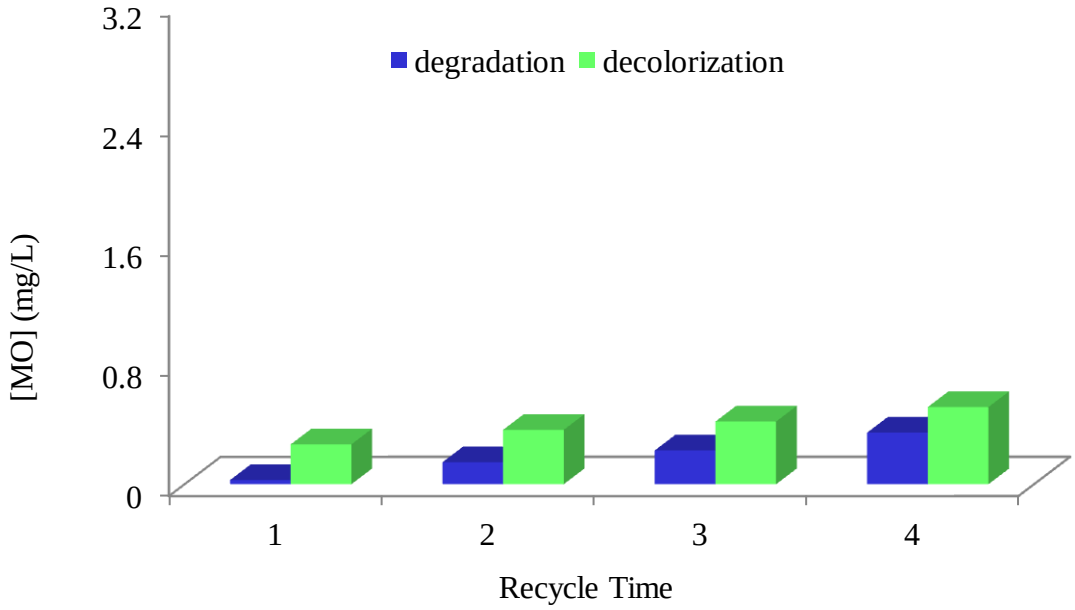


Figure 4.164. Results of recycling studies in the presence of 0.5M ZnO-NC1 (500˚C). Conditions: pH: 6.5 (Natural), $[MO]_0$= 3.27 mg/L, T=298 K, Flow rate= 2000 rpm.

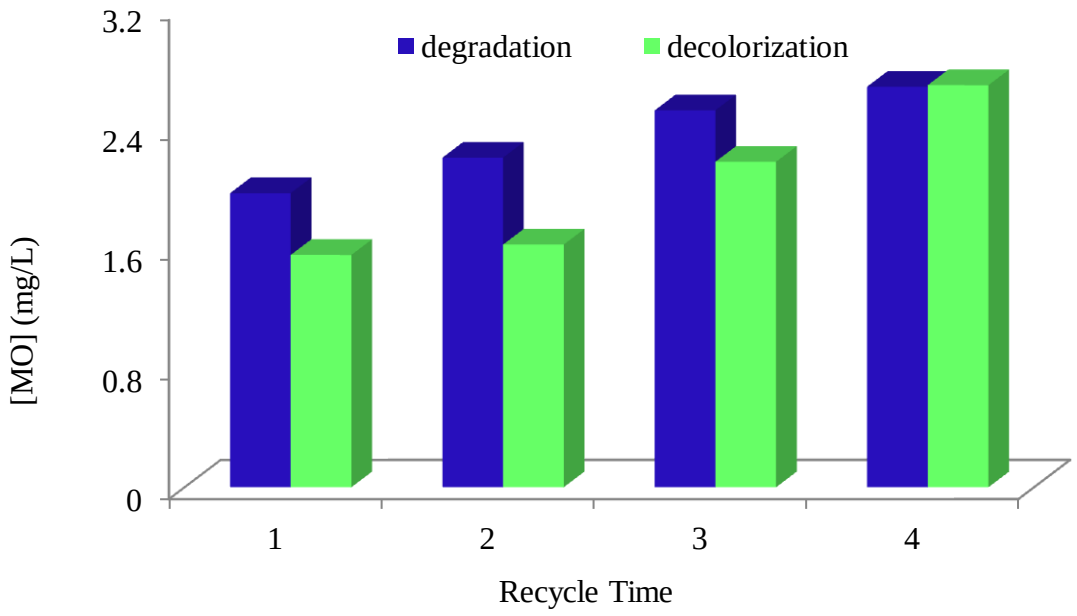


Figure 4.165. Results of recycling studies in the presence of 0.5M ZnO-NC2 (300˚C). Conditions: pH: 6.5 (Natural), $[MO]_0$= 3.27 mg/L, T=298 K, Flow rate= 2000 rpm.

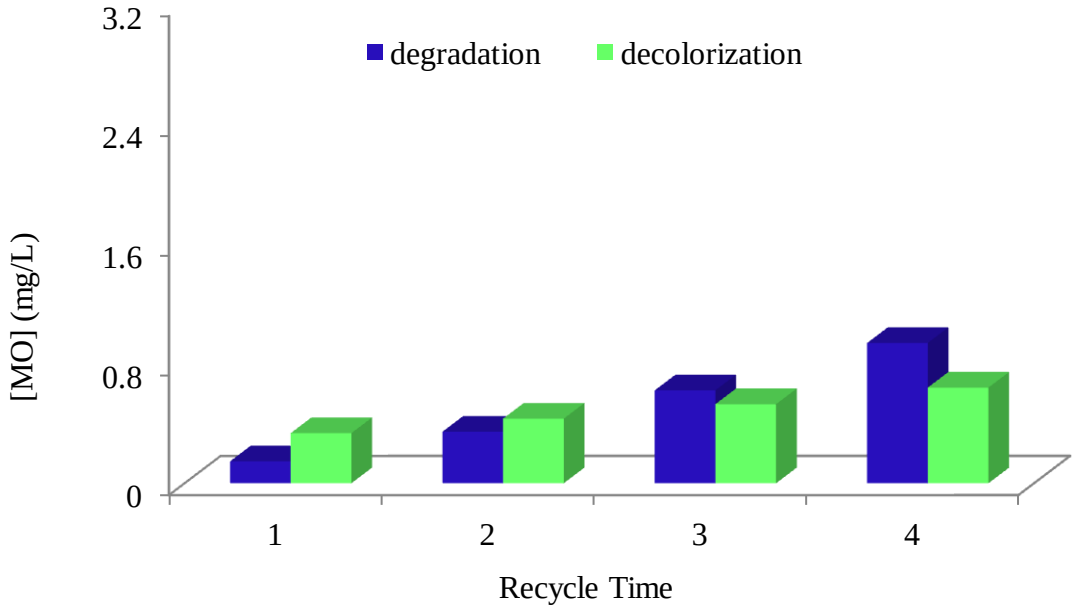


Figure 4.166. Results of recycling studies in the presence of 0.5M ZnO-NC2 (500˚C). Conditions: pH: 6.5 (Natural), $[MO]_0$= 3.27 mg/L, T=298 K, Flow rate= 2000 rpm.

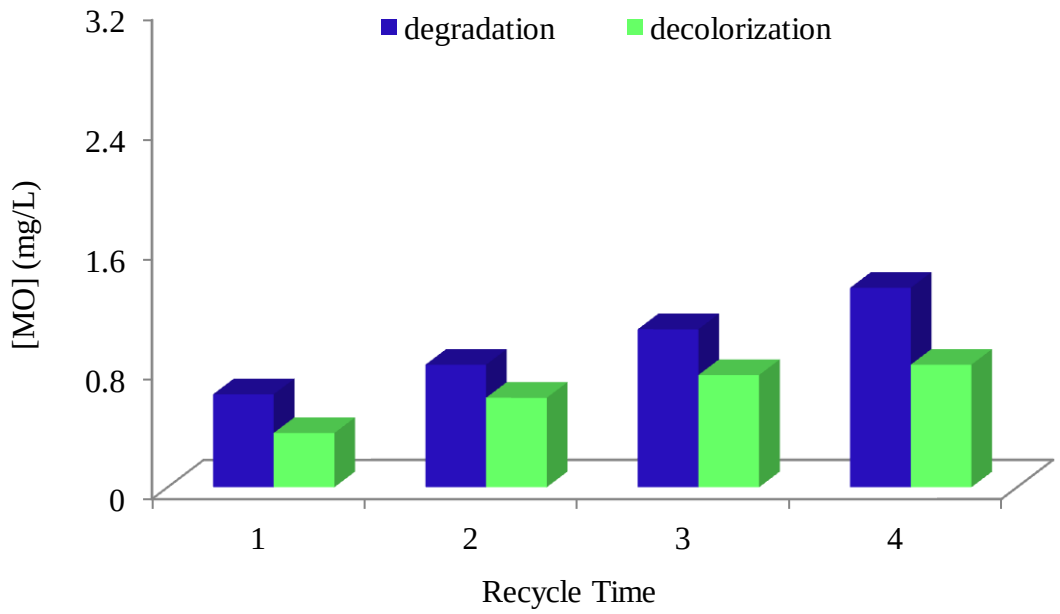


Figure 4.167. Results of recycling studies in the presence of 0.5M ZnO-MMT2 (300˚C). Conditions: pH: 6.5 (Natural), $[MO]_0$= 3.27 mg/L, T=298 K, Flow rate= 2000 rpm.

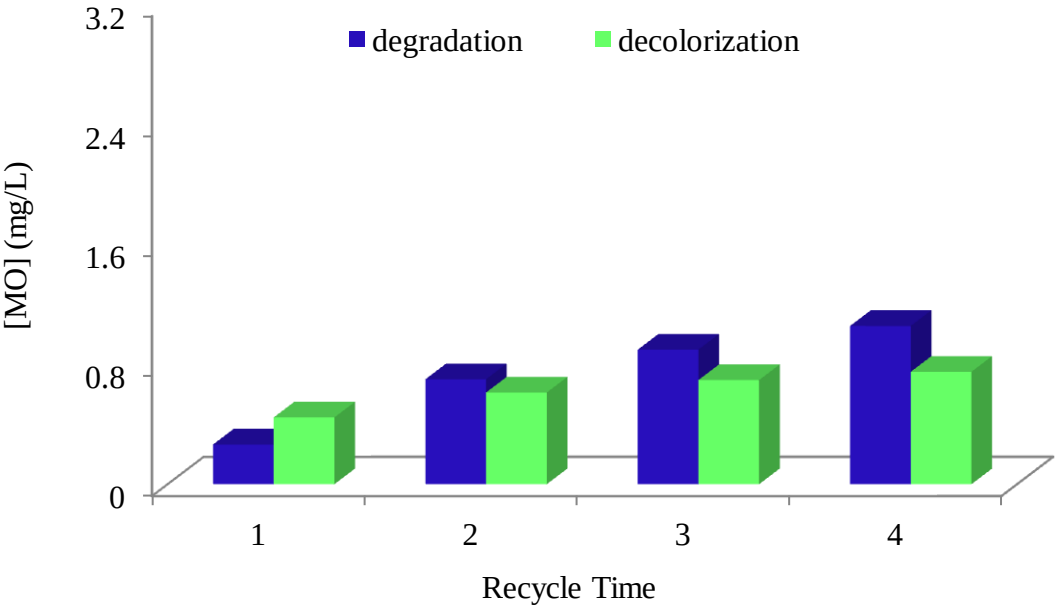


Figure 4.168. Results of recycling studies in the presence of 0.5M ZnO-MMT2 (500˚C). Conditions: pH: 6.5 (Natural), $[MO]_0$= 3.27 mg/L, T=298 K, Flow rate= 2000 rpm.

4.10. General Remarks

The characteristic (001) peaks of raw NC1, NC2 and MMT2 are noticed as 4.9˚, 4.2˚ and 2.6˚ (2θ), respectively. The corresponding d-spacing values (18.17Å for NC1, 21.22 Å for NC2 and 34.2 Å for MMT2) are found to be higher than that of raw MMT (12.8 Å). These characteristic disappeared with ZnO loading owing to the deformation of neat layered structures. Also, decrements in the high-angle peak intensities of the bare clay minerals increase with the loading concentrations of ZnO. Meanwhile, supported catalysts prepared at 300˚C reveal a peak around 8.2˚ (2θ) that referring to the tactoid formation which can be expressed as the random distribution of distracted layers.

XRD analysis also supplied information about the crystalline sizes of ZnO nanoparticles. For the catalysts prepared at 300˚C, crystalline sizes are calculated as 13.7-15.5 nm while relatively higher values (16.4-22.6 nm) are evaluated for those prepared at 500˚C. In the line of these results, it is not possible for support materials to host the ZnO crystals among their layered structures. The possible active adsorption sites can be suggested as surface-and/or-edges, comers in between the layers. Thus, the randomness of layers (tactoid formation) decreases the dark adsorption capacities of the catalysts prepared at 300˚C. The vacancies created by the calcination at 500˚C and, thus, complete loose of organic species among the layers may enhance the adsorption of MO molecules and their contact with the ZnO nanoparticles in the overall matrix.

MMT, NC1, NC2 and MMT2 show quite similar surface morphologies. ZnO loading obviously generate a variation in the images of the supports. The existence of ZnO nanoparticles is confirmed by EDX analysis, mapping and detection of ZnO adsorption edges in the UV region. Larger surface areas and wider pore volumes of the supported catalysts in comparison to the bare supports indicate formation of more active sites for the adsorption of MO molecules.

All supports show excellent adsorption abilities under dark conditions, due to their high basal spacings. Supported catalysts, however, demonstrate relatively lower dark adsorption sites of the clays. Their dark adsorption nature can be explained by the Freundlich adsorption model, where multilayer adsorption is possible. The perfect

monolayer adsorption cannot be possible due to the deformation of layers or creation of tactoids.

Under UV illumination, supported catalysts follow pseudo-first order kinetic model. Accordingly, an inverse relation exists between the rate constants and MO concentrations.

The photocatalytic activities of 0.5M ZnO loaded supports can be expressed by the following order;

0.5M ZnO-NC1 (500˚C) > 0.5M ZnO-MMT2 (500˚C) > 0.5M ZnO-NC1 (300˚C) > 0.5M ZnO-NC2 (500˚C) > 0.5M ZnO-MMT2 (300˚C) > 0.5M ZnO-MMT (500˚C) > 0.5M ZnO-MMT (300˚C) > 0.5M ZnO-NC2 (300˚C).

The trend is consistent with the results of characterization experiments. The catalysts prepared at 500˚C reveal better adsorption capabilities and degradation/decolorization efficiencies.

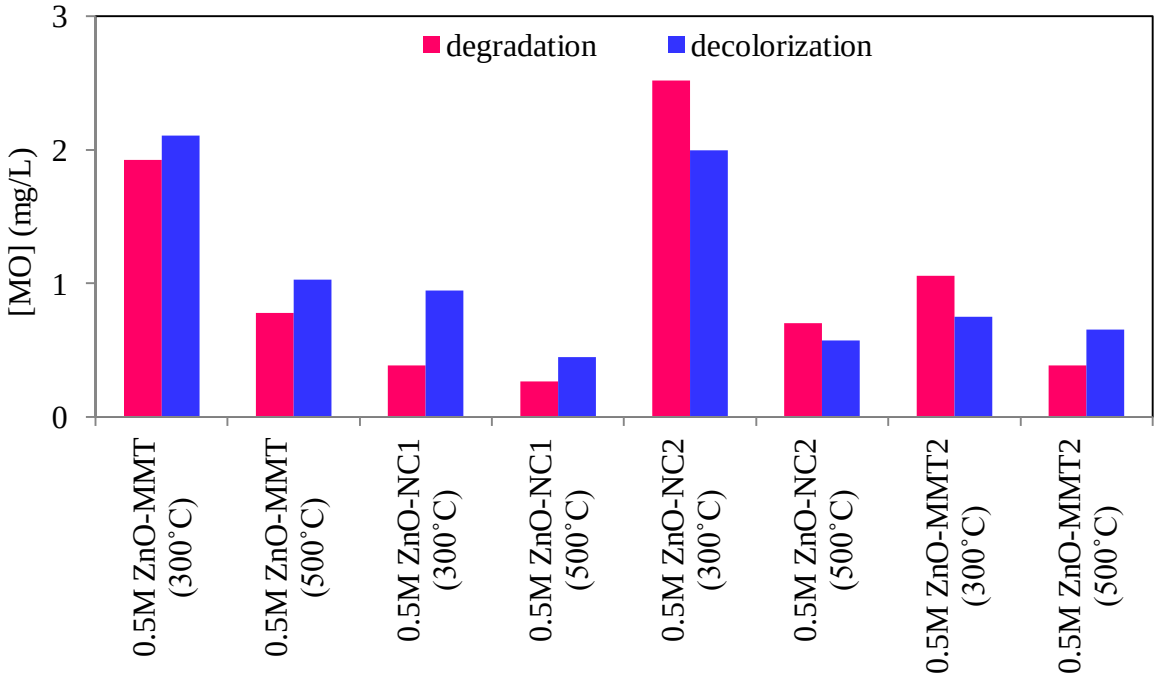


Figure 4.169. Comparison between photocatalytic activities of supported catalysts. Conditions: pH= 6.5 (Natural), $[MO]_0$= 3.27 mg/L, T= 298 K, Flow rate= 2000 rpm.

5. CONCLUSION

This study focuses on the characterization and photo catalytic activity of ZnO loaded commercially available (MMT, NC1, and NC2) and laboratory prepared (MMT2) supports prepared at two different temperatures (300˚C and 500˚C). The following general remarks can be made from our detailed characterization analysis and experiments under UV irradiation.

The characteristic ZnO diffractions are clearly observed with the decrement in the reflections of raw MMT, NC1, NC2 and MMT2 which indicates uniform distribution of ZnO nanoparticles, in both calcination temperatures. ZnO formation is more intensely occurred at the catalysts prepared at 500˚C than 300˚C. Tactoid formation is also detected for the catalysts prepared at 300˚C. Moreover, Zn existence is evidenced by EDX and elemental mapping analysis. The mesoporous structure of the clays is remained after ZnO loading; surface areas and pore sizes of the supported catalysts increased with respect to the raw clays. Slight decrease in the band-gap energies of the supported catalysts is a sign of activity in the visible region. Among all, the catalysts prepared at 500˚C show the best dark adsorption ability due to the decomposition of the organic material between the destructed layers. Freundlich adsorption model is found to be more convenient to describe adsorption processes of the supported catalysts under dark conditions. Additionally, the dark adsorption capacities of the catalysts prepared at 300˚C fit to the pseudo-second order kinetics, while those prepared at 500˚C fit to the pseudo-first order kinetic model. Under irradiation, ZnO loading amount plays a significant role. The rate of the photocatalytic reactions obeys pseudo first order kinetics. Langmuir-Hinshelwood model is found to be applicable for such as-prepared catalysts. Reusability of the supported catalysts can be suggested up to a certain extent. Moreover, the catalysts prepared in the presence of modified clays result in higher photoactivities in comparison to ZnO loaded MMT. Among all, 0.5M ZnO-NC1 (500˚C) shows the best photocatalytic performance.

REFERENCES

1. Wu, C. H, C. L. Chang, "Decolorization of Reactive Red 2 by Advanced Oxidation Processes: Comparative Studies of Homogeneous and Heterogeneous Systems", *Journal of Hazardous Materials*, Vol. 128, pp. 265-272, 2006.

2. Fox, M. A., M. T. Dulay, "Heterogeneous Photocatalysis", *Chemical Reviews*, Vol. 93, pp. 341-357, 1993.

3. Slater, J. C., "Band Theory", *Journal of Physics and Chemistry of Solids*, Vol. 8, pp. 21-25, 1959.

4. Muslim, M., M. A. Habib, A. J. Mahmood, T. S. A. Islam, I. M. I. Ismail, "Zinc Oxide-Mediated Photocatalytic Decolorization of Ponceau S in Aqueous Suspension by Visible Light", *International Nano Letters*, Vol. 2, pp.1-9, 2012.

5. Serpone, N., "Relative Photonic Efficiencies and Quantum Yields in Heterogeneous Photocatalysis", *Journal of Photochemistry and Photobiology A: Chemistry*, Vol. 104, pp. 1-12, 1997.

6. Marshall, R., L. Wang, "Non-Metal Doping of Transition Metal Oxides for Visible-Light Photocatalysis", *Catalysis Today*, Vol. 255, pp. 111-135, 2014.

7. Battez, A. H., R. Gonzalez, J. L. Viesca, J. E. F. Machado, R. Chou, J. Riba, "CuO, ZrO_2 and ZnO Nanoparticles as Antiwear Additive in Oil Lubricants", *Wear*, Vol. 265, pp. 422-428, 2008.

8. Völz, H. G., J. Kischkewitz, P. Woditsch, A. Westerhaus, W. Griebler, M. Liedekerke, G. Buxbaum, H. Printzen, M. Mansmann, D, Rade, G. Trenczek, V. Wilhelm, S. Schwarz, H. Wienand, J. Adel, G. Adrian, K. Brandt, W. B. Cork, H. Winkeler, W. Mayer, K. Schneider, L. Leitner, H. Katherin, E. Schwab, H. Jakusch, M. Ohlinger, R. Veitch, G. Etzrodt, G. Pfaff, K. D. Franz, R. Emmet, K. Nitta, R.

Besold, H. Gaedcke, *Ullmann's Encyclopedia of Industrial Chemistry*, Wiley & Sons, New York, 2006.

9. Özgür, Ü., Y. I. Alivov, C. Liu, A. Teke, M. A. Reshchikov, S. Doğan, V. Avrutin, S. J. Cho, H. Morkoç, "A Comprehensive Review of ZnO Materials and Devices", *Journal of Applied Physics*, Vol. 98, pp. 1-103, 2005.

10. Rodnyi, P. A., I. V. Khodyuk, "Optical and Luminescence Properties of Zinc Oxide", *Optics and Spectroscopy*, Vol. 111, pp. 776-785, 2011.

11. Meng, X., Z. Qian, H. Wang, X. Gao, S. Zhang, M. Yang, "Sol–gel Immobilization of SiO_2/TiO_2 on Hydrophobic Clay and Its Removal of Methyl Orange From Water", *Journal of Sol-Gel Science and Technology*, Vol. 46, pp. 195-200, 2008.

12. Johannesson, B., *Verification of the BET-theory by Experimetal Investigations on the Heat of Adsorption*, Lund Institute of Technology, Lund, 2000.

13. Sayınsöz, E., *Characterization and Photocatalytic Activity of Sepiolite and Na-Montmorillonite-TiO_2 Catalysts*, Ms. Thesis, Bogazici University, 2006.

14. Vogel, R., P. Hoyer, H. Weller, "Quantum-Sized PbS, CdS, Ag_2S, Sb_2S_3, and Bi_2S_3 Particles as Sensitizers for Various Nanoporous Wide- Bandgap Semiconductors", *The Journal of Physical Chemistry*, Vol. 98, pp. 3183-3188, 1994.

15. Jung Y. K., S. B. Park, "Anatase-phase Titania: Preparation by Embedding Silica and Photocatalytic Activity for the Decomposition of Trichloroethylene", *Journal of Photochemistry and Photobiology A: Chemistry*, Vol. 127, pp. 117-122, 1999.

16. Yablonovitch, E., "Photonic Band-gap Structures", *Journal of the Optical Society of America B*, Vol. 10, pp. 283-295, 1993.

17. Morales, A. E., E. S. Mora, U. Pal, "Use of Diffuse Reflectance Spectroscopy for Optical Characterization of Un-supported Nanostructures", *Revista Mexicana De Fisica S*, Vol. 53, pp. 18-22, 2006.

18. Zhou, L., C. Gao and W. Xu, "Magnetic Dendritic Materials for Highly Efficient Adsorption of Dyes and Drugs", *ACS Applied Materials and Interfaces*, Vol. 2, pp. 1483–1491, 2010.

19. Zhou, L., C. Gao and W. Xu, "Magnetic Dendritic Materials for Highly Efficient Adsorption of Dyes and Drugs", *ACS Applied Materials and Interfaces*, Vol. 2, pp. 1483–1491, 2010.

20. Zhou, M., X. Gao, Y. Hu, J. Chen, X. Hu, "Uniform Hamburger-like Mesoporous Carbon-Incorporated ZnO Nanoarchitectures: One-Pot Solvothermal Synthesis, High Adsorption and Visible-Light Photocatalytic Decolorization of Dyes", *Applied Catalysis B: Environmental*, Vol.138, pp. 1-8, 2013.

21. Zhou, Li., C. Gao, W. Xu, "Magnetic Dendritic Materials for Highly Efficient Adsorption of Dyes and Drugs", *Applied Materials and Interfaces*, Vol. 2, pp. 1483-1492, 2010.

22. Kumar, S. S., P. Venkateswarlu, V. R. Rao, G. N. Rao, "Synthesis, Characterization and Optical Properties of Zinc Oxide Nanoparticles", *Interational Nano Letters*, Vol. 3, pp. 1-6, 2013.

23. Muhhtar, M., L. Munisa, R Saleh, "Co-Precipitation Synthesis and Characterization of Nanocrystalline Zinc Oxide Particles Doped with Cu^{2+} Ions", *Materials Sciences and Applications*, Vol. 3, pp. 543-551, 2012.

24. Zhao, D., J. Zhou, N. Liu, "Characterization of the Structure and Catalytic Activity of Copper Modified Palygorskite/TiO_2 (Cu^{2+}-PG/TiO_2) catalysts", *Materials Science & Engineering A*, Vol. 431, pp. 256-262, 2006.

25. Hussain, M., N. Abbas, D. Fino, N. Russo, "Novel Mesoporous Silica Supported ZnO Adsorbents for the Desulphurization of Biogas at Low Temperatures", *Chemical Engineering Journal*, Vol. 188, pp. 222-232, 2012.

26. Shaheen, W. M., N. M. Deraz, M. M. Selim, "Effect of ZnO Doping on Surface and Catalytic Properties of Manganese Oxides Supported on Alumina", *Materials Letters*, Vol. 52, pp. 130-139, 2002.

27. Raizada, P., P. Singh, A. Kumar, G. Sharma, B. Pare, S. B. Jonnalagadda, P. Thakur, "Solar Photocatalytic Activity of Nano-ZnO Supported on Activated Carbon or Brick Grain Particles: Role of Adsorption in Dye Degradation", *Applied Catalysis A: General*, Vol. 486, pp. 159-169, 2014.

28. Nezamzadeh-Ejhieh, A., S. Khorsandi, "Photocatalytic Degradation of 4-nitrophenol with ZnO Supported Nano-clinoptilolite Zeolite", *Journal of Industrial and Engineering Chemistry*, Vol. 20, pp. 937-946, 2014.

29. Nugraha, J., I. Fatimah, "Evaluation of Photodegradation Efficiency on Semiconductor Immobilized Clay Photocatalyst by Using Probit Model Approximation", *International Journal of Chemical and Analytical Science*, Vol. 4, pp. 125-130, 2013.

30. Yoneyama, H., T. Torimoto, "Titanium Dioxide/Adsorbent Hybrid Photocatalysts for Photodestruction of Organic Substances of Dilute Concentrations", *Catalysis Today*, Vol. 58, pp. 133-140, 2000.

31. Anthony, J. W., R. A. Bladh, W. Kenneth, M. C. Monte, *Handbook of Mineralogy II*, Chantilly, VA, USA, 2011.

32. Tahir, M., N. S. Amin, "Photocatalytic CO_2 Reduction with H_2O Vapors Using Montmorillonite/TiO_2 Supported Microchannel Monolith Photoreactor." *Journal of Chemical Engineering*, Vol. 230, pp. 314–327, 2013.

33. Chmielarz, L, M. Zbroja, P. Kustrowski, B. Dudek, A. Rafalska-Lasocha, R. Daiembaj, "Pillared Montmorillonites Modified with Silver." *Journal of Thermal Analysis and Calorimetry*, Vol. 77, pp. 115–123, 2004.

34. Liu, P., L. Zhang, "Adsorption of Dyes From Aqueous Solutions or Suspensions with Clay Nano-adsorbents." *Seperation and Purification Technologies*, Vol. 58, pp. 32–39, 2007.

35. Chen, K., J. Li, Y. Zhang, W. Wang, "Synthesis and Characterization of TiO_2 – Montmorillonites Doped with Vanadium and/or Carbon and Their Application for the Photodegradation of Sulphorhodamine B under UV–vis Irradiation", *Colloids and Surfaces A: Pysicochemical and Engineering Aspects,* Vol. 360, pp. 47–56, 2010.

36. Kun, R., R. Mogyorósi, R. Dékány, Imre, "Synthesis and Structural and Photocatalytic Properties of TiO_2/montmorillonite Nanocomposites", *Applied. Clay. Science,* Vol. 32, pp. 99–110. 2005.

37. Mao, H., B. Li, X. Li, L. Yue, J. Xu, B. Ding, X. Gao, Z. Zhou, "Facile Synthesis and Catalytic Properties of Titanium Containing Silica-Pillared Clay Derivatives with Ordered Mesoporous Structure Through a Novel Intra-gallery Templating Method." *Microporous and Mesoporous Materials*, Vol. 130, pp. 314–321, 2010.

38. Fatimah, I., S. Wang, D. Wulandari, "ZnO/montmorillonite for Photocatalytic and Photochemical Degradation of Methylene Blue", *Applied Clay Science*, Vol. 53, pp. 553–560, 2011.

39. NanoAll, *Nano Clay Applications*, 2010, http://nanoall.blogspot.com.tr/2010/11/nano-clay-applications.html, [Accessed April 2014].

40. Shi, H., T. L. Thomas, J. Pinnavaia, "Interfacial Effects on the Reinforcement Properties of Polymer-Organoclay Nanocomposites", *Chemistry of Materials*, Vol. 8, pp. 1584-1587, 1996.

41. Chen, J. H., M. C. Yang, "Preparation and Characterization of Nanocomposite of Maleated Poly(butylene adipate-co-terephthalate) with Organoclay", *Materials Science and Engineering C*, Vol. 46, pp. 301-308, 2015.

42. Beall, G. W., "The Use of Organo-Clays in Water Treatment", *Applied Clay Science*, Vol. 24, pp. 11-20, 2003.

43. Santano, P., R. Trujillano, C. Belver, A. Gil, M. A. Vicente, "Effect of the Intercalation Conditions of a Montmorillonite with Octadecylamine", *Journal of Colloid and Interface Science*, Vol. 284, pp. 239-244, 2005.

44. Gieseking, J. E., "The Mechanism of Cation Exchange in the Montmorillonite–Beidellite–Nontronite Type of Clay Minerals", *Soil Science*, Vol. 47, pp. 1-14, 1939.

45. Jordan, J. W., "Organophilic Bentonites I. Swelling in Organic Liquids", *Journal of Physical Chemistry*, Vol. 53, pp. 294-306, 1949.

46. Chou, C. C., J. L. McAtee, "Thermal Decomposition of Organo-ammonium Compounds Exchanged onto Montmorillonite and Hectorite", *Clays and Clay Minerals*, Vol. 17, pp. 339-346, 1969.

47. Xie, W., Z. Gao, K. Liu, W. P. Pan, R. Vaia, D. Hunter, A. Singh, "Thermal Characterization of Organically Modified Montmorillonite", *Thermochimica Acta*, Vol. 367, pp. 339-350, 2001.

48. Beall, G. W., "The Use of Organo-clays in Water Treatment", *Applied Clay Science*, Vol. 24, pp. 11-20, 2003.

49. Yalçın, M, A. Gürses, Ç. Doğar, M. Sözbilir, ”The Adsorption Kinetics of Cethyltrimethylammonium Bromide (CTAB) onto Powdered Active Carbon”, *Adsorption*, Vol. 10, pp. 339-348, 2004.

50. Beall, G. W., M. Goss, “Self-assembly of Organic Molecules on Montmorillonite”, *Applied Clay Science*, Vol. 27, pp. 179-186, 2004.

51. Santano, P., R. Trujillano, C. Belver, A. Gil, M. A. Vicente, “Effect of the Intercalation Conditions of a Montmorillonite with Octadecylamine”, *Journal of Colloid and Interface Science*, Vol. 284, pp. 239-244, 2005.

52. Capkova, P., M. Pospisil, M. Valaskova, D. Merinska, M. Trchova, Z. Sedlakova, Z. Weiss, J. Simonik, “Structure of Montmorillonite Cointercalated with Stearic Acid and Octadecylamine: Modeling, Diffraction, IR Spectroscopy”, *Journal of Colloid and Interface Science*, Vol. 300, pp. 264-269, 2006.

53. Ha, R. S., K. Y. Rhee, H. C. Kim, J. T. Kim, “Fracture Performance of Clay/epoxy Nanocomposites with Clay Surface-modified Using 3-aminopropyltriethoxysilane”, *Colloids and Surfaces A: Physicochemical and Engineering Aspects*, Vol. 313, pp. 112-115, 2008.

54. Ha, S. R., S. H. Ryu, S. J. Park, K. Y. Rhee, “Effect of Clay Surface Modification and Concentration on the Tensile Performance of Clay/epoxy Nanocomposites”, *Materials Science & Engineering A*, Vol. 448, pp. 264-268, 2007.

55. Ha, S. R., K. Y. Rhee, “Effect of Surface-modification of Clay Using 3-Aminopropropyltriethoxysilane”, *Colloids and Surfaces A: Physicochemical and Engineering Aspects*, Vol. 322, pp. 1-5, 2008.

56. Wicklein, B., M. Darder, P. Aranda, E. Ruiz-Hitzky, “Bio-organoclays Based on Phospholipids as Immobilization Hosts for Biological Species”, *Langmuir Article*, Vol. 26, pp. 5217-5225, 2010.

57. Fatimah, I. S. Wang, D. Wulandari, "ZnO/montmorillonite for Photocatalytic and Photochemical Degradation of Methylene Blue", *Applied Clay Science*, Vol 53, pp. 553-560, 2011.

58. Mana, M., M. S. Ouali, L. C. Menorval, J. J. Zajac, C. Charnay, "Regeneration of Spent Bleaching Earth by Treatment with Cethyltrimethylammonium Bromide for Application in Elimination of Acid Dye", *Chemical Engineering Journal*, Vol. 174, pp. 275-280, 2011.

59. Chen, J. H., M. C. Yang, "Preparation and Characterization of Nanocomposite of Maleated Poly(butylene adipate-co-terephthalate) with Organoclay", *Materials Science and Engineering C*, Vol. 46, pp. 301-308, 2015.

60. Khumchoo, N., N. Khaorapapong, M. Ogawa, "Formation of Zinc Oxide Particles in Cetyltrimethylammonium-smectites", *Applied Clay Science*, Vol. 105, pp. 236-242, 2015.

61. Patil, S. P., V. S. Shrivastava, G. H. Sonawane, "Photocatalytic Degradation of Rhodamine 6G Using ZnO-montmorillonite Nanocomposite: A Kinetic Approach", *Desalination and Water Treatment*, Vol. 54, pp. 374-381, 2015.

62. Dai, S., Y. Zuhang, L. Chen, "Study on the Relationship Between Structure of Synthetic Organic Chemicals and Their Biodegradability", *Environmental Chemistry*, Vol. 14, pp. 354-67, 1995.

63. S. Anandan, A. Vinua,, K. L. P. Sheeja Lovely, N. Gokulakrishnan, P. Srinivasu, T. Mori, V. Murugesan, V. Sivamurugan, K. Ariga, "Photocatalytic Activity of La-doped ZnO for the Degradation of Monocrotophos in Aqueous Suspension", *Journal of Molecular Catalysis A: Chemical*, Vol. 266, pp. 149–157, 2007.

64. Sayinöz, E., "*Characterization and Photocatalytic Activity of Sepiolite-TiO_2 and Na Montmorillonite-TiO_2-catalyst*", M.S. Thesis, Bogazici University, 2006.

65. Ökte, A. N., "Characterization and Photocatalytic Activity of Ln (La, Eu, Gd, Dy and Ho) Loaded ZnO Nanocatalysts", *Applied Catalysis A: General*, Vol. 475, pp. 27-39, 2014.

66. Is, F., S. Wang, V. Narsito, K. Wijaya, "Composites of TiO_2-aluinum Pillared Montmorillonite: Synthesis, Characterization and Photocatalytic Degradation of Methylene Blue", *Applied Clay Science*, Vol. 50, pp. 588-593, 2010.

67. Morgan, A. B., J. W. Gilman, "Characterization of Polymer-Layered Silicate (Clay) Nanocomposites by Transmission Electron Microscopy and X-Ray Diffraction: A Comparative Study", *Journal of Applied Polymer Science*, Vol. 87, pp. 1329-1338, 2003.

68. Chen, Y. F., C. Y. Lee, M. Y. Yeng, H. T. Chiu, "The Effect of Calcinations Temperature on the Crystallinity of TiO_2 Nanopowders", *Journal of Crystal Growth*, Vol. 247, pp. 363-370, 2003.

69. Ha, S. R., S. H. Ryu, S. J. Park, K. Y. Rhee. "Effect of Clay Surface Modification and Concentration on the Tensile Performance of Clay/epoxy Nanocomposites", *Materials Science & Engineering A*, Vol. 448, pp. 264-268, 2007.

70. Is, F., S. Wang, Narsito, K. Wijaya, "Composites of TiO_2-aluinum Pillared Montmorillonite: Synthesis, Characterization and Photocatalytic Degradation of Methylene Blue", *Applied Clay Science*, Vol. 50, pp. 588-593, 2010.

71. Damardji, B., H. Khalaf, L. Duclaux, B. David, "Preparation of TiO_2-pillared Montmorillonite as Photocatalyst Part I. Microwave Calcination, Characterization, and Adsorption of a Textile Azo Dye", *Applied Clay Science*, Vol. 44, pp. 201-205, 2009.

72. Morgan, A. B., J. W. Gilman, "Characterization of Polymer-Layered Silicate (Clay) Nanocomposites by Transmission Electron Microscopy and X-Ray Diffraction: A Comparative Study", *Journal of Applied Polymer Science*, Vol. 87, pp. 1329-1338, 2003.

73. Ha, S. R., S. H. Ryu, S. J. Park, K. Y. Rhee. "Effect of Clay Surface Modification and Concentration on the Tensile Performance of Clay/epoxy Nanocomposites", *Materials Science & Engineering A*, Vol. 448, pp. 264-268, 2007.

74. Is, F., S. Wang, Narsito, K. Wijaya, "Composites of TiO_2-aluminum Pillared Montmorillonite: Synthesis, Characterization and Photocatalytic Degradation of Methylene Blue", *Applied Clay Science*, Vol. 50, pp. 588-593, 2010.

75. Damardji, B., H. Khalaf, L. Duclaux, B. David, "Preparation of TiO_2-pillared Montmorillonite as Photocatalyst Part I. Microwave Calcination, Characterization, and Adsorption of a Textile Azo Dye", *Applied Clay Science*, Vol. 44, pp. 201-205, 2009.

76. Morgan, A. B., J. W. Gilman, "Characterization of Polymer-Layered Silicate (Clay) Nanocomposites by Transmission Electron Microscopy and X-Ray Diffraction: A Comparative Study", *Journal of Applied Polymer Science*, Vol. 87, pp. 1329-1338, 2003.

77. Ha, S. R., S. H. Ryu, S. J. Park, K. Y. Rhee. "Effect of Clay Surface Modification and Concentration on the Tensile Performance of Clay/epoxy Nanocomposites", *Materials Science & Engineering A*, Vol. 448, pp. 264-268, 2007.

78. Is, F., S. Wang, Narsito, K. Wijaya, "Composites of TiO_2-aluinum Pillared Montmorillonite: Synthesis, Characterization and Photocatalytic Degradation of Methylene Blue", *Applied Clay Science*, Vol. 50, pp. 588-593, 2010.

79. Damardji, B., H. Khalaf, L. Duclaux, B. David, "Preparation of TiO_2-pillared Montmorillonite as Photocatalyst Part I. Microwave Calcination, Characterization, and Adsorption of a Textile Azo Dye", *Applied Clay Science*, Vol. 44, pp. 201-205, 2009.

80. Morgan, A. B., J. W. Gilman, "Characterization of Polymer-Layered Silicate (Clay) Nanocomposites by Transmission Electron Microscopy and X-Ray Diffraction: A

Comparative Study", *Journal of Applied Polymer Science*, Vol. 87, pp. 1329-1338, 2003.

81. Ökte, A. N., "Characteristic and Photocatalytic Activity of Ln (La, Eu, Gd, Dy and Ho) Loaded ZnO Nanocatalysts", *Applied Catalysis A: General*, Vol. 475, pp. 27-39, 2014.